High throughput manufacturing of nanoparticles by membrane emulsification-precipitation processes

Medina Llamas, Maria

Award date:
2018

Awarding institution:
University of Bath

High throughput manufacturing of nanoparticles by membrane emulsification-precipitation processes

María de la Luz Medina Llamas

A thesis submitted for the degree of Doctor of Philosophy

University of Bath

Department of Chemical Engineering

September 2018

Acknowledgments

I would like to express my deepest gratitude to my supervisor Davide Mattia, who his continuous support and guidance helped me to fulfil one of the most enriching experiences in my life. For the opportunities he gave me to attend conferences and be involved in different collaborative work. But I thank him the most, for his advice and patience when I needed.

I'm grateful to my parents who´s constant love and unconditional support encouraged me to accomplish my goals. I'm deeply thankful to my siblings Juan Carlos and Verónica, for your love, support.

Thanks to Anyela, Alin, Lili, Salida and Yen, my dearest friends, who became my family in UK; your friendship, laughs and support helped me to go throughout all these years. I will always cherish the time I shared with you. I would like to thank Mariano and Abouther, for keeping me laughing and smiling on the long office days, while they were trying to teach me Italian and Arab.

I must extend my gratitude to the technical team of the Chemical Engineering Department, Alex Ciupa, Brigite Simões, Daniel Lou-Hing, Fernando Acosta, John Bishop, Robert Brain and Paul Frith, my work wouldn't be possible without your constant support and expertise. Thanks to the technical team of the Microscopy Analysis Suite, Philip Fletcher and Ursula Potter, for your invaluable help and advice over the course of my PhD. Similarly, I would like to thanks Rémi Castaing for his kind help in the characterization of my samples.

Finally, I would like to thank the Mexican National Council for Science and Technology (CONACYT) for the doctoral scholarship granted.

Abstract

The large-scale production of nanomaterials with fine control over their shape, size and properties remains a major obstacle towards their further use in a wide range of industrial applications. Therefore, the aim of the present PhD thesis is to assess the manufacturing of metal oxide NPs at large-scale using a membrane emulsification (ME)-precipitation process.

In the project, flat and ring-shaped anodic alumina membranes (AAMS) were fabricated and their synthesis conditions optimised to obtain membranes with a narrow pore size distribution. Flat AAMs were used to produce *oil-in-water* nanoemulsions (NEs) in a dead-end stirred cell ME setup for the first time. Results show the regular pore structure and narrow pore size distribution of the AAMs enabled the formation of NEs with narrow droplet size distributions. The results demonstrated that rotational speed and membrane pore size were the key parameters in controlling the droplet size, with droplets as small as 144 ± 18 nm obtained, when D_{pore} = 58 ± 6 nm. Low proportionality values, $D_{droplet}/D_{pore}$, ranging from 1.8 to 3.5, were obtained. Ring-shaped AAMs (D_p = 77 ± 9 nm) were synthetized for the first time with the purpose of producing *oil-in-water* NEs using a commercial stirred ME setup operating in a dead-end configuration. A systematic investigation of process parameters showed that narrow NEs were produced, obtaining proportionality constant values, as small as 2.8. Then, it was first reported the production of metal oxide NPs using an *oil-in-water* ME-precipitation process that can be easily scaled-up. For instance, we synthesized hematite NPs in a commercial dead-end ME setup fitted with a ring-shaped AAM and operating in a semi-continuous mode. The average primary particle size was 4.2 ± 0.5 nm and 18 ± 4 nm for the as-synthetized and calcined hematite NPs, respectively. Nevertheless, drying and calcination of the NPs leads to the formation of clusters in the micrometre range. Calculations of the emulsion production rate demonstrate the potential of the ME setup to produce up to 1.4 kg of per hour per metre square of membrane. Then, TiO_2 NPs were synthesized in a continuous ME setup operating in a crossflow configuration, with the intention to produce NPs in a larger scale, with an average primary particle size ranging from 9.7 to 13.4 nm. The results show this manufacturing method can produce up to 2.8 kg NPs per hour per metre square of membrane. Non-metal doping was investigated, the results demonstrated the successful incorporation of interstitial nitrogen and carbon in the TiO_2 lattice and showing a reduction of 1.05 eV in the band gap, which results in the formation of TiO_2 NPs with photocatalytic response in the visible light spectrum.

List of publications and presentations

Peer-reviewed journal articles:

Medina-Llamas, M., & Mattia, D. (2017). Production of nanoemulsions using anodic alumina membranes in a stirred-cell setup. *Industrial & Engineering Chemistry Research*, *56* (26), 7541-7550. The results of the publication are presented in Chapter 5.

Ramirez-Canon, A., **Medina-Llamas, M**., Vezzoli, M., & Mattia, D. (2018). Multiscale design of ZnO nanostructured photocatalysts. *Physical Chemistry Chemical Physics*, *20* (9), 6648-6656.

Duran, N. M., **Medina-Llamas, M.,** Cassanji, J. G., de Lima, R. G., de Almeida, E., Macedo, W. R., & Pereira de Carvalho, H. W. (2018). Bean seedling growth enhancement using magnetite nanoparticles. *Journal of agricultural and food chemistry*.

Medina-Llamas, M., & Mattia, D. (2019). Semi-continuous production of iron oxide nanoparticles via membrane emulsification. *Applied Surface Science*, *463*, 504-512. The results of the publication are presented in Chapter 6.

In preparation:

Continuous production of titania nanoparticles via crossflow membrane emulsification-precipitation. The results of the publication are presented in Chapter 7.

Conferences:

Medina-Llamas, M., Mattia, D. 2015. Controlled production of nanoemulsions using AAMs in a stirred-cell setup. Neuromembrane. Aachen, Germany, September 6th – 10th.

Medina-Llamas, M., Mattia, D. 2016. Controlled production of nanoemulsions using AAMs in a stirred-cell setup. ChemEngday UK. Bath, United Kingdom, April 6th.

Medina-Llamas, M., Mattia, D. 2016. Controlled production of nanoemulsions using AAMs in a stirred-cell setup. The 14th International Conference on Inorganic Membranes, Atlanta, United States of America, July 10th – 13th.

Medina-Llamas, M., Mattia, D. 2017. Synthesis of nanoparticles by membrane emulsification. BATH-YONSEI Workshop 2017. Partaking Innovations in Separations, Catalysis and Porous Materials. February 16th and 17th.

Table of contents

List of Figures

List of tables

Abbreviations

AAMs	Anodic alumina membranes
BE	Binding energy/eV
BSE	Back-scattered electrons
CTAB	cetyltrimethylammonium bromide (surfactant)
DFT	Density functional theory
DLS	Dynamic light scattering
DI	Deionized water
FFT	Fast Fourier transformation
FT-IR	Fourier-transform infrared spectroscopy
FWHM	Full width half maximum
HLB	Hydrophilic-lipophilic balance
HOMO	Highest occupied molecular orbital
IFT	Interfacial tension
LUMO	Lowest unoccupied molecular orbital
ME	Membrane emulsification
NEs	Nanoemulsions
NPs	Nanoparticles
o/w	Oil-in-water
SDS	Sodium dodecyl sulphate (surfactant)
SE	Secondary electrons
SFO	Sunflower oil
SEM	Scanning electron microscope
SPG	Shirasu porous glass
TEM	Transmission electron microscopy
UV-Vis	Ultraviolet visible spectroscopy
w/o	Water-in-oil
XPS	X-ray photon electron spectroscopy
XRD	X-ray diffraction spectroscopy

Nomenclature

		Units
A_{mem}	Membrane area	mm^2
b	Blade height	m
c	Proportionality constant of droplet diameter to pore diameter	-
Ca	Capillary number	-
Ca_{crit},	Critical capillary number	-
D_s	Surfactant diffusion coefficient	$m^2\ s^{-1}$
D_{AAM}	Average domain size in an AAM	μm^2
D_i	Impeller diameter	m
D_c	Interpore distance	nm
D_d	Droplet diameter	nm
D_h	Hydrodynamic diameter	m
d_h	Interplanar distance	nm
D_p	Pore diameter	nm
D_{NP}	Nanoparticle diameter	nm
D_{XRD}	Nanoparticle crystal size	nm
E	Energy	J
Eu	Euler number	-
f	Correlation friction factor	-
F_B	Buoyancy force	N
F_D	Drag force	N
F_i	Inertial force	N
F_L	Dynamic lift force	N
F_{st}	Static pressure force	N
F_γ	Interfacial tension force	N
g	Gravitational constant, 9.81	$m\ s^{-2}$
h	Droplet height	m
h_k	Constant of the Carman-Kozeny equation,4.5	-
h_p	Planck's constant, $9.26x10^{-34}$	$J\ s^{-1}$
J	Membrane volumetric flux	$m^3\ m^{-2}\ s^{-1}$
J_d	Dispersed phase flux	$m^3\ m^{-2}\ s^{-1}$
K	Shape factor in Scherrer equation, 0.9	-
k	Boltzmann's constant,1.38×10^{-23}	$m^2\ kg\ s^{-2}\ K^{-1}$

k_{act}	Fraction of active pores	-
k_{max}	Maximum fraction of active pores	-
K_s	Surfactant mass transfer coefficient	m s^{-1}
k_x	Coeficiente de corrección de la ley de Stokes	-
M_w	Surfactant molecular weight	g mol^{-1}
$\dot{m_{hem}}$	Nanoparticle mass production rate	m^3 h m^{-2}
N	Impeller rotational speed	rps
n	Pore density	pores m^{-2}
n_b	Number of blades	-
ΔP	Transmembrane pressure	Pa
P_c	Continuous phase pressure	Pa
$P_{c\text{-in}}$	Pressures of the continuous phase at the inlet of the membrane module	Pa
$P_{c\text{-out}}$	Pressures of the continuous phase at the outlet of the membrane module	Pa
P_{cap}	Capillary pressure	Pa
P_d	Dispersed phase pressure	Pa
Q_d	Flow rate of the dispersed phase	m^3 s^{-1}
Re	Reynolds number	-
R_g	Surfactant gyration radius	nm
r_c	Critical radius	m
r_d	Droplet radio	m
r_p	Pore radio	m
U	Anodization potential	V
V_D	Droplet volume	m^3
v_d	Velocity of the dispersed phase	m s^{-1}
V_g	Volume of the droplet in the growth stage	m^3
t	Droplet formation time	s
T	Temperature	K
t_f	Droplet formation time	s
t_a	Time of the first anodization	h
t_d	Duration of the detachment period	s
T_D	Tank diameter	m
W	Wall thickness	nm
We	Weber number	-
We_c	Critical weber number	-

Greek alphabet symbols

β	Line broadening in Scherrer equation	rad
γ	Interfacial tension	mN m^{-1}
ε	Membrane porosity	-
θ	Contact angle between a dispersed phase droplet and the membrane surface	degrees
λ	Incident wavelength	nm
λ_p	Proportionality constant of pore diameter to anodization potential	-
λ_c	Proportionality constant of interpore distance to anodization potential	-
δ	Boundary layer thickness	m
δ_{act}	Membrane active layer thickness	µm
κ_m	Membrane resistance coefficient	m^{-1}
μ_c	Dynamic viscosity of the continuous phase	Pa s
μ_d	Dynamic viscosity of the dispersed phase	Pa s
ν	Frequency	s^{-1}
ρ_c	Density of the continuous phase	kg m^{-3}
ρ_d	Density of the dispersed phase	kg m^{-3}
$\rho_{hematite}$	Density of hematite, 5.03	g cm^{-3}
$\rho_{titania}$	Density of titanium dioxide, 4.23	g cm^{-3}
τ_w	Shear stress	Pa
Ψ	Membrane tortuosity	-
ω	Angular speed	rad s^{-1}

Chapter 1: Introduction

Nanotechnology is a broad interdisciplinary area of research, development and industrial activity that has been growing rapidly worldwide for the past decades. It involves the manufacture, processing and application of materials that are in the size range of up to 100 nm (Aitken et al., 2006). Due to their small size, nanoparticles exhibit different or enhanced properties compared to bulk materials with the same chemical composition. This has led to an extensive research worldwide to study the fundamental properties of nanoparticles and their practical applications (Tsuzuki, 2009). Despite this strong interest, progress, in this area, in translating scientific innovations from the laboratory to commercially available products has been slow due to a lack of methods to manufacture nanoparticles at large-scale that provides a high control over the properties of the material. Although there are already a number of nanoparticle-based consumer products available on the market (Willems, 2005), these are limited to just a few of nanomaterials. For instance, Table 1.1 show the estimated production per year of ten nanomaterials worldwide, while Table 1.2 shows the distribution of these nanomaterials in different commercial products.

Table 1.1 Estimated production of few nanomaterials.

Nanomaterial	Production/t $year^{-1}$			
	Worldwide	Europe	US	Switzerland
	Median and 25/75 percentile (Piccinno et al., 2012)		(Hendren et al., 2011)	(Schmid and Riediker, 2008)
TiO_2	3 000 (550 - 5 000)	550 (55 - 3 000)	7 800 - 38 000	435
ZnO	550 (55 - 500)	55 (5.5 - 28 000)		70
SiO_2	5 500 (55 - 50 000)	5 500 (55 - 55 000)		75
Fe_xO_y	55 (5.5 - 550)	550 (30 - 5 550)		365
Al_xO_y	55 (5.5 - 550)	550 (0.55 - 500)		0.005
Ce_xO_y	55 (5.5 - 550)	550 (0.55 - 2 800)	35 - 700	1

Carbon Nanotubes	300 (55 - 550)	550 (180 - 550)	55 - 1 101	3.1
Fullerenes	0.6 (0.6 - 5.5)	0.6 (0.6 - 5.5)	2 - 8	
Ag	55 (5.5 - 550)	5.5 (0.6 - 5.5)	2.8 - 20	
Quantum dots	0.6 (0.6 - 5.5)	0.6		

Table 1.2 Distribution of each nanomaterials in commercials products (Piccinno et al., 2012).*

Nanomaterial	Application	% of total use
TiO_2	Cosmetics (incl. sunscreens)	70 - 80
	Coating, cleaning agents	< 20
	Plastics	< 20
	Paints	10 - 30
	Cement	1
	Others	< 10
ZnO	Cosmetics (incl. sunscreens)	70
	Paints	30
Ce_xO_y	Chemical mechanical planarization	45 - 80
	Fuel catalyst	1 - 50
	UV-coatings, paints	5 - 10
Carbon nanotubes	Composites and polymer additives	20
	Materials	80
	Composites	50
	Batteries	50
Fullerenes	Research and development	80
Ag	Paints, coatings and cleaning agents	10 - 30
	Textiles	30 - 50
	Consumer electronics and conductivity	10 - 20
	Cosmetics	20
	Medical technology	20
	Anti-microbial coating	80 - 100

*Each line represents different answers obtained from nanomaterial suppliers therefore; the percentages do not sum up to 100%.

The tabulated data show, for instance, that titanium dioxide is the most produced nanomaterial worldwide, with an estimated production of up to 3 000 ton/year (Piccinno et al., 2012), being the main current nanoparticle-based consumer products: cosmetics, paints and cleaning agents; which are relatively simple applications where a high control over the properties of nanoparticles is not required. Nevertheless, there is a wide range of laboratory-based applications where, for instance, TiO_2 NPs have a superior performance, but a high control over its properties is required. For instance, TiO_2 it is an outstanding material in the degradation of organic compounds in aqueous systems (Linsebigler et al., 1995) and a promising photocatalytic material for hydrogen production by water splitting (Ni et al., 2007). Other reports show its ability to destroy cancer cells (Kalbacova et al., 2008), bacteria (Wei et al., 1994) and even to carry out the photocatalytic reduction of CO_2 to produce higher carbon chain molecules such as methane, methanol and formaldehyde, in which the conversion of CO_2 can be considered in view of climate remediation by reducing greenhouse gases and obtain the additional benefit of producing useful chemicals (Paramasivam et al., 2012). The former examples demonstrate that to take such innovations to improve people's life, the large-scale production of bespoke nanoparticles is necessary; as the performance of nanomaterials depends on their properties.

Undoubtedly, the gap between fundamental research relating nanomaterials and their application in real life will be exceeded in the future. However, it will be necessary to overcome significant challenges by setting up a small number of synthesis techniques that allow a controlled production of nanoparticles, using an environmentally friendly approach, while considering aspects such as occupational and safety regulations, as there is substantial experimental evidence of the toxicity of the nanoparticles based on their size (Dowling et al., 2004). With this concern and to overcome the challenges mentioned above, we propose to investigate the large-scale production of metal oxide nanoparticles using a membrane emulsification method.

1.1 Overall aim

The large-scale manufacturing of nanoparticles with bespoke properties is still at an early stage of development. The main reason is the lack of understanding on how to combine a fine control of nanomaterials' properties and their large-scale production. Therefore, the overall aim of the present PhD project is to assess the manufacturing

of metal oxide nanoparticles at large-scale using a membrane emulsification-precipitation process. To do so, each aspect involved in the synthesis of the nanoparticles, from the manufacturing of the membrane to the production of the nanoemulsions, was investigated.

To fulfil the overall aim, several specific objectives were established:

- Fabricate flat and ring-shaped anodic alumina membranes and investigate the effect of different synthesis conditions on the membrane morphology and, thus, obtain membranes with a narrow pore size and size distribution.
- Fabricate a membrane emulsification setup operating in a dead-end configuration and use flat anodic alumina membranes to produce *oil-in-water* nanoemulsions. Then evaluate the main parameters that influence the emulsion droplet size and size distribution.
- Use a commercial stirred-cell membrane emulsification setup to evaluate the production of *oil-in-water* nanoemulsions using bespoke ring-shaped anodic alumina membranes. Then, asses the production of nanoemulsions with a narrow droplet size distribution by varying different parameters, i.e. rotational speed, type of surfactant.
- Modify the commercial membrane emulsification setup fitted with a ring-shaped AAMs to operate in a semi-continuous mode and synthesize a model metal oxide nanoparticle (hematite) using a membrane emulsification-precipitation process. Carry out the characterization of the metal oxide nanoparticles and evaluate the nanoparticles production rate.
- Fabricate a continuous membrane emulsification setup operating in a crossflow configuration using commercial aluminium oxide membrane and thus, evaluate the production of model metal oxide nanoparticles (titanium oxide) by a membrane emulsification-precipitation process. Finally, characterize the obtained nanoparticles and evaluate the incorporation of doping agents, such as carbon and nitrogen, to asses the photocatalytic activity of the titanium oxide in the visible range and evaluate the nanoparticle production rate.

1.2 Thesis structure

The present PhD thesis is divided into nine chapters. Following the introduction, Chapter 2 provides a comprehensive literature review relevant to this research. A detailed description of each synthesis procedure, equipment operation and a brief description of every characterization technique used will be presented in Chapter 3. A systematic investigation of the effect of different synthesis conditions on the fabrication of flat and ring-shaped anodic alumina membranes and their quality in terms of pore size and size distribution is given in Chapter 4. Next, Chapter 5 discusses the production of *oil-in-water* NEs using a dead-end stirred-cell ME setup fitted with a flat AAM, while Chapter 6 evaluates the production of NEs using a commercial ME setup fitted with the ring-shaped AAM and its use to produce hematite NPs in a semi-continuous mode. Chapter 7 analyses the production of *oil-in-water* NEs using a continuous membrane emulsification setup in a crossflow configuration fitted with a commercial aluminium oxide membrane and evaluate the production of titanium oxide nanoparticles using a continuous membrane emulsification setup. For both chapters, a deep characterization of the nanoparticles is carried out and an estimation of the nanoparticles production rate is presented. Finally, the conclusions and suggestions for future work are presented.

Chapter 2: Literature review

This chapter provides first an overview of the current methods to produce nanoparticles; followed by an in-depth analysis of membrane emulsification (ME) and how it can be applied to the large-scale synthesis of nanoemulsions and nanoparticles. This is followed by a review of anodic alumina membranes, the main type of membrane used and a careful analysis of the production methods and characteristics of the two metal oxide nanoparticles used as models to demonstrate the thesis aim, hematite and titanium oxide.

2.1 Large- scale synthesis of nanoparticle

At the nanoscale, size and shape often determine function, as in the case of iron oxide nanoparticles which switch from ferromagnetic to superparamagnetic below 15 nm (Chatterjee et al., 2003), or gold, which switches from an inert material to an active catalyst for particle sizes below 5 - 7 nm (Janssens et al., 2007). Surface chemistry and crystal structure also affect properties, for instance anatase becomes more stable than rutile for particle sizes below 14 nm (Zhang and Banfield, 2005). Thus, the ability to manufacture nanoparticles at large scale with fine control of their properties is essential to deliver on the promise of nanotechnology to revolutionize a wide range of fields, from medicine to energy to manufacturing (Dowling et al., 2004). The incorporation of nanoparticles into commercial goods is a growing market but it is still limited to a few nanomaterials such as gold, aluminium oxide, silica, titanium oxide and zinc oxide, with limited control over their particle size distribution. The main applications of nanosized materials are as catalysts for automotive emission reduction, magnetic recording materials and sunscreens (Tsuzuki, 2009). Thus, the promised profound impact that nanoparticles can bring to our daily life has not yet occurred, as there are still no methods to produce nanoparticles at a large-scale with the same high control over their properties as the laboratory-scale ones. Therefore, to overcome these current limitations, it is crucial to develop the ability to scale-up laboratory-scale methods to produce bespoke nanoparticles at large-scale via an economically and ecologically sustainable approach.

Current nanoparticle synthesis methods can be broadly divided in two families, wet and dry methods. The former allow inexpensive production at a large scale but with a limited control over properties, as in the case of co-precipitation (Valenzuela et al.,

2009), liquid-liquid interface (Rao and Kalyanikutty, 2008), or reverse micelles (Zhang et al., 2002). Hydrothermal, solvothermal synthesis and thermal decomposition afford a higher degree of uniformity in morphology (Cai et al., 2017), but suffer from long reaction times and require moderate to high temperatures (Diamandescu et al., 1999). Microwave-assisted synthesis results in the production of monodisperse nanoparticles but is a difficult technology to scale-up due to the limited penetration depth of the radiation into the reaction medium (Liao et al., 2001). At the other end of the spectrum are dry methods which, while offering a high property control, require complex equipment which is expensive to scale-up. Examples of these methods include physical vapor deposition (Xiang et al., 2005), laser vaporization (Lohbauer et al., 2010), or thermal plasma synthesis (Lin et al., 2005). Consequently, an ideal method would combine the best of both approaches, while also taking into account manufacturing considerations, such as safe operation and waste minimization (Dowling et al., 2004). Amongst the wet methods to produce nanoparticles, liquid-liquid reactions at the interface of emulsions combine good morphology control with a relatively inexpensive process. This is because the reactions to form the particles take place in a confined volume (the emulsion's droplet), with a homogeneous distribution of the reactive species surrounded by the protective layer of the surfactant. Under the former approach, Fe_2O_3 (Shi and Verweij, 2005) and TiO_2 (Lee et al., 2005) nanoparticles have been synthetized by reverse microemulsions. These examples consisted of small droplets of an aqueous phase surrounded by an organic phase, leading to the formation of *water-in-oil* emulsions. Under this approach, nanoparticles are usually produced by mixing two phases, one carrying the metal precursor and the other one the precipitation agent. The reaction(s) occurs inside the droplets due to the interchange of reactants taking place during the collision of two phases due to Brownian motion. Although the main advantage of this method is the wide range of inorganic salts precursors available, the main drawback relies in the utilization of large amounts of organic solvents as the continuous phase, making the process costly for scale-up and challenging from an environmental and, potentially, a health and safety perspective. A better alternative is the formation of nanoparticles by *oil-in-water* emulsions, with the production of CeO_2, ZrO_2, TiO_2, and ZnO_2, by *oil-in-water* high-energy emulsions reported in the literature (Pemartin et al., 2012, Sanchez-Dominguez et al., 2010, Tiseanu et al., 2012).

2.2 Emulsion properties and manufacturing methods

An emulsion can be defined as a two-phase system of immiscible liquids in which the liquid with lower volume fraction is dispersed in the form of micro- or nano-sized droplets in the other surrounding liquid (Pathak, 2011). The substance with the lowest volume fraction is called the dispersed phase and the other is called the continuous phase. Different types of emulsions can be obtained according to which substance is in the highest or the lowest proportion. For example, an *oil-in-water* (*o/w*) emulsion is obtained when oil is dispersed in water and *water-in-oil* (*w/o*) is a system where water droplets are surrounded by oil. Figure 2.1 shows different types of emulsions that can be produced.

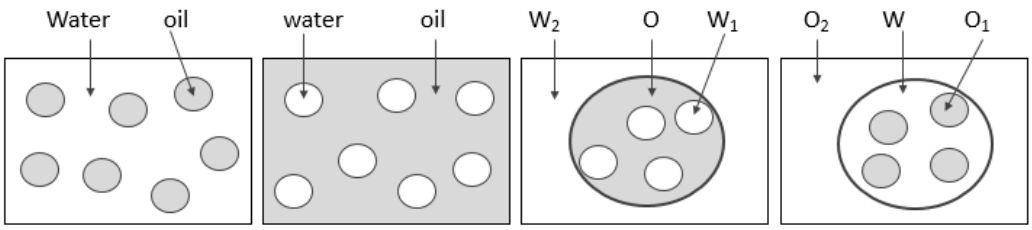

Figure 2.1 Different types of emulsions.

Emulsions are classified as macroemulsions, microemulsions and nanoemulsions and can be distinguished by their preparation methods, their physical properties and their thermodynamic and kinetic stability (McClements, 2012). For example, microemulsions are thermodynamically stable colloidal dispersions with dispersed phase diameters from 4 nm up to 100 nm that form spontaneously (McClements, 2011) and interfacial tension values range from 10^{-1} to 10^{-3} mN m^{-1} (Koroleva and Yurtov, 2012). On the other hand, nanoemulsions (NEs) have dispersed phase diameters from 20 nm to 200 nm (Solans et al., 2005). Nevertheless, some literature establishes 500 nm as an upper diameter limit (Anton et al., 2008). NEs have interfacial tension values between 1 to 10 mN m^{-1} (Koroleva and Yurtov, 2012), but they are not thermodynamically stable an energy input is required to form them. However, both look like transparent or slightly turbid solutions because the dispersed phase droplets are smaller than the visible wavelength of light (390 nm – 700 nm). On the other hand, macroemulsions (or also named emulsions) have higher dispersed phase diameters from 200 nm to 100 μm; therefore, they look like turbid

Table 2.1 Main differences between macroemulsions, nanoemulsions and microemulsions (McClements, 2011).

Type	Microemulsions	Nanoemulsions	Macroemulsions
Dispersed phase diameter	4 nm - 100 nm	20 nm - 500 nm	200 nm - 200 μm
Stability	Thermodynamic	Kinetic	Kinetic
Appearance	Transparent	Transparent/turbid	Turbid/opaque
Surfactant concentration	High (20% wt.)	Low (3 - 10% wt.)	High

solutions and they also require an energy input to be formed (McClements, 2011). Table 2.1 highlight some differences between each type of emulsion. At industrial scale, emulsions are usually produced by conventional emulsification methods such as rotor-stator, high-pressure homogenizers and ultrasound systems. All produce polydisperse emulsions due to the need to break down the initial coarser emulsion via different disrupting forces (e.g. turbulence, cavitation or shear) (Piacentini et al., 2010). Figure 2.2 shows a schematic representation of each conventional emulsification method. The former processes are characterized by their significant energy requirements, in the order of 10^6 – 10^8 J m^{-3} (Schubert and Engel, 2004), most of which is dissipated as heat. On the other hand, membrane emulsification (ME), is a scalable, continuous, low energy (10^4 – 10^6 J m^{-3}) emulsification process (Schubert and Engel, 2004), which can produce large quantities of low dispersity emulsions.

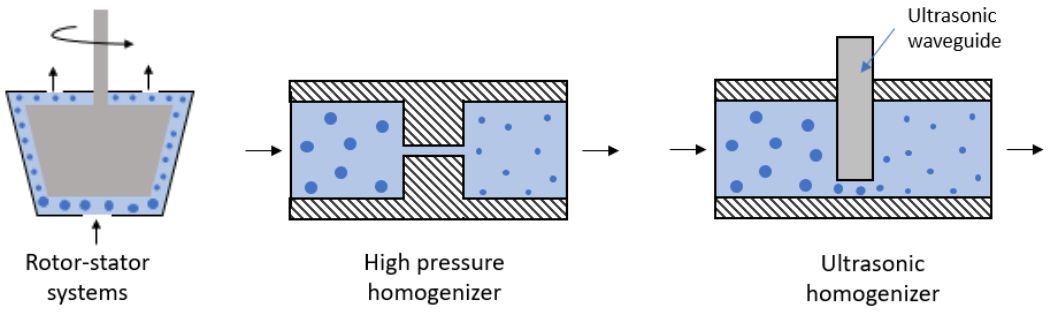

Figure 2.2 Schematic representation of three conventional emulsification methods, adapted from Koroleva and Yurtov (2012).

Table 2.2 highlights some of the main characteristics of each emulsification process, while a further discussion about ME given in the following section.

Table 2.2 Main differences between different high-energy methods for the productions of emulsions (Piacentini et al., 2010).

Preparation method	Droplet formation mechanism	Droplet size/μm	Energy density/J m^{-3}	Droplet size distribution
High pressure systems	Cavitation, droplet break-up	<0.2	10^6 - 10^8	Polydisperse
Ultrasound	Cavitation, droplet break-up, microturbulences	≈ 0.4	10^7 - 10^8	Polydisperse
Roto-stator systems	Droplet break-up by shear	> 2	10^5 - 10^8	Polydisperse
Microchannel	Droplet detachment by instability phenomenon	> 3	-	Monodisperse
Membrane emulsification	Droplet detachment by shear	0.1 - 10	10^3 - 10^6	Narrow

2.3 Membrane Emulsification

Membrane emulsification (ME) is a process where the future dispersed phase is permeated through the pores of a membrane into a continuous phase under the driving force of a transmembrane pressure differential (Vladisavljević and Schubert, 2003). The dispersed phase droplets will grow up at the edge of the pores and will detach due to a balance between all the forces acting over the droplet. Meanwhile, the surfactant molecules in the continuous phase will migrate at the *water-oil* interface preventing coalescence.

The most common membrane configurations are crossflow and dead-end. In the former, the continuous phase flows along the membrane surface and the shear stress is produced by the recirculation of the continuous phase (Figure 2.3a). In dead-end configuration (Figure 2.3b) the detachment of the droplets is achieved by the agitation of the continuous phase. Other configurations are when the detachment of the droplets is accomplished by the rotation or vibration of the membrane in a stationary continuous phase (Figure 2.3c).

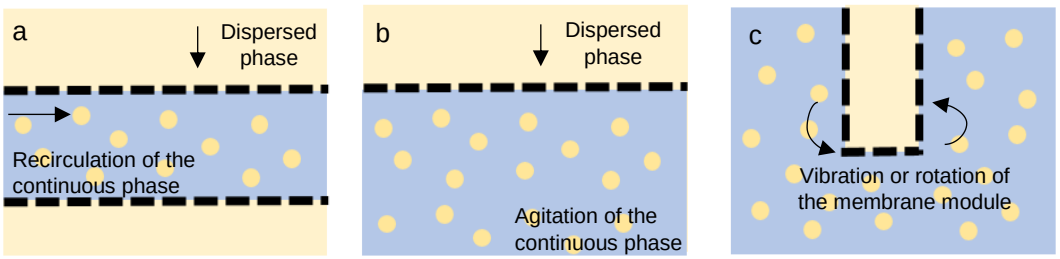

Figure 2.3 Schematic representation of different ME configurations a) crossflow b) dead-end and c) vibration or rotation of the membrane.

ME is characterized by the direct relationship between membrane pore diameter, D_p, and droplet size, D_d (Charcosset et al., 2004):

$$D_d = cD_p \qquad 2\text{-}1$$

where c is a proportionality constant with values between 2 and 10 for SPG membranes and from 2 to 50 for other types of membranes (Mine et al., 1996). Charcosset (2009) established that the main parameters that control the droplet size in ME can be divided into process parameters, membrane parameters, and phase parameters. Hence, all these factors should be considered when producing emulsions and each one will be discussed next.

2.3.1 Membrane and phase parameters

The selection of the membrane is a key factor that governs the performance in ME, where the type of membrane, its pore size and size distribution are the three main parameters considered. SPG membranes are the most extensively used membranes in ME. These are glass-based, hydrophilic membranes synthetized from a mixture of CaO-Al_2O_3-B_2O_3-SiO_2, with interconnected cylindrical pores and pore sizes ranging from 0.05 to 30 µm (Charcosset, 2012b). Other types of membranes used in ME include polymeric ones, polypropylene (Vladisavljević et al., 2002), polyamide (Giorno et al., 2003), polytetrafluoroethylene (Suzuki et al., 1998); ceramic membranes, alumina (Vladisavljević and Schubert, 2003) and zirconia (Berot et al., 2003); metallic (Egidi et al., 2008) and micro-engineered membranes (Wagdare et al., 2010a).

In ME, the type of emulsion that can be produced is determined by how the dispersed and continuous phases wet the membrane. For instance, the hydrophilic character of SPG membranes makes them suitable to produce *o/w* emulsions, while hydrophobic ones are suitable for *w/o* emulsions. Thus, a hydrophilic membrane should be fully

wetted first with water as continuous phase and then the oil phase should be dispersed into the continuous phase. This avoids wetting or spreading of the oil dispersed phase on the membrane surface, which leads to an increase in the droplet size distribution (Vladisavljević and Williams, 2005). Nevertheless, it is possible to modify a hydrophilic membrane by silanization and thus obtain a hydrophobic surface (Silva et al., 2017). An alternative approach involves pre-soaking the pores of a hydrophilic membrane (SPG) with an oil to carry out the formation of *w/o* emulsions, thus obtaining an increase in the dispersed phase flux close to 100 times compared to fluxes obtained using a hydrophobic membrane (Katoh et al., 1996).

In ME a surfactant is usually added to the continuous phase, as it plays a key role in the droplet formation mechanism by reducing the interfacial tension force and limiting droplet coalescence. A surfactant is a molecule with an amphiphilic structure consisting of two sections, one which is hydrophilic and the other one hydrophobic. The hydrophobic section, commonly called the tail, is a long hydrocarbon chain, while the hydrophilic section (head) is a functional ionic or non-ionic group. The head of the surfactant is used to classify them into: ionic (cationic or anionic), non-ionic and zwitterion;

Table 2.3 shows an example of each type of surfactant. The selection of the surfactant should be based on two main principles. First, the surfactant molecules should not have the opposite charge in relation to the membrane surface charge. Otherwise, electrostatic attractions between surfactant molecules and the membrane surface will cause spreading of the dispersed phase (Vladisavljević and Williams, 2005). For example, SPG membranes have a negative zeta potential of -15 to -35 mV within a range of pH from 2 to 8 due to the dissociation of silanol groups in the membrane surface (Nakashima et al., 1994). Hence the use of cationic surfactants must be avoided in SPG membranes. Secondly, the surfactant selection should follow Bancroft's rule, which states that the phase in which the surfactant is more soluble should be the continuous phase; the last can be inferred through the hydrophilic-lipophilic balance (HLB) value (Davis, 1994). This parameter measures the degree of how hydrophobic or hydrophilic a surfactant is. For example, for non-ionic surfactants the HLB values range between 0 and 20. Surfactant with HLB values above 10 are more water soluble (hydrophilic) and are suitable for oil-in-water (*o/w*) emulsions. In contrast, surfactants with HLB below 10 tend to be used for water-in-oil (*w/o*) emulsions because they are more hydrophobic (Charcosset, 2012a).

Table 2.3 Examples of surfactants.

Type of surfactant	Name (abbreviation)	Formula
Anionic	Sodium dodecyl sulphate (SDS)	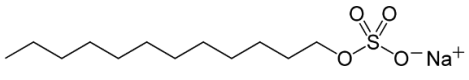
Cationic	cetyltrimethylammonium bromide (CTAB)	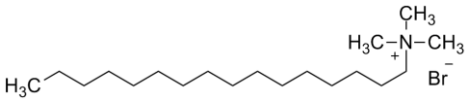
Non-ionic	Polyoxyethylene (20) sorbitan monolaurate (Tween 20)	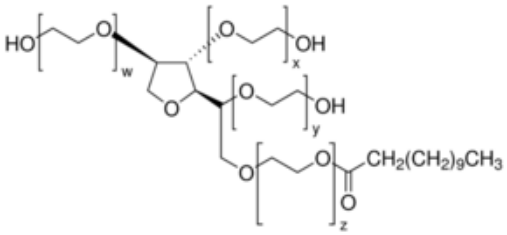
Zwitterionic	3-(4-tert-Butyl-1-pyridinio)-1-propanesulfonate (-)	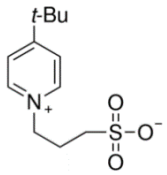

2.3.2 Process parameters

The equation that describes the flux of dispersed phase through a porous media is known as Darcy's law:

$$J = \frac{\Delta P}{\mu_d \kappa_m} \qquad 2\text{-}2$$

where J is the membrane volumetric flux through the pores of the membrane, ΔP is transmembrane pressure, μ_d is the dynamic viscosity of the fluid and κ_m is a term that involves all the material characteristics and it is known as the membrane resistance coefficient. According to Darcy's Law, there is a positive relationship between the flux of the dispersed phase and the transmembrane pressure. The latter parameter can be described as the driving force that makes possible the permeation of a fluid through the pores of the membrane and it is defined as the difference of pressure between the dispersed phase (P_d) and the continuous phase (P_c), as the equation below describes:

$$\Delta P = P_d - \frac{(Pc_{in} - Pc_{out})}{2} \quad \text{2-3}$$

where $P_{c\text{-in}}$ and $P_{c\text{-out}}$ are the pressures of the continuous phase at the inlet and outlet of the membrane module, respectively. The minimum transmembrane pressure required to achieve the dispersed phase permeation through the pores is the capillary pressure (P_{cap}):

$$P_{cap} = \frac{4\gamma cos\theta}{D_p} \quad \text{2-4}$$

where γ is the interfacial tension between the dispersed and the continuous phase; and θ is the contact angle between the dispersed phase droplet and the membrane surface. In general, transmembrane pressure values are higher than the capillary pressure due to pore tortuosity, irregular pore opening and effects of surface wettability (Williams et al., 1998). At industrial scale, higher dispersed phase flux can be considered as a desirable aspect as will lead to a higher emulsion formation rate. However, an increase in the dispersed phase flux is prone to produce droplet coalescence and the outcome is an increase in both droplet diameter and droplet size distribution (Vladisavljević and Schubert, 2003). Hence, there is a trade-off between the emulsion production rate and the quality of the emulsion, with an empirical optimum value achieved when transmembrane pressure values range between 2 and 10 times the capillary pressure (Williams et al., 1998). Another strategy to evaluate the droplet dynamics in ME is using dimensionless numbers, some of them are listed in Table 2.4.

Table 2.4 Dimensionless numbers commonly used in membrane emulsification.

Dimensionless numbers	Equation	Relates
Reynolds	$Re = \frac{D_p \rho_c v_c}{\mu_c}$	$\frac{\text{inertial force}}{\text{viscous force}}$
Capillary	$Ca = \frac{\mu_c v_c}{\gamma}$	$\frac{\text{viscous force}}{\text{interfacial tension force}}$
Weber	$We = \frac{D_p \rho_d v_d^2}{\gamma}$	$\frac{\text{inertial force}}{\text{interfacial tension force}}$
Euler	$Eu = \frac{\Delta P}{\rho_c V_c^2}$	$\frac{\text{pressure}}{\text{inertial force}}$

Dimensionless numbers have been extensively used to gain an insight on the performance of a ME setup under specific conditions. For example, Capillary and Weber numbers have been previously used to determine the transition between two possible droplet formation regimes, dripping and jetting (Pathak, 2011). Figure 2.4 depicts both regimes for different Weber numbers. Dripping is observed at low *We* numbers and is characterized by the formation of individual droplets with constant volume and with droplet detachment occurring at the pore's tip (Figure 2.4a). For intermediate *We* numbers the formation of a "neck" is observed and the location of the droplet detachment occurs far away from the pore edge (Figure 2.4b); this behaviour is indicative of the transition from the dripping to the jetting regime. For higher *We* numbers, the formation of a downstream of dispersed phase from the pore is observed and droplet detachment occurs at the end of the jet due to Raleigh instabilities (Figure 2.4c). A plot of *We* against *Ca* was obtained (Figure 2.5) by (Pathak, 2011) and an equation of the critical Weber number as a function of the Capillary number was derived, which helps identifying the conditions leading to the transition from dripping to jetting behaviour in ME:

$$We_c = k_1\left\{1 + k_2 Ca^2 - [(1 + k_2 Ca^2)^2 - 1]^{1/2}\right\}^2 \qquad 2\text{-}5$$

where the We_c is the critical Weber number, k_1=1.188 and k_2 =3455.

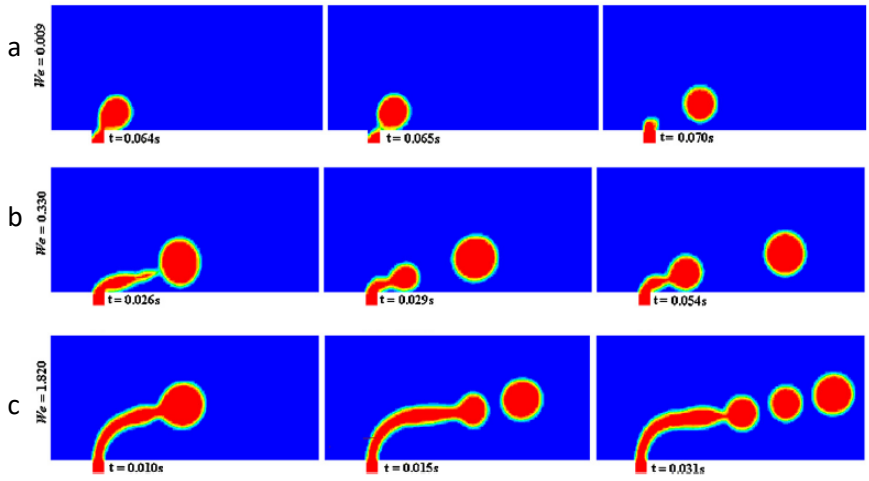

Figure 2.4 Transition from dripping to jetting regime observed at different Weber number value, adapted from Pathak (2011).

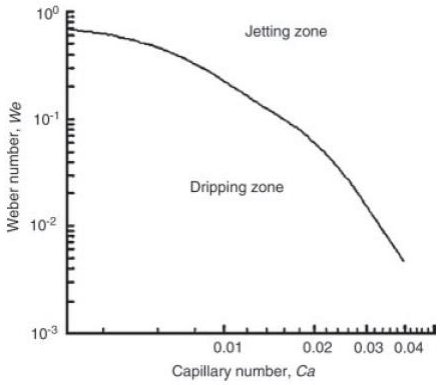

Figure 2.5 Map of the *We* against of the *Ca* number (Pathak, 2011).

2.3.3 Droplet formation mechanism in membrane emulsification

The production of dispersed phase droplets by ME involves two stages: first, droplet growth, when the droplet inflates at the pore, followed by droplet detachment, when the droplet breaks off and moves away from the pore (Peng and Williams, 1998a). From this perspective, a droplet is considered as a particle immersed in a fluid and its final size is determined by the relative magnitude of the forces acting over the droplet before its detachment, which can be divided in detaching and retaining forces and each one of them will be described next:

Drag force (F_D) is produced by the velocity of the continuous phase and its direction is parallel to the membrane surface.

$$F_D = 6k_x\pi\tau_w r_d^2 \quad \text{2-6}$$

Interfacial tension force (F_γ) represents the effect of the disperse phase adhesion at the edge of the membrane pore. Consequently, it is the force that keeps the droplet attached to the membrane surface.

$$F_\gamma = 2\pi r_p \gamma \quad \text{2-7}$$

Buoyancy force (F_B) is caused by the difference of density between the two phases.

$$\mathrm{F}_B = \frac{4}{3}\pi r_d^3 g(\rho_c - \rho_d) \quad \text{2-8}$$

Inertial force (F_i) is associated with the continuous flow of the dispersed phase through the membrane pores. The direction of the force is normal to the membrane surface.

$$\mathrm{F_i} = \rho_d \pi r_p^2 v_d^2 \qquad 2\text{-}9$$

Static pressure force (F_{st}) is due to the pressure difference between the dispersed phase and the continuous phase at the membrane surface.

$$F_{st} = \gamma\pi \frac{D_p^2}{D_d} \qquad 2\text{-}10$$

Dynamic lift force (F_L) results from the asymmetric velocity profile of the continuous phase near the pore edge when the droplet is being formed:

$$F_L = 0.761 \frac{\tau_w^{1.5} \rho_c^{0.5} D_d^3}{\mu_c} \qquad 2\text{-}11$$

The force that keeps the droplet attached to the pore edge is the interfacial tension force, meanwhile the rest of them induce droplet detachment. Figure 2.6 show a diagram of all these forces acting over a single droplet at the membrane pore.

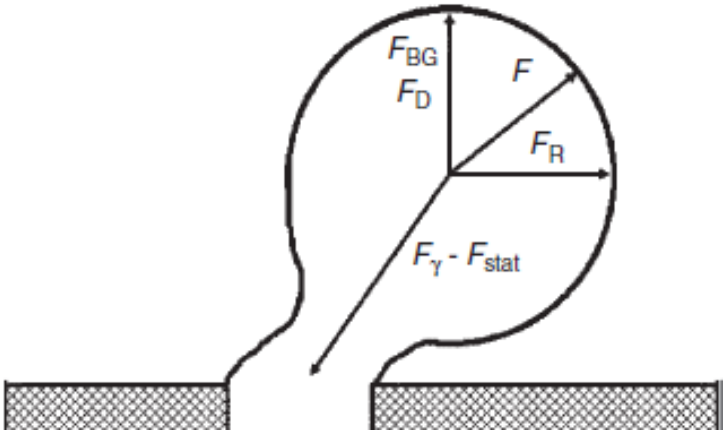

Figure 2.6 Forces acting on a droplet at the membrane pore (Spyropoulos et al., 2014).

Shear stress (τ_w), is the main parameter behind the drag force and can be calculated depending on the membrane configuration. For instance, in a crossflow configuration it can be calculated from the correlation friction factor (f) as (Peng and Williams, 1998a):

$$f = \frac{2\tau_w}{V_c^2 \rho_c} = \begin{cases} \dfrac{16}{Re} & Re < 500 \\ 0.0792 Re^{-1/4} & 500 \leq Re \leq 2000 \end{cases} \qquad 2\text{-}12$$

where V_c is the velocity of the continuous phase, Re is the Reynolds number. While most publications on ME reported have a crossflow configuration. Kosvintsev et al.

(2005) introduced the concept of a batch stirred-cell to produce emulsions with dispersed phase droplets in the micrometre scale. In a stirred tank, the shear stress has a radial profile, having their highest value at the critical radius (r_c). Along the shear stress profile, there are two regions: the first one for positions $r < r_c$, is a forced vortex region, which exhibits a rigid-body motion with an angular speed of the impeller (ω); the second is a free vortex region ($r > r_c$) in which the angular momentum (ru) is constant (Kosvintsev et al., 2005). The position of the critical radius can be found based on Yamamoto's method reported by Nagata (1975):

$$r_c = \frac{D_i}{2} 1.23 \left(0.57 + 0.35 \frac{D_i}{T_D}\right) \left(\frac{b}{T_D}\right)^{0.036} \left(\frac{Re}{1000 + 1.43Re}\right) n_b^{0.116} \qquad \text{2-13}$$

where D_i is the impeller diameter, T_D is the tank diameter, b is the blade height, n_b is the number of blades:

$$Re = \frac{\rho_c \omega D_i^2}{2\pi\mu} \qquad \text{2-14}$$

where ω is the angular speed. For each region, the shear stress at the membrane surface can be calculated using the equations (Kosvintsev et al., 2005):

$$\tau_w = 0.825 \mu_c \omega r \frac{1}{\delta} \qquad r \leq r_c \qquad \text{2-15}$$

$$\tau_w = 0.825 \mu_c \omega r \frac{1}{\delta} r_c \left(\frac{r_c}{r}\right)^{0.6} \qquad r > r_c \qquad \text{2-16}$$

where the boundary layer thickness is defined using the equation:

$$\delta = \sqrt{\frac{\mu_c}{\rho_c \omega}} \qquad \text{2-17}$$

The magnitude of each force changes according to the membrane, process and phase parameters. However, it has been reported that the inertial and buoyancy forces are 6 and 9 orders of magnitude smaller, respectively, than the interfacial and drag forces (Rayner and Trägårdh, 2002). Therefore, they are generally neglected from force balance models. Different models based on a torque or a force balance have been developed to estimate the droplet size in a ME setup and some of them are listed on Table 2.5.

Table 2.5 Models for the estimation of the droplet size in membrane emulsification based on force or torque balances and the type of membrane configuration.

Balance	Model expression	Reference
	Crossflow configuration	
$F_\gamma = F_D$ (force)	$D_d = \sqrt{\frac{2r_p\gamma}{6k_x\tau}}$	(Rayner and Trägårdh, 2002)
$(F_D + F_B)h = F_\gamma r_p$ (torque)	$\left[6k_x\pi\tau h^2 + \frac{4}{3}\pi r_d^3(\rho_c - \rho_d)g\right]h = 2\pi\gamma r_p^2$ $\frac{4}{3}\pi r_d^3 = \frac{\pi}{6}h\left(3r_p^2 + h^2\right)$	(Lee and Mattia, 2013)
	Stirred-cell	
$F_\gamma = F_D$ (force)	$D_d = \frac{\sqrt{18\tau^2 r_p^2 + 2\sqrt{81\tau^4 r_p^4 + 4\tau^2 r_p^2\gamma^2}}}{3\tau}$	(Kosvintsev et al., 2005)
$M_{\gamma z} = F_D\left(\frac{D_d}{2}\right)cos\alpha$ (torque)	$D_d = \frac{12^{1/3}\left[r_p^2\tau^2\left(\gamma + \sqrt{\gamma^2 - 12r_p^2\tau^2}\right)\right]^{1/3}}{3\tau} + \frac{12^{2/3}r_p^2\tau}{3\left[r_p^2\tau^2\left(\gamma + \sqrt{\gamma^2 - 12r_p^2\tau^2}\right)\right]^{1/3}}$	
$F_{st} = F_D$ (force)	$\frac{D_d}{D_p} = \left(\frac{2\gamma}{3k_x D_p\tau}\right)^{1/3}$	(Suárez et al., 2013)

2.4 Anodic alumina membranes

As briefly discussed before, the intrinsic characteristics of the membrane are a key factor affecting the quality of an emulsion formed by membrane emulsification. Therefore, selecting a membrane with a narrow pore size distribution will enable producing an emulsion with narrow dispersed phase droplets. A class of membranes that offers the former characteristic is the one represented by anodic alumina membranes (AAMs), which are self-ordered nanostructured membranes with a

hexagonal pore arrangement. They are synthesized by the electrochemical oxidation of aluminium in mild anodization conditions (Alkire et al., 2008) and one of their main features is that pore size can be tuned from about 5 to 300 nm, depending on the anodization voltage and electrolyte type (Gong et al., 2010, Lee et al., 2012).

2.4.1 Anodization of aluminium

The anodization of aluminium is an electrochemical process where the aluminium surface is oxidized under acidic conditions. During the anodization, an aluminium oxide structure grows perpendicular to the metal surface. However, the anodization of aluminium might result in two different types of oxide films, a barrier-type and a porous one, depending on the nature of the electrolyte and the pH of the solution (Keller et al., 1953). A barrier-type aluminium oxide layer is formed using neutral or basic solutions in which the aluminium oxide layer is practically insoluble (Alkire et al., 2008). Examples of these electrolytes are ammonium borate, ammonium tartrate solutions and mixtures of ethanol with some diprotic acids like citric, malic or succinic (Poinern et al., 2011). The resulting oxide is a flat non-porous layer that behaves as an electrical insulator. On the other hand, using electrolytes in which the formed anodic oxide film is slightly soluble, will lead to the production of a porous-oxide layer (Diggle et al., 1969b). Examples of these electrolytes are sulfuric, oxalic, phosphoric and chromic acid solutions. In this case, an aluminium oxide porous structure is obtained due to an equilibrium between the growth of the aluminium oxide layer and a localized dissolution of the aluminium oxide film, as will be later discussed in Section 2.4.2 . Figure 2.7 shows an illustration of a barrier-type and a porous aluminium oxide layer.

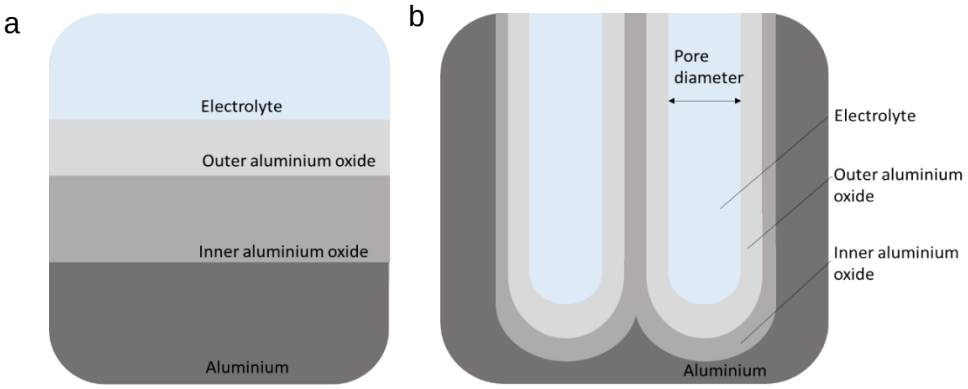

Figure 2.7 Illustration of a) barrier-type and b) porous oxide film produced by the anodization of aluminium.

The close-packed array of hexagonal cells contains a pore in each cell centre and is characterized by parameters such as pore diameter, wall thickness, barrier layer thickness, pore length and interpore distance, also known as cell diameter (Figure 2.8). One of the main features of AAMs is that these parameters can be tuned by altering the synthesis conditions (Alkire et al., 2008). For instance, it is possible to obtain pore diameters ranging from about 5 to 300 nm, interpore distances from 50 - 600 nm, porous layer thickness from 10 nm to 150 μm, pore density values from 10^9 to 10^{11} pores cm^{-2} and porosities ranging from 5% up to 50% (Li et al., 1998a, Furneaux et al., 1989). For pore diameters and interpore distances there is a well-established relationship between the former parameters and the anodization potential, according to the following equations (O'sullivan and Wood, 1970):

$$D_p = \lambda_p U \qquad D_c = \lambda_c U \qquad \text{2-18}$$

where D_p is pore diameter (nm), U is the anodization voltage (V), λ_p is the proportionality constant with value of 1.29 nm V^{-1}, D_c is interpore distance or cell diameter (nm) and λ_c is the proportionality constant with value of 2.5 nm V^{-1} (Ono et al., 2004b). A similar correlation has also been reported between the barrier layer thickness (B), which is the hemispherical aluminium oxide layer formed at the bottom of the pores (Figure 2.8) and the anodization potential, with a dependence value of 1.15 nm V^{-1}, λ_B (O'sullivan and Wood, 1970):

$$B = \lambda_B U \qquad \text{2-19}$$

In addition, Ebihara et al. (1983) found a relation between the barrier layer thickness and the wall thickness, with proportionality constant values ranging from 0.66 to 0.89, when oxalic acid is used as electrolyte. The wall thickness (W) can be calculated from:

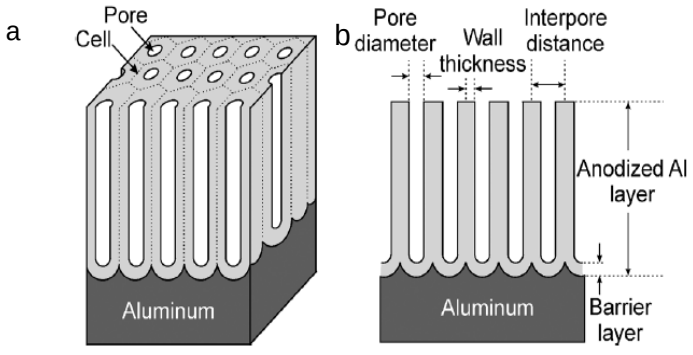

Figure 2.8 Ideal structure of an a) anodic porous alumina and its b) cross-sectional view (Alkire et al., 2008).

$$W = \frac{D_c - D_p}{2} \quad \text{2-20}$$

For an AAM, the surface porosity (ε), which is defined as the ratio of the surface occupied by the pores to the total surface area, can be estimated using the following equation, where it is assumed the membrane consists of circular and straight pores:

$$\varepsilon = 0.907\left(\frac{D_p}{D_c}\right)^2 \quad \text{2-21}$$

For an AAM, the governing factors that affect porosity are anodization potential, temperature, pH of the solution and anodization time. For instance, an inverse relation between porosity and anodization potential has been observed using sulphuric, phosphoric, chromic or oxalic acids, with reported values of porosity ranging from 0.05 to 0.5 (Furneaux et al., 1989). However, Nielsch et al. (2002) measured the porosity for different self-ordering regimes and different concentrations of electrolytes and found that the porosity was always about 10%. While pore density (n), which is expressed as the total number of pores occupying a square centimetre can be obtained from:

$$n = \frac{2 \cdot 10^6}{\sqrt{3}D_c^2} \quad \text{2-22}$$

AAMs are characterized by a hexagonal arrangement of cells, in which each one has an inner and outer aluminium oxide layer (Figure 2.7). The outer layer is in contact with the electrolyte and has anions incorporated within its structure due to the presence of the electric field. Meanwhile, the inner layer is pure alumina (Alkire et al., 2008). However, the thickness of the inner layer depends on the nature of the electrolyte as each one has a specific concentration profile along the outer oxide layer thickness. For example, Figure 2.9 shows the distribution diagram of the SO_4^{2-} concentration in a porous-type alumina film.

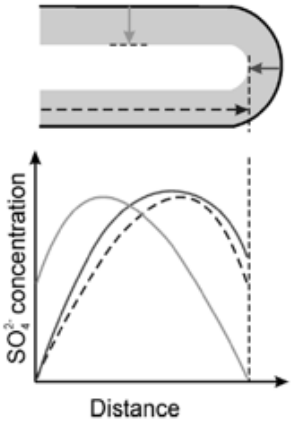

Figure 2.9 Distribution of the sulphate concentration in a porous-type alumina film.

2.4.2 Kinetics on the self-organized porous alumina films

Porous alumina structures can be produced under potentiostatic (constant voltage) or galvanostatic conditions (constant current) and while the exact origin of the pore formation mechanism is still a matter of debate, the most accepted theory is the field-assisted mechanism proposed by Keller et al. (1953). An illustration of the kinetics and pore growth proposed mechanism during early stages of the anodization is shown in Figure 2.10.

The field-assisted theory states that at the beginning of the anodization a thin barrier-type oxide layer is formed over the aluminium surface. As the aluminium oxide is a non-conductive material, this can be tracked in a plot of current density versus time (Figure 2.10a) as a sudden drop in the current density (stage I). When the aluminium oxide thickness reaches a threshold value, the magnitude of the current density reaches a minimum value. The presence of defects, impurities or subgrain boundaries produces some local variation in the field strength, which creates “pores precursors” where the electric field-assisted dissolution starts (stage II). Then, a slight increase in the current is observed due to the higher surface area created by the pore precursors (stage III). Further anodization increases the depth of the pores until the system reaches a steady state, where further pore growth is the result of a combination of two factors: the enhanced electric-field alumina dissolution at the pore tip (electrolyte/oxide interface) and the oxide growth at the oxide/metal interface (stage IV) (Yuan et al., 2004, Thamida and Chang, 2002).

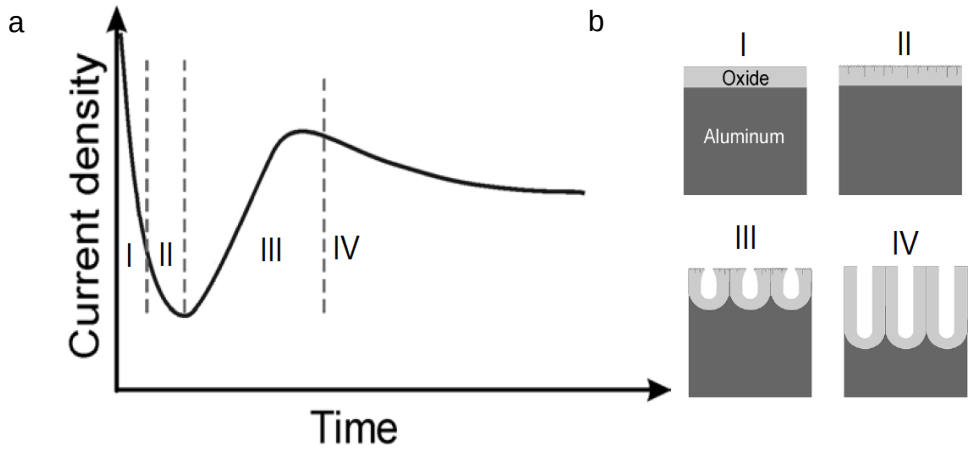

Figure 2.10 a) Illustration of the kinetics of porous growth in potentiostatic regime b) schematic representation of the pore formation steps (Alkire et al., 2008).

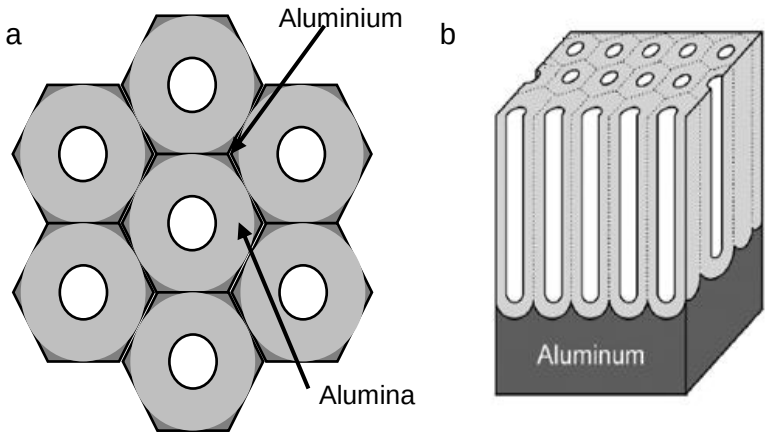

Figure 2.11 a) Illustration of the conversion from an ideal cylindrical oxide cell arrangement until a close-packed hexagonal cell arrangement is obtained (Keller et al., 1953) b) hemispherical alumina arrangement at the pore base (Alkire et al., 2008).

According to Hoar and Mott (1959), the characteristic behaviour of the current density versus time observed in Figure 2.10a is the result of two overlapping process. The first one is an exponential decrease in the current density due to the formation of the aluminium oxide barrier, while the second one represents the pore formation process as shown in Figure 2.12.

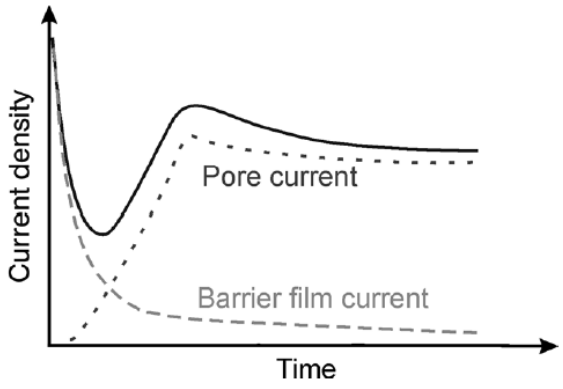

Figure 2.12 Schematic diagram of overlapping processes occurring during the porous oxide growth under potentiostatic conditions (Alkire et al., 2008).

Keller et al. (1953) stated that the hexagonal arrangement observed in porous anodic alumina films is derived from a spherical shape due to steric factors when the aluminium oxide porous structures are growing. They proposed the starting pore cell is cylindrical and each one is surrounded by other six cylinders as Figure 2.11a

illustrates; and at the beginning of the anodization, the contact point of three cylinders is an aluminium column that will be consumed evenly for each cylindrical oxide cell. As the anodization proceeds, the metal is consumed, and steric interactions lead to the conversion into a hexagonal arrangement. Meanwhile, at the bottom of the cell, current flows from adjacent pores and induces a quicker conversion into alumina, leading to a hemispherical structure array at the bottom of the pores (Figure 2.11b).

The vertical growth of the pores was studied by Garcia-Vergara et al. (2006) using tungsten tracers incorporated into an anodic film. Their results demonstrate the flow of alumina from the pore base to the cell walls, which is attributed to the mechanical stress generated by the continuous formation of adjacent aluminium oxide pores and the higher density of the aluminium oxide (3.2 g cm^{-3}) compared to aluminium (2.7 g cm^{-3}) that leads to a volume of expansion of the final thickness, as shown in Figure 2.13. Nevertheless, experimental reports suggest the volume of expansion varies according to the type of electrolyte and anodization potential with values ranging from 1.35 to 1.63 and 1.23 to 1.60 for anodizations conducted in sulfuric and oxalic acids, respectively (Poinern et al., 2011, Li et al., 1998a, Vrublevsky et al., 2004).

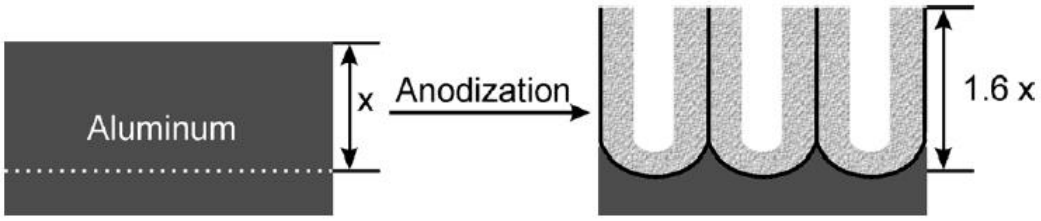

Figure 2.13 Volume of expansion observed during the anodization of aluminium (Alkire et al., 2008).

The synthesis of aluminium oxide porous films, therefore, is a complex process where a series of reactions take place. The overall equation that represents the anodization of the aluminium can be expressed as:

$$2Al + 3H_2O \rightarrow Al_2O_3 + 3H_2 \qquad 2\text{-}23$$

The process starts with the formation of Al^{3+} ions followed by their migration from the metal substrate towards the cathode:

$$Al \rightarrow Al^{3+} + 3e^- \qquad 2\text{-}24$$

During the anodization, it has been estimated that approximately 70% of Al^{3+} cations generated react with O^{2-} or OH^- species to contribute to the oxide layer formation,

whilst the remaining Al^{3+} ions migrate through the oxide layer until they reach the electrolyte solution (Palibroda, 1995). Although the anodization of aluminium is a widely investigated process, is not yet clear whether the anodization involves one or both O^{2-} or OH^- species (Alkire et al., 2008). For example, hydroxide ions might be generated by two possible pathways: the first one is water splitting (Equation 2-25) and the second one is the reduction of water and its reaction with dissolved oxygen at the cathode (Equation 2-26):

$$2H_2O + 2e^- \rightarrow 2OH^- + H_2 \qquad 2\text{-}25$$

$$O_2 + 2H_2O + 4e^- \rightarrow 4OH^- \qquad 2\text{-}26$$

Hydroxide ions might also decompose under the high-strength electric field, producing O^{2-} and H^+ (Patermarakis, 2009). O'sullivan and Wood (1970) proposed that O^{2-} and OH^- species can also be produced by the interaction between electrolyte species and water molecules adsorbed at the electrolyte/oxide (*e/o)* interface, a process illustrated in Figure 2.14.

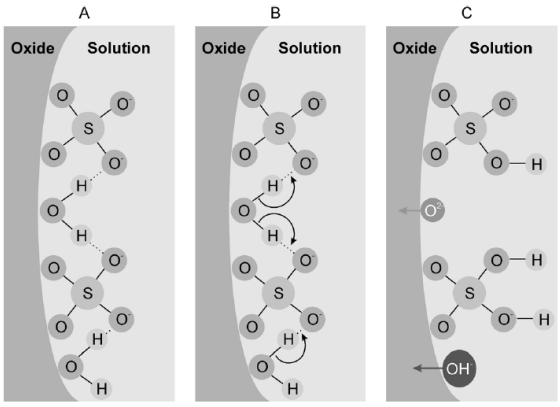

Figure 2.14 Schematic representation of the O^{2-} and OH^- ions formation at the oxide/electrolyte interface from water interacting with adsorbed SO_4^{2-} anions (Alkire et al., 2008).

The production of aluminium oxide take place at both the metal/oxide (*m/o)* interface and the *e/o* interface:

$$Al^{3+} + 3OH^- \rightarrow Al_2O_3 + 3H^+ \qquad 2\text{-}27$$

Meanwhile, the dissolution of the aluminium oxide occurs at the *e/o* interface:

$$Al_2O_3 + 6H^+ \rightarrow 2Al^{3+} + 3H_2O \qquad 2\text{-}28$$

Finally, hydrogen is produced at the cathode:

$$6H^+ + 6e^- \rightarrow 3H_2 \qquad 2\text{-}29$$

Figure 2.15 summarizes all the reactions involved during the anodization of porous aluminium oxide films.

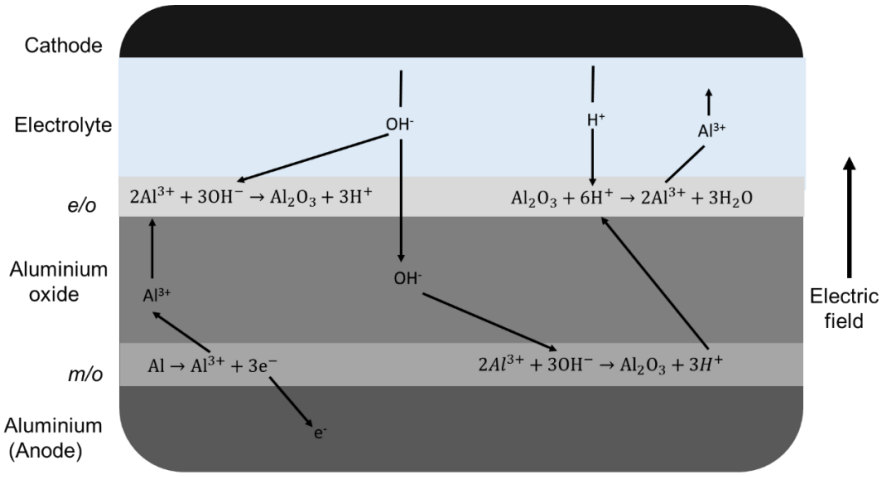

Figure 2.15 Schematic diagram showing the electrochemical reactions and ionic paths involved during the anodization of a porous aluminium films, adapted from Thamida and Chang (2002).

2.4.3 Fabrication of anodic alumina membranes (AAMs)

AAMs can be fabricated by a single anodization; but the degree of regularity that can be achieved is far from that of an ideal structure. Therefore, different approaches have been developed to improve pore arrangement such as multiple anodization steps and lithography. Among these techniques, the two-step anodization process is an inexpensive and feasible method to obtain highly ordered porous structures. The method was developed by Masuda and Fukuda (1995) and can be divided in three main steps: pre-treatment, anodization and post-treatment, each one will be described next.

In the **pre-treatment** step high purity aluminium sheets (99.99%) are subjected to annealing, degreasing and electro-polishing to reduce both microscopic and macroscopic defects. First aluminium is heated under controlled conditions at temperatures above two-thirds of its melting point to reduce mechanical stress on the surface and increase the domain size (Poinern et al., 2011). Then, the substrate is degreased to remove any organic residues over the surface. Finally, electro-polishing

is used to reduce macroscopic defects such as cracks, roughness and cavities leaving a smooth and shiny surface for anodization.

In the **anodization** step an anodic alumina layer can be produced by one-step, two-step and even a three-step anodization process. However, Sulka et al. (2002) used a three-step anodization process and their results do not show a significant improvement of the pores ordering compared to a two-step anodization process. Therefore, a two-step anodization is the most common method to achieve a highly ordered pore arrangement. In the former process, an aluminium substrate is first subjected to a short anodization time, followed by the removal of the aluminium oxide layer formed using an acid mixture of H_3PO_4/H_2CrO_4, at temperatures between 55 to 80 °C (Li et al., 2008), (Montero-Moreno et al., 2007). However, the time needed for the removal of the first aluminium oxide layer depends on the time and voltage of the first anodization step. After the removal of the first alumina layer, the resulting aluminium substrate serves as a template for pore formation in the second anodization, which is carried out at the same conditions as the first one, but for a longer period of time. The optimal anodization conditions giving the most ordered structures for each electrolyte have been identified, being 40 V for $C_2H_2O_4$, 25 V for H_2SO_4 and 195 V for H_3PO_4 (Lee et al., 2006).

In the **post-treatment**, the removal of both the residual aluminium and the aluminium oxide barrier is performed. The former is commonly accomplished by a chemical wet method using $CuCl_2$ or $HgCl_2$ solutions (Xu et al., 2003), (Jessensky et al., 1998). These solutions contain hydrochloric acid to reduce the pH of the solution and increase the aluminium dissolution rate. When the former step is finished, at the bottom of the anodic alumina porous structure remains a scalloped aluminium oxide barrier (Figure 2.11b) that must be removed to obtain an open-through structure. Several methods exist to remove the aluminium oxide barrier such as ion milling and plasma etching, although a wet chemical etching is the most commonly used (Xu et al., 2002, Ba and Li, 2000). In the latter method, a phosphoric acid solution at concentrations between 5% and 10% and temperatures ranging from 25 to 60 °C are commonly used. As the thickness of the aluminium oxide barrier varies according to anodization conditions such as voltage and electrolyte type; which could produce an uncertainty over the time of the pore opening process. To address this, Lillo and Losic (2009) developed an electrochemical detection method coupled with a wet chemical dissolution method, resulting in an improvement of the reproducibility of the pore opening process. Figure 2.16 shows each step involved in the synthesis of anodic alumina membranes.

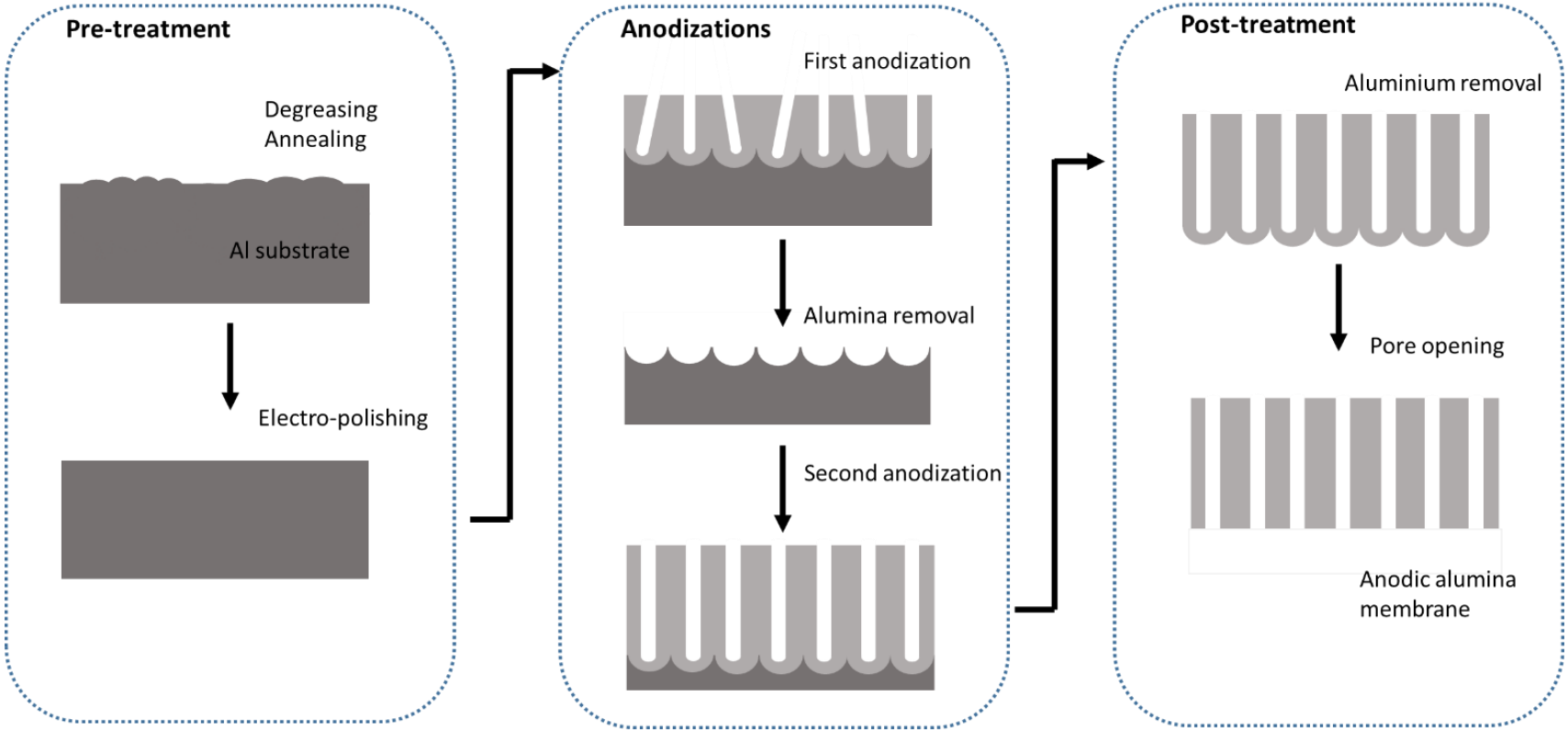

Figure 2.16 Scheme of the fabrication of anodic alumina membranes.

2.5 Synthesis of metal oxide nanoparticles

Transition metal oxides constitute one of the most fascinating classes of inorganic solids, as they exhibit a wide variety of structures, properties, and behaviours (Hyeon, 2003). As such, attempts are continuously made to take advantage of them in a multitude of applications including separation, catalysis, environmental remediation, sensing, biomedical applications and others (Sarkar et al., 2012). In this section, a brief description of the properties of titanium and iron oxide nanoparticles and the current ways to manufacture them at large scale is provided.

2.5.1 Titanium oxide nanoparticles

The chemical and physical properties of titanium oxide combined with its abundance on Earth make it one of the most extensively investigated semiconductors for a wide range of applications such as photocatalytic water splitting, photovoltaics and photosynthesis (Carp et al., 2004, Fujishima, 1972, Asahi et al., 2001); purification of pollutants (Gupta and Tripathi, 2011), photocatalytic self-cleaning surfaces and as antibacterial materials (Kazuhito et al., 2005).

Titanium oxide has eleven polymorphs, of which anatase, brookite and rutile are the best known ones (Gupta and Tripathi, 2011). The first two are metastable phases that irreversibly convert to rutile upon heating. However, the small difference in the Gibbs free energy (4 – 20 kJ mol^{-1}) among these polymorphs suggest that they are almost as stable as rutile at normal pressures and temperatures (Carp et al., 2004). The most common way to represent the crystallographic structure of these polymorphs is by using TiO_6 octahedrons as building blocks, as seen in Figure 2.17; where each Ti^{4+} is surrounded by an octahedron of six O^{2-} ions. Rutile, consists of corner-shared TiO_6 octahedra in a tetragonal cell, but the octahedron is not regular and shows a slightly orthorhombic distortion (Baur and Khan, 1971). The anatase polymorph has a similar structure as rutile, a tetragonal arrangement; the main difference relies on an additional displacement of the oxygen ions. In the rutile structure, each octahedron is in contact with 10 neighbour octahedrons, two sharing an edge oxygen pair and eight sharing corner oxygen atoms while in the anatase structure each octahedron is in contact with eight neighbours, four sharing an edge and four sharing a corner. The Ti-Ti distances in anatase are greater than in rutile, 3.79 and 3.04 Å in anatase compared to 3.57 and 2.96 Å in rutile. Meanwhile, the Ti-O distances are shorter in anatase (1.937 and 1.965) compared to rutile (1.949 and 1.980 Å). The third polymorph, brookite has an orthorhombic crystal system. Its unit cell is composed of

8 formula units of TiO_6 and its formed by edge-sharing TiO_6 octahedra. Brookite has a larger cell volume and it's also the least dense of the three polymorphs, but it is not a photocatalytic active polymorph (Lan et al., 2013).

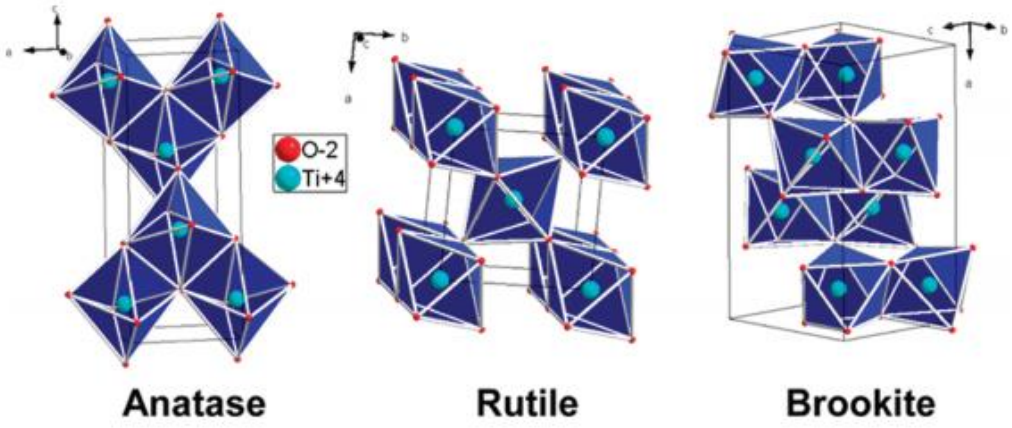

Figure 2.17 Crystallographic structure of anatase, rutile and brookite (Dambournet et al., 2009).

Figure 2.18a. shows the equilibrium shape of rutile at the zero Kelvin based in a Wulff construction (Ramamoorthy et al., 1994). The theoretical crystal shape is obtained by calculating the surface energy of the (110), (100), (011) and (001) facets; being the facet (001) the one with the highest surface energy and therefore the most reactive. In contrast, the facet (110) has the lowest surface energy and contributes to the 56% of the total surface area (Selloni, 2008). The theoretical crystal shape of anatase is illustrated on Figure 2.18b and show a high similarity degree compared to macroscopic anatase crystals (Diebold, 2003). The crystals have a truncated bipyramidal shape being the facets (101) and (011) the ones with the highest surface area and therefore the lowest reactivity, they contribute to more than 94% of the surface area (Lazzeri et al., 2001). The lower surface energy of the (001) facet of anatase compared to the same facet in rutile indicate the high stability of the anatase particles below 14 nm (Zhang and Banfield, 2005). However, the characteristic high reactivity of anatase nanoparticles is attributed to the (001) plane, due to the large Ti-O-Ti bond angle at the surface meaning that the *2p* states on the surface oxygen atoms are destabilized and therefore they are very reactive (Gong and Selloni, 2005). Table 2.6 show some crystallographic data for the three TiO_2 polymorphs.

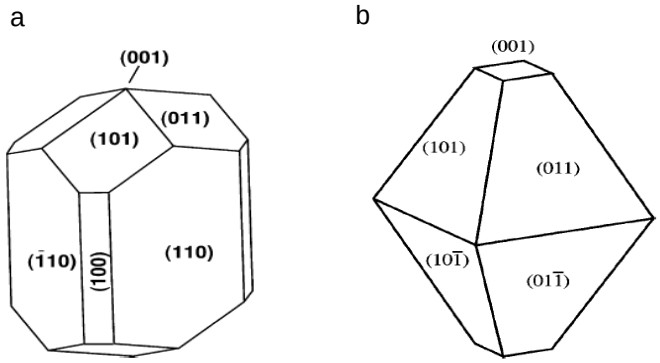

Figure 2.18 Equilibrium shape of TiO_2 in a) rutile crystal and b) anatase (Diebold, 2003).

Table 2.6 Crystal structure data for three titanium oxide polymorphous (Gupta and Tripathi, 2011).

Properties	Rutile	Anatase	Brookite
Crystal structure	Tetragonal	Tetragonal	Ortorhombic
Lattice constant/Å	a = 4.5936 c = 2.9587	a = 3.784 c = 9.515	a = 9.184 b = 5.447 c = 5.154
Volume/molecule $Å^{-1}$	31.2160	34.061	32.172
Density/g cm^{-3}	4.13	3.79	3.99
Ti-O bond length/Å	1.949 1.980	1.937 1.965	1.87 - 2.04
O-Ti-O bond angle/°	81.2 90.0	77.7 92.6	77.0 - 105

Doping of titanium oxide to enhance its photocatalytic activity

TiO_2 is considered almost an ideal photocatalyst because of its long chemical stability, wide range of production methods, some of them with low production costs and the fact it is an environmentally safe material (Zaleska, 2008). However, the two main drawbacks of TiO_2 as a photocatalyst are (i) the high recombination probability between the electron and electron-hole that results in a reduction of its efficiency and

the unproductive release of heat or photons; and (ii) its inability to use the visible light as the band gap of the TiO_2 is 3.2 eV (387 nm), which falls in the UV spectrum. As this represents 4% of the solar radiation compared to 50% of the visible light (Ni et al., 2007), only a small fraction of the available solar irradiation is effectively used. To address the latter phenomenon, several approaches have been considered such as the incorporation of metals, non-metal dopants or the synthesis of oxygen-deficient TiO_2 (Zaleska, 2008). Amongst these methods, non-metal doping has become the most attractive approach to achieve a shift in the absorption threshold of TiO_2 to the visible light using elements such as N, C, S, B, P and F (Fujishima et al., 2008). Although, the origin of the red-shift adsorption of TiO_2 doped with non-metal elements is still a matter of debate, with the origin of the absorption of light in the visible spectrum and the state of the non-metal elements in the TiO_2 lattice considered the two main explanations. Regarding the former, Asahi et al. (2001) suggested that the combination of the *2p* nitrogen orbitals with the *2p* oxygen hybridized orbitals from TiO_2 results in a band gap narrowing. However, Irie et al. (2003a) proposed the formation of a midgap level slightly above the top of the VB. To further elucidate the state of the non-metal elements, XPS studies conducted on TiO_2 surfaces showed two kinds of Nitrogen *1s* peaks, one about 396 eV and another one close to 400 eV (Nakano et al., 2005). The first peak is assigned to nitrogen that substitutes oxygen in the TiO_2 lattice, whereas the second peak is believed to be related to interstitial nitrogen compounds in the form N_xO_y (Reyes-Garcia et al., 2007). According to density of states (DOS) experiments conducted by Asahi and Morikawa (2007), this results in localized impurity states in the band gap below the CB and thus contributing to the visible-light absorption. Figure 2.19 show the schematic representation of both types of nitrogen doping.

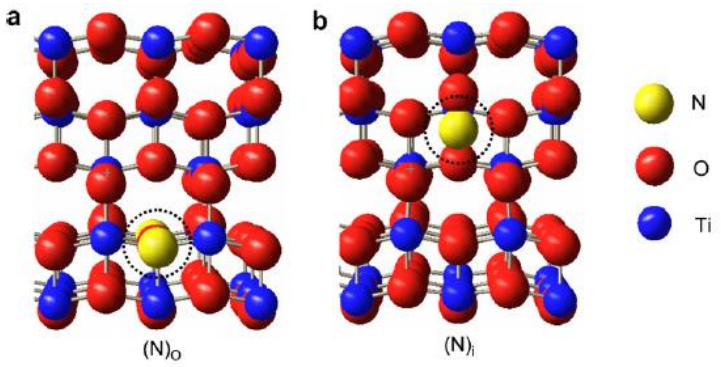

Figure 2.19 Schematic representation for a) substitutional N-doping and b) interstitial N-doping (Asahi and Morikawa, 2007).

In addition, Figure 2.20 show the relative energy position of various dopants in the TiO_2 lattice relative to the band edges of several non-metal elements. For instance, substitutional nitrogen states lie just above the VB due to the introduction of N *2p* orbitals, while interstitial nitrogen states lead to the formation of midgap states (Di Valentin et al., 2005b). Asahi et al. (2001) studied substitutional doping of C, N, P, F, and S in anatase crystals and found that nitrogen was the most promising doping agent as the N 2*p* states contribute to band gap narrowing, by mixing them with the O *2p* states; even though their results show S had a similar band gap narrowing as N, it is suggested that its incorporation into the TiO_2 lattice is more difficult because of the larger ionic radius of S (Asahi et al., 2014).

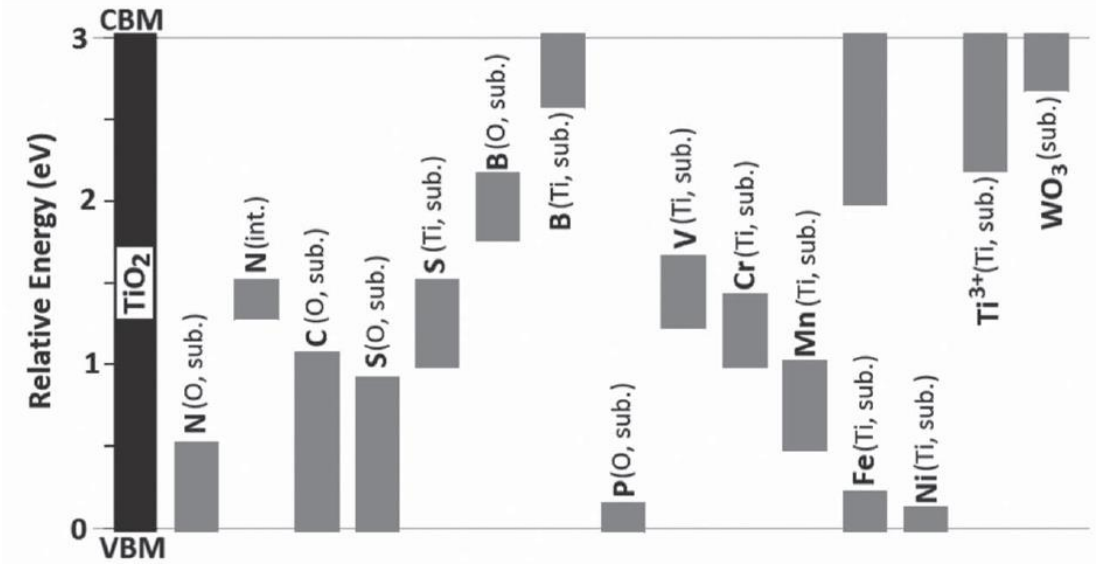

Figure 2.20 Schematic illustration of the energy level positions for various dopants in TiO_2 relative to its band edges (Paramasivam et al., 2012).

2.5.2 Iron oxide nanoparticles

The synthesis of iron oxide nanoparticles has flourished in the last decade driven by the possibility of exploiting their properties for applications such as drug delivery systems, hyperthermia treatments, contrast agents in magnetic resonance imaging; production of magnetic inks; magnetic seals in motors, and many other technological uses (Figuerola et al., 2010).

The most commonly known iron oxide structures are magnetite (Fe_3O_4) maghemite (γ-Fe_2O_3) and hematite (α-Fe_2O_3). Magnetite has the strongest magnetism of any transition metal oxide (Majewski and Thierry, 2007) and its oxidation leads to the

production of maghemite. Hematite is the final transformation of both oxides (Teja and Koh, 2009). Table 2.7 show some of their physical and magnetic properties.

Table 2.7 Physical and magnetic properties of iron oxides.

	Magnetite	Maghemite	Hematite
Molecular formula	Fe_3O_4	γ-Fe_2O_3	α-Fe_2O_3
Density/g cm^{-3}	5.5	5.0	6.5
Type of magnetism	Ferro-	Ferri-	Weakly ferro- or antiferro-
Curie Temperature/°C	850	820 - 926	956
Magnetization saturation at 300 K/A m^2 kg^{-1}	92 - 100	60 - 80	0.3
Crystallographic system	Cubic	Cubic or tetrahedral	Rhombohedral, hexagonal
Lattice parameters/nm	a =0.8396	Cubic (a = 0.8347) Tetragonal (a= 0.8347 c= 2.501)	Hexagonal (a = 0.5034 c = 1.375) Rhombohedral (a= 0.5427 α= 55.3°)

The three iron oxides consist of arrays of Fe ions and O^{2-} ions. The latter has a higher ionic radius (O^{2-} = 0.14 nm compared to Fe^{2+} = 0.065 nm and Fe^{3+} = 0.082 nm) and its arrangement governs the crystal structure and ease off phase transformation between the iron oxides (Cornell and Schwertmann, 2003). The crystal structure of the three iron oxides can be described as a closed-packed plane of oxygen anions with iron cations in octahedral or tetrahedral interstitial sites. Magnetite and maghemite have their oxygen atoms in a cubic close packed arrangement and their iron ions in a spinel structure. Magnetite contains Fe(III) and Fe(II) ions, the former ones randomly distributed between octahedral and tetrahedral sites and the latter limited to octahedral sites (Teja and Koh, 2009). In contrast, Maghemite, has mostly Fe(III) ions with cation vacancies in octahedral sites which compensates for the absence of Fe(II). The magnetite formula can be written as $Fe^{3+}_{tetra}[Fe^{3+}Fe^{2+}]_{octa}O_4$ and maghemite is represented as $(Fe^{3+}_8)_{tetra}\left[Fe^{3+}_{40/3}V_{8/3}\right]_{oct}O_{32}$, where *V* represents

iron vacancies (Parkinson, 2016). Hematite might have a hexagonal or a rhombohedral crystallographic system, the arrangement consisting of two thirds of the sites filled with Fe(III) ions, with a regularity of two sites filled followed by one vacant site. Therefore, the arrangement of the cations produces pairs of $Fe(O)_6$ octahedra and each one shares with three neighbouring octahedra in the same plane and one face with an octahedron in an adjacent plane (Parkinson, 2016). Figure 2.21 show the crystal structure of magnetite and hematite.

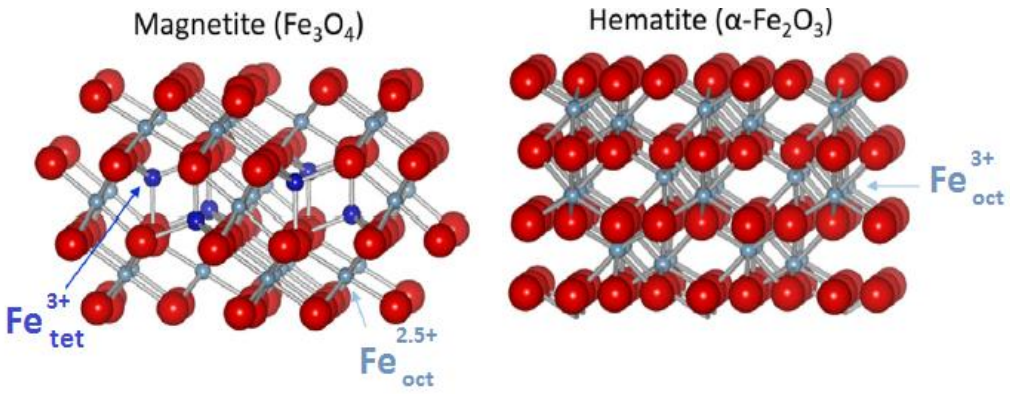

Figure 2.21 Crystal structure of magnetite and hematite (Parkinson, 2016).

Figure 2.22a show the equilibrium morphology of a magnetite crystal based in a Wulff construction at zero Kelvin (Santos-Carballal et al., 2014). The resulting structure is cubic with truncated corners, being the plane (001) the one who dominates the morphology, with the lowest surface energy, followed by the (111). The resulting equilibrium structure is similar to crystals obtained by Zhao et al. (2007). Other reported magnetite crystal shapes also include cubic, truncated octahedral (Kim et al., 2009), tetrahedral and almost spherical (Zhang et al., 2006) ones. For hematite, the morphological important surface areas are (001), (012), (100), (104) (018) and (113) being the (001) surface the most extensively studied in the literature (Cornell and Schwertmann, 2003). Guo and Barnard (2011) investigated its morphology over a range of sizes and shapes as can be seen on Figure 2.22b. Their results based on a Wulff construction predict the most stable form is a pseudocube, followed by prisms and rhombohedrum. However, under their modelling the (001) surface was not considered as they only evaluated “clean” surfaces that have the absence of impurities, adsorbates and defects, such as hydroxyl groups that are commonly attached to the (001) surface under ambient or vacuum conditions (Shaikhutdinov and Weiss, 1999). Their theoretical estimations on the morphology of hematite are in

good agreement with reported crystal structure that have cubic (Cao et al., 2006), hexagonal, spherical (Wang et al., 2008) and rhombohedral nanocrystals (Wang et al., 2008) shapes.

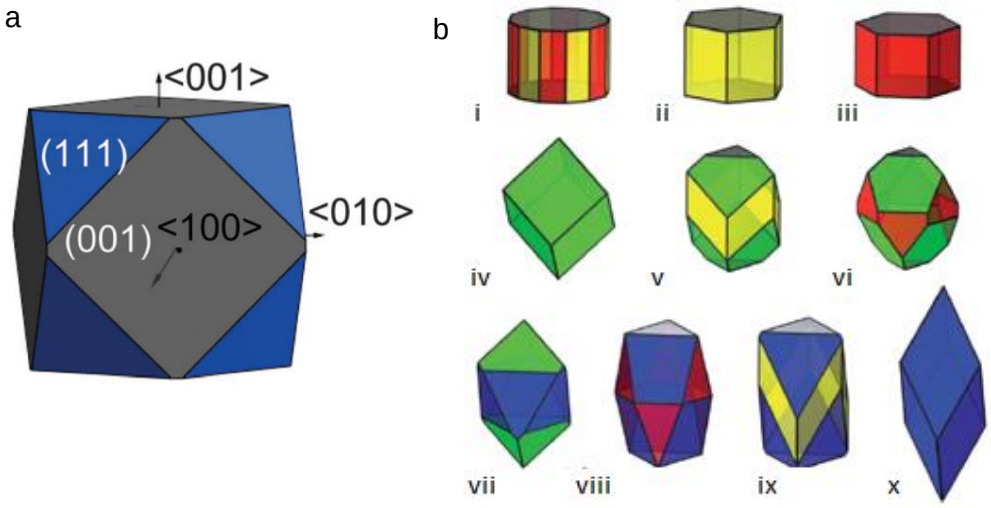

Figure 2.22 Equilibrium morphology of a) magnetite (Santos-Carballal et al., 2014) and b) different hematite morphologies (Guo and Barnard, 2011) colours: red (110), yellow (100), green (012) and blue (101). *i, ii* and *iii* are dodecagonal and hexagonal prism, *iv* pseudocube*, v, vi* and *vii* are truncated pseudocubes, *viii, ix* truncated hexagonal prims and *x* rhombohedron.

For the three iron oxides, the conduction band is composed of empty *3d* iron orbitals. In contrast, the valence band consist of full *3d* Fe orbitals with oxygen antibonding *2p* orbitals, while the band gap values are 2.2, 2.1 and 2.03 eV for hematite, magnetite and maghemite, respectively (Cornell and Schwertmann, 2003). Therefore, they are photocatalytic active materials under the visible wavelength and have been widely used for the degradation of pollutants in water (Kwan and Voelker, 2003, Munoz et al., 2015).

2.5.3 Photocatalytic activity of titanium dioxide and iron oxide

Titanium dioxide and iron oxide are semiconductors, which means that they have a void region where no electronic states exist. This region extends from the top electron filled Valance Band (VB) to the bottom of the electron vacant conduction band (CB)

and is called the *band gap, E_g.* When a semiconductor, is exposed to light with an energy equivalent or greater than the band gap, electrons from the VB are promoted to the CB. Therefore, an electron is excited from the VB to the CB and thus leaves an electron-hole in the VB. The electrons in the CB are unstable and they might recombine with electron holes or interact with adsorbed species on the surface of the material. However, it is the promotion of these electrons to the CB that enables materials such as titanium dioxide and iron oxide to be used for applications such as photocatalytic, water splitting (Fujishima, 1972) and purification of pollutants from water (Gupta and Tripathi, 2011).

Equation 2-30 illustrates the promotion of an electron (e_{CB}^-) and the formation of an electron-hole (e_{VB}^+) when the surface of a metal oxide is irradiated by light with energy equal or higher than the band gap.

$$M_xO_y + h\upsilon \rightarrow\ e_{CB}^- + e_{VB}^+ \qquad 2\text{-}30$$

After the generation of electrons and electron holes, a series of reactions might proceed by different pathways as shown on Figure 2.23. For instance, electron-holes might react with electron-donor species (D) adsorbed on the surface of the catalyst, meanwhile electrons might react with acceptor species (A). However, other possible pathways involve the recombination of an electron and electron-hole on the surface causing the release of heat in the interior of the particle. The interaction between the electrons and the electron-holes with adsorbed molecules such as water or hydroxyl groups on the surface of the semiconductor lead to the generation of radicals which can oxidize a wide range of compounds as the next equations describes:

$$e_{VB}^+ + OH^- \rightarrow \bullet OH \qquad 2\text{-}31$$

$$e_{VB}^+ + H_2O \rightarrow \bullet OH + H^+ \qquad 2\text{-}32$$

At the same time, the photon-produced electrons in the CB, carry out the reduction of electron acceptors adsorbed on the surface of the semiconductor such as oxygen:

$$e_{CB}^- + O_2 \rightarrow \bullet O_2^- \qquad 2\text{-}33$$

Equations 2-31 to 2-33 show the formation of hydroxyl ($\bullet OH$) and the superoxide ($\bullet O_2^-$) radicals, which are highly reactive species with a free unpaired electron, that make possible the degradation of pollutants (Lan et al., 2013).

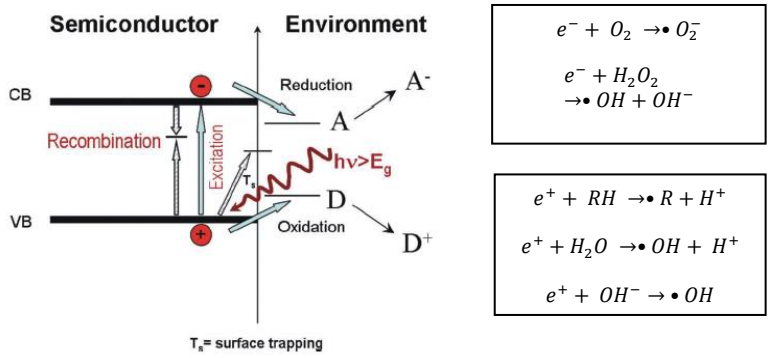

Figure 2.23 Process occurring on the surface of a semiconductor after UV excitation modified from Paramasivam et al. (2012).

2.6 Summary

The chapter gave an overview of the different methods to synthesize NPs at laboratory-scale and the current challenges to achieve mass production of NPs, including advantages and disadvantages associated of each synthesis method. This was followed by an in-depth overview of membrane emulsification. ME was compared to other emulsification methods in terms of emulsion polydispersity and energy requirements. In addition, a description of different droplet size prediction models was given with the intention to have a further understanding of the droplet formation mechanism in ME. Then, AAMs were introduced as a membrane uniquely suited for ME due to its self-ordering porous structure and tuneable pore size within the nanometre range. Consequently, the chapter reviewed the main parameters that influence pore size, gave a description of the pore growth mechanism and the main reactions involved during the anodization of the aluminium oxide. Finally, a brief description of the main properties of titanium and iron oxide nanoparticles was given.

Chapter 3: Materials and methods

The chapter describes the experimental procedures and characterization techniques involved in the synthesis of anodic alumina membranes, the design of membrane emulsification rigs and the production of nanoparticles. It is divided in three main sections, the design of two membrane emulsification rigs is described in Section 3.1 the manufacturing of anodic alumina membranes and the synthesis details for iron oxide, titanium oxide and polystyrene nanoparticles are explained in Section 3.2 finally, Section 3.3 provides a brief description of each characterization technique used.

3.1 Design of membrane emulsification rigs

A batch and a continuous membrane emulsification rig were designed to produce nanoemulsions and metal oxide nanoparticles. The description of both rigs is shown next:

3.1.1 Batch membrane emulsification setup

Oil-in-water NEs were produced using a dead-end 3D-printed membrane emulsification rig with an overhead stirrer (IKA, RW 11). The batch membrane emulsification setup (Figure 3.1a) consist of a 50 ml tank filled with 25 ml of continuous phase. The tank was connected at the base to a 13 mm membrane holder (Millipore) where the AAM was placed (Figure 3.1b). The membrane was flush with the base of the tank, leaving an exposed membrane area of 6 mm in diameter (Figure 3.1c). A syringe pump (KR analytical, Nexus 200) was used to push the disperse phase, through the membrane pores. The shear stress was provided via the overhead stirrer (IKA, RW 11) with a 5 mm diameter, 3 mm thick and 4 mm high paddle-blade impeller at different rotational speeds ranging from 100 to 1750 rpm.

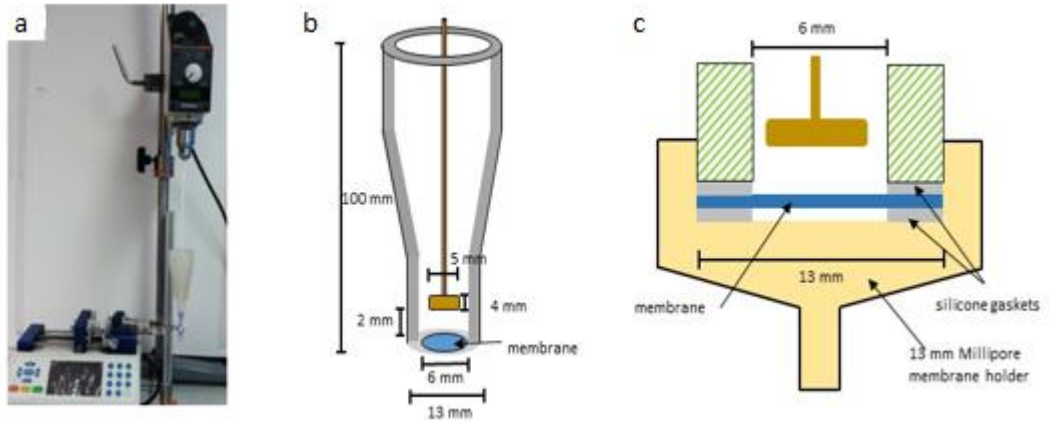

Figure 3.1 a) Batch membrane emulsification apparatus; b) dimensions of the tank; and c) close-up of the membrane holder and paddle-blade impeller.

Several membrane parameters (average pore size), process parameter (rotational speed and injection rate) and surfactant parameters (effect of the molecular weight of the surfactant) were evaluated. Table 3.1 shows the molecular weight and HLB values of the surfactants used during the production of nanoemulsions in the batch membrane emulsification rig.

Table 3.1 Molecular weight and HLB values of selected surfactants.

Surfactant	Molecular weight/g mol^{-1}	HLB
Brij O10	709	12.4
Tween 20	1228	16.7
Tween 80	1310	15.0
Span 80	428	4.3

3.1.2 Continuous membrane emulsification rig

A continuous membrane emulsification rig with a tubular membrane in a crossflow configuration was designed (Figure 3.2). The rig includes a continuous phase tank (A) with a temperature controller (Grant). The disperse phase was kept in a stainless-steel cylinder (B) and was fed into the emulsification module using compressed air via a two-stage pressure regulator (Swagelok), (C). Meanwhile, the continuous phase is pumped (Ismatec MPC-Z) (D) into the membrane emulsification module (E). The produced emulsion is collected in a glass container (F). All the data is recorded using the software LabVIEW (National Instruments).

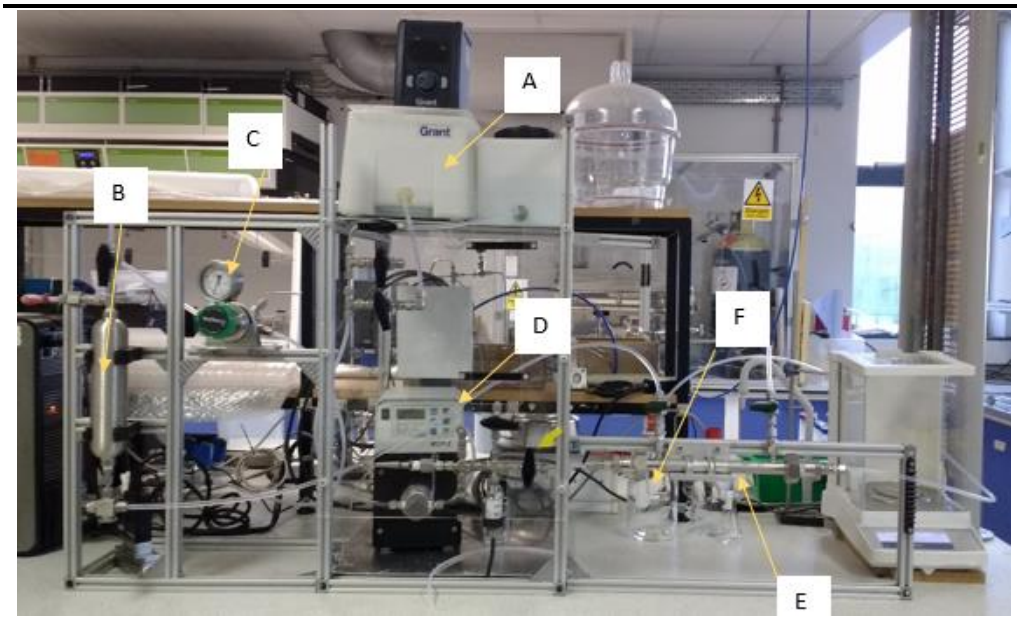

Figure 3.2 Continuous membrane emulsification rig.

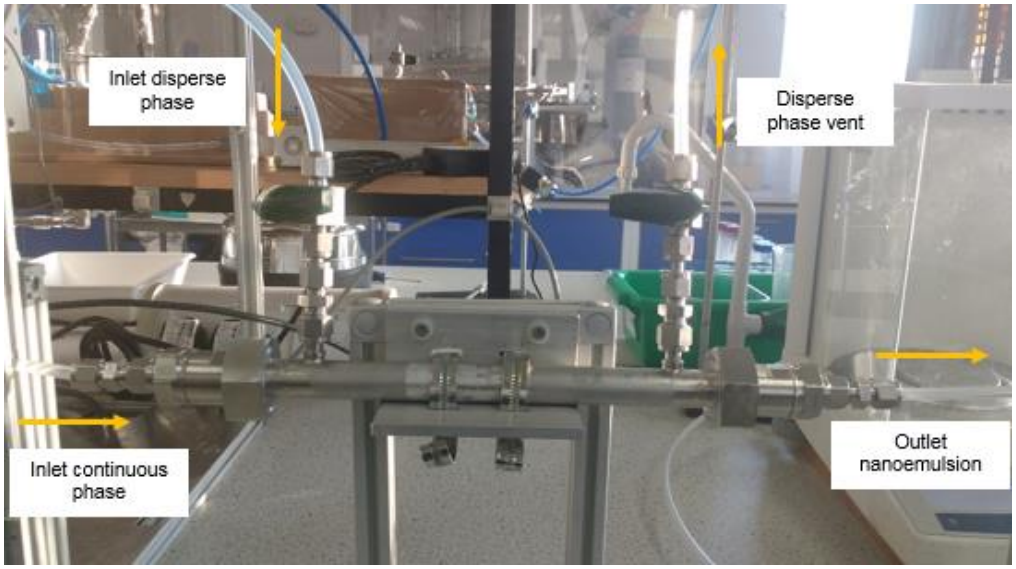

Figure 3.3 Close-up of the membrane emulsification module.

The membrane emulsification module and the membranes were purchased from Fraunhofer IKTS. The membranes consisted on tubular alumina membranes. A close up of the membrane module is shown Figure 3.3. The characteristic of the membrane are in Table 3.2.

.

Table 3.2 Characteristics of ceramic membranes according to Fraunhofer IKTS.			
Outer diameter/mm	10	Substrate	α-Al_2O_3, d_{50} = 3 µm
Channel diameter/mm	7	Membrane	α-Al_2O_3, d_{50} = 100 nm
Membrane length/mm	250	End sealing	glass, 13 mm
Filtration area/m^2	$5.5x10^{-3}$		

3.1.3 Semi-continuous membrane emulsification setup

A batch ME setup (Micropore LDC-1 dispersion cell) was used to produce *an oil-in-water* NE by adapting a ring-shaped AAM at the bottom of the setup, the description of the synthesis procedure can be found in Section 3.2 . The continuous phase consisted of 120 ml of 1.0% wt. Tween 20 in DI water (Figure 3.4). The dispersed phase injection line was first filled with continuous phase using a syringe pump until the bottom of the dispersion cell was filled with the continuous phase. The membrane was then placed at the bottom of the dispersion cell, the glass container placed on top of the dispersion cell, followed by an overhead stirrer and the rotational speed adjusted. Next, 2 ml of hexane as dispersed phase was pumped using an injection rate of 0.25 ml min^{-1}.

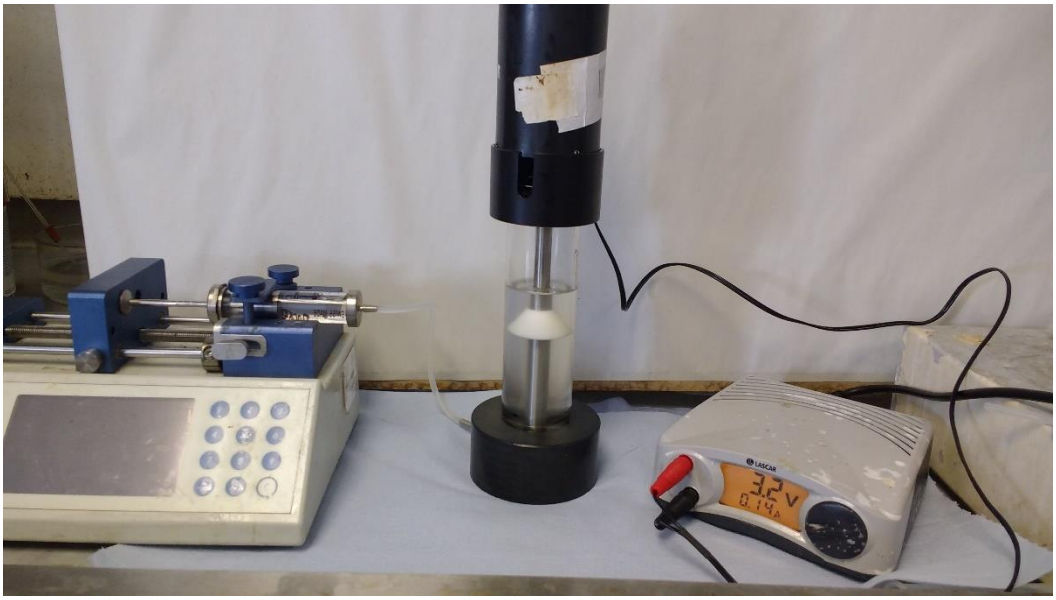

Figure 3.4 Commercial dead-end membrane emulsification (Micropore LDC-1 dispersion cell).

3.2 Synthesis methods

In the following section the production of anodic alumina membranes and ring-shaped anodic alumina membranes are described in Section 3.2.1 and Section 3.2.2 respectively. The experimental procedures to synthesize titanium oxide and iron oxide nanoparticles by membrane emulsification are described in Sections 3.2.3 and 3.2.4 respectively.

3.2.1 Synthesis of anodic alumina membranes

Anodic alumina membranes were prepared by a two-step anodization, a method originally proposed by Masuda and Fukuda (1995). This method was chosen as it allows the production of high quality membranes in terms of narrow pore size distribution, low tortuosity and high uniformity. The AAMs manufacturing can be divided as a series of three main steps: pre-treatment, anodization and post-treatment. Figure 3.5 shows an overall scheme of the synthesis procedure.

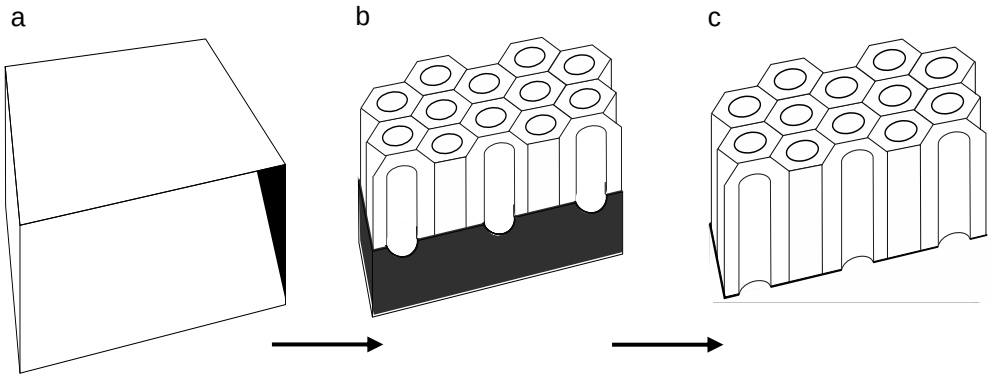

Figure 3.5 Schematic representation of the main steps during the synthesis of AAMs.

Materials

High purity aluminium foil (99.99%) with a 0.25 mm thicknesses was purchased from Alfa Aesar. Phosphoric acid (H_3PO_4) 85 % wt., perchloric acid ($HClO_4$) 70% wt., hydrochloric acid (HCl) 37% wt., acetone (C_3H_6O) 99%, ethanol (C_2H_5OH) 96% and copper (II) chloride dihydrated ($CuCl_2 \cdot 2H_2O$), all reagent grade, were purchased from Sigma Aldrich, UK. Chromium (VI) oxide (CrO_3) and sulphuric acid (H_2SO_4), reagent

grade, were purchased from Fisher Scientific. Oxalic acid anhydrous ($C_2H_2O_4$) 98% was purchased from Across Organics.

Pre-treatment

The aluminium foil was cut in 16 mm x 25 mm rectangles and their corners were rounded. The aluminium pieces were annealed in a Carbolite CWF 1100 furnace, placed between two stainless steel plates, with a 1 kg weight on top to flatten the aluminium. The annealing conditions were 500 °C for 1 hour, using a temperature ramp of 20 °C min^{-1}.

Later, the samples were degreased using a sonication bath in acetone for 15 minutes. Next, the aluminium was electro-polished by submerging the sample into a solution prepared by mixing 800 ml ethanol (96 %) and 200 ml perchloric acid (62 %) at - 77.0 °C ± 5.0 °C. The solution was cooled using dry ice, $CO_{2(s)}$, in an acetone bath. During the electro-polishing, a potentiostatic value of 20.0 V was applied for 15 minutes (Figure 3.6). Then, the sample was cleaned using first ethanol (96.0%) and then deionized water. The objective of the electro-polishing was the removal of the natural aluminium oxide layer and the reduction of microscopic defects, leaving a smooth aluminium surface. Therefore, as soon as the electro-polishing step is over the sample must be anodized.

Figure 3.6 Electro-polishing of the aluminium.

Anodization

The two-step anodization process consists of exposing an aluminium foil to a first short anodization to form a thin aluminium oxide porous layer. The former layer is removed leaving an aluminium surface with a scalloped pattern as a template for the

second anodization. The anodization takes place inside an electrolytic cell (Figure 3.7a) but the aluminium foil is previously placed in bespoke Teflon holders (Figure 3.7b) with an effective anodization diameter of 12 mm. Table 3.3 shows the anodization conditions according to the applied voltage. Next, the sample is washed thoroughly with deionized water and placed in a new set of Teflon holders to remove the first aluminium oxide layer using a solution prepared with 500 ml of 1.8% wt. H_2CrO_4 and 500 ml of 6 % wt. H_3PO_4, at 60 °C for approximately 20 minutes (Figure 3.7c). When the process is over, a shiny aluminium template is obtained for a subsequent second anodization, which is carried out at the same conditions as the first anodization.

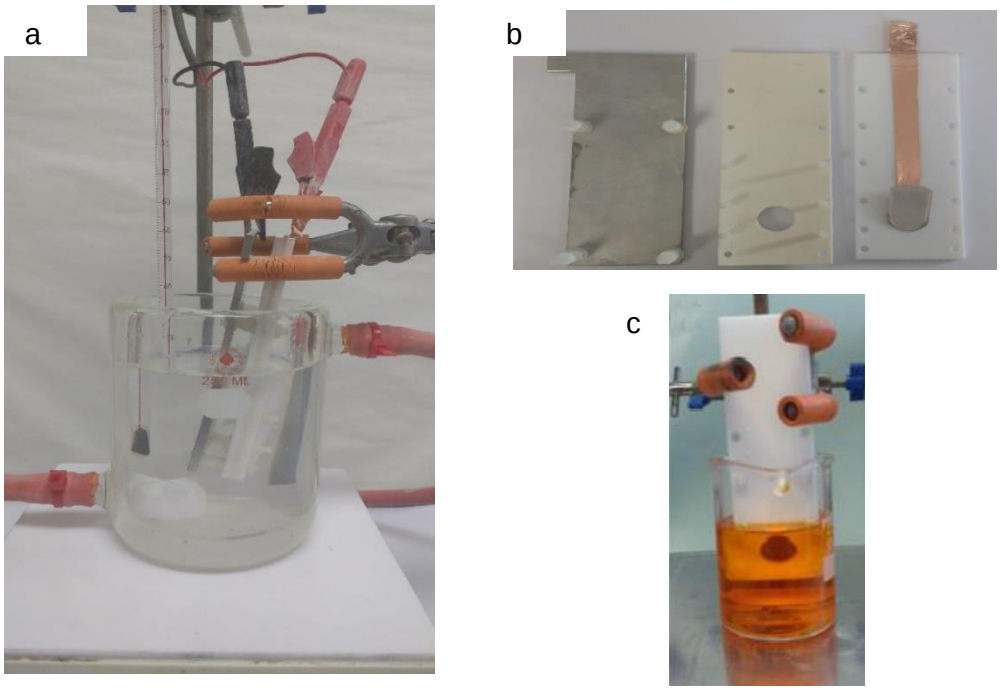

Figure 3.7 a) Anodization cell b) holders for anodization c) removal of the aluminium oxide layer.

Table 3.3 Synthesis conditions for a two-step anodization process

Electrolyte	Voltage/V	Temperature/°C	Anodization time/h	
			First	Second
0.50 M H_2SO_4	20	1 ± 1	2 - 3	5 - 8
	25	1 ± 1	2 - 3	5 - 8
0.30 M $C_2H_2O_4$	40	13 ± 1	1.5	12
	50	10 ± 1	1.5	9
	60	10 ± 1	1.0	7
	70	6 ± 1	0.5	6
	80	0 ± 1	0.5	5

Post-treatment

After the second anodization, the aluminium substrate layer is removed using a 1:1 solution of 0.20 M $CuCl_2$/20% wt. HCl. This step lasts until a complete removal is achieved and the transparent aluminium oxide porous structure is visible; this step might last approximately 25 minutes (Figure 3.8a).

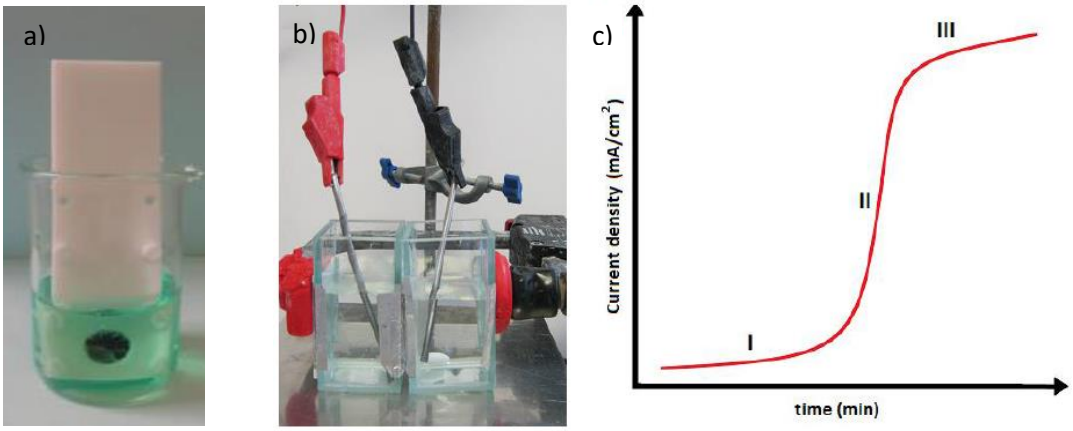

Figure 3.8 a) Aluminium base layer removal step b) pore opening process c) current density versus time plot behaviour during the pore opening process.

The final process involves the dissolution of the residual aluminium oxide barrier where a wet chemical method developed by Lillo and Losic (2009) was adopted. In this process, the membrane was placed between two glass beakers, each one with a hole in one of their sides (Figure 3.8b). A rubber layer was glued surrounding the holes, which provides support for the membrane and improves sealing. The main objective of this method is that the anodized aluminium oxide is exposed to both solutions. Figure 3.9 shows an illustration of the pore opening setup. The beaker that

will face the “top side” of the membrane was filled with a 0.2 M KCl solution. The second beaker, the one that will face the “bottom side” of the membrane, was filled with a 6.0% wt. H_3PO_4 solution at 60 °C. The “top side” is where the pore formation starts and the “bottom side” is where the scalloped aluminium oxide layer remains. The aluminium oxide barrier was slowly dissolved by the H_3PO_4 solution and the process can be tracked by measuring the current density over time. The latter is done by placing an electrode in each beaker and applying a small potential (2.5 V). When the current density reached a plateau value the pore opening has finished. Figure 3.8c illustrates the plot behaviour obtained from the pore opening process were the three main steps are when the pores are closed (I), pore opening (II) and pore widening (III). Finally, Figure 3.10 illustrates the different stages of the production of a flat anodic alumina membrane, since using aluminium as starting material until we obtain an open porous structure.

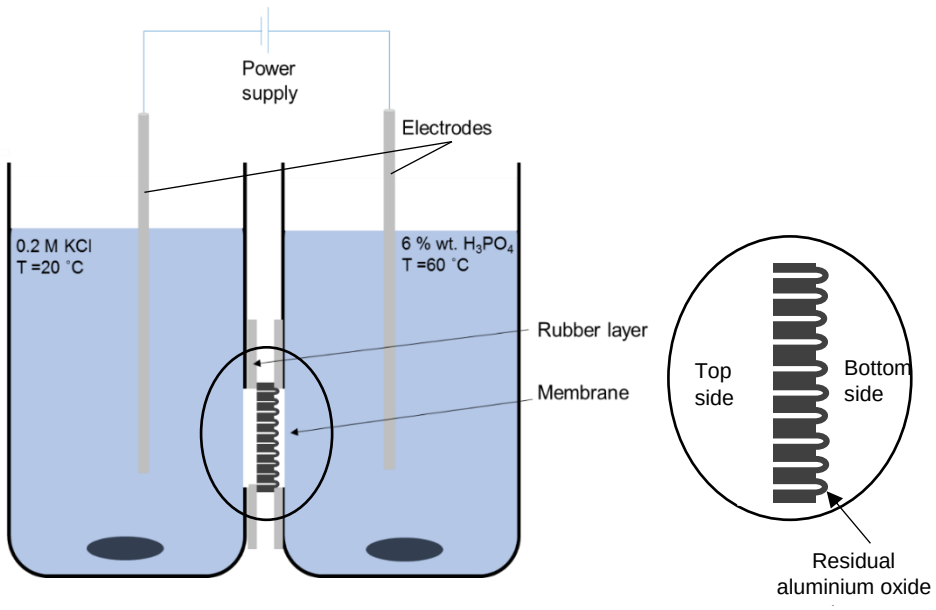

Figure 3.9 Schematic representation of the pore opening setup.

Figure 3.10 Illustration of the different stages to produce a flat anodic alumina membrane.

3.2.2 Ring-shaped anodic alumina membranes

Ring-shaped anodic alumina membranes were fabricated by a two-step anodization process using a similar procedure for the pre-treatment and the anodization as the one described in Section 3.2.1 The main difference relies in the post-anodization steps, which will be briefly discussed next:

Post-anodization

Ring-shaped membranes were produced using a 60 V anodization potential. After the second anodization, the back side of the membrane was carefully covered with a protective layer leaving exposed an annular area that would subsequent dissolved. Then, the sample was placed in custom-made Teflon holders and exposed to a 0.2 M $CuCl_2$/20% wt. HCl until a complete removal of the aluminium was achieved. Finally, the residual aluminium oxide layer was removed as described above in the pore opening process. Figure 3.11 shows the different stages during the production of the ring-shaped AAMs.

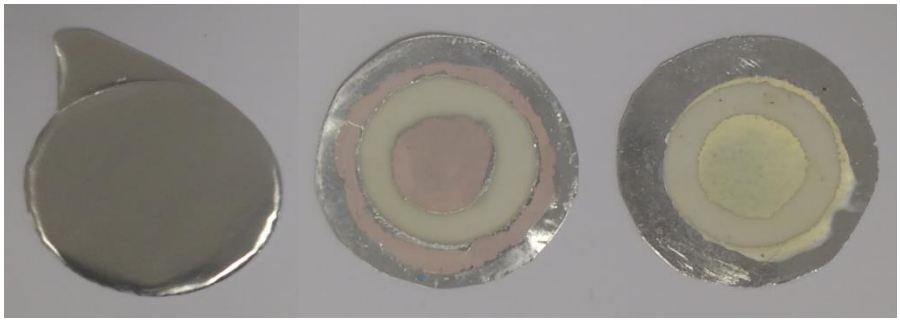

Figure 3.11 a) Electro-polished aluminium b) ring-shaped membrane back section and c) front section.

3.2.3 Synthesis of titanium oxide nanoparticles

Materials

Titanium(IV) 2-ethylhexanoate, $Ti(EH)_4$ was used as a titanium precursor and purchased from Alfa Aesar. Hexane (C_6H_{14}), sodium dodecyl sulphate, SDS, ($NaC_{12}H_{25}SO_4$) and 28 % wt. NH_4OH solution were purchased from sigma Aldrich; ethanol (C_2H_5OH) and acetone (C_3H_6O) from VWR.

Synthesis procedure

Titanium oxide nanoparticles were synthesized in the continuous tubular membrane emulsification rig shown in Section 3.1.2 The disperse phase consisted of a solution of 33 % v/v $Ti(EH)_4$ in hexane. Meanwhile the continuous phase was a 1 % wt. SDS in deionised water. The nanoemulsions were produced using 250 mm tubular aluminium oxide ceramic membranes with pore sizes of 100 nm. The specification for both membranes can be found in

Table 3.2.

The resultant nanoemulsion was collected in a glass container where the NH_4OH was added drop wise, with a 10 % molar excess of NH_4OH based on the stoichiometric amount of $Ti(EH)_4$ added in the disperse phase. The titanium oxide nanoparticles precipitated in the glass container and the system was kept under agitation for one hour. After the synthesis, the nanoparticles were immediately washed using first acetone, then ethanol and finally water in consecutive cycles of centrifugation and sonication four times for each type of solvent. Later the nanoparticles were dried at 70 °C for 24 h and then calcined at different temperatures (200, 300 and 400 °C) using a heating ramp of 5 °C min^{-1} and 1 hour of dwell.

3.2.4 Synthesis of iron oxide nanoparticles

Materials

Iron(III) 2-ethylhexanoate, $Fe(EH)_3$ was used as an iron precursor and purchased from Alfa Aesar. Hexane (C_6H_{14}), sodium dodecyl sulphate, SDS, ($NaC_{12}H_{25}SO_4$) and 28 % wt. NH_4OH solution were purchased from sigma Aldrich; ethanol (C_2H_5OH) and acetone (C_3H_6O) from VWR.

Synthesis procedure

To produce iron oxide nanoparticles, the dispersion cell (Micropore LDC-1), Figure 3.4, was modified to run as a semi-continuous process, with a constant injection of fresh continuous phase and a constant withdrawal of the emulsion using a double peristaltic pump with a rate of 15 ml min^{-1} (Figure 3.12). The dispersed phase consisted of 17 ml of a 60 % v/v $Fe(EH)_3$ in hexane solution. The continuous phase consisted of 1.5 L of 0.5 % wt. Tween 20 in DI water. Iron (III) 2-ethylhexanoate in mineral spirits (Fe 6 %), $Fe(C_8H_{15}O_2)_3$ or $Fe(EH)_3$ was used as the iron precursor and purchased from Alfa Aesar. Hexane, Tween 20 and 28 % wt. NH_4OH solution were

purchased from sigma Aldrich; ethanol and acetone from VWR. 50 ml of 1.5 M NH_4OH were poured into the flask containing the produced emulsion using an injection rate of 1.5 ml min^{-1}, while the system was kept under a gentle agitation for 24 h using a magnetic stirrer. The as-produced nanoparticles were then washed using first acetone, then ethanol and finally water in consecutive cycles of centrifugation and sonication four times for each type of solvent. Finally, the nanoparticles were dried at 70 °C for 24 h and calcined at 700 °C using a heating ramp of 5 °C min^{-1} and 0.5 hours as dwell time.

Figure 3.12 Semi-continuous ME setup to produce iron oxide nanoparticles.

3.3 Material Characterization Techniques

3.3.1 Scanning electron microscopy

Scanning electronic microscopy (SEM) is a versatile characterization technique that uses an electron beam to obtain information about the morphology of a sample.

Figure 3.13 is a schematic diagram of a SEM and consist of an electron gun fitted with a thin tungsten filament as a cathode. By applying an electric field electrons are emitted from the cathode and drawn towards the anode. The anode has an aperture that produces a narrow electron beam that then passes through a series of lenses to correct the direction of the beam (condenser lens) and reduce the diameter of the electron beam (objective lens) to produce an image with an enhanced resolution (Zhou and Wang, 2007). When the electron beam hits the sample two types of interactions might occur. The first one is that incident electrons are scattered back with an angle higher than 90°, these are called back-scattered electrons (BSE). The

second one, occurs when incident electrons interact with atoms from the sample. These interactions lead to the emission of electrons from the sample, which are called secondary electrons (SE). These are used to obtain the topographic information of the sample. An electron detector is located close to the sample holder and consists of a scintillator and a photomultiplier system. The first one converts the electron signal into photons, meanwhile the second one amplifies the signal and converts back into an electron signal (photomultiplier) and finally the topographic information of the sample is displayed as brightness distribution on the screen on the SEM (Zhou and Wang, 2007).

A scanning electronic microscope using a field emission gun (FESEM) from the Microscopy and Analysis Department of the University of Bath (JEOL JSM 6330F) was used to determinate the average pore size of the AAMs. The samples were analysed by FESEM because this technique offers the possibility to work at lower voltages, which allows charge reduction and is possible to obtain micrographs with higher resolution.

Statistical analysis of the SEM micrographs

The obtained SEM micrographs were analysed using *ImageJ*. The software was used to determinate the average pore diameter, interpore distance, porosity and pore density. The procedure for the analysis is presented as sequence of images in Figure

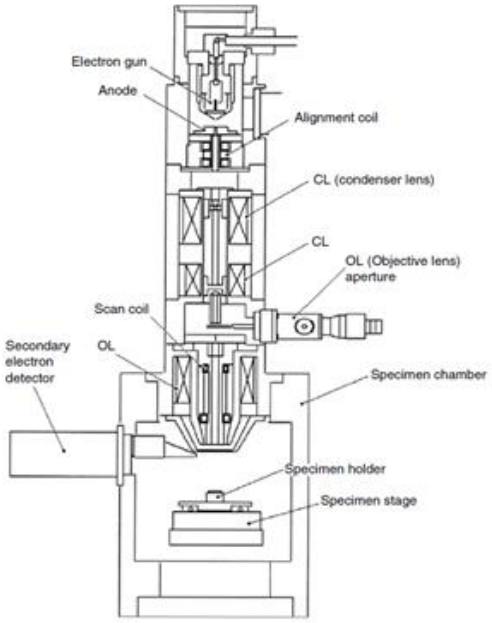

Figure 3.13 Schematic diagram of a scanning electron microscope (Yao and Wang, 2005).

3.14. The first step is to establish the scale of the image using the scale bar from the original SEM micrograph (a) and a specific area is selected for the analysis (b). Secondly, the software allows the improvement of contrast and brightness (c). Next, the threshold tool converts any grey scale image into a black and white image (d), which allows the program to calculate the desired parameters and the measured area is shown in a black contour line (e). However, the threshold conversion from a grey scale image into a black and white image leads to a small error in the pore diameter calculation due to the presence of black pixels surrounding the pore diameter (Figure 3.14d) and that can interfere with the estimation of the pore diameter when the contour area is obtained (Figure 3.14e).

The porosity is calculated as the ratio of the area of the pores to the area of analysis. Meanwhile the pore diameter is estimated as the product of the ferret diameter and the circularity. For each SEM micrograph, at least three different areas were selected for the statistical analysis to have a more accurate estimation of the desired parameters.

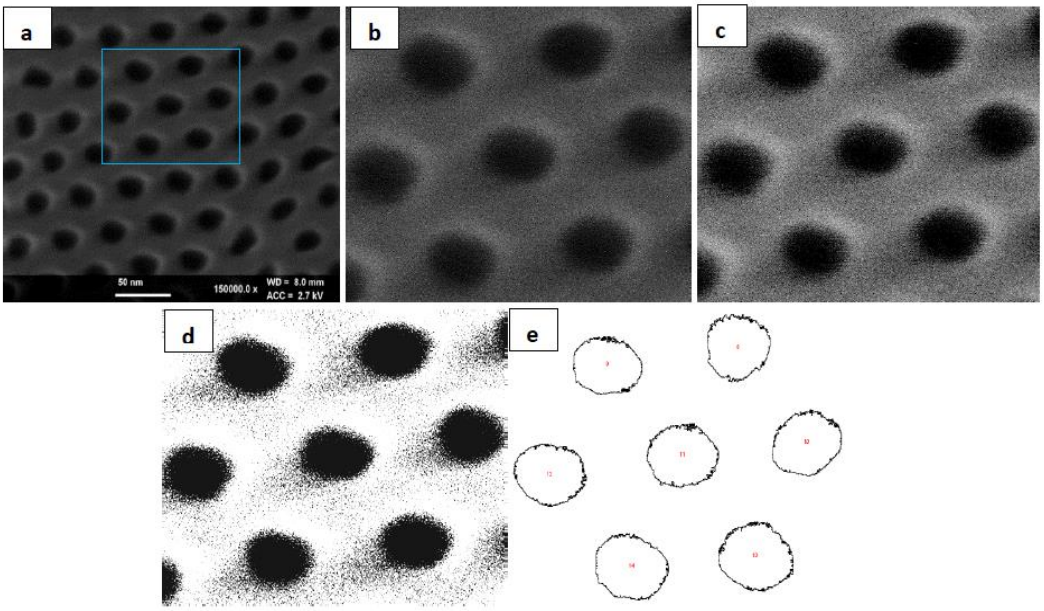

Figure 3.14 Procedure of the statistical analysis using ImageJ a) original SEM image b) selected area for analysis c) improvement of the contrast and brightness d) applying threshold to the image and e) contour area of the analysed pores.

3.3.2 Transmission electron microscopy

In a transmission electron microscope (TEM), the electron beam is generated using

a similar principle as in a SEM but the microscope column of a TEM operates under ultra-high vacuum. Figure 3.15 shows a diagram of the components of a TEM. The process of image formation in a TEM starts when an electron beam generated in the tungsten filament passes through a set of electrostatic lenses to reduce its size until it hits an ultra-thin specimen. A fraction of these electrons will be transmitted through the sample and then passes through a set of lenses to form an enlarged image that can be observed either in a fluorescent screen or a camera. Finally, a set of detectors are placed at the bottom of the column to provide information about the sample such as bright field, annular dark field and an x-ray detector.

A transmission electron microscope from the Microscopy and Analysis Department of the University of Bath (JEOL-JEM-2100 Plus) was used to characterize the titanium and iron oxide nanoparticles.

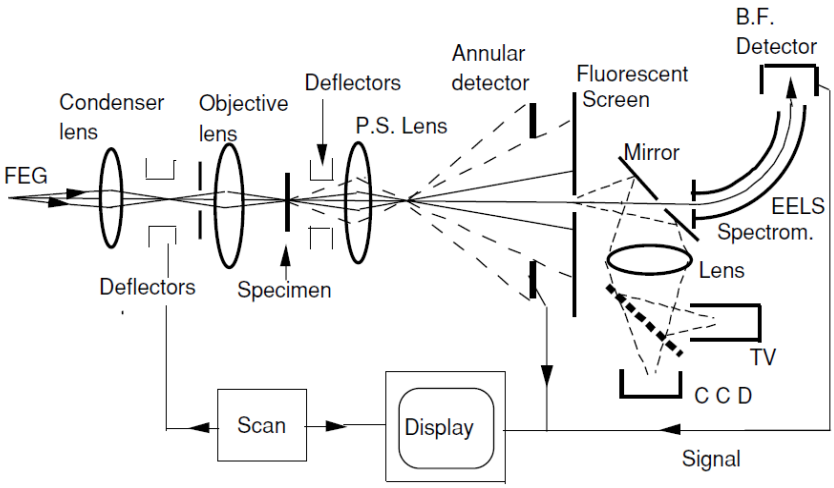

Figure 3.15 Diagram of a transmission electron microscope (Yao and Wang, 2005).

3.3.3 X-ray diffraction

X-ray diffraction (XRD) is a widely known method to characterize the crystal structure of materials. The principle is based on analysing the position and the intensities of the diffraction peaks that are observed when a crystalline structure diffracts with a constructive interference an incident electromagnetic wave (x-ray). Figure 3.16 illustrates this principle, in a crystalline structure the atoms have a periodic arrangement and the diffraction of two incident rays by two adjacent atoms (B and D) in a lattice plane are separated by an interplanar distance, d_h, that can be described by Bragg's Law:

$$\lambda = 2d_h sin\theta \qquad 3\text{-}1$$

where λ is the incident wavelength (0.1542 nm) and θ is the diffraction angle of the wavelength. As every crystal has a unique interplanar distance, consequently is a useful method to obtain the phase identification of crystalline structures by analysing the plot generated from the intensity of the diffracted peaks against the incident angle. XRD diffraction patterns for the titanium and iron oxide nanoparticles were recorded using a Bruker D8-Advance using a silica plate. Measurements were recorded between 2θ values from 10 to 80°.

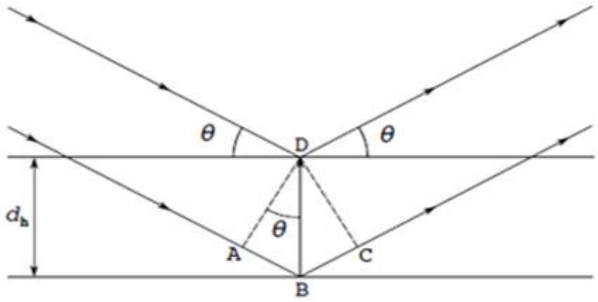

Figure 3.16 Bragg representation of x-ray diffraction by two atoms (*B* and *D*) separated with an interplanar distance d_h.

3.3.4 Ultraviolet-visible spectroscopy

The principle of this characterization technique lies on the excitation of electrons from a sample when is irradiated using light in the UV-Visible range. This region of this electromagnetic radiation comprises wavelengths between 10^{-6} to 10^{-7} m. The energy (*E*) associated with a specific wavelength can be obtained using the equation:

$$E = h_p \nu \qquad 3\text{-}2$$

where h_p is Planck's constant (9.26x10^{-34} J s^{-1}) and *v* is frequency (s^{-1}). When the energy of an incident wavelength corresponds to an energy transition between two electronic states this leads to the promotion of an electron from the highest occupied molecular orbital (HOMO) to the lowest unoccupied molecular orbital (LUMO). This energy transition is called band gap and can be obtained by quantifying the absorbed light as a function of the wavelength. The band gap of the titanium oxide nanoparticles was obtained by measuring the reflection spectra using a UV-vis spectrophotometer (Cary 100).

3.3.5 Dynamic light scattering

Dynamic light scattering (DLS) also known as photon correlation spectroscopy measures the diffusion coefficients of particles undergoing Brownian motion to estimate the particle size (D_h) using the Stokes-Einstein equation:

$$D_h = \frac{kT}{6\pi\mu_c D_s} \quad \text{3-3}$$

where k is Boltzmann's constant (1.38×10^{-23} m^2 kg s^{-2} K^{-1}), T is temperature (K), μ_c is the viscosity of the continuous phase (Pa s) and D_s is the diffusion coefficient (m^2 s^{-1}). In DLS the particle size is estimated using a correlation function that measures the degree of similarity on the intensity of the scattered light between two signals produced over time. In Brownian motion, smaller particles have higher diffusion speed coefficients compared to larger particles, and the rate of the decrease on the correlation function is used to extract information to obtain a particle size distribution.

The droplet size distribution of the NEs was analysed by dynamic light scattering using a backscattering mode with a detection angle of 173° (Zetasizer Nano-ZS, Malvern Instruments) using light scattered intensity (%) in the *y*-axis to show the droplet size distribution as the latter is the basic data obtained from a DLS measurement (Goddeeris et al., 2006).

3.3.6 Interfacial tension measurements

The interfacial tension of the disperse phase/continuous phase were measured using a goniometer (Dataphysics OCA20) based on the pendant drop method.

In this method a high-resolution camera determines the shape of a droplet immersed in the other liquid at mechanical equilibrium. During this equilibrium, the interfacial tension force can be measured by the balance that exists between the gravitational force and the surface forces that determine the shape of the droplet according to the equation (Drelich et al., 2002):

$$\gamma = \frac{\Delta\rho g D_d^2}{H} \quad \text{3-4}$$

where γ is the interfacial tension, $\Delta\rho$ is the density difference between the two liquids, g is the gravitational constant, D_d is the droplet diameter and H is a shape parameter that depends on the shape factor, S, $\left(S = {}^{d}/_{D_d}\right)$. A schematic representation of each parameter is shown in Figure 3.17. However, the interfacial tension values are automatically obtained by software installed in the goniometer.

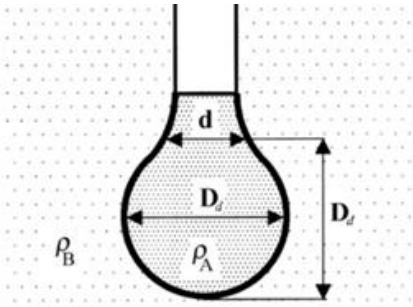

Figure 3.17 Schematic representation of the pendant drop method (Drelich et al., 2002).

3.3.7 Raman spectroscopy

In Raman spectroscopy a sample is illuminated with a monochromatic light and most of the light will be scattered with the same frequency in all the directions (Rayleigh scattering) due to its interaction with the sample. However, only a small fraction of the incident light will have a shift in its frequency compared to the incident radiation and this one constitutes Raman scattering (Bumbrah and Sharma, 2016). When the incident radiation has a lower frequency compared to the scattered light is called anti-Stokes lines and when the frequency is higher is called Stokes lines; and it is the change in the wavelength of the scattered light, the one that provides information about the chemical structure of the sample. The Stokes lines are the ones used to construct the Raman spectrum as they have a higher intensity and the resulting plot is presented as intensity versus frequency shift and is usually displayed from 4000 to 400 cm^{-1}.

3.3.8 X-ray Photon electron spectroscopy

X-ray Photon Electron Spectroscopy (XPS) is the most used surface technique in chemical characterization of solid materials due to the easy interpretation of the obtained spectra (Malitesta and Margapoti, 2013). The principle behind this technique relies in emission of photoelectrons when an X-ray beam hits the surface of a sample, the photoelectrons that leave the sample are detected by an electron spectrometer according to their kinetic energy. As the energy of the emitted electrons is quantized, it can be related to the binding energy of the electrons from the core levels. The obtained plot is a spectrum of the number of detected electrons per energy interval versus their kinetic energy. As each element has a unique spectrum that results in

characteristic peaks due to the electronic structure of the atoms. Consequently, XPS can be used to quantify concentration of elements in the sample as % atomic concentration. In addition, other values such as full width half maximum (FWHM) can be used as an indication of chemical state of a specific element and the broadening of the peak might indicate a change in the number of chemical bonds contributing to the peak shape.

X-ray photoelectron spectroscopy (XPS) was performed on a Thermo Fisher Scientific K-alpha+ spectrometer. Samples were analysed using a micro-focused monochromatic Al x-ray source (72 W) over an area of approximately 400 µm. Data was recorded at pass energies of 150 eV for survey scans and 40 eV for high resolution scan with 1 eV and 0.1 eV step sizes respectively. Charge neutralisation of the sample was achieved using a combination of both low energy electrons and argon ions. Data analysis was performed in CasaXPS using a Shirley type background and Scofield cross sections, with an energy dependence of -0.6.

3.3.9 FT-IR

FT-IR spectroscopy is a technique based on the vibrations of the atoms of a molecule caused by the absorption of light when an incident infrared radiation strikes the sample. The absorption of light produces a change in the molecular dipoles, which are associated with movements such as stretching, bending that are referred globally as vibrations. Consequently, the energy in which any peak in the absorption spectrum appears correspond to the frequency of a vibration of a pat of a sample molecule from the sample. The obtained plot is a spectrum of the absorbed light against frequency. Molecular vibrations give rise to absorption bands generally localized in the mi-infrared range (4000 to 400 cm^{-1}).

Chapter 4: Synthesis of anodic alumina membranes

The tuneable properties and highly ordered pore arrangement of AAMs make them an interesting material for a wide range of cutting-edge applications, as discussed in Section 2.4 . The present chapter covers the synthesis of AAMs under different conditions and their characterization by scanning electron microscopy. The chapter is divided in six sections, the first one is a brief comparison in terms of pore quality between AAMs produced by a single and a two-step anodization process. Section 4.2 provides the statistical image analysis of the AAMs synthetized under different anodization conditions. The following section 4.3 gives a description of the aluminium removal and pore opening steps. Section 4.4 discusses pore aluminium oxide growth rate, Section 4.5 illustrates common defects during the manufacturing of AAMs. Finally, section 4.6 describes the synthesis conditions and the statistical image analysis of ring-shaped AAMs.

4.1 One-step and two-step anodization process

Template synthesis is a simple, inexpensive and relatively fast method to achieve the formation of nanomaterials and AAMs have been extensively used as a template to produce nanomaterials such as nanowires (Choi et al., 2003) or nanotubes (Choi et al., 2003) due to their high pore regularity. However, different synthesis conditions have a direct impact on their quality in terms of pore size and size distribution. For instance, Figure 4.1 compares two AAMs synthetized at 50 V using 0.30 M $C_2H_2O_4$ at 10 ˚C using a single (Figure 4.1a) or a two-step anodization process (Figure 4.1b). The micrograph in Figure 4.1a shows the pores are almost randomly distributed, they have wide sizes distributions and a lower degree of circularity degree is observed. On the other hand, an almost perfectly arranged honeycomb structure with narrow pore size distributions was achieved via a two-step anodization process (Figure 4.1b). These results are in good agreement with literature (Sulka et al., 2002) In addition, Figure 4.1a and Figure 4.1b confirm that the pre-pattering effect of the first anodization improves the pore regularity when a two-step anodization process is conducted, as can be observed in the fabrication scheme in Figure 2.16. As the intended application of the AAMs is the production of NEs and the further synthesis

of nanoparticles by ME, a two-step anodization process was preferred as the quality of the NEs strongly depends on the quality of the membrane, as will be discussed later in Chapter 5.

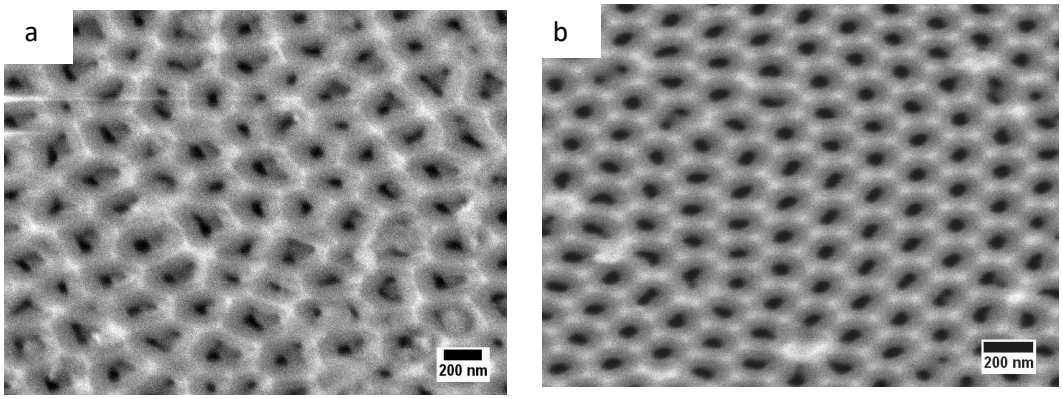

Figure 4.1 Micrographs of AAMs synthesised at 50 V 0.30 M $C_2H_2O_4$ at 10 °C via a) one-step and b) two-step anodization process.

4.2 Two-step anodization process

4.2.1 Pore formation and growth

The exact origin of the pore formation mechanism is still a matter of debate, however, the most accepted theory is the field-assisted mechanism proposed by Keller et al. (1953). This theory attempts to describe pore formation by the characteristic behaviour of the plot current density versus time when an anodization is conducted at potentiostatic conditions. The theory comprises four stages and all of them occur within the first minutes of the anodization until a steady state pore growth formation is achieved as it was described in Section 2.4.2

Figure 4.2 shows the current density-time transients for the first and second anodization for AAMs synthesized at different voltages. The plots denote there are two additional characteristics that can be highlighted. The first one is that the time needed to achieve the steady state pore growth (plateau zone) is shorter for the second anodization compared to the first one. Secondly, is that comparing the nadir of the graph for both anodizations, is the first one that has a lower value of the current density compared to the second anodization. The former behaviour is attributed to the presence of a pore pattern over the aluminium surface at the beginning of the second anodization, which promotes the pore initiation process by creating a higher

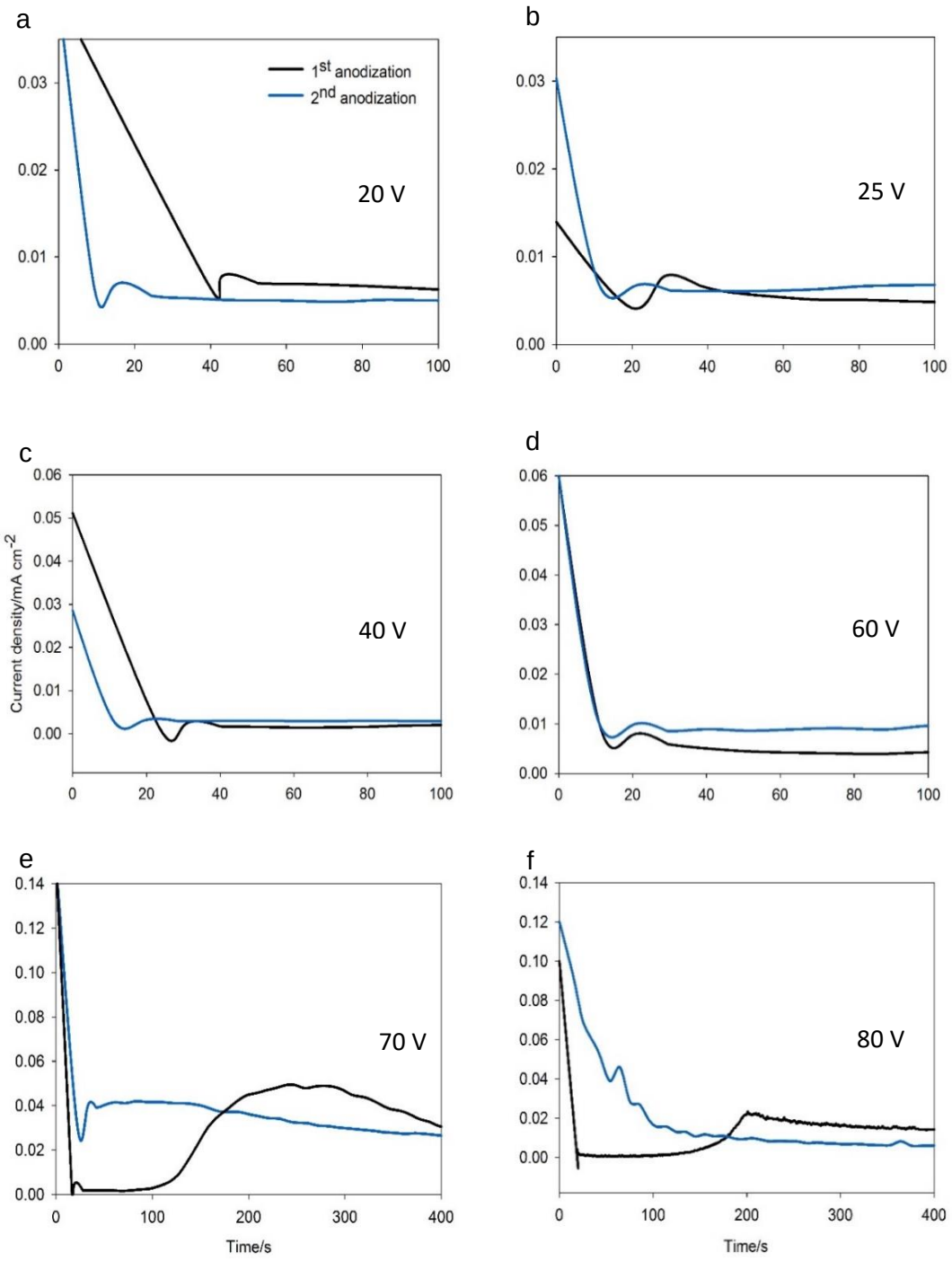

Figure 4.2 Current density as a function of time for anodization conducted at a) 20 V b) 25 V in 0.50 M sulfuric acid, c) 40 V d) 60 V e) 70 V and f) 80 V in 0.30 M oxalic acid.

surface area (compared to the electro-polished aluminium layer). This causes a slight decrease in the electrode resistance and, therefore, a reduction in the pore formation time (Gong et al., 2010). Another general trend observed in Figure 4.2 is that the time

to achieve the steady state pore growth increases with the anodization voltage. For anodization conducted at the same temperature (20, 25 and 80 V, T_{anod} = 0˚ C) it is possible to compare the effect of the electrolyte pH, as anodizations at 20 and 25 V were conducted using a 0.50 M sulfuric acid as electrolyte, meanwhile 80 V anodizations were carried out using 0.30 M oxalic acid. The results in Figure 4.2 indicate the steady state porous growth occurs faster with the decrease of the electrolyte pH; a trend previously reported by Hoar and Mott (1959). Finally, it is also possible to relate that the nadir of the plots has lower current density values with the increase of the anodization voltage, a trend previously reported by Diggle et al. (1969a).

4.2.2 Properties of the anodic aluminium oxide porous structure

AAMs were characterized by FESEM and a statistical image analysis was conducted using *ImageJ* as discussed in Section 3.3.1. The obtained parameters were pore diameter, circularity, interpore distance, pore density and porosity, which will be discussed next:

Figure 4.3 shows the micrographs of AAMs synthetized at 20 and 25 V using 0.50 M H_2SO_4 as electrolyte at T = 0 ± 1 °C. A highly ordered pore arrangement for both anodization conditions can be observed. The latter is a result of the combination of two factors: the low temperature allowing the dissipation of heat during the anodization and the low aluminium oxide growth rates leading to the formation of a self-organized porous structure. Narrow pore size distributions were obtained (Figure 4.3b and Figure 4.3d) with an average pore size of 23 ± 2 nm and 32 ± 3 nm for anodization conducted at 20 and 25 V, respectively. For instance, Sulka and Parkoła (2007) reported the formation of an almost self-organized porous structure using sulphuric acid, at 25 V and 1 °C, with an average pore size of 26 ± 4 nm, similar to our experimental conditions and results. In addition, they reported a reduction in the number of defects under the former anodization conditions compared to anodization conducted at - 8 or 10 °C.

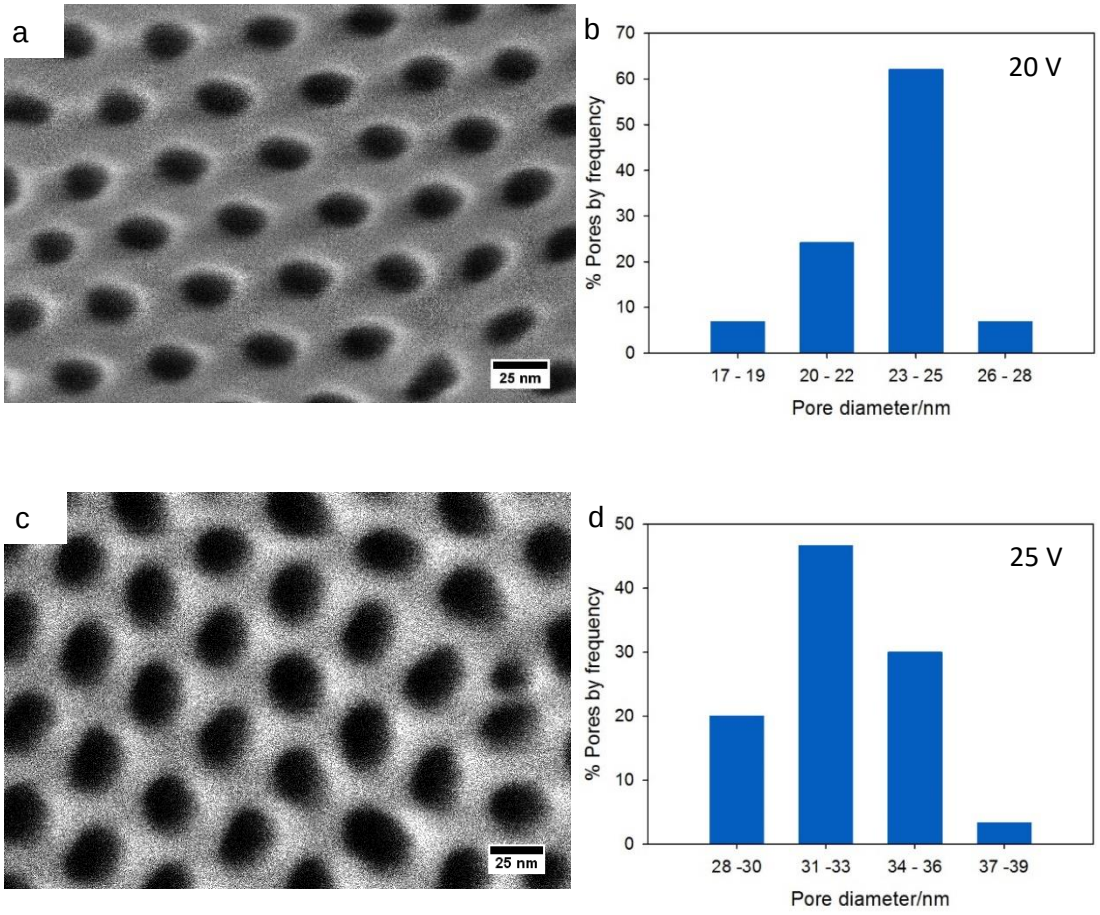

Figure 4.3 AAMs synthetized at a) 20 V and c) 25 V, 0.50 M H_2SO_4 at T = 0˚ C with their respective pore size distribution histograms.

At higher anodization potentials oxalic acid is preferred as electrolyte. Therefore, AAMs were synthesized using 0.30 M $C_2H_2O_4$ at anodization potentials ranging from 30 to 80 V. Figure 4.4 shows the micrographs for AAMs synthetized from 30 and 80 V. The pore size distributions histograms for all the membranes can be found in Figure 4.5. The average pore size was 40 ± 4 nm and 58 ± 6 nm, for membranes synthesized at 30 and 40 V, respectively. The pore size distributions histograms (Figure 4.5a and Figure 4.5b) highlight the high pore regularity for both anodization potentials. However, the pore circularity is slightly lower compared to membranes synthesized at lower anodization potentials (20 and 25 V). Circularity values for all the membranes can be found in Table 4.1. Nevertheless, for AAMs synthetized in oxalic acid, a potential of 40 V led to the highest pore circularity and pore ordering. In addition, Table 4.1 shows a decrease in pore regularity and circularity as the anodization potential is increased when oxalic acid is used as electrolyte.

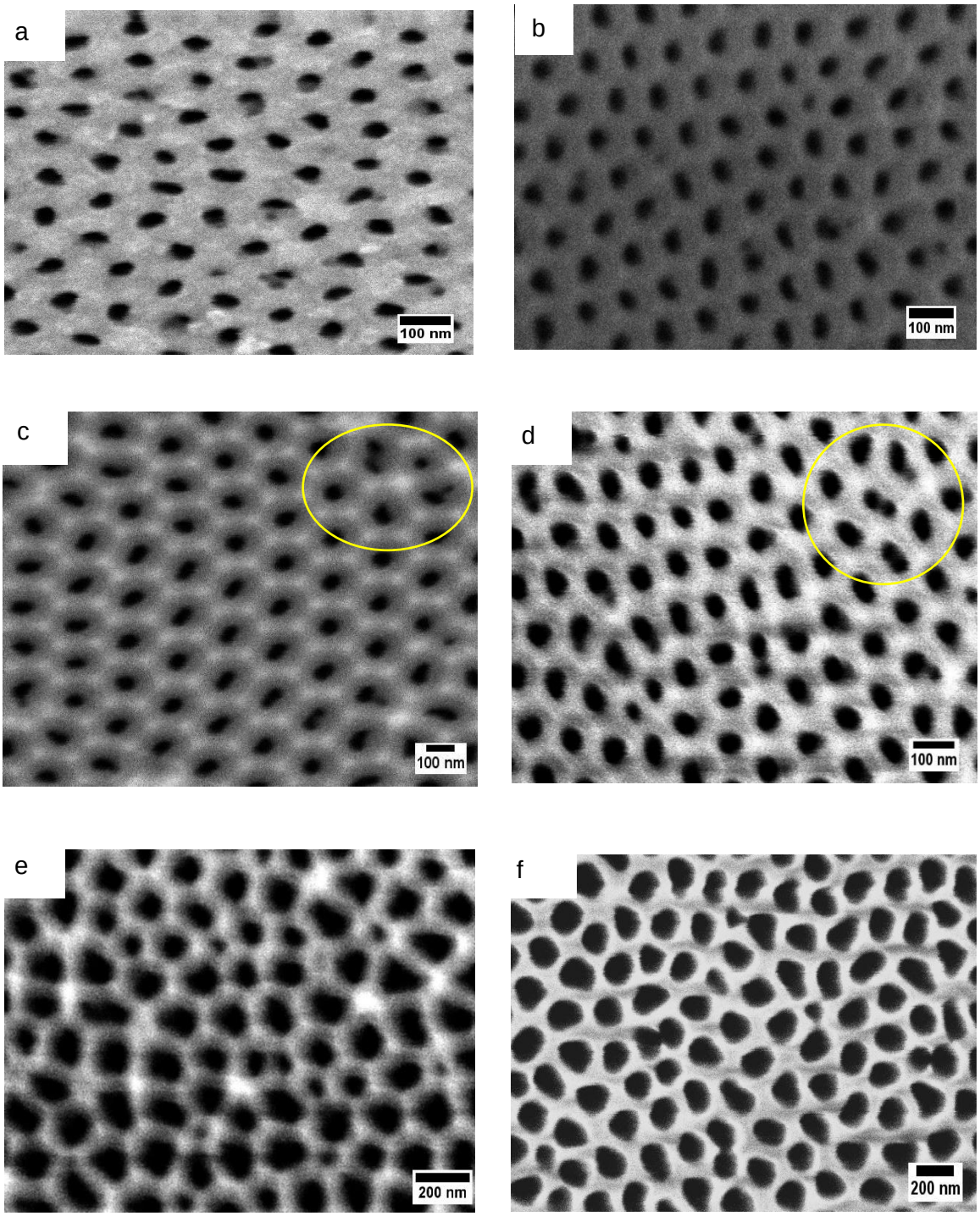

Figure 4.4 Micrographs of AAMs synthetized at a) 30, b) 40 V, c) 50 V, d) 60 V, e) 70 V and f) 80 V in 0.30 M $C_2H_2O_4$.

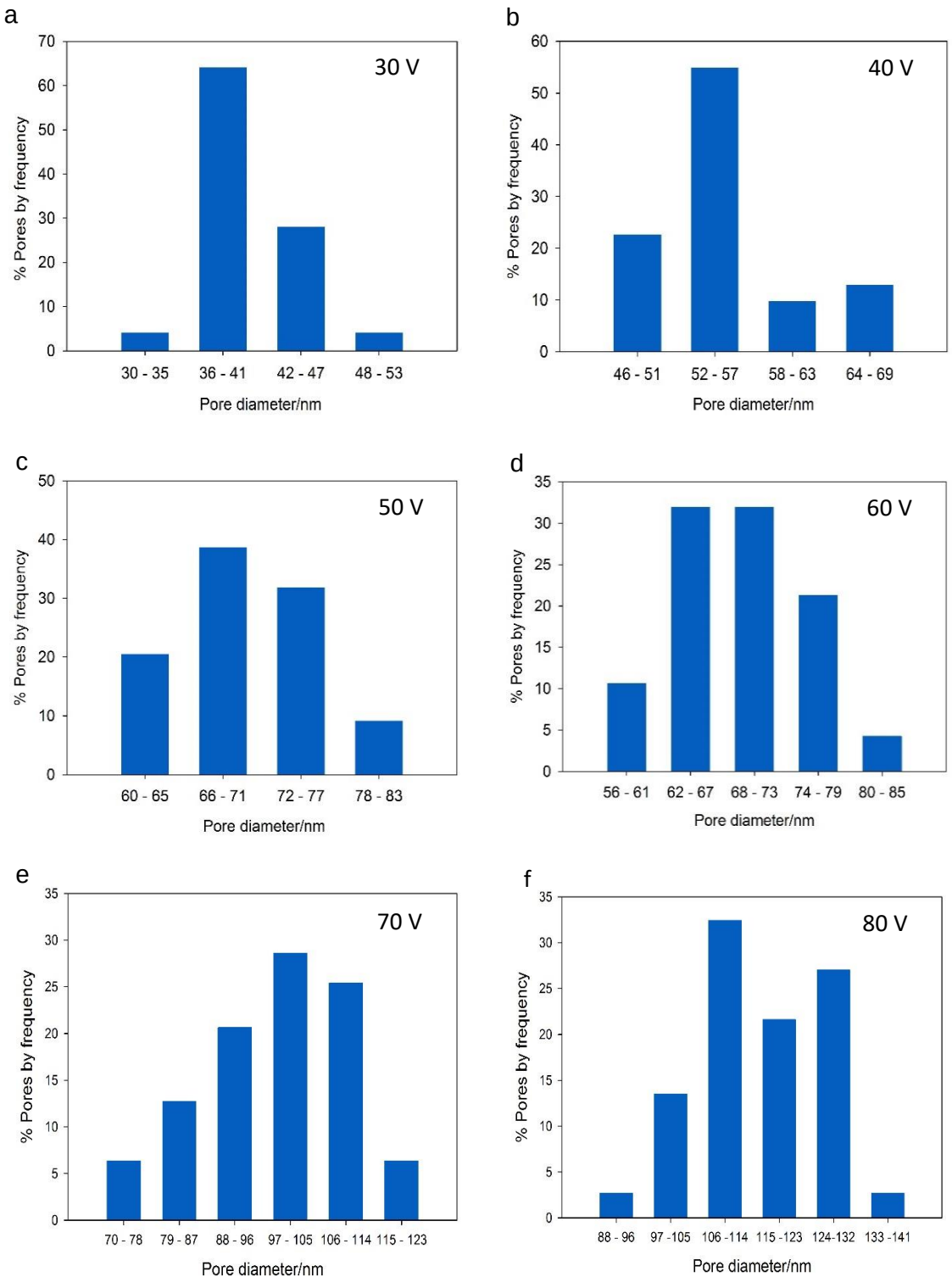

Figure 4.5 Pore size distribution by frequency for a) 30 V, b) 40 V, c) 50 V, d) 60 V, e) 70 V and f) 80 V for AAMs synthetized using 0.30 M $C_2H_2O_4$.

Micrographs of the AAMs synthetized at 50 and 60 V can be found in Figure 4.4c and Figure 4.4d respectively. The average pore size was 69 ± 5 nm and 73 ± 6 nm, respectively. The pore size distributions expressed as percentage of pore frequency can be found in Figure 4.5c and Figure 4.5d, respectively. Under the former conditions a high degree of pore arrangement is still observed for both membranes, however, both micrographs show the formation of small defects examples of which can be found on the top-right side of the micrographs. These are likely due to pore formation competition during early stages of the anodization. The higher anodization voltages tested using oxalic acid as electrolyte were 70 and 80 V. Under these conditions a considerable amount of heat is produced due to the higher reaction rates (alumina assisted-dissolution and alumina porous growth) and consequently lower electrolyte temperatures should be used. Figure 4.4e and Figure 4.4f shows the micrographs for both anodizations. The former conditions lead to the production of AAMs with wider pore size distributions (Figure 4.5e and Figure 4.5f) and the lowest circularity values (Table 4.1).

Table 4.1 Pore diameter, circularity, effective pore diameter, interpore distance, porosity and pore density values for AAMs synthesized at different anodization potentials.

Voltage/ V	Pore diameter/nm	Circularity /-	Effective pore diameter/nm*	Interpore distance/nm	Porosity/-	Pore density/10^{13} pores m^{-2}
20	23 ± 2	0.86	20	42 ± 5	0.20	13.4
25	32 ± 3	0.90	29	57 ± 6	0.18	8.0
30	40 ± 4	0.82	33	105 ± 12	0.22	9.3
40	55 ± 5	0.85	47	101 ± 5	0.22	8.3
50	69 ± 5	0.84	58	129 ± 6	0.14	6.6
60	67 ± 6	0.82	55	117 ± 11	0.22	8.3
70	96 ± 13	0.81	78	166 ± 9	0.17	6.5
80	154 ± 22	0.77	119	177 ± 17	0.26	2.2

*the effective pore diameter is calculated by multiplying pore diameter to circularity, as reported by Lee et al. (2012)

Figure 4.6a illustrates the linear relationship between the anodization potential and the pore diameter with an experimental proportionality constant value of 1.34 nm V^{-1}, a value in good agreement with the one reported by O'sullivan and Wood (1970) of

1.29 nm V^{-1}. The best results in terms of narrowest of the pore size distribution were achieved for membranes fabricated at 20 V with sulphuric acid and 40 V with oxalic acid in agreement with literature (Lee et al., 2006, Lee et al., 2012). Also, the low pore arrangement obtained at 70 and 80 V using oxalic acid can be explained in terms of the applied potential: at higher potentials an increase of the overall reaction rate is observed (aluminium assisted dissolution and porous alumina formation), which enhances pore growth competition, resulting in less ordered pore structures with larger pore size distributions. On the other hand, when a combination of factors such as low potential and low temperature is applied, a decrease in the overall reaction rate is observed, promoting a self-organised arrangement and ideal honeycomb structures. In Figure 4.6b a linear behaviour is observed between the interpore distance and the anodization potential for AAMs synthetized from 20 to 80 V with a gradient of 2.3 nm V^{-1}, which is close to the reported value of 2.5 nm V^{-1} reported by O'sullivan and Wood (1970). For instance, the experimental Interpore distance values are 57 ± 6 nm and 101 ± 5 nm for anodizations conducted at 25 and 40 V, respectively; whereas the reported values by Li et al. (1998b) are 63 nm and 100 nm for membranes synthetized in sulphuric acid at 25 V and 40 V in oxalic acid, respectively.

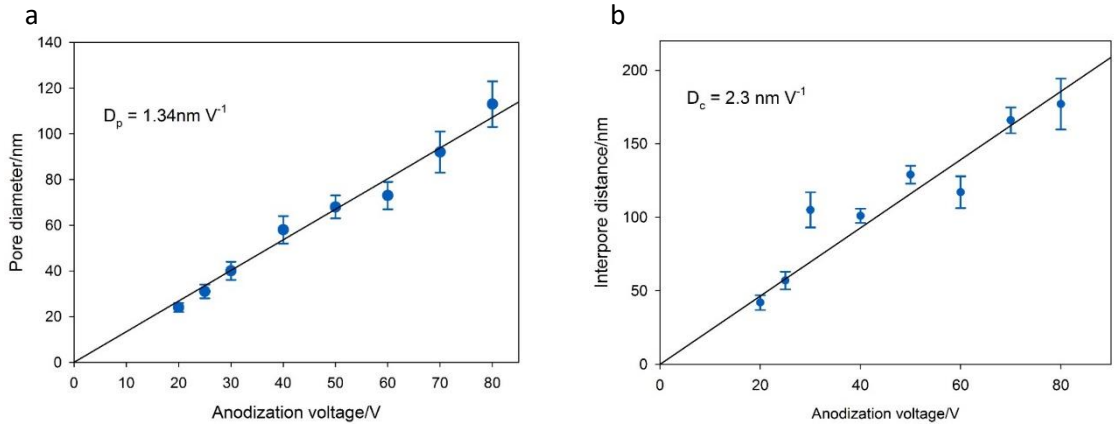

Figure 4.6 a) Pore diameter and b) Interpore distance against anodization potential for the synthetized AAMs.

Table 4.1 reports the porosity and pore density values for AAMs from the statistical image analysis of the micrographs by *ImageJ*. The porosity values are 0.18 and 0.20 for membranes synthetized in sulphuric acid at 20 and 25 V, respectively. Whilst, the same parameter varied from 0.14 to 0.26 when oxalic acid was used as electrolyte. Reported porosity values for AAMs range from 0.10 to 0.30 depending on the anodization conditions(Ono et al., 2004a, Alkire et al., 2008). Nevertheless, Nielsch

et al. (2002) proposed an empirical rule that an ideal self-ordered porous structure must have a porosity value of 0.10. In addition, Table 4.1 shows a negative correlation between pore density and the anodization potential; a trend which is in good agreement with the literature (O'sullivan and Wood 1970).

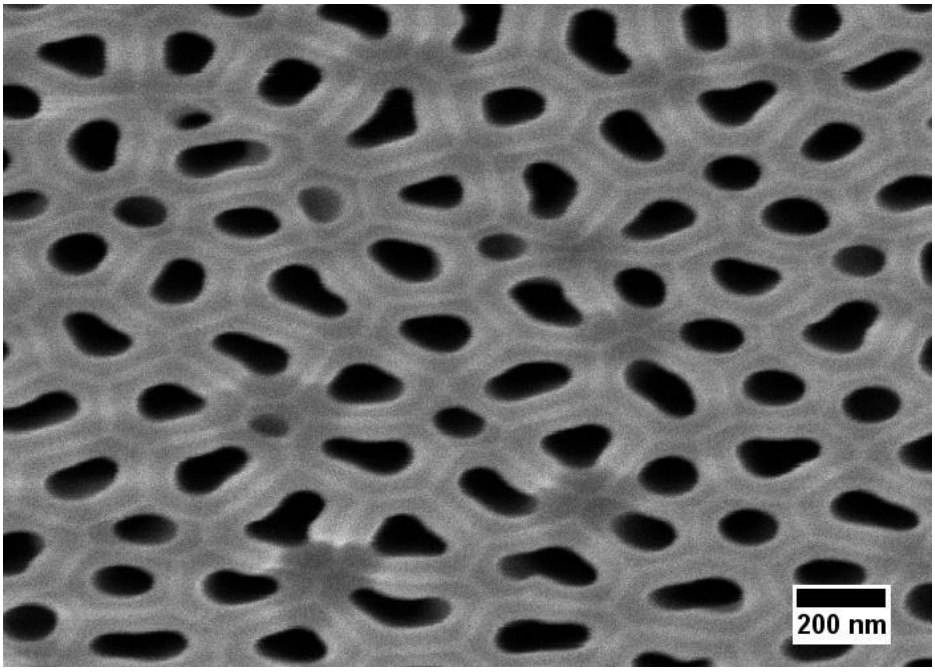

Figure 4.7 Micrograph of an AAM synthetized at 70 V. The wall thickness for a single cell can be calculated from the boundary of the cell (bright contour) to the edge of the pore.

Figure 4.7 is a micrograph of an AAM synthetized at 70 V in oxalic acid and shows the area delimited by each cell. The brighter section at the edge of each cell corresponds to the thickness of the inner aluminum oxide layer, which is free of electrolytes (Nielsch et al., 2002). Meanwhile the aluminium oxide adjacent to the pores is commonly named as the outer aluminium oxide layer, which has a specific electrolyte concentration profile depending on nature of the electrolyte as discussed in Section 2.4.1 and Figure 2.9. For instance, it has been reported that the outer layers have concentrations ranging from 2 - 4 % wt. and 12 - 14 % wt. when oxalic and sulphuric acid are used as electrolytes, respectively. In addition, Thompson and Wood (1983) found that the ratio of the inner layer to the outer layer (D_{inner}/D_{outer}) depends on the type of electrolyte with values of 0.05 and 0.1 for sulphuric and oxalic acid, respectively. The wall thickness of the AAMs membranes can be estimated from Equation 2-20 for the whole range of applied voltages, the results are displayed in Table 4.2. However, the obtained SEM micrograph for a 70 V AAM (Figure 4.7)

allowed us to calculate the wall thickness, 63 ± 31 nm, which is a slightly higher value than the estimated value (37 nm) using Eq 2-20. A possible reason for the difference is the high heterogeneity of the pore arrangement when a high voltage is applied during the synthesis.

Table 4.2 Estimated wall thickness for AAMs synthetized using equation 2-20.

Electrolyte	Voltage/V	Wall thickness/nm
0.50 M H_2SO_4	20	9
	25	13
0.30 M $C_2H_2O_4$	30	33
	40	22
	50	31
	60	22
	70	37
	80	32

Figure 4.8 shows the aluminium oxide barrier of an AAM synthetized at 80 V in 0.30 M oxalic acid with an estimated thickness of 65 nm and a wall thickness of 56 nm. For the former AAM the ratio of wall thickness to barrier layer thickness is 0.86, which is quite close to the experimental value of 0.89 reported by Ebihara et al. (1983).

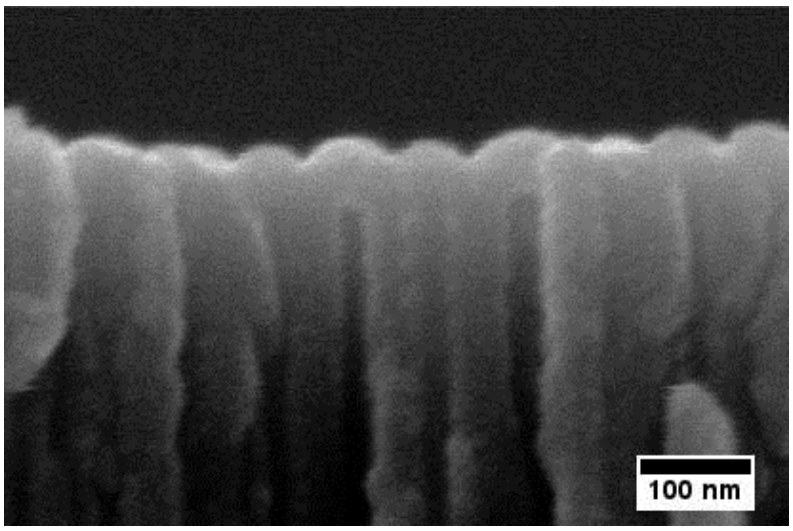

Figure 4.8 Aluminium oxide barrier for an 80 V AAM.

One of the main reasons that AAMs are an attractive material for nanoapplications is the high pore regularity and the close-packed arrangement that can be obtained under certain reaction conditions and Figure 4.9 demonstrates this feature by showing a larger area of an AAM synthetized at 40 V in 0.30 M $C_2H_2O_4$. The low magnification of the micrograph allows observing the grain boundaries from the original aluminium structure and shows that a hexagonal pore ordering is obtained within the domains of the grains, with different orientations obtained in neighbouring domains. Annealing of the aluminium promotes an increase in grain size and thus larger areas where a self-ordered porous structure can be achieved (Jessensky et al., 1998). The insets in Figure 4.9 highlight the area of ten domains, from the central area of the micrograph, giving an average area of 0.47 ± 0.12 μm^2. Nasirpouri et al. (2009) proposed an empirical equation to calculate the average domain size based on the time of the first anodization:

$$D_{AAM} = 0.52 t_a^{0.7} \qquad 4\text{-}1$$

where D_{AAM} is the average domain size (μm^2) and t_a is the time of the first anodization (h). The equation gives an estimated domain area of 0.69 μm^2 which is comparable to our experimental results. The driving force between the domain size and the anodization time is the grain boundary energy per unit of area. This is a measure of the fact that as anodization proceeds, pores located at the boundary of a domain will gradually move or re-arrange, leading to an increase in their size or, eventually, to the matching orientations in adjacent domains (Li et al., 1998b). Another factor to consider is the self-ordering process that take place at the bottom of the pores (*metal/oxide* interface) as the anodization proceeds. This leads to a higher pore arrangement at the bottom side compared to the top side of the membrane. Therefore, depending on the final application of the AAMs, it is important to select the proper time for the first anodization and thus obtain a highly pre-patterned template for the second anodization.

4.3 Post-anodization processes

As was described in Section 3.2.1, after the second anodization the aluminium base layer was removed by using 1:1 0.2 M $CuCl_2$/20 % wt. HCl with the aim to exposing the scalloped-shape aluminium oxide barrier. Figure 4.10 is a micrograph of the top view of the scalloped aluminium oxide barrier that must be etched away to obtain an open-through porous structure for a 40 V AAM and the inset corresponds to a 80 V AAM. The Figures illustrate the higher cell arrangement that is achieved using 40 V

as anodization potential compared to 80 V.

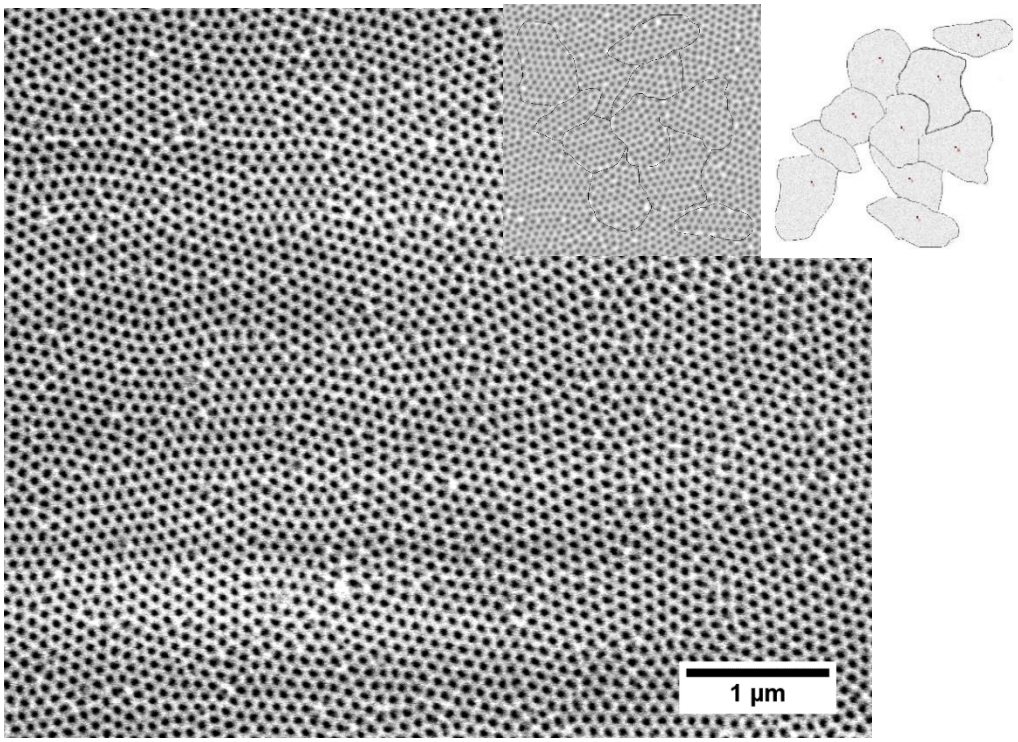

Figure 4.9 Low magnification micrograph of a 40 V an AAM. Insets highlight ten domains from the central micrograph.

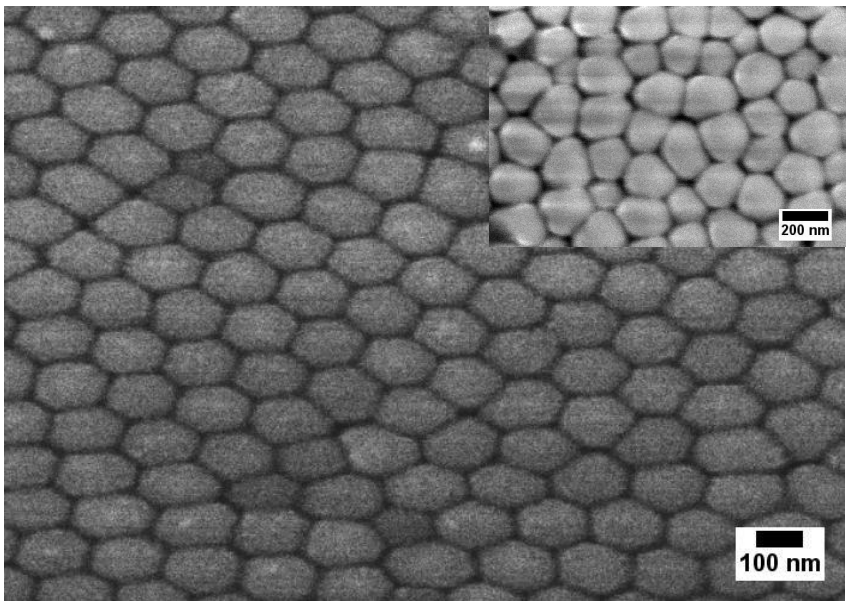

Figure 4.10 Aluminium oxide barrier layer of a 40 V AAM synthetized using 0.30 M $C_2H_2O_4$ at T = 13 ˚C, Inset aluminium oxide barrier of a 80 V AAM.

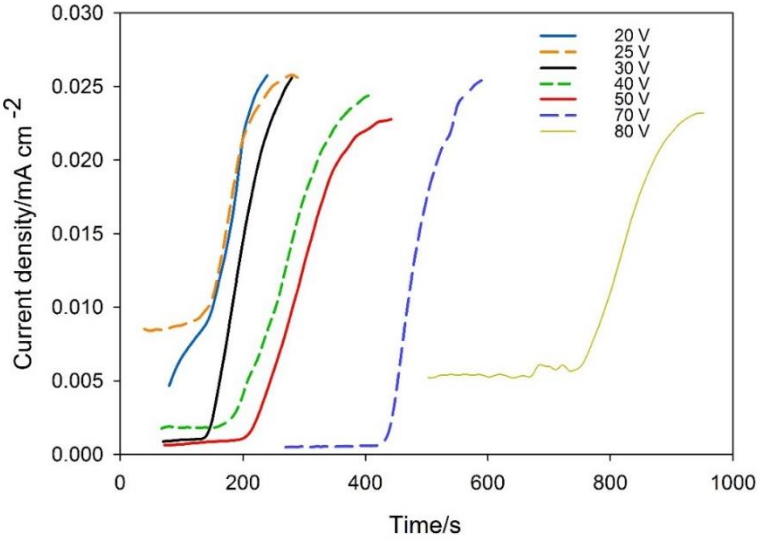

Figure 4.11 Current density against time during the pore opening process for AAMs fabricated at different anodization potentials.

As the intended application of the AAMs is the production of monodisperse NEs it is necessary to have a membrane with a narrow pore size distribution. Consequently, pore opening is a paramount step during the synthesis of AAMs. As described in Section 3.2.1, the former was conducted by a chemical wet method proposed by Lillo and Losic (2009) and coupled with an electrochemical detection method that allowed tracking the pore opening state. Figure 4.11 illustrates the plot of current density versus time for the pore opening process for membranes synthetized at different anodization potentials. The different curves show a similar pattern as the one in Figure 3.8c, which can be divided in three segments; the first one at the beginning of the process is when the pores are closed and there is no ion permeation through pores. The second section is when the current density starts to rise suggesting the beginning of the pore opening until it reaches a constant value, implying the pores are completely open (third segment) and a further contact of the membrane with the acid solution (H_3PO_4) will cause only pore widening. Figure 4.11 also denotes that the time required to observe the initial inflection of the current density varies according the anodization potential no matter the electrolyte type employed during the anodization. For instance, 20 and 25 V, the membranes were prepared with sulphuric acid, meanwhile at anodizations from 40 to 80 V were conducted in oxalic acid. This is due to the direct relationship between the thickness of the barrier layer and the anodization potential. Reported value of the ratio barrier layer thickness to

anodization potential is 1.15 nm V^{-1} (Wernick et al., 1987). However, it's worth establishing conditions like temperature and concentration of the acid in the pore opening that might alter the time required to achieve a complete pore opening. However, the incorporation of the electrochemical tracking method allowed us to have a standardized procedure for the pore opening.

Figure 4.12 shows the fully open pores of a 30 V and a 70 V AAM. The sharp edges at the edge of the membrane are due to chemical etching by H_3PO_4 during the pore opening process. Although chemical etching is the most common method to remove the aluminium oxide layer (Poinern et al., 2011), an undesirable outcome is the formation of an uneven surface at the bottom side of the membrane.

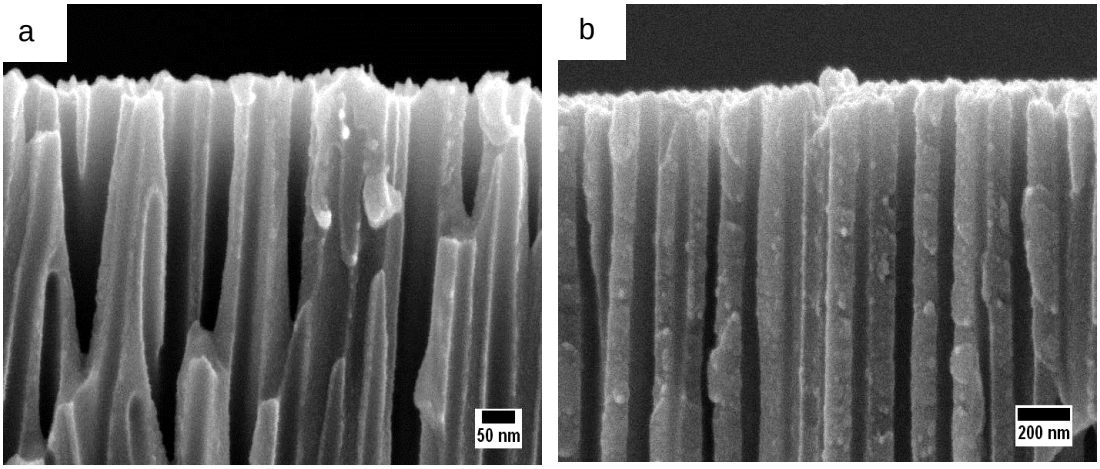

Figure 4.12 Close-up of the cross section of fully open pores of a) 30 V and b)70 V AAMs.

4.4 Average pore growth

The cross section of five AAMs was analysed by FESEM and used to calculate the average pore growth by estimating the ratio of the length of the cross section against the total anodization time. Figure 4.13a shows the full cross section of a 40 V AAM. The roughness observed in Figure 4.13a is due to the preparation method before placing the specimen in the FESEM. However, a close-up of the image (Figure 4.13b shows the formation of straight and non-interconnected pores, which is a characteristic feature of AAMs. Table 4.3 shows the average pore growth of AAMs fabricated at different anodization potentials. The data show a positive correlation between the anodization voltage and the average pore growth. The experimental pore growth rates are in good agreement with reported values of 2 – 6 μm h^{-1} (Lee et al., 2006) for AAMs synthetized at similar conditions. For instance, Zaraska et al. (2011)

reported an average growth rate of 1.61 μm h^{-1} for an AAM synthesized in 0.30 M $C_2H_2O_4$ at 1 °C and 40 V. Reported data in the literature suggest different values of the average pore growth according to the type of electrolyte, with the highest rate obtained in the following order $H_2SO_4 > C_2H_2O_4 > H_3PO_4$ (O'sullivan and Wood, 1970). However, it has been reported a decrease in the pore growth rate as the anodization proceeds. The former behaviour is explained due to the diffusion constriction of the species O^{2-}/OH^- to the pore base and therefore a net decrease in the aluminium oxide reaction rate is observed (Alkire et al., 2008). An increase in the average pore growth rate seems attractive as AAMs are commonly used as a hard template. However, high anodization voltages lead to a reduction of the pore self-arrangement as an increase of the overall reaction rate enhances pore growth competition, resulting in less ordered pore structures with larger pore size distributions, as discussed in Section 4.2.2.

Table 4.3 Average pore growth rate for AAMs synthetized at different anodization potentials.

Voltage/V	Cross section thickness/μm	Anodization time/h	Average pore growth rate/μm h^{-1}
30	54	12	4.5
40	65	11.5	5.7
60	48	6.0	8.0
70	41	4.0	10.3
80	52	3.9	13.4

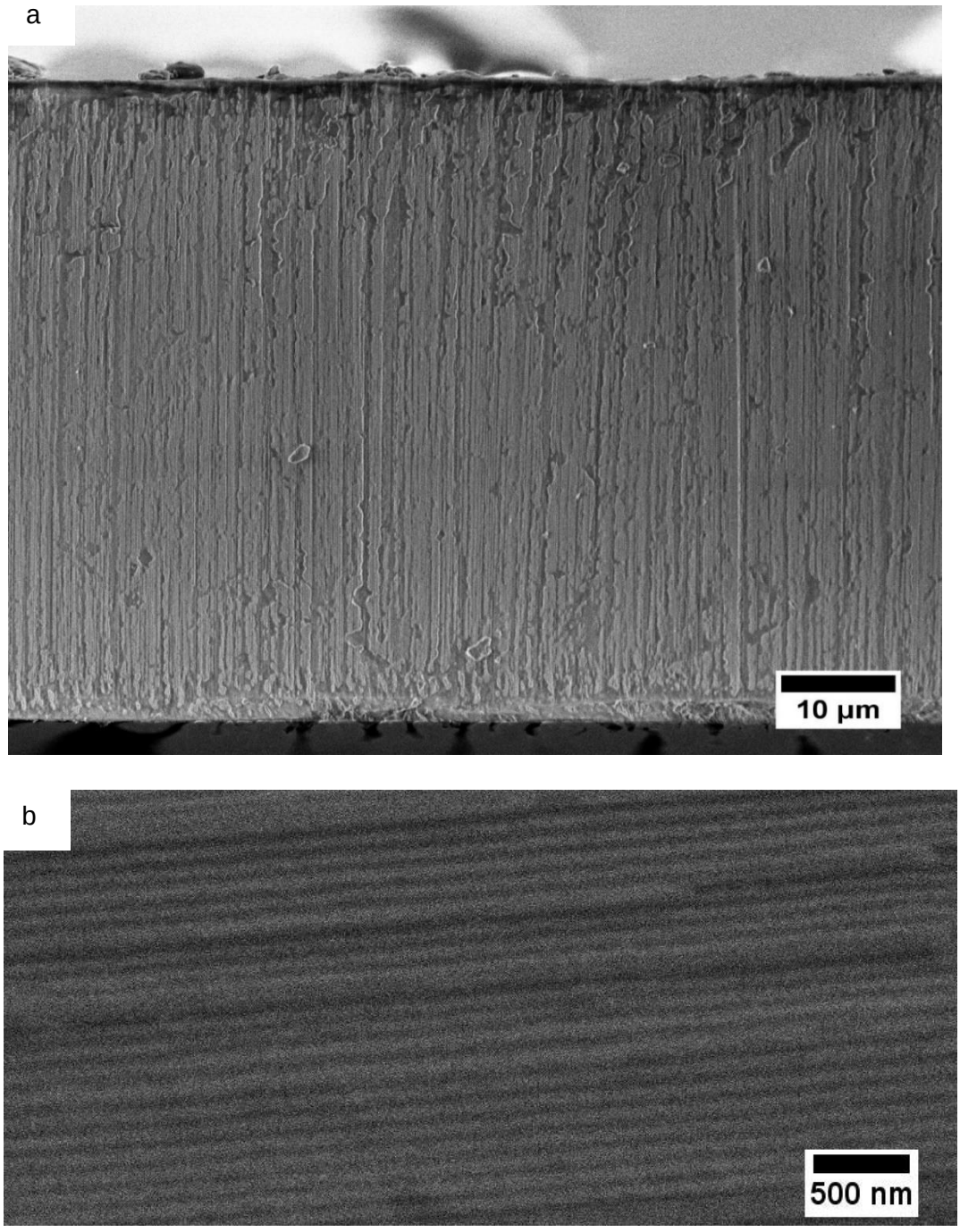

Figure 4.13 a) Full cross-sectional area and b) close-up for a 40 V AAM.

4.5 Stability of anodizations

Long anodization times, up to 12 hours for a 40 V membrane and the delicate equilibrium among all the reactions sometimes lead to the destruction of the AAMs during the anodization. Figure 4.14 shows the current density transients of two AAMs

that were destroyed by different causes and compared to a successful anodization. For instance, the first membrane was affected by localized pitting due to the localized corrosion that leads to the creation of small holes in the metal surface. Meanwhile the second scenario is a localized aluminium substrate depletion due to an increase of the general reactions rate. The obtained alumina films for each scenario can be observed in the insets.

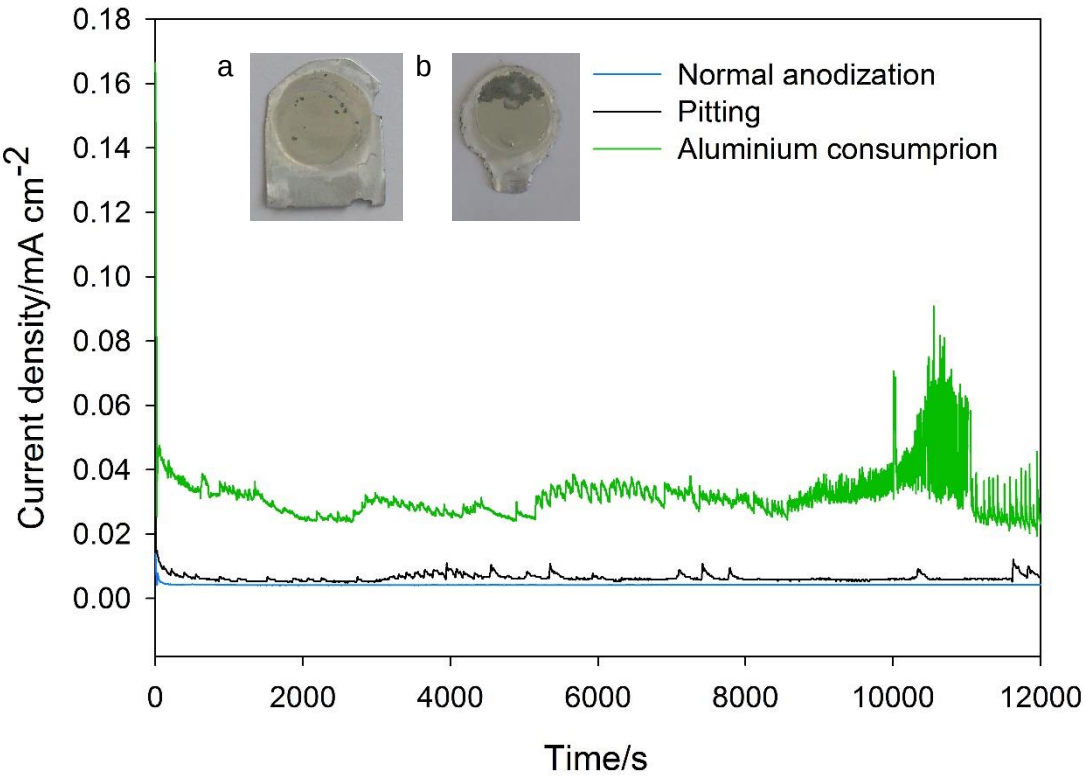

Figure 4.14 Comparison of a successful current density transient during the synthesis of AAMs and one affected by a) pitting and b) aluminium consumption.

4.6 Ring-shaped anodic alumina membranes

Ring-shaped anodic alumina membranes were designed for the first time with the intention to provide a suitable membrane to fit a commercial membrane emulsification rig (Micropore LDC-1) and carry out the production of NEs with a small droplet size distribution on a larger scale.

The ring-shaped AAMs were fabricated via a two-step anodization process as described in Section 3.2.2. Figure 4.15a shows a picture of the ring-shaped AAM and Figure 4.15b shows a micrograph of the top area of the AAM. The average pore

diameter is 77 ± 9 nm with a proportionality constant value pore diameter to anodization voltage of 1.30 nm V^{-1}. The average interpore distance is 156 ± 6 nm, giving a proportionality constant value of 2.60 nm V^{-1}. These values are in good agreement with reported values of 1.29 nm V^{-1} and 2.50 nm V^{-1} for pore diameter and interpore distance, respectively (O'sullivan and Wood, 1970). Pore size distribution expressed as percentage of pore frequency can be found in Figure 4.16. The results show the high degree of regularity that can be achieved using 60 V as anodization potential. However, the micrograph shows the formation of a small number of defects, as a results of pore competition at the early stages of the anodization. Table 4.4 reports: circularity, porosity and pore density obtained from the statistical image analysis from the FESEM micrograph by *ImageJ*. Circularity values are similar to those obtained for a standard AAM under the same anodization conditions (Table 4.1). Nevertheless, the pore diameter values are slightly higher compared to a standard AAM. A possible reason is pore widening, as a result of the longer anodization times used to have a thicker membrane (8 h compared to 7 h for the second anodization).

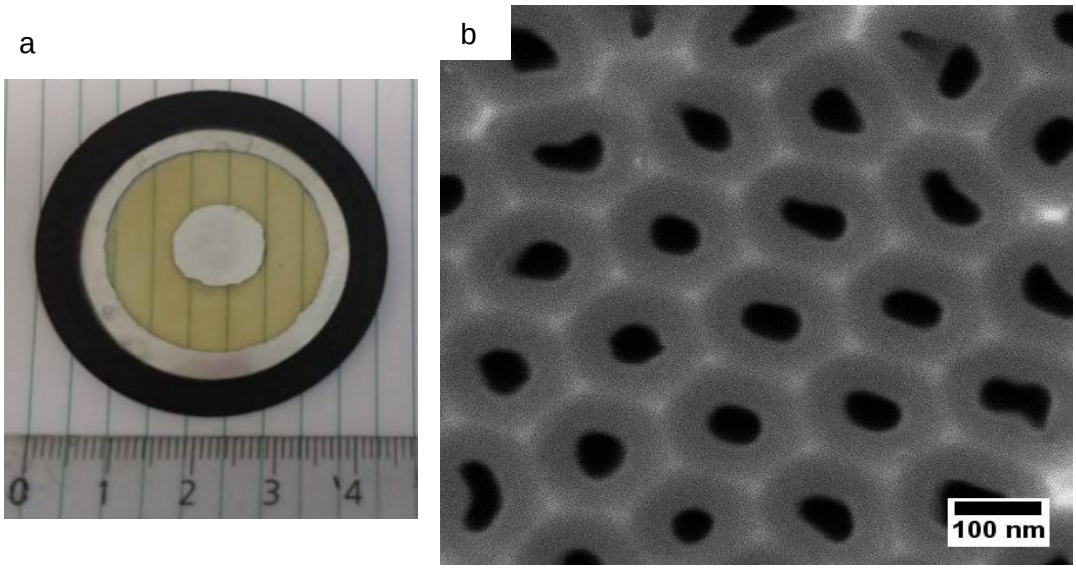

Figure 4.15 a) Ring-shaped AAMs with a black viton o-ring; and b) SEM micrograph of the porous section, the transparent section in a.

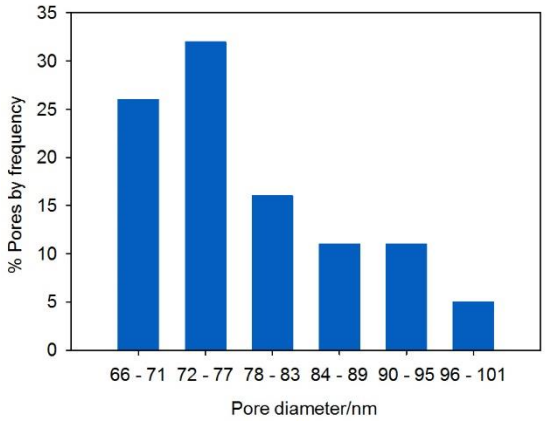

Figure 4.16 Pore size distribution by frequency for a 60 V ring-shaped AAM synthetized at T = 10 °C using 0.30 M $C_2H_2O_4$.

Table 4.4 Statistical parameters obtained by *ImageJ* from the ring-shaped AAM synthetized at 60 V using 0.30 M oxalic acid at T = 10 ± 1º C.

Voltage/V	Pore diameter /nm	Circularity /-	Effective average pore diameter/nm	Interpore distance/ nm	Porosity/ -	Pore density/$\cdot 10^{13}$ pores m^{-2}
60	77 ± 9	0.83	64	156 ± 6	0.14	5.13

Figure 4.17 is a SEM micrograph of the transition zone between the aluminium support and the aluminium oxide porous section and shows the formation of surface irregularities with an average extension of 14 ± 3 μm, compared to a membrane diameter of 41 mm (Figure 4.15a). A potential explanation for the formation of this transition zone is the inefficient removal of the aluminium oxide layer during the first anodization as the edge of Teflon holders doesn't ensure a perfect contact between the H_3PO_4/H_2CrO_4 solution and the aluminium oxide located at the edge of the holder.

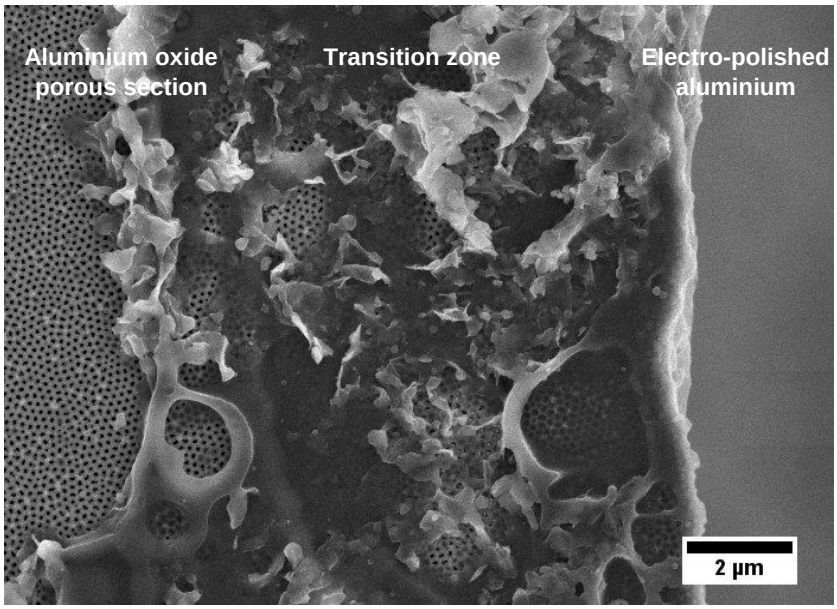

Figure 4.17 Transition zone between the porous aluminium oxide section and the aluminium support for a ring-shaped AAM.

A close-up of the transition section near the aluminium oxide porous structure can be seen in Figure 4.18. The micrographs show the formation of nanostructures with some nanopores underneath. The formation of these structures has been previously reported by Zhang et al. (2005) in a standard AAM due to the slow dissolution of the anodic alumina walls when the anodization take place at higher temperatures or higher acid concentrations.

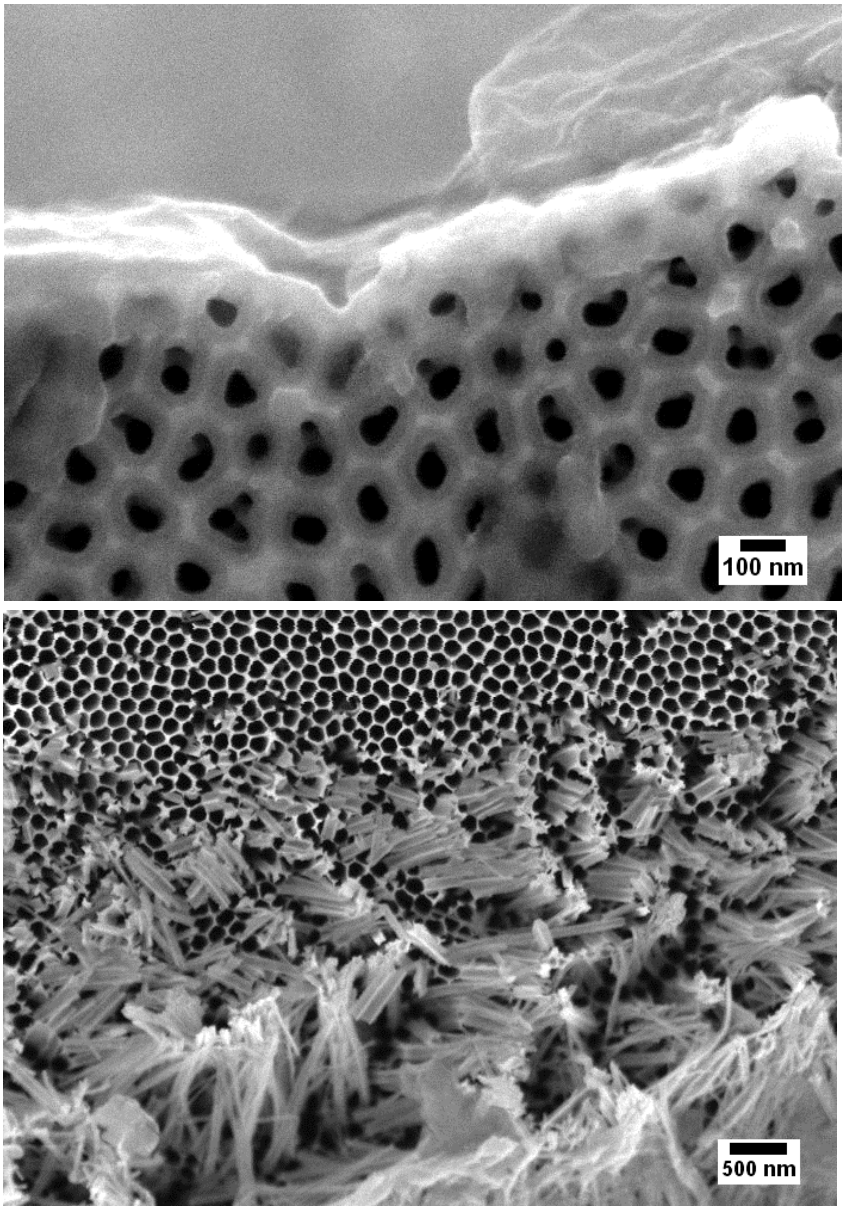

Figure 4.18 Close up to different areas of the transitional area between the anodized and the electro-polished section for a ring-shaped AAM.

Chapter 5: Membrane emulsification in a stirred-cell setup

The chapter evaluates the potential use of AAMs to produce nanoemulsions using a bespoke 3D-printed dead-end batch membrane emulsification setup; AAMs were chosen due to their narrow pore size distribution and highly ordered pore arrangement (Figure 5.1), as discussed in Chapter 4.

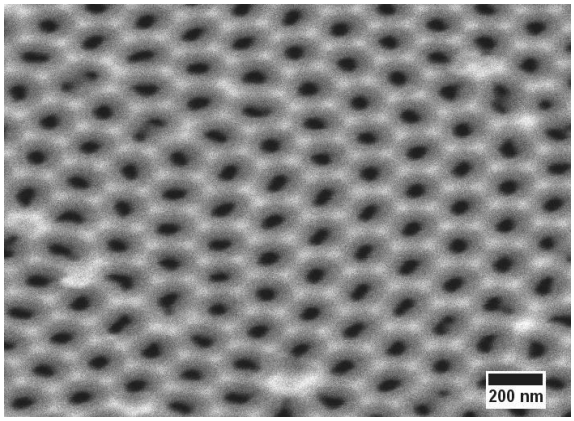

Figure 5.1 Micrograph of an AAM synthesised at 50 V 0.30 M $C_2H_2O_4$ at 10 °C.

The chapter is divided in eight sections. Section 5.1 evaluates the effect of the interfacial tension force due to the presence of surfactant in the continuous phase and the dispersed phase. Section 5.2 covers the effect on droplet size due to the addition of surfactant in the continuous and the dispersed phase. Section 5.3 assesses the effect of different surfactants in the continuous phase on droplet size due to their different molecular weight. Different process parameters such as: injection rate and shear stress and their effect on droplet size are evaluated in Section 5.4 ; while, membrane parameters (pore diameter) are discussed in section 5.5 In addition, section 5.6 , correlates the droplet diameter of NEs to dimensionless numbers commonly used in ME, to evaluate the performance of the ME rig under certain operational conditions. The next one, section 5.7 , discusses the main forces acting over a droplet growing in a single pore and compares the experimental droplet

size to several droplet size prediction models from the literature. Finally, the stability of the nanoemulsions is discussed in section 5.8 . The results obtained have been recently accepted for a publication in Industrial & Engineering Chemistry Research.

5.1 Interfacial tension measurements

Interfacial tension (IFT) measurements of the dispersed/continuous phase were carried out via the pendant drop method using a goniometer (Dataphysics OCA20). The non-ionic surfactant, Tween 20, was evaluated as surfactant in the continuous phase (M_w = 1228 g mol^{-1}) while the dispersed phase was sunflower oil (SFO). Tween 20 was selected as it is a hydrophilic surfactant widely used in ME (Hancocks et al., 2013, Thanasukarn et al., 2004). Different concentrations of Tween 20 were selected, and the results are shown in Figure 5.2. Four repetitions for each experimental condition were carried out at T = 18˚ C. However, the standard deviation for each condition is not shown as their values are quite small (i.e. $IFT_{SFO/water}$ = 28.30 ± 0.70 mN m^{-1}). The experimental IFT value SFO/water is close to the reported value in the literature of 25 mN m^{-1} at 21 ˚C, 1 atm (Mousavichoubeh et al., 2011), with the small discrepancies attributed to differences in temperature, experimental conditions or in composition of the SFO. The results from Figure 5.2 indicate the minimum IFT value has been reached for concentrations above 0.5 % wt. Tween 20 in the continuous phase, with values ranging from 6.1 to 6.8 mN m^{-1}. As such, 1 % wt. Tween 20 was selected as an optimum concentration of surfactant in the continuous phase. The experimental results are in good agreement with the experimental work reported by Hancocks et al. (2013) who evaluated the emulsion droplet size for different surfactant concentrations using a 1 µm SPG membrane. Their results indicate that the minimum droplet size was achieved for concentrations above 0.4 % wt. Tween 20 and that above this concentration value, the droplet size is only affected by the hydrodynamic conditions of the ME rig.

Once 1 % wt. Tween 20 was selected as the optimum surfactant concentration in the continuous phase, the addition of a second surfactant in the dispersed phase was evaluated. As previous reports suggest the formation of monodispersed emulsions with the addition of a hydrophobic surfactant in an *oil-in-water* emulsion (Wagdare et al., 2010a), Span 80 was selected as surfactant in the dispersed phase, (*Mw* = 428 g mol^{-1}, *HLB* = 4.3). For this set of experiments, the composition of the continuous phase was kept constant (1 % wt. of Tween 20 in DW) but varying the concentration of Span 80. The results are shown in Figure 5.2 as well. The plot indicates a further reduction of the IFT force compared to experiments carried out using only Tween 20

in DI water as continuous phase. The lowest measurable IFT value was 0.22 mN m^{-1} using 4 % wt. Span 80 in SFO/1% wt. Tween 20 in DW. Figure 5.3 shows the images obtained from the camera of the goniometer under the two different conditions. The former concentration of surfactant was selected as the optimal one in the dispersed phase as a 30-fold decrease in the IFT was observed.

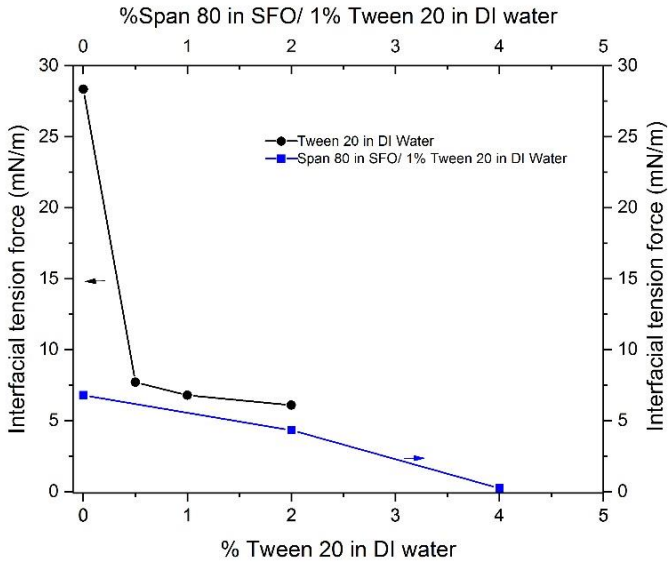

Figure 5.2 IFT values using different concentrations of Tween 20 in DW as continuous phase and SFO as dispersed phase (left and bottom axes) and IFT values using different concentrations of Span 80 in SFO and 1 % Tween 20 in DW as optimum concentration in the continuous phase (right and top axes).

The droplet size and size distribution of NEs was analysed via dynamic light scattering (DLS) using a backscattering mode with a detection angle of 173° using light scattered intensity (%) in the *y*-axis to show the droplet size distribution as the latter is the basic data obtained from a DLS measurement (Goddeeris et al., 2006). A DLS analysis of the continuous phase (1 % wt. Tween 20 in DW) was conducted and it's shown in Figure 5.4a. The plot shows a single peak due to the presence of the surfactant, with a value of 8.7 ± 1.5 nm. Figure 5.4b shows a bimodal distribution, being the first peak due to the presence of surfactant, while the second peak corresponds to the dispersed phase droplets with an average droplet size of 396 ± 62 nm.

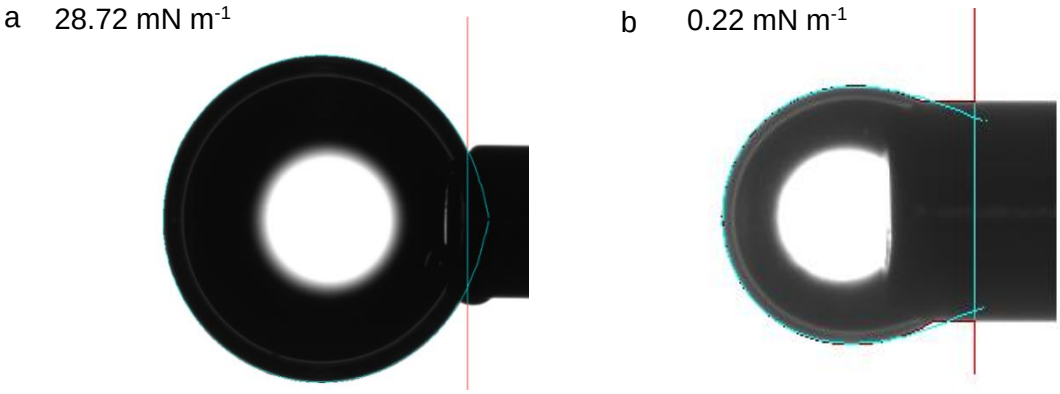

Figure 5.3 Optical images of the interfacial tension force measurements captured with a goniometer of a) SFO/water b) 4 % wt. Span 80/1 % wt. Tween 20 in water.

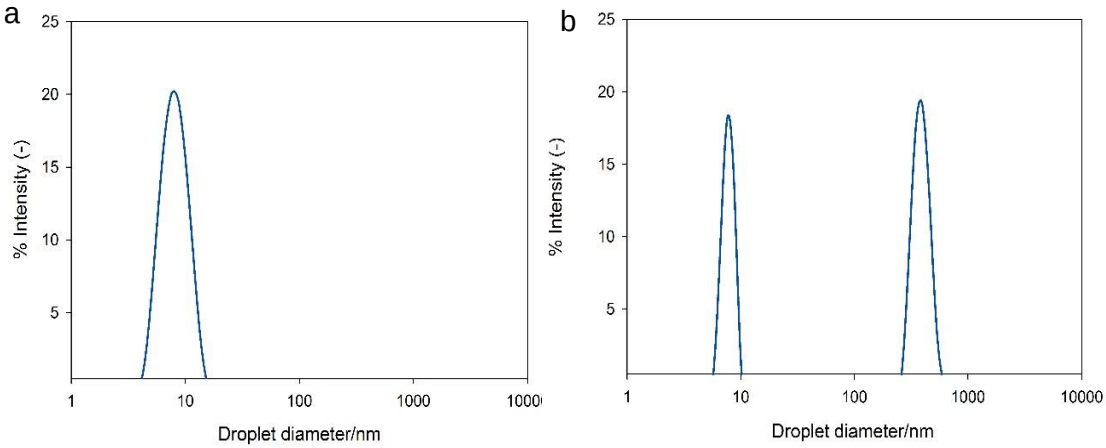

Figure 5.4 DLS analysis of a) 1 % wt. Tween 20 in DW b) NE produced using an 80 V AAMs (D_p = 113 ± 10 nm and 4 % Span 80 in SFO/1 % wt. Tween 20).

5.2 Effect of the surfactant addition in the dispersed phase

As discussed in the previous section, the addition of surfactant in the continuous phase reduces the IFT force between the two phases. To further probe the effect of the addition of the surfactant to the dispersed phase, the droplet size and size distribution of NEs produced using the setup described in Section 3.1.1 were analysed via DLS using (i) only a hydrophilic surfactant (1 % wt. Tween 20) in the continuous phase and (ii) surfactants in both the dispersed (4 % wt. Span 80 in SFO)

and the continuous phases (1 % wt. Tween 20 in DW). A set of experiments were carried out using a 40 and a 60 V membrane at different rotational speeds (100 - 1750 rpm). For a 40 V membrane, the results are shown in Table 5.1, showing the formation of bimodal NEs in the whole range of rotational speeds when only a hydrophilic surfactant is added to the continuous phase (1 % wt. Tween 20). In contrast, a monomodal distribution is obtained when a 4 % wt. Span 80 was incorporated in the dispersed phase and 1 % wt. Tween 20 in the continuous phase (for the whole range of rotational speeds). Figure 5.5a and Figure 5.5b compares the DLS intensity curves of the obtained NEs for a 40 V AAM at the lowest and highest rotational speed (100 and 1750 rpm, respectively). In the former, the results show the formation of a bimodal distribution with peaks at 216 ± 49 nm and 761 ± 145 nm when only 1 % wt. Tween 20 was used. In contrast, when both surfactants were present in the NE, the droplet size distribution was monomodal with an average value of 277 ± 72 nm. On the other hand, at 1750 rpm, the results from the DLS analysis show a bimodal distribution of 148 ± 39 nm and 393 ± 82 nm, using 1 % Tween 20 in DW, and a monomodal distribution with average diameter of 154 ± 19 nm when both surfactants were added.

Table 5.1 Droplet diameter of NEs obtained at different rotational speed with 1 % wt. Tween 20 in DW and with or without the incorporation of 4 % wt. Span 80 in SFO using a 40 V AAM (D_p = 58 ± 6 nm).

Rotational speed/rpm	SFO – 1 % Tween 20 in DW			4 % wt. Span 80 in SFO – 1 % wt. Tween 20 in DW
	Droplet diameter/nm		$\frac{D_{peak\,2}}{D_{peak\,1}}$	Droplet diameter/nm
	Peak 1	Peak 2		Peak 1
100	206 ± 56	632 ± 134	3.1	275 ± 74
250	146 ± 31	695 ± 148	4.8	182 ± 24
500	160 ± 36	707 ± 152	4.4	199 ± 57
750	178 ± 46	727 ± 130	4.1	175 ± 30
1000	147 ± 33	465 ± 92	3.2	184 ± 26
1250	130 ± 25	549 ± 110	4.2	155 ± 23
1500	143 ± 25	572 ± 117	4.0	144 ± 18
1750	148 ± 39	393 ± 82	2.6	154 ± 19

For a 60 V membrane (D_p = 73 ± 6 nm), monomodal NEs were produced regardless of the additional incorporation of surfactant in the dispersed phase and only wider

NEs were obtained at lower rotational speeds when SFO was in the dispersed phase. Figure 5.5c and Figure 5.5d compare the DLS intensity curves of NEs droplets formed at 100 and 1750 rpm under both conditions, respectively. At 100 rpm, the results show a single peak at 435 ± 109 nm, when 1 % wt. Tween 20 in DW is used, whereas a peak at 292 ± 91 nm is obtained when both surfactants were added. In contrast, at 1750 rpm narrower droplet size distributions are obtained for both conditions 181 ± 45 nm (1 % Tween 20 in DW) and 174 ± 27 nm (1 % Tween 20 in DW/4 % wt. Span 80 in SFO). The droplet diameter obtained for the complete range of rotational speeds for a 60 V membrane with and without the addition of a surfactant in the dispersed phase can be found in Figure 5.6. The effect of the addition of a second surfactant is clearly visible at low rotational speeds, 100 - 500 rpm (Figure 5.5c), where a considerable difference between the average droplet size for both conditions is obtained. The former behaviour is attributed to the drag force being not high enough to produce droplet detachment. The addition of Span 80 in the system decreases the interfacial tension rate faster than when only a surfactant in the continuous phase is added.

The different behaviour for the two membranes under the same process conditions can be explained by a difference in the interpore spacing (Table 4.1) between the 60 V membrane (117 ± 10 nm) and the 40 V one (101 ± 5 nm). The former might allow adjacent droplets to grow without producing droplet coalescence. Besides, the incorporation of Span 80 and Tween 20 in the dispersed and continuous phase, respectively; provides a high concentration of surfactant when the droplet is growing that avoids droplet coalescence (Wagdare et al., 2010b). In the case of the membrane with a smaller interpore distance and no lipophilic surfactant, the bimodal distribution can be explained by three factors: the first one is droplet coalescence when droplets are growing in adjacent pores due to the combined effect of the small interpore distance and the slow incorporation of the surfactant molecules (Tween 20) at the *oil/water* interface. The second factor is wetting, where a localized spread of oil might occur on the membrane surface, leading to the interconnection of oil-wetted pores (Abrahamse et al., 2002, Wagdare et al., 2010a). The third factor is droplet break-up when the system was provided with only 1 % Tween 20 as a surfactant, due to the high shear stress.

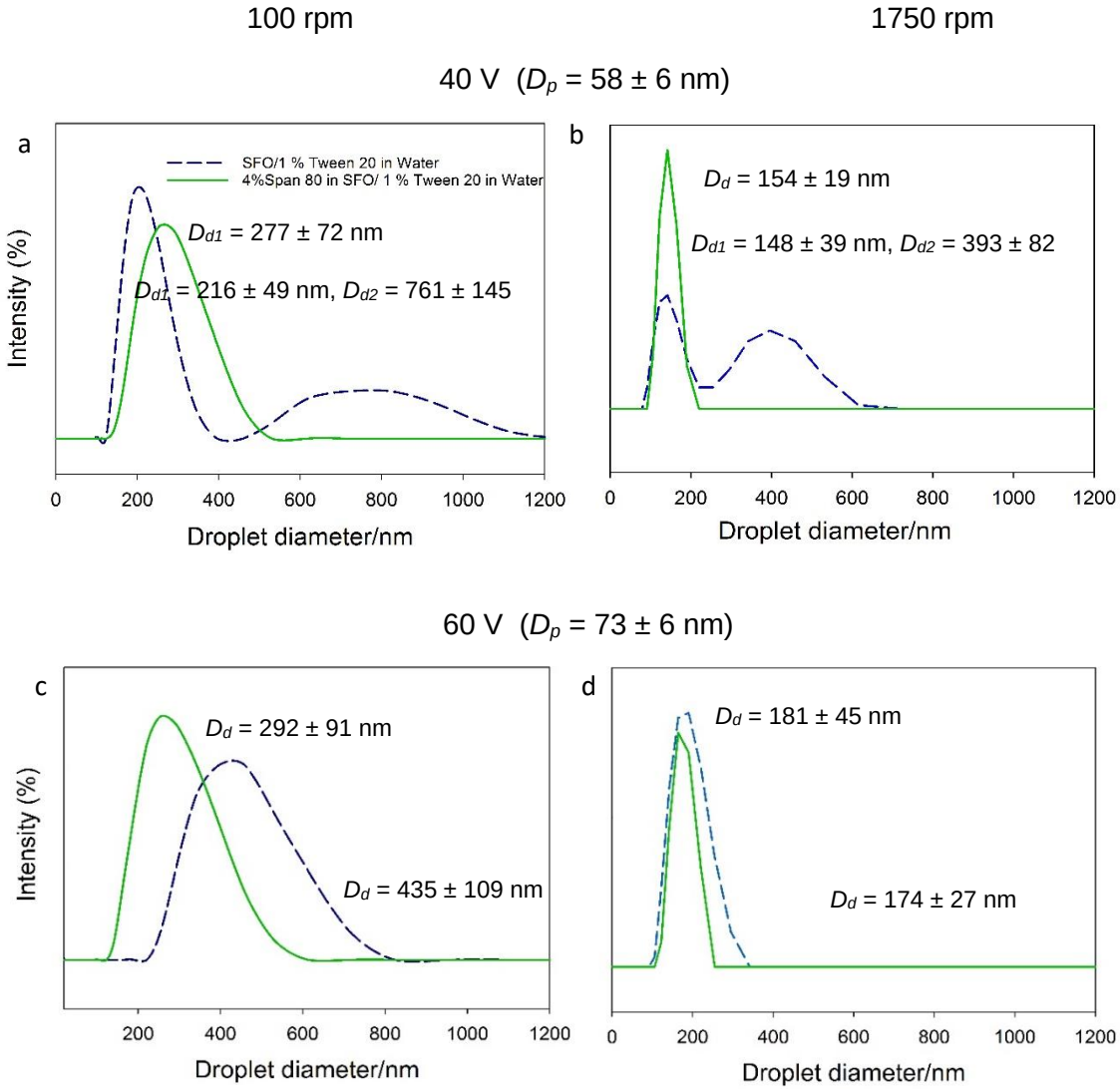

Figure 5.5 Intensity against droplet size for a NE formed for 40 V (D_p = 58 ± 6 nm) AAM a) at 100 rpm b) at 1750 rpm and 60 V (D_p = 73 ± 6 nm) c) 100 rpm d) at 1750 rpm.

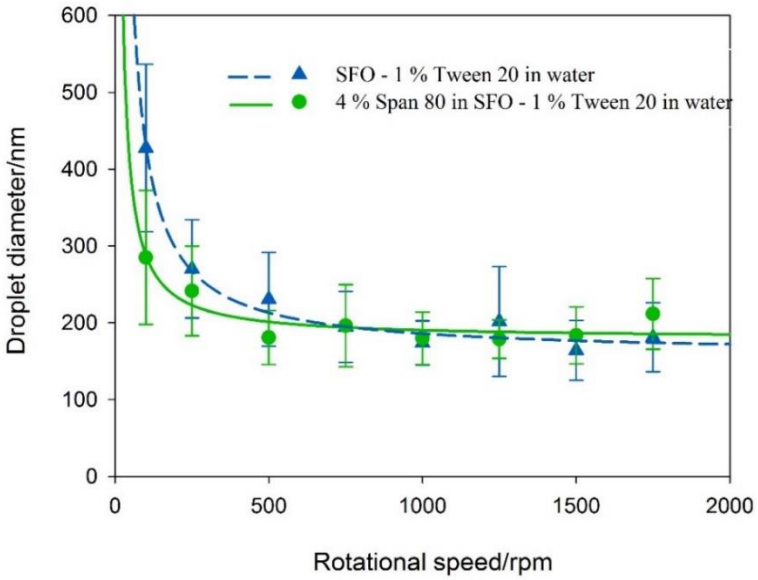

Figure 5.6 Droplet diameter of NEs obtained at different rotational speeds with 1 % wt. Tween 20 as surfactant in DW and with or without the incorporation of 4 % wt. Span 80 in the dispersed phase (SFO) using a 60 V membrane (D_p = 73 ± 6 nm).

5.3 Effect of the type of surfactant in the continuous phase

Based on the results from the previous section, the addition of Span 80 in SFO was an essential aspect to obtain monodispersed emulsions, especially using membranes with smaller pore diameters. However, the effect of varying the molecular weight of the surfactant in the continuous phase was also investigated. Two different non-ionic surfactants were tested, Brij O10 and Tween 80, with a molecular weight of 709 and 1310 g mol^{-1}, respectively. The experiments were carried out using 40 V membranes and varying the rotational speed. the dispersed phase consisted of 4 % wt. Span 80 in SFO. The results in Figure 5.7 shows that at the lowest rotational speed (100 rpm), a considerable reduction of the droplet diameter with decreasing molecular weight of the surfactant was observed. In addition, droplets with a narrower size distribution were produced. This effect can be explained in terms of the surfactant diffusion coefficients (D_s), which can be estimated using the Stokes-Einstein equation:

$$D_s = \frac{kT}{6\pi\mu D_h} \qquad 5\text{-}1$$

where k is the Boltzmann constant (1.3806x10^{-23} J K^{-1}), T is temperature (K), μ is viscosity of the continuous phase (Pa s), and D_h is the hydrodynamic diameter (m), which can be considered as equal to $2R_g$, the surfactant's gyration radius $\left(R_g = M_w^{0.6} \cdot 10^{-9}\right)$, and M_w is the molecular weight of the surfactant. Furthermore, the diffusion coefficient is related to the surfactant mass transfer coefficient (k_s) by:

$$k_s = \sqrt{\frac{D_s}{\pi t}} \qquad 5\text{-}2$$

where t is the droplet formation time (Rayner et al., 2005). The last two equations express the fact that surfactants with higher molecular weight have a larger hydrodynamic diameter and slower diffusion from the bulk of the continuous phase to the *oil/water* interface. A surfactant with a lower diffusion coefficient will have a lower mass transfer coefficient*, leading to the formation of bigger droplets and wider size distributions. Consequently, at low rotational speeds, a localized depletion of the surfactant might occur at the pore edge, leading to the formation of droplets with different sizes, which will be determined by the diffusion rate of each surfactant. However, when the rotational speed is increased beyond a certain threshold value, the effect of the surfactant molecular weight on the droplet diameter becomes minimal, with only a narrowing of droplet size distribution due to the higher shear rate, as observed in Figure 5.7.

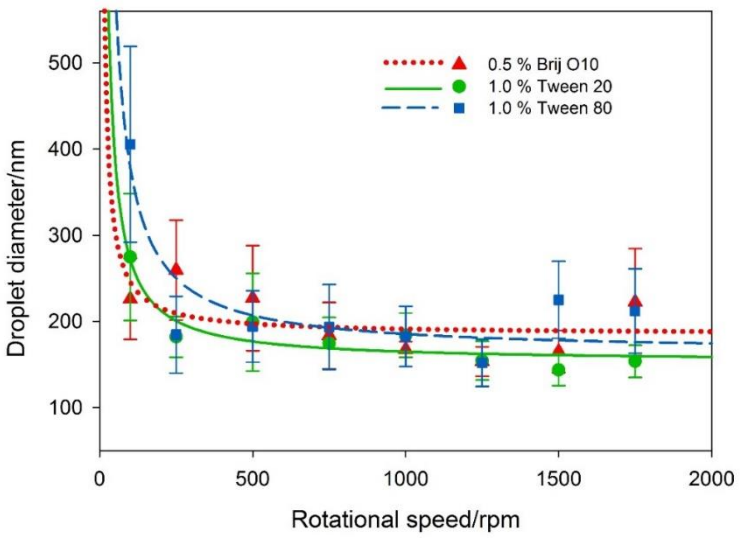

Figure 5.7 Droplet diameter against rotational speed for three different surfactants added in the continuous phase using a 40 V membrane (D_p = 58 ± 6 nm) with R^2 value of 0.26, 0.86 and 0.78 for Brij O10, Tween 20 and Tween 80, respectively, using an inverse first order fit.

5.4 Effect of the dispersed phase injection rate

Three different dispersed phase injection rates (0.015, 0.030 and 0.045 ml min^{-1}) were tested using 40 and 60 V membranes for different rotational speeds (100 - 1750 rpm). The surfactants were 1 % wt. Tween 20 in the continuous phase and 4 % wt. Span 80 in the dispersed phase.

The results for the 40 V membrane (Figure 5.8) show that above 300 rpm, there is only a weak effect of both the rotational speed and the injection rate on the droplet diameter. For the three injection rates tested, the droplet diameters lie in a range from 144 to 275 nm. However, droplets as small as 144 ± 18 nm and 154 ± 19 nm can be achieved with an injection rate of 0.015 ml min^{-1} at 1500 and 1750 rpm, respectively. However, slightly bigger droplet size distributions are obtained using 0.030 and 0.045 ml min^{-1}.

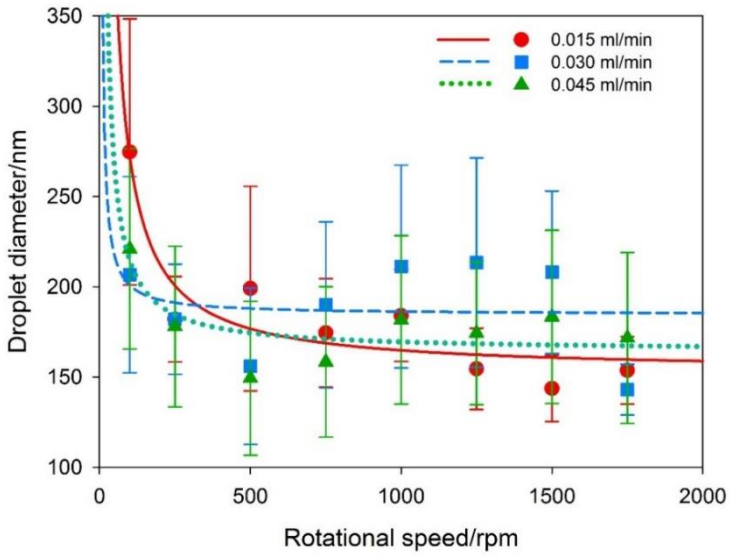

Figure 5.8 Droplet diameter of NEs using a 40 V (D_p = 58 ± 6 nm) 1 % wt. Tween 20 in DW and 4 % wt. Span 80 in SFO, for different rotational speeds and different injection rates. The R^2 values are 0.86, 0.11 and 0.75 for 0.015, 0.030 and 0.045 ml min^{-1}, respectively, using an inverse second order fit.

For a 60 V membrane the results shown in Figure 5.9 demonstrate that there is a stronger influence of both the rotational speed and the injection rate over the droplet diameter at low rotational speeds, where the droplet diameter has a negative correlation with the rotational speed. In this region, larger droplet diameters and wider size distributions are observed due to a combined effect of the increase of the

dispersed phase flux and the insufficient drag force to produce droplet detachment. The second region occurs at higher rotational speeds, where the droplet diameter is almost independent of the injection rate and the shear stress. This region is observed at rotational speeds higher than 750 rpm where narrower droplets are obtained for the three injection rates tested. This different behaviour between a 40 and a 60 V membrane in terms of the rotational speed and droplet size dependence is similar to what was observed previously for micrometre size droplets produced via crossflow ME where the smaller the pore size, the smaller the shear stress value needed for droplet detachment (Schröder and Schubert, 1999).

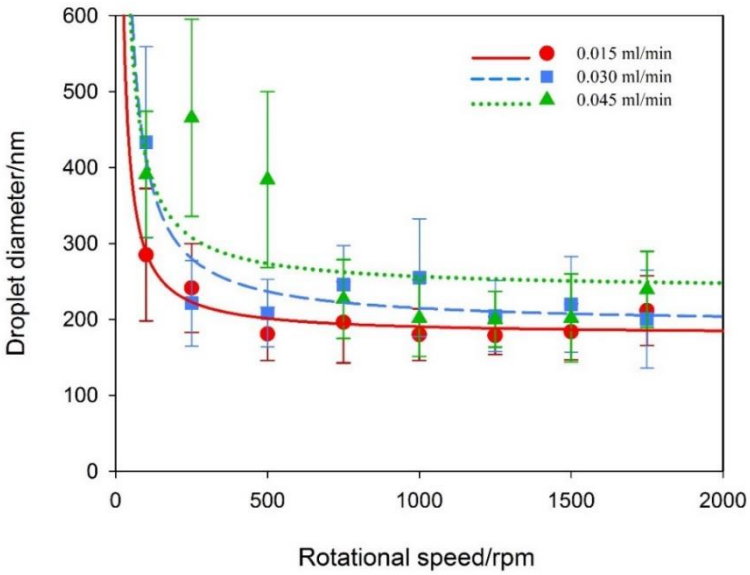

Figure 5.9 Droplet diameter of NEs using a 60 V (D_p = 73 ± 6 nm) membrane with 1 % wt. Tween 20 in DW and 4 % wt. Span 80 in SFO for different rotational speeds and different injection rates. The R^2 values are 0.84, 0.83 and 0.44 for 0.015, 0.030 and 0.045 ml min^{-1}, respectively, using an inverse first order fit.

The wider droplet size distributions observed in Figure 5.8 and Figure 5.9 at low rotational speeds and their further reduction at higher rotational speeds for the three injection rates can be explained from the experiments of Peng and Williams (1998b) and Xu et al. (2005) where the final volume of a droplet (V_D) is determined by two factors as the next equation describes:

$$V_D = V_g + Q_d t_d \qquad 5\text{-}3$$

where V_g is the volume of the droplet in the growth stage, Q_d is the flow rate of the dispersed phase and t_d is the duration of the detachment period. From equation 5-3

it can be noted that as Q_d increases, an increase in V_d can also be expected. However, experimental results from Xu et al. (2005) demonstrated that the detachment period decreases as the crossflow velocity increases, almost independently of the dispersed phase injection rate. Consequently, at high rotational speeds, a reduction in the term $Q_d t_d$ is observed as the injection rate is increased. Therefore, as the shear stress velocity increases, a final decrease in V_D is observed due to an earlier droplet detachment.

5.5 Effect of the pore size

The effect of membrane pore size on the droplet diameter was evaluated by fabricating AAMs at different voltages to achieve different average pore sizes (Figure 4.4). Figure 5.10a shows the droplet diameter of NEs obtained by injecting 0.15 ml of dispersed phase (4 % wt. Span 80 in SFO) at 0.015 ml min^{-1} in 25 ml of continuous phase (1 % wt. Tween 20 in DW) as a function of the pore size for defined rotational speed values. The results show a positive correlation between the membrane pore size and the droplet diameter. Furthermore, it is possible to identify two regions in Figure 5.10b: the first one at low rotational speeds, where the shear stress is not high enough to produce droplet detachment and bigger droplets with wider size distribution are obtained. In this region, the sharpest decrease on the droplet diameter is observed especially at the lowest rotational speeds (100 rpm), a trend previously reported for ME using flat membranes at the micrometre scale (Suárez et al., 2013), (Kosvintsev et al., 2005). A distinct behaviour is observed at higher rotational speeds (> 1000 rpm) where the droplet diameter is nearly independent of rotational speed (Figure 5.10b). The behaviour of the droplet diameter at these high rotational speeds shows that the minimum value of the droplet has been reached and consequently the membrane pore size and rotational speed will be the key parameters for controlling droplet size.

a

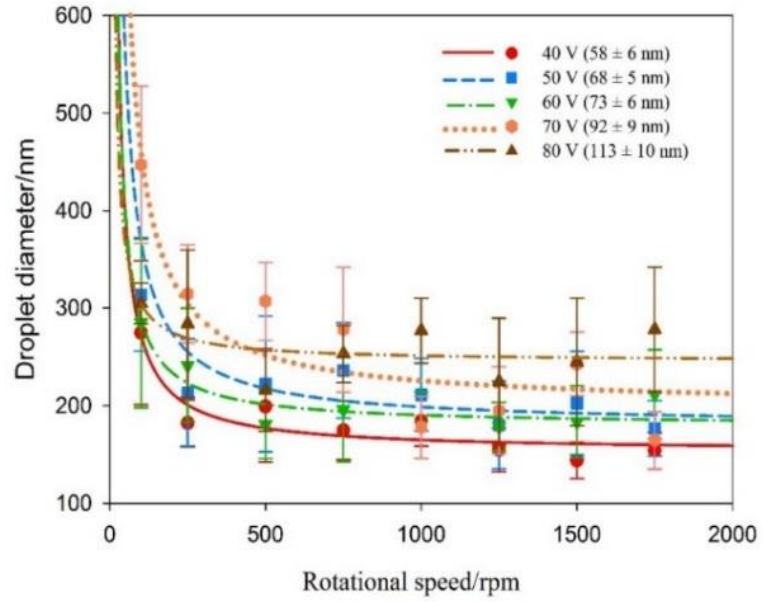

b

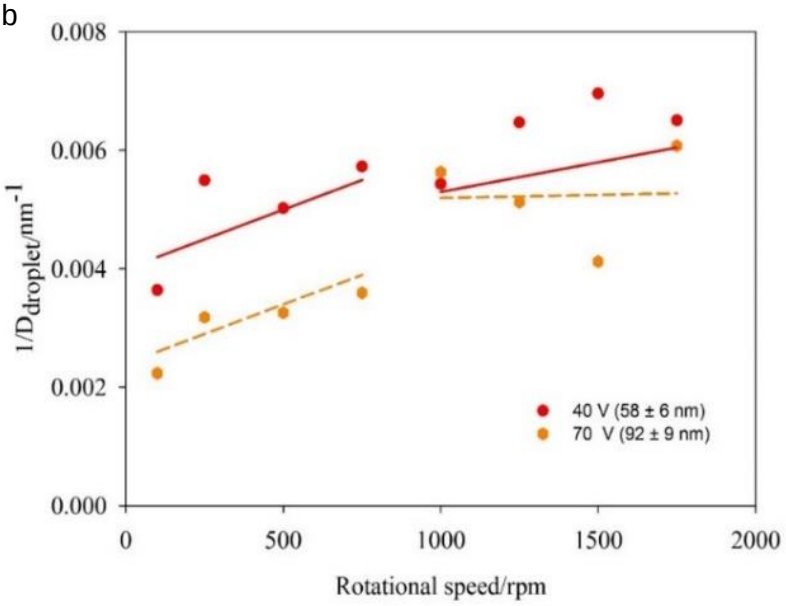

Figure 5.10 a) Droplet diameter of NEs against the rotational speed, for membranes with different pore sizes with R^2 value of 0.86, 0.69, 0.84, 0.81, 0.38 for a 40, 50, 60, 70 and 80 V membrane, respectively, using an inverse first order fit and b) Inverse of the droplet diameter against rotational speed for AAMs of 40 and 70 V.

Another trend observed is that wider droplet size distributions are obtained with the increase on the membrane pore size along all the rotational speeds. This is a consequence of the decrease on the membrane quality in terms of pore circularity, as can be seen in Table 4.1. As discussed in Section 4.2.2, during membrane

fabrication higher potentials produce less ordered porous structures with wider pore size distributions and an increase in the pore heterogeneity. These translate into the formation of broader NEs with wider size distributions, an issue that cannot be overcome with an increase of the rotational speed. For instance, a droplet size reduction of 44 % is observed for a 40 V membrane when the shear stress is increased from 100 to 1750 rpm, but only a 9 % reduction is observed for a 80 V membrane under the same conditions (Figure 5.10a).

Figure 5.11 shows the ratio of the average droplet diameter to the average pore size (D_d/D_p) for AAMs with different pore sizes. The results show the proportionality constant values lies between 1.8 and 3.5, for rotational speeds above 200 rpm. Only for rotational speeds below 200 rpm, this value goes up to 4.9, for the given conditions. The low proportionality values obtained are due to the nearly circular pores in a highly-ordered arrangement and the narrow pore size distribution of the AAMs. The obtained proportionality constant values are small compared to the ones in the literature, which typically go up to 10 for SPG and up to 50 for other less ordered membranes (Charcosset et al., 2004). ME experiments on disk SPG membranes (D_p = 9.83 µm) show *c* values small as 3.01 can be achieved and with a span of 0.53 when a 2 % wt. of SDS solution is used as a continuous phase (Kukizaki, 2009).

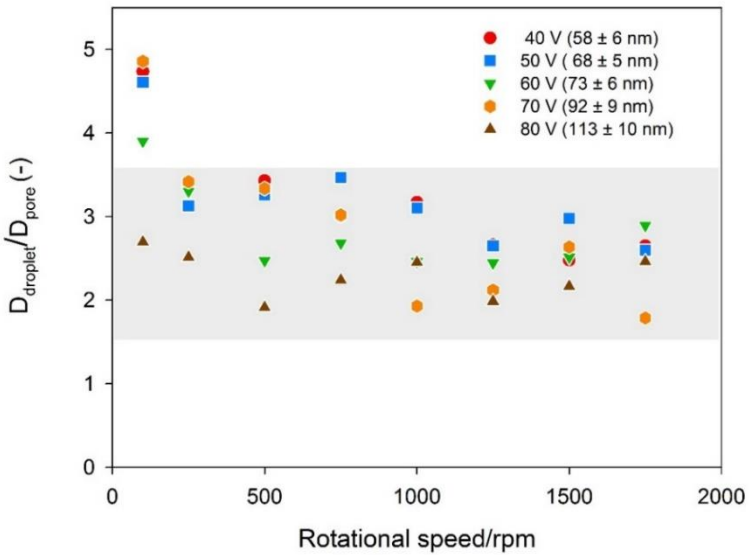

Figure 5.11 Droplet diameter to pore diameter against rotational speed for AAMs for different pore diameters.

5.6 Bespoke nanoemulsions using dimensionless numbers

When a droplet is growing over the edge of a pore it can be considered as a particle immersed in a fluid in which its final size is determined by the relative magnitude of the forces acting over the droplet before its detachment, as shown in Figure 5.12. The ratio of two forces can be represented using dimensionless numbers, some of them were listed in Table 2.4.

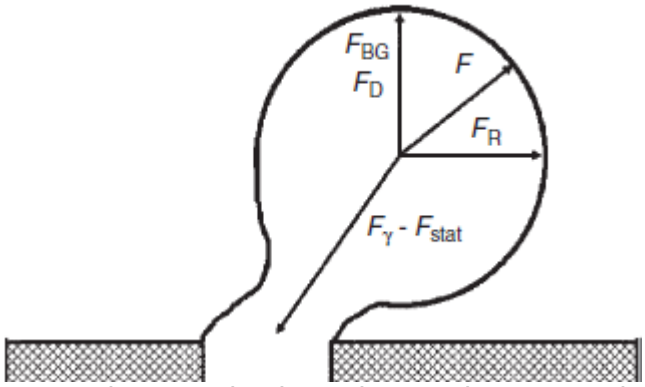

Figure 5.12 Forces acting on a droplet at the membrane pore (Spyropoulos et al., 2014).

Dimensionless numbers are a powerful tool to have an insight on the performance of a ME setup and be able to produce bespoke emulsions in terms of droplet size or emulsion production rate. For instance, the Capillary number has been extensively used to predict the droplet diameter in ME and is defined as the ratio of the viscous forces to the interfacial tension force. For instance, Lepercq-Bost et al. (2008) found that an optimal emulsion is obtained when the Capillary number is kept above a critical Capillary number, Ca_{crit}, = 0.5, with droplet size reaching a plateau zone and becoming independent of the type of emulsifier. Figure 5.13 shows the plot for the proportionality constant (D_d/D_p) versus the capillary number for AAMs of different pore sizes. The results demonstrate that at Capillary numbers above 0.45 the minimum droplet size has been obtained with proportionality constant values ranging from 1.8 to 2.9 which are slightly smaller than reported values of close to 3 for Ca_{crit} > 0.5 (Lepercq-Bost et al., 2008, Christov et al., 2002). A possible explanation of the smaller proportionality constant values is the highly ordered pore arrangement of the AAMs that make possible to achieve the minimum droplet size at lower Capillary values.

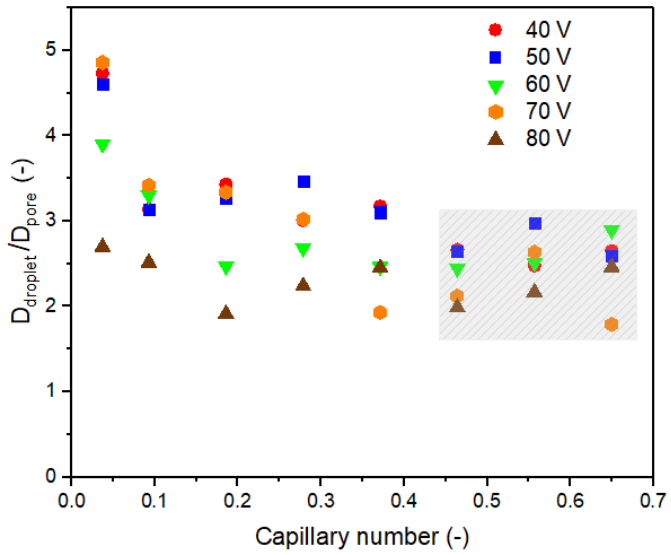

Figure 5.13 Droplet diameter to pore diameter against capillary number for AAMs for different pore sizes.

Figure 5.13 has a similar trend to Figure 5.10a as the Capillary number relates shear stress to IFT force. However, the two main parameters influencing droplet size on ME are membrane pore size and shear stress (as it was discussed in Section 5.5).

Although the Capillary number only allows correlating the shear stress with the droplet size, using the Weber number allows evaluating the effect of the dispersed phase. Therefore, it is convenient to express the contribution of both phases in a single dimensionless number, the Euler number. The Euler number relates the dispersed phase injection rate, calculated from the transmembrane pressure, with the rotational speed of the continuous phase. As the experiments were done using a syringe pump, it is reasonable to assume that the pressure produced by the syringe pump was relatively close to the critical pressure. As such, it is possible to express the Euler number using the critical pressure value (Suárez et al., 2014):

$$Eu_{trans} = \frac{\Delta P}{\rho_c N^2 D_i^2} = \frac{4\gamma}{\rho_c N^2 D_i^2 D_p^2} \qquad 5\text{-}4$$

Figure 5.14 relates the proportionality constant value to the Euler number for AAMs with different pore sizes, showing a positive correlation between the Euler number and the proportionality constant. A power regression was used to fit the data for each membrane pore size and the equation that describes the data for each condition with their respective R^2 values can be found in Table 5.2. The correlation coefficient values range from 0.72 to 0.86 for AAMs from 40 to 70 V. For a 80 V AAM the correlation coefficient fell down to 0.26. A possible explanation of the latter result is the high heterogeneity of the membranes synthesized under this condition, which lead to the

production of NEs with wider droplet size distributions (as was observed in Figure 5.10a).

Table 5.2 Correlation of the proportionality constant value and the Euler number for AAM with different pores sizes.

	Anodization voltage/V				
	40	50	60	70	80
$\frac{D_d}{D_p} =$	$0.875Eu_{trans}^{0.097}$	$1.13Eu_{trans}^{0.082}$	$1.06Eu_{trans}^{0.077}$	$0.465Eu_{trans}^{0.148}$	$1.61Eu_{trans}^{0.026}$
R^2	0.83	0.76	0.72	0.86	0.26

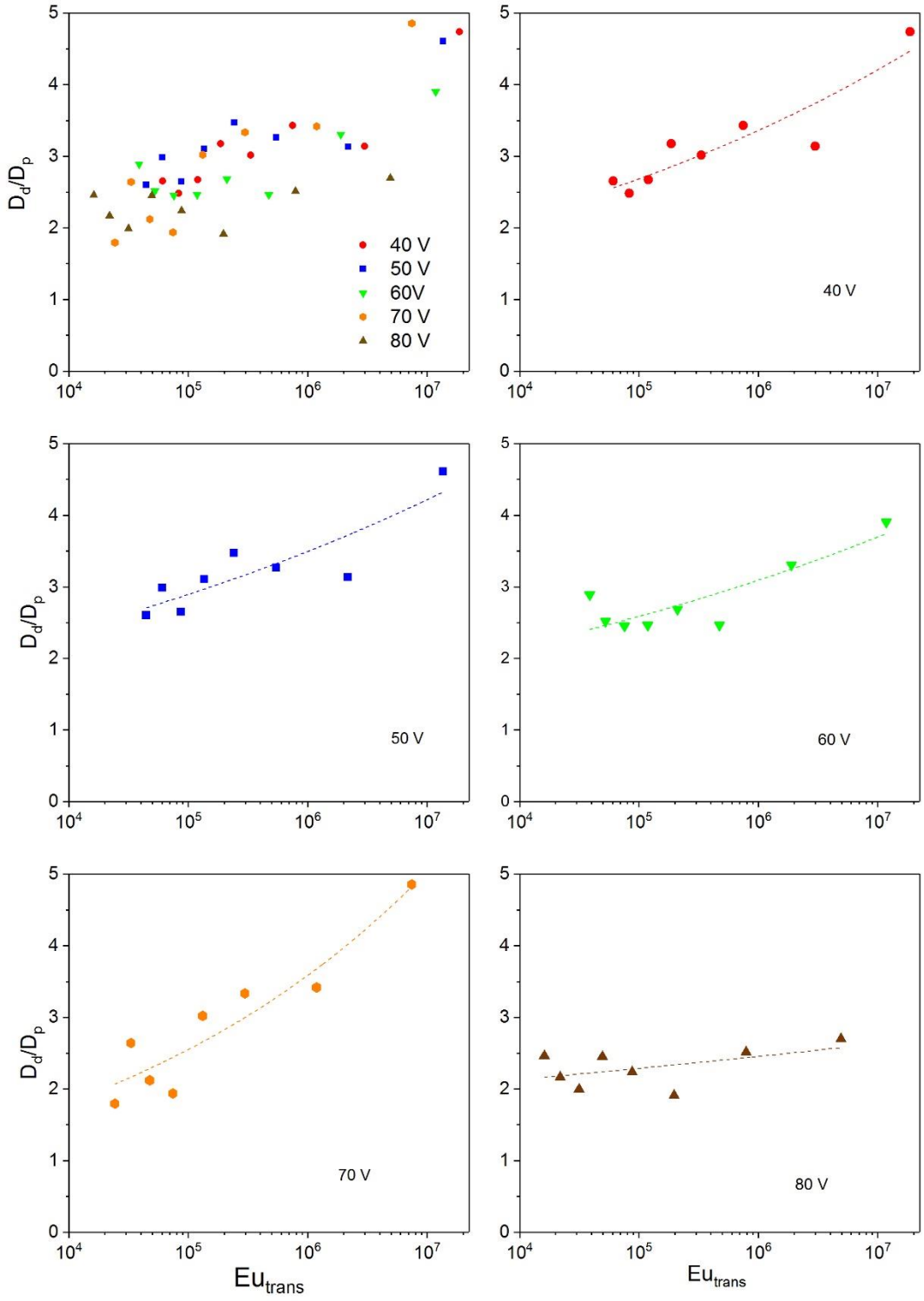

Figure 5.14 Droplet diameter to pore diameter against Euler number for NEs produced using AAMs with different pore sizes.

5.7 Droplet formation mechanism

Five different models from the literature presented in Table 2.5 were used to estimate the droplet size and compared to experimental values for NEs obtained using a 40 V AAM. To estimate the droplet diameter, the shear stress for a stirred cell configuration was calculated as described in the Section 2.3.3 . Figure 5.15 shows the shear stress profile along the membrane radius for different rotational speeds. For each rotational speed, the highest point in the curve represents the critical radius (r_c). Along the shear stress profile, there are two regions: the first one for positions $r < r_c$, is a forced vortex region, in which the continuous phase exhibits a rigid-body motion with an angular speed of the impeller (ω); the second is a free vortex region ($r > r_c$) in which the angular momentum ($r\tau$) is constant (Kosvintsev et al., 2005).

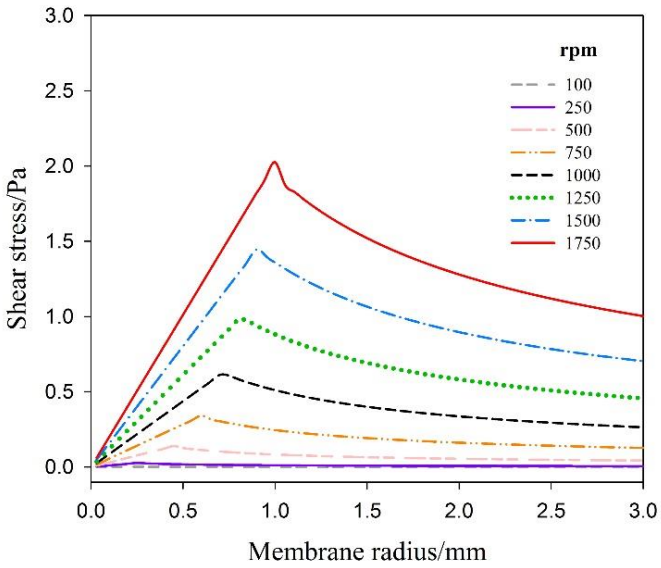

Figure 5.15 Estimated shear stress profile along the membrane radius at different rotational speeds for a 40 V AAM (D_p = 58 ± 6 nm).

Table 5.3 shows the estimated values of the critical radius and the boundary layer thickness at different rotational speeds. Shear stress values were calculated for the whole membrane radius using Equations 2-15 and 2-16. Table 5.3 shows the minimum and maximum values of the shear stress along the membrane radius. In addition, the ratio maximum to minimum shear stress demonstrates that at low rotational speeds there is a narrower shear stress distribution across the membrane radius compared to higher rotational speeds. Nevertheless, the values of the shear stress are not high enough to produce a fast droplet detachment and consequently larger droplet size with larger droplet size distributions are obtained at low rotational speeds (as observed in Figure 5.10a).

Table 5.3 Values of critical radius, boundary layer thickness and shear stress calculated as described in Section 2.3.3.

Rotational speed/rpm	Critical radius/mm	Boundary layer thickness/mm	Shear stress/Pa		
			Maximum	Minimum·10^{-3}	Ratio
100	0.11	0.31	0.003	0.4	6.8
250	0.25	0.19	0.027	3.3	8.3
500	0.44	0.14	0.14	9.3	15
750	0.59	0.11	0.34	17	20
1000	0.71	0.1	0.61	26	23
1250	0.82	0.09	0.98	37	27
1500	0.90	0.08	1.4	48	30
1750	0.97	0.07	2.0	61	33

The shear stress value at the critical radius was used to estimate the magnitude of each force acting over a droplet before its detachment, as discussed in Section 2.3.3 Figure 5.16 shows the magnitude of each force for all the rotational speeds. The drag force is based on Stokes's drag force. The equation assumes that droplet formation takes places in the boundary layer. The correction factor, which considers the effect of the nearby walls in the motion of a droplet, is k_w = 3.4926 as reported in Keh and Chen (2001). The results in Figure 5.15a demonstrate there are three main forces acting over a droplet before its detachment: interfacial tension, static pressure and drag force, while the buoyancy and inertial force are several orders of magnitude smaller than the main forces. These results are in good agreement with previous reports on micrometre-scale droplets (Rayner and Trägårdh, 2002). The main detaching forces are the drag and static pressure force; the first one pushes the droplet in a parallel direction to the membrane surface, whereas the second one pushes the droplet in a perpendicular direction. The interfacial tension force is the main retaining force during droplet formation. For instance, Figure 5.16b shows the ratio of interfacial tension to drag force versus rotational speed to estimate the relative magnitude of their effects during droplet formation. The resulting curve shows that at rotational speeds between 100 to 250 rpm, the interfacial tension is 3 to 4 orders of magnitude larger than the drag force, being the static pressure force the main one counteracting the interfacial tension force. However, at rotational speed above 500 rpm, the drag force becomes significant, and the dual action of the static pressure force and drag force induce a quick droplet detachment, leading to the reduction in droplet size and size distribution.

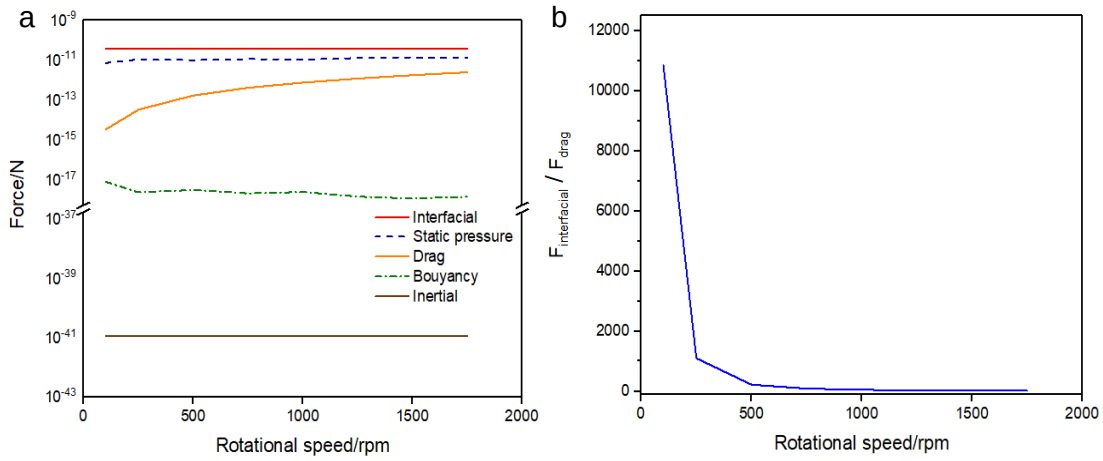

Figure 5.16 a) Estimated magnitude of the drag, buoyancy, static pressure, inertial and interfacial tension forces in a stirred-cell setup for ME based in a 40 V AAMs (D_p = 56 ± 6 nm) and b) ratio interfacial tension force to drag force against rotational speed.

The estimation of the magnitude of each force enabled the use of five different droplet size estimation models from the literature (Table 2.5) to estimate the droplet size of a NE. Figure 5.17 compares the experimental and the estimated droplet diameters for the five models for a 40 V AAM, with the numerical data reported in Table 5.4.

The force and the torque model developed by Kosvintsev et al. (2005) result from the force and the torque balance between the interfacial tension force and the drag force. For both models, the buoyancy and the inertial forces have been neglected. A decrease in the droplet diameter is observed as the shear stress increases, as in the experiments, but a comparison between the experimental values and the theoretical values from both models at the highest rotational speed (1750 rpm) produces an overestimation of 643 % and 170 % of the droplet diameter for the torque and force balance, respectively.

The model developed by Rayner and Trägårdh (2002), Table 2.5, as a force balance between the interfacial tension and the drag force also leads to an overestimation of the experimental data of 244 % for the highest shear stress. The results for the droplet size estimation model follow the trend shown in Figure 5.16b, as the model is a balance between the interfacial and drag force.

The model proposed by Suárez et al. (2013) is a force balance between the static pressure force and drag force. The model results from the assumption that prior to droplet detachment, a neck constriction occurs (Schröder et al., 1998), which is favoured by the action of the drag force. They also noted that neck constriction is unlikely to happen when the static pressure is higher than the drag force.

Consequently, they proposed that droplet detachment will occur when there is an equilibrium between both forces.

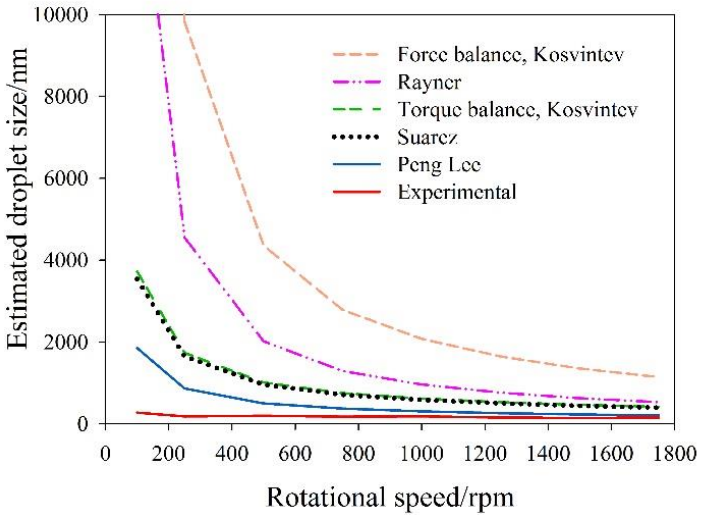

Figure 5.17 Comparison between droplet size estimations obtained from the five different models and the experimental data for a NEs prepared using a 40 V membrane (D_p = 58 ± 6 nm).

Table 5.4 Comparison of the experimental NEs obtained with a 40 V AAM (D_p = 58 ± 6 nm) with current droplet size estimation models.

Rotational Speed /rpm	Droplet diameter/nm				
	Experimental Values	Peng Lee and Mattia	Rayner and Trägård	Torque Balance (Kosvintsev et al.)	Force balance (Kosvintsev et al.)
100	275	1 852	14 312	3 721	30 885
250	182	864	4 553	1 734	9 825
500	199	502	2 018	1 009	4 354
750	175	373	1 289	749	2 782
1000	184	307	962	617	2 076
1250	155	262	761	528	1 643
1500	144	230	626	464	1 351
1750	154	206	529	415	1 142

For the Suárez et al. (2013) model, the results show a smaller overestimation of 155 % for the highest rotational speed. The similarity observed in Figure 5.17 between

the former model and the torque balance from Kosvintsev et al. (2005) for all the rotational speeds is due to the similar magnitude between the static pressure force and interfacial tension force.

The fifth model was developed by Lee and Mattia (2013) for crossflow ME with membrane with pores in the nanometre range and is a two equation system where drag, buoyancy and interfacial tension force are considered. The model results in a much smaller overestimation of only 34 % for the highest shear rate, providing a better, while not yet ideal, fit with the experimental data.

For all the five models, the predicted values tend to converge at higher rotational speeds, while larger discrepancies with the experimental values were observed at low rotational speeds. This difference can be attributed to two possible explanations: the first one, that at low rotational speed, below 200 rpm, the magnitude of the buoyancy force becomes significant (Peng and Williams, 1998b). For instance, as observed in Figure 5.16, the magnitude of the drag force is relatively low and the ratio between these two forces will be smaller. In fact, at the lowest rotational speed, the drag force is only two orders of magnitude higher that the buoyancy force, while at the highest rotational speed the ratio increases to about five orders of magnitude. The second reason is the possible existence of an additional force that has an impact on the formation and detachment of droplets at the nanometre scale. The origin of the force might be attributed to the electrostatic repulsion between the negatively charged groups on the surface of the aluminium oxide membrane and the hydroxyl groups of Tween 20 (Table 2.3).

5.8 Stability of emulsions

The stability of the NEs was evaluated by analysing a sample by DLS at 20 ˚C the same day that it was produced (analysis 1) and after twelve days stored at 8 ˚C (analysis 2). The average droplet diameter was 200 ± 30 nm and 207 ± 50 nm in the first and second analysis, respectively. The negligible difference in the droplet size between both analyses suggests that no coalescence or ripening occurred during storage.

Table 5.5 Stability analysis of a NE using a 40 V AAM (D_p = 56 ± 6 nm).

Measurement number	Analysis 1	Analysis 2
	Droplet diameter/nm	
1	192 ± 28	196 ± 46
2	176 ± 24	216 ± 53
3	233 ± 38	209 ± 51
Average	200 ± 30	207 ± 50

Chapter 6: Synthesis of hematite nanoparticles using a micropore setup

The present chapter evaluates the performance of ring-shaped AAMs (Figure 6.1) in the production of NEs using a commercial stirred-cell setup, described in Section 3.1.3. Seven sections comprise the present chapter, Section 6.1 evaluates the addition of surfactant in both the continuous and dispersed phase and their effect on the IFT force. The following one, investigates the effect of the shear stress over droplet diameter and droplet size distribution. Section 6.3 compares the droplet size obtained from different droplet size estimation models from the literature to the experimental droplet size values. Section 6.4, the Euler number is used to evaluate the performance of the membrane emulsification rig. Section 6.5 describes the synthesis procedure of iron oxide nanoparticles. Section 6.6 discuss the characterization of the iron oxide nanoparticles by TEM, XRD, Raman and XPS. The following one, Section 6.7, evaluates the nanoparticle productivity of the ME setup. The results presented in the chapter are a part of a journal publication currently under review.

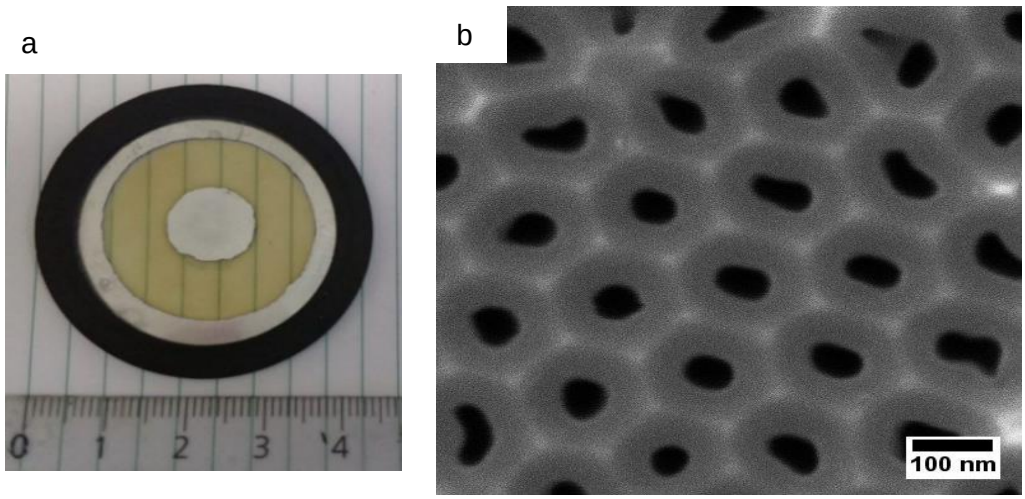

Figure 6.1 a) Ring-shaped AAMs (60 V, 0.30 M $C_2H_2O_4$, 10 °C) with a black viton o-ring; and b) SEM micrograph of the porous section, the transparent section in a.

6.1 Effect of the addition of surfactant in the continuous and dispersed phase

Interfacial tension (IFT) measurements of hexane/water were carried out at different surfactant concentrations (Figure 6.2). Tween 20 was selected as surfactant in the continuous phase as is widely used in ME due to its non-ionic nature (Hancocks et al., 2013, Thanasukarn et al., 2004). Four repetitions for each experimental condition were carried out at a constant temperature of 18 ± 1 °C. The results show that for Tween 20 concentrations higher than 1.0 %, the equilibrium IFT has been reached (8.0 ± 0.1 mN m^{-1}). Higher surfactant concentrations were avoided as an experimental work reported by Hancocks et al. (2013) concluded that for concentrations above 0.4 % wt. of Tween 20, the minimum droplet size can be achieved using a 1 µm SPG membrane.

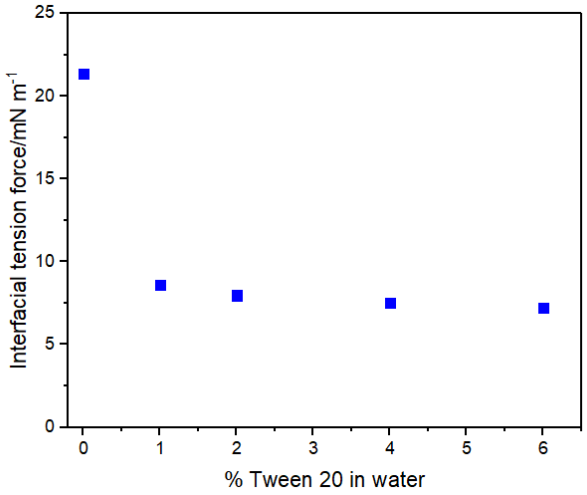

Figure 6.2 Interfacial tension between hexane/water at different surfactant concentrations (Tween 20) in the continuous phase.

However, the slow adsorption kinetics of Tween 20 at the hexane/water interface due to a combined effect of its high molecular weight (1228 g mol^{-1}) and its non-ionic nature (Rayner et al., 2005), can result in broadening of average droplet size and widening of its distribution, especially for membranes with small interpore distance values (in the present case equal to 156 ± 6 nm, Table 4.4). Therefore, the incorporation of a second surfactant in the dispersed phase was evaluated to induce a faster reduction of the interfacial tension force. The addition of the hydrophobic surfactant sodium dioctyl sulfosuccinate, commonly named docusate, ($C_{20}H_{37}NaO_7S$), allowed a further reduction of the IFT down to 1.80 mN m^{-1} when 1 % wt. was added to the dispersed phase.

6.2 Effect of the shear stress over droplet size

Figure 6.3a and Figure 6.3b compare the emulsion droplet size distribution at lowest and highest rotational speed tested, 250 and 1250 rpm, for two surfactant conditions: first when 1 % Tween 20 in DI water is used as continuous phase and hexane is used as dispersed phase; secondly when the dispersed and continuous phases consist of 1 % of docusate in hexane and 1 % Tween 20 in DI water, respectively.

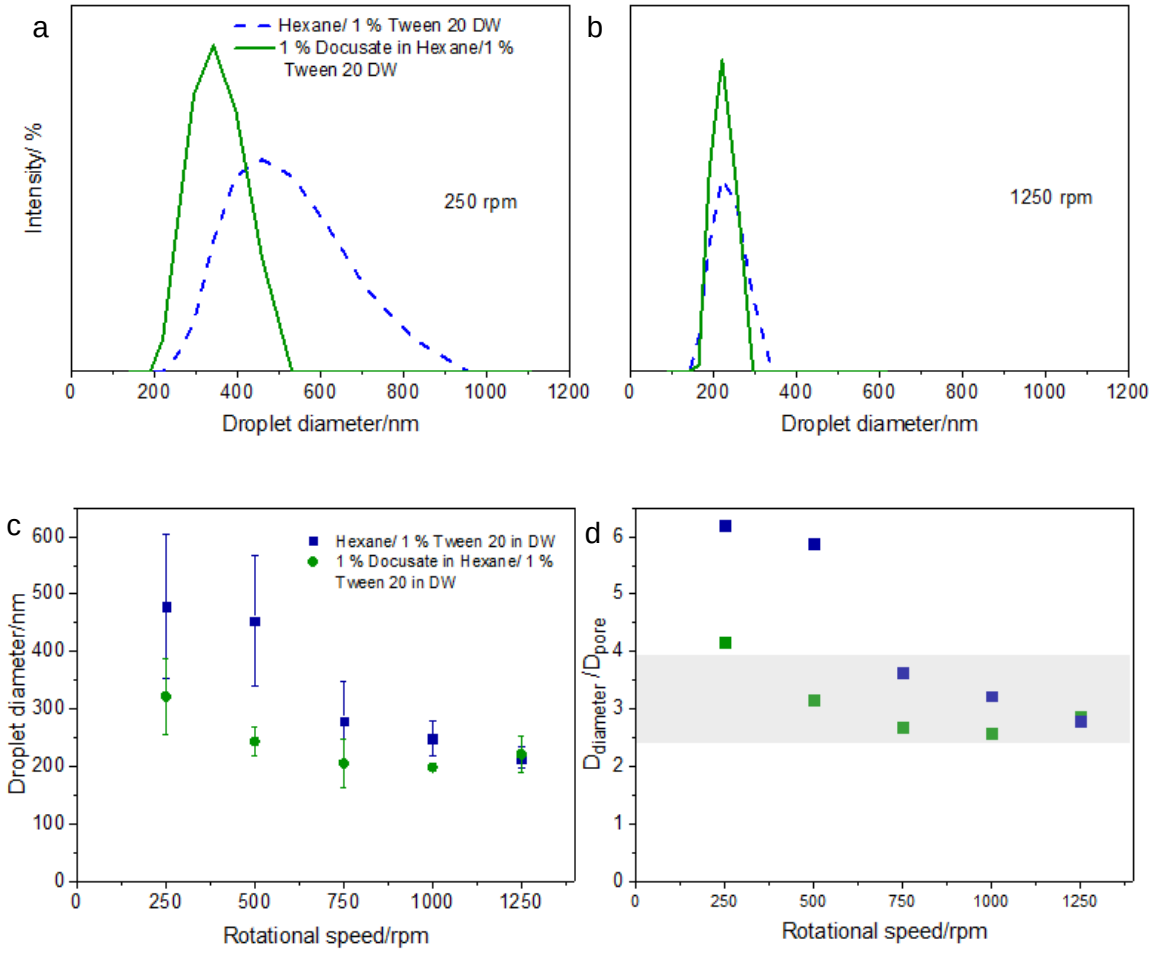

Figure 6.3 Intensity against droplet diameter for emulsions produced using 1 % wt. Tween 20 in DI Water as continuous phase and with and without the incorporation of surfactant (1% wt. Docusate) in the dispersed phase (hexane) at rotational speeds of a) 250 rpm and b) 1250 rpm; c) Droplet size of emulsion obtained at different rotational speed with 1 % wt. Tween 20 in DI water and with and without the incorporation of 1 % wt. docusate in dispersed phase (hexane); and d) ratio droplet diameter to pore diameter (proportionality constant c) against rotational speed.

At 250 rpm, the results show a single peak at 489 ± 127 nm, when only 1 % wt. Tween 20 in the DI water is used, while a peak at 373 ± 64 nm is obtained when both surfactants were added. In contrast, at 1250 rpm narrower droplet size distributions are obtained for both conditions: 230 ± 36 nm (1 % Tween 20 in DI water) and 220 ± 25 nm (1 % Docusate in hexane/1 % Tween 20 in DI water). The droplet diameter obtained for the complete range of rotational speeds for a 60 V ring-shaped AAM with and without the addition of a surfactant in the dispersed phase can be found in Figure 6.3c.

The addition of a second surfactant is clearly visible at low rotational speeds, 100 - 500 rpm (Figure 6.3c), where a considerable difference between the average droplet size for both conditions is obtained. The former behaviour is attributed to the drag force not being high enough to produce droplet detachment, as discussed in Chapter 5. The addition of docusate in the system decreases the interfacial tension rate faster than when only a surfactant in the continuous phase is added, although above 1000 rpm, its effect becomes minimal. This can be attributed to the fact that above this value, the droplet size becomes independent of the shear stress and, pore diameter will be the main parameter that determines droplet diameter, as discussed in Section 5.4 . Above 1000 rpm, the average droplet diameter to pore diameter is approximately 2.8 (Figure 6.3d), an indication of the high regularity of the membranes produced, compared to values up to 10 for SPG membranes (Charcosset et al., 2004). In addition, the proportionality constant values are in good agreement with the results on the production of emulsions using AAMs using a fully open porous membrane (Section5.5).

6.3 Droplet size estimation models

The droplet diameter was estimated using the shear stress equation in a stirred-cell configuration (Section 2.3.3). Figure 6.4a shows the shear stress profile along the radius at the porous section of the membrane for different rotational speeds. As discussed before, for each rotational speed, the highest point in the curve represents the critical radius (r_c). The radial position of the porous section is from 6 mm < r < 14 mm (Figure 6.1a), with an effective membrane area of ~ 503 mm^2. Based on Eq 2-13, the position of the critical radius is located between 10 to 11 mm for 250 and 1250 rpm, respectively, with the sharpest increment at 1250 rpm.

For each rotational speed, the shear stress value at the critical radius was selected to estimate the droplet size, using three droplet size estimation models

from the literature (Table 2.5). The results in Figure 6.4b compare the estimated droplet size values from the literature with experimental values. The predicted values for the three models tend to converge at higher rotational speeds. The torque model developed by Kosvintsev et al. (2005) and the Suárez et al. (2013) models have overestimation values up to 154 % and 140 %, respectively, at the highest rotational speed, while the model developed by Lee and Mattia (2013) has an overestimation at 1250 rpm of only ~22 %. The estimated droplet values can be found in Table 6.1.

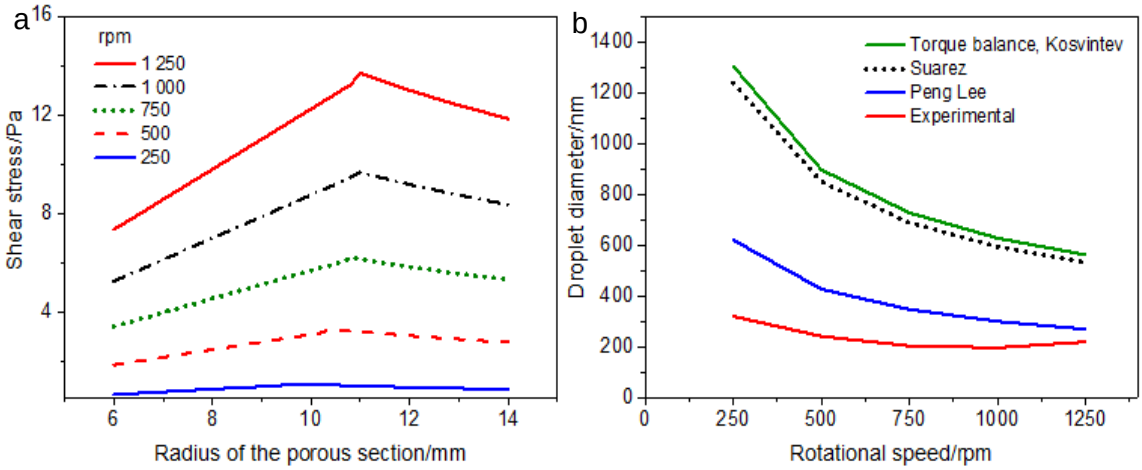

Figure 6.4 a) Shear stress profile against radius at the porous section of the membrane for different rotational speeds b) comparison of the experimental droplet diameter and estimated droplet diameter at the critical radius.

Table 6.1 Comparison of the experimental NEs droplet size obtained with a ring-shaped AAM (D_p = 77 ± 9 nm) to estimated droplet size obtained by different droplet size estimation models.

Rotational speed/rpm	Droplet diameter/nm			
	Experimental Values	Lee and Mattia (2013)	Torque Balance, Kosvintsev et al. (2005)	Force balance Suárez et al. (2013)
250	322 ± 66	622	1303	1237
500	244 ± 25	429	897	850
750	206 ± 42	349	728	690
1000	199 ± 5	303	629	595
1250	222 ± 31	271	563	532

Using the shear stress at the critical radius it is possible to estimate the magnitude of each force acting over an individual droplet, as discussed in Section 5.7 . The results in Figure 6.5a show there are three main forces acting over an individual droplet before its detachment: interfacial tension, static pressure and drag forces, while the buoyancy, dynamic lift and inertial forces are several orders of magnitude smaller than the main ones. These trends are in good agreement with the results for a fully porous AAMs, Section5.7 . IFT force is the main retaining force, counteracting the detaching forces, static pressure force and the drag force. Figure 6.5b compares the magnitude of the interfacial tension force to the drag force for different rotational speeds. The results show a decrease in the ratio ($F_{interfacial}/F_{drag}$) as the rotational speed is increased, with the sharpest decrease between 250 and 500 rpm. For instance, the relative magnitude of both forces is 238 at the lowest rotational speed. However, as the shear stress increases, the value of the ratio of the forces drops close to 40 at 1250 rpm. The former trend is similar as the one observed in Figure 6.3c, where a decrease in the droplet size is observed as the rotational speed is increased. These results demonstrate that only at high rotational speeds the dual action of the detaching forces (drag and static pressure) counteract the retaining force (interfacial tension), as previously discussed in section 5.7 .

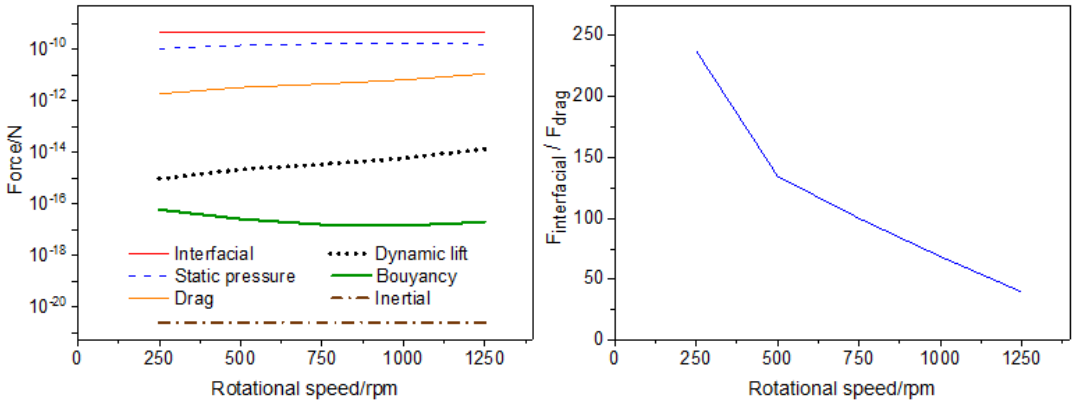

Figure 6.5 a) Magnitude of the forces acting over a single droplet before its detachment and b) ratio of interfacial tension force to drag force at different crossflow velocities.

6.4 Bespoke NEs using dimensionless numbers

Figure 6.6 correlates the Euler number to the proportionality constant values (D_d /D_p) for NEs produced using the ring-shaped AAMs when the surfactant conditions are 1 % Docusate in Hexane/1 % wt. Tween 20 in DI water. The results were fitted using a linear regression, the equation that describes the data can be found in Table 6.2. The correlation coefficient value is 0.93. The obtained correlation coefficients for the ring-shaped AAM is close to the obtained values for a stirred-cell configuration using a fully porous AAM (Table 5.2).

Table 6.2 Euler number and correlation of the proportionality constant value for NEs produced using ring-shape anodic aluminium oxide membranes.

$\frac{D_d}{D_p}$ =	2.2 +0.03*Eu*
R^2	0.93

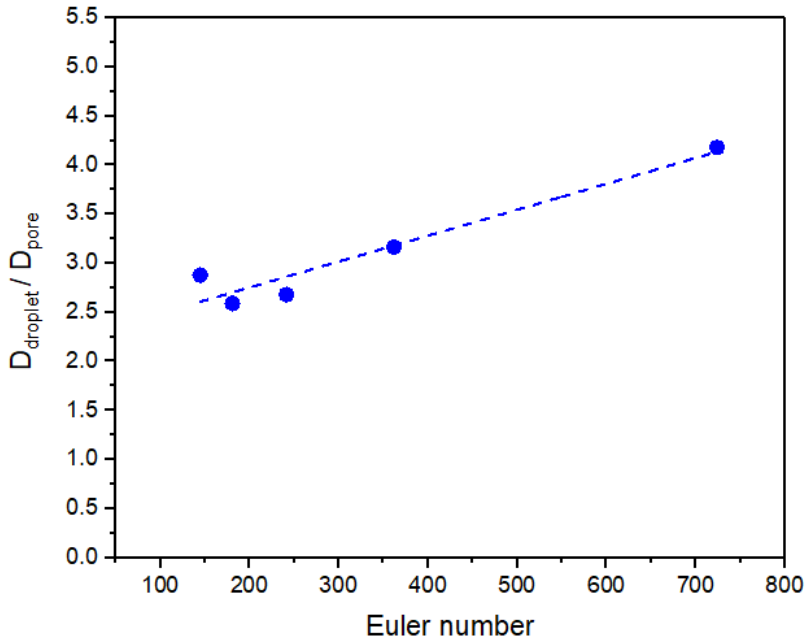

Figure 6.6 Droplet diameter to pore diameter against Euler number for NEs produced using a ring-shaped anodic aluminium oxide membrane.

6.5 Synthesis of hematite nanoparticles

To synthesize iron oxide nanoparticles, a NE was first produced using the semi-

continuous stirred ME setup operating in a dead-end configuration. As discussed in Section 6.1 and 6.2 show the best results, in terms of droplet size and size distributions, were achieved using 1 % wt. docusate in hexane/1 % wt. Tween 20 in DI water and rotational speeds of 1000 and 1250 rpm and an injection rate of 0.25 ml min^{-1}. Under the former ME conditions, iron oxide nanoparticles were produced using a liquid-liquid approach by dissolving in the dispersed phase an organometallic precursor, Iron (III) 2-ethylhexanoate in mineral spirits (Fe 6 %), $Fe(C_8H_{15}O_2)_3$ or $Fe(EH)_3$, prior its emulsification. Two rotational speeds were tested to produce iron oxide nanoparticles, 1000 and 1250 rpm. Figure 6.7 show the DLS analysis of the obtained NEs.

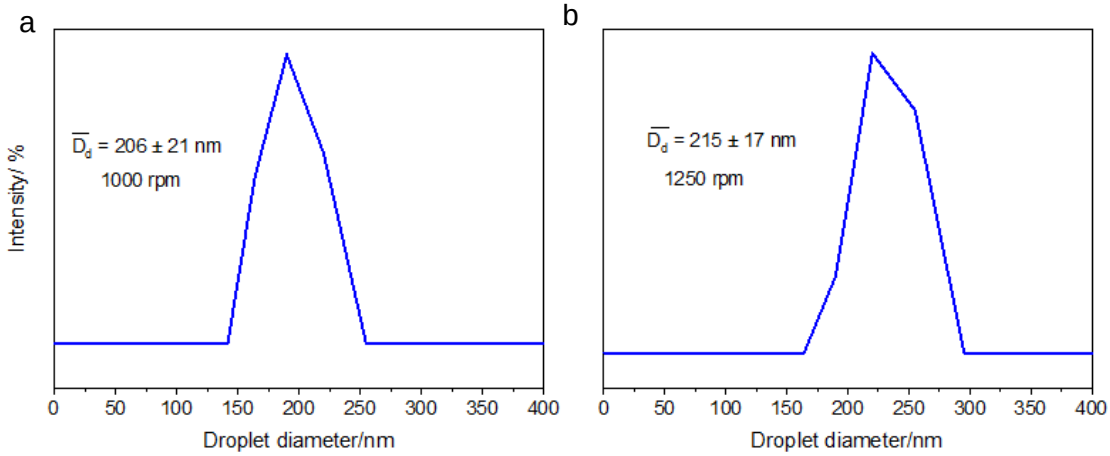

Figure 6.7 Droplet size distribution of NE produced at a) 1000 and b) 1250 rpm.

The resultant NEs was collected and NH_4OH was added drop wise, with a 10 % molar excess of NH_4OH based on the stoichiometric amount of $Fe(EH)_3$ added to the dispersed phase, as described in Section 3.2.4 . The reaction between $Fe(EH)_3$ and NH_4OH can be expressed as:

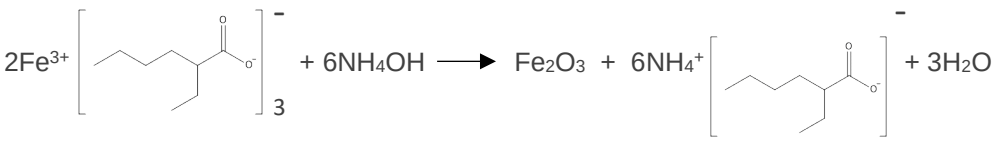

6-1

Equation 6-1 states the formation of hematite nanoparticles when NH_4OH is added as a precipitation agent, as previously reported by Okoli et al. (2012). The as-synthesised nanoparticles were washed, dried as described in Section 3.2.4 Subsequently, the NP were calcined at 700 °C to ensure the formation of hematite.

6.6 Characterization of iron oxide nanoparticles

The iron oxide NPs were characterized by TEM to obtain further information about the crystal phase and particle size. Figure 6.8 shows the TEM micrographs of the as-synthetized iron oxide NPs, giving an average primary particle size of 3.7 ± 1 nm and 4.2 ± 0.5 nm for the nanoparticles synthetized at 1000 and 1250 rpm, respectively. A FFT analysis of the TEM micrographs showed the formation of nanoparticles in direction of the planes (024) and (113) with an interplanar distance of 0.19 nm and 0.22 nm, respectively. The difference in the nanoparticle diameter for the two rotational speeds is within the error, with no meaningful difference between the two. As only a small reduction in the particle size was achieved by varying the rotational speed, further iron oxide nanoparticles were produced using 1000 rpm.

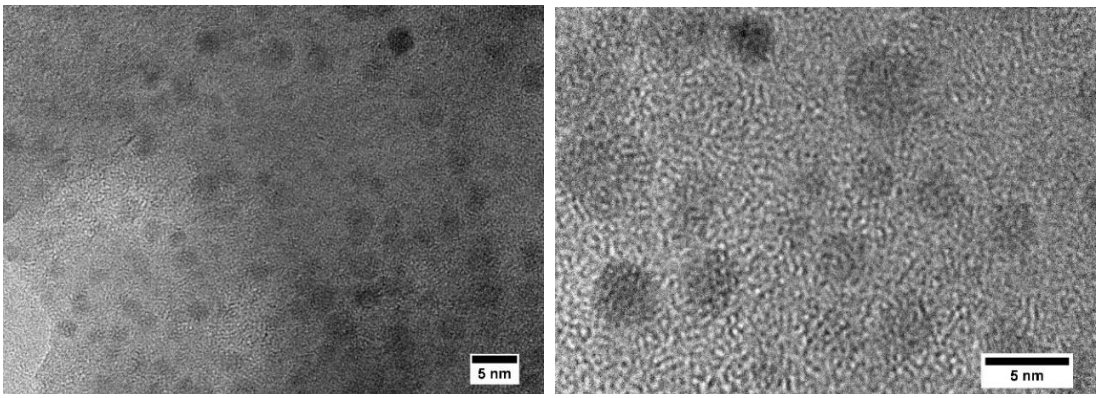

Figure 6.8 TEM micrographs of as-synthetized hematite nanoparticles.

The as-synthesized nanoparticles were characterized and then calcined at 700 °C, to ensure the formation of hematite. Figure 6.9 shows the TEM micrographs for the calcined nanoparticles, giving an average primary particle size of 18 ± 4 nm. In this case, the FFT showed the formation of nanoparticles in the direction of the planes (024), (113), (110) and (104) with an interplanar distance of 0.19, 0.22, 0.25 and 0.27 nm, respectively, which are characteristic of hematite (Cornell and Schwertmann, 2003). Calcination promoted grain boundary enlargement due to the high surface energy of the nanocrystalline nanoparticles and thus an increase in the nanoparticle size was observed (Shukla et al., 2003). In addition, drying and calcination of the NPs for their characterization leads to their agglomeration into clusters as observed in Figure 6.9. The dimensions of the clusters were in the micrometre scale, with values ranging from 2 to 15 µm.

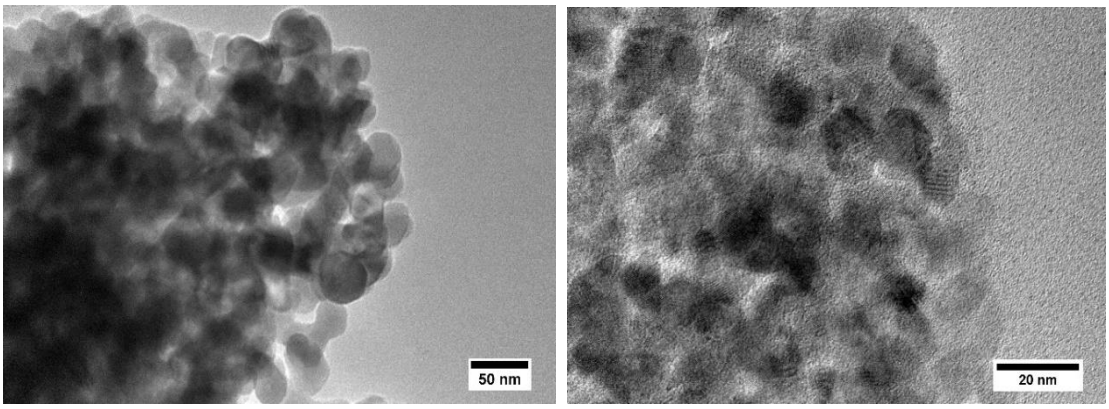

Figure 6.9 TEM micrograph of hematite nanoparticles calcined at 700 °C.

The hematite nanoparticles were further characterized by XRD, Raman and XPS spectroscopy. For the calcined nanoparticles the XRD pattern confirms the formation of hematite (JCPDS cards 13-0534), Figure 6.10a. The average particle size was deduced using the Scherrer equation of the two strongest peaks (104) and (110) is 25 nm, which is slightly larger than the TEM values.

Figure 6.10b shows the Raman spectrum of the as-synthetized and calcined iron oxide nanoparticles with distinctive Raman frequencies for hematite. The Raman frequencies at 227, 293, 412 and 612 cm^{-1} correspond to the E_g modes, in good agreement with the literature (De Faria and Lopes, 2007). The bands at 227 and 498 cm^{-1} are assigned to $A1_g$ modes (Chernyshova et al., 2007). However the as-synthetized nanoparticles have broader Raman frequencies with values shifted to lower wavenumbers due to their smaller particle size (White, 2005).

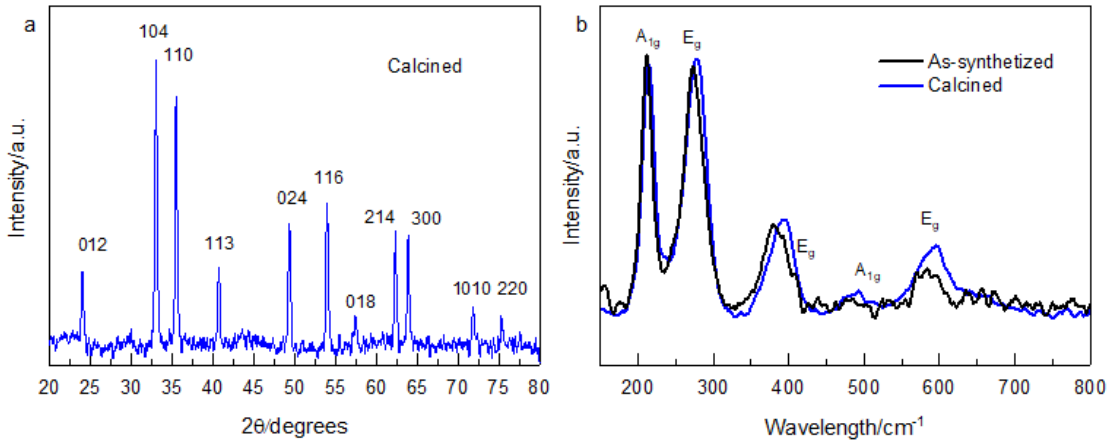

Figure 6.10 a) X-ray diffraction pattern of calcined hematite nanoparticles b) Raman spectra of the as-synthetized and calcined hematite nanoparticles.

To further investigate the composition and bonding of the iron oxide nanoparticles an XPS analysis was carried out for the as-synthetized and calcined nanoparticles. The global XPS profile for all the samples is shown in Figure 6.11a. The results show the incorporation of sodium and carbon within the iron oxide matrix. The former comes from the surfactants (Docusate), while the latter is likely to originate from the hexane of the dispersed phase. For a further analysis, the chemical structure of both iron oxide samples is examined in four specific areas of the XPS spectrum. Figure 6.11b shows the iron core level region for the as-synthesised and calcined samples. The characteristic peaks for hematite are clearly visible for both samples at 710.8 eV (Fe $2p_{3/2}$) and 724 eV (Fe $2p_{1/2}$), with their respective shake-up satellites are at 718 and 732 eV (Yamashita and Hayes, 2008). The peak separation between the Fe 2*p* peaks and their respective satellites is 8 eV, which indicates iron atoms have +3 as oxidation state (Descostes et al., 2000). Figure 6.11g shows the characteristic peaks for hematite at 93 eV (Fe 3*s*) and 55 eV (Fe $3p_{3/2}$) (Desai et al., 2005).

The O *1s* core level region (Figure 6.11c and Figure 6.11d) shows that the as-synthetized samples not only have the characteristic peak for the O^{2-} from hematite with binding energy (BE) of 529 eV, (Cornell and Schwertmann, 2003) but also two other peaks, one at 531 eV, which can be attributed to the presence of hydroxyl species over the surface of the iron oxide (Aronniemi et al., 2004), originated from the addition of NH_4OH during synthesis, and one at 533 eV which indicates the presence of absorbed water molecules (Grosvenor et al., 2004b). This latter peak is absent from the calcined samples, whereas the hydroxyl one is significantly attenuated. The C *1s* core level (Figure 6.11e Figure 6.11f) show the first peak at 284 eV is associated with carbon on the surface due to the nature of the iron precursor and the dispersed phase. The peaks at 286 and 288 eV are due to oxidized carbon species C – O and COOH, respectively (Park et al., 2009). The first peak is associated with carbon residues on the iron oxide surface from the surfactant, while the second peak is due to carboxylic groups from the organometallic precursor (Chen et al., 2007).

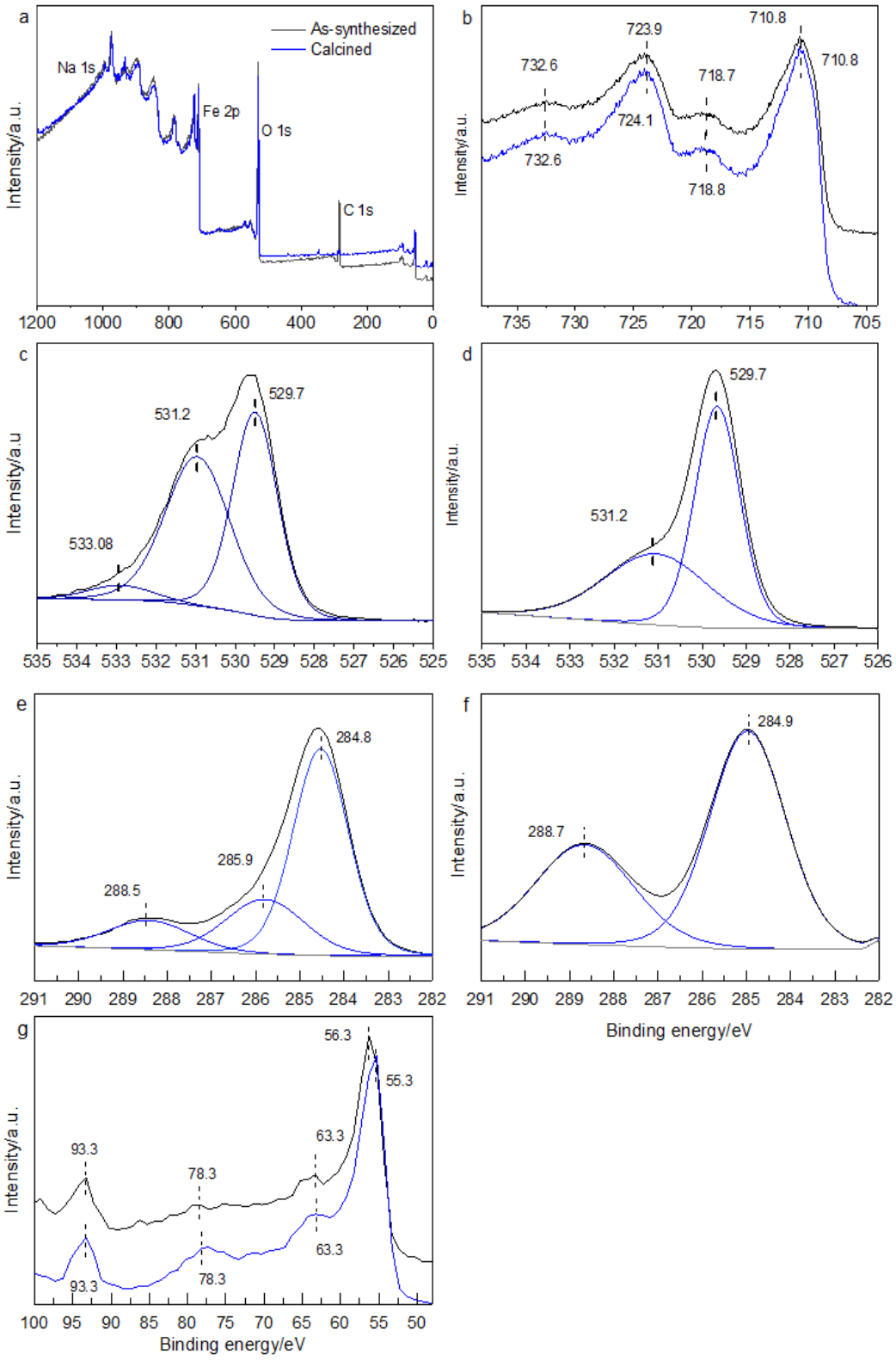

Figure 6.11 a) Global XPS analysis of the iron oxide NPs, high resolution analysis of the b) Fe *2p* region, O *1s* core level for the c) as-synthetized and d) calcined, C *1s* of the e) as-synthetized and f) calcined sample, g) Fe *3s* (93 eV) and Fe $3p_{3/2}$ (55 eV) levels.

In addition, Figure 6.12a and Figure 6.12b show the deconvoluted peaks for the Fe $2p_{3/2}$ core level of the as-synthetized and calcined samples, respectively. The deconvoluted peaks were obtained using a similar procedure as described elsewhere (Grosvenor et al., 2004a). The contribution of its shake-up satellite (718 eV) was included. The envelope (black line) was fitted with a series of peaks decreasing its intensity and constrained to similar FWHM values. In addition, a single low-intensity peak on the side of the low binding energy envelope was added, similar as reported by Grosvenor et al. (2004a) to account for the formation of Fe ions with a lower oxidation state by the production of defects in neighbouring sites (Vohs, 1998). Figure 6.12a and Figure 6.12b shows the resulting envelope (black line) fit well the spectra (dotted line) for both samples.

Table 6.3 reports the multiplet peak parameters used to fit the Fe $2p_{3/2}$ envelope for both samples. The BE of the multiplets is close to the reported values for hematite (Biesinger et al., 2011, Grosvenor et al., 2004a). The binding energy for the main peak (obtained as a percentage of area) is 710.3 eV for both samples, which is close reported BE for hematite (Grosvenor et al., 2004a, Wandelt, 1982, Asami et al., 1976). The BE of the pre-peak is not shown in

Table 6.3 as its percentage of area is almost 1 % and 3 % for the as-synthetized and calcined sample, respectively. All these features indicate both, the as-synthetized and calcined nanoparticles consist of hematite.

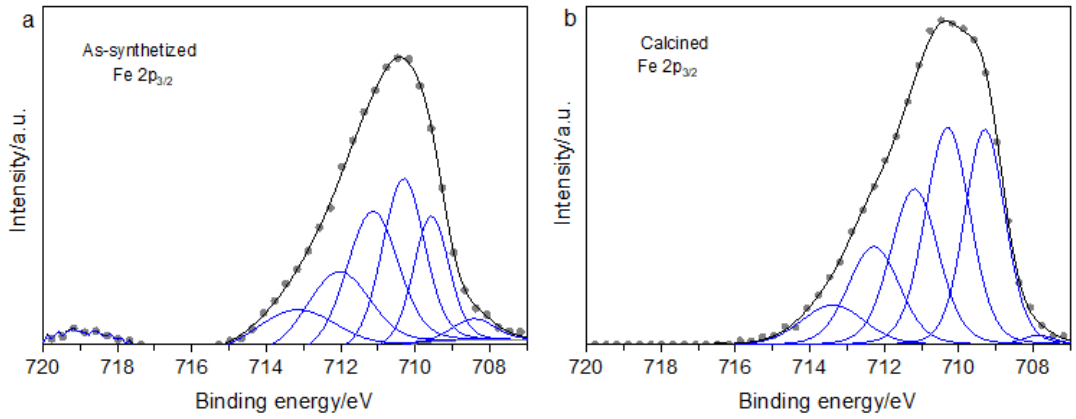

Figure 6.12 High resolution analysis of the Fe $2p_{3/2}$ core level of the a) as-synthetized and b) calcined sample.

Table 6.3 Fe $2p_{3/2}$ spectral fitting parameters: binding energy, percentage of total area, FWHM value.

peak	1	2	3	4	5
		As-synthetized			
Binding energy/eV	709.6	710.3	711.2	712.1	713.3
FWHM/eV	1.1	1.4	1.6	2.0	2.4
% total area	15.2	25.6	24.9	19.2	11.9
		Calcined			
Binding energy/eV	709.3	710.3	711.2	712.3	713.4
FWHM/eV	1.3	1.4	1.5	1.6	1.9
% total area	25.7	28.9	22.2	15.0	7.4

6.7 Productivity and manufacturing considerations of hematite NPs produced by ME

The nanoparticle productivity was calculated starting from the flow rate of the dispersed phase, the average droplet size and the area of the porous section of the membrane, which can be found in Table 6.4.

Table 6.4 Raw data to calculate the nanoparticle productivity for the semi-continuous ME setup

A_{mem}/mm^2	503	$Mw_{Fe_2O_3}$ / g mol^{-1}	159.6
$\rho_{Fe(EH)3}$/g cm^{-3}	0.91	Q_{disp}/ml min^{-1}	0.25
Mw_{Fe3+} / g mol^{-1}	55.8	V_{disp}/ml	17 ml of a 60 % v/v $Fe(EH)_3$ in hexane

For the calculations the following assumptions are made:

1) That each droplet will convert into one hematite nanoparticle.
2) There is 100 % conversion of iron to hematite, as the following reaction indicates:

$$2Fe^{3+} + 6OH^- \rightarrow Fe_2O_3 + 3H_2O \qquad 6\text{-}2$$

The mass flow rate of dispersed phase is given by the equation:

$$\dot{m}_{Fe(EH)3} = 0.6 \cdot Q_{disp} \cdot \rho_{Fe(EH)3} = 0.137 \frac{g}{min} \quad \text{6-3}$$

As the iron precursor is composed of a 6 % wt. Fe^{3+}:

$$\dot{m}_{Fe3+} = 0.06\left(\dot{m}_{Fe(EH)3}\right) = 0.008 \frac{g}{min} \quad \text{6-4}$$

Assuming there is a 100 % conversion to hematite and considering the stochiometric coefficients of the reaction (equation 6-2):

$$\dot{m}_{Fe2O3} = 0.008\ g\ Fe^{3+}\left(\frac{1\ mol\ Fe}{55.8\ g\ \ Fe^{3+}}\right)\left(\frac{1\ mol\ Fe_2O_3}{2\ mol\ Fe}\right)\left(\frac{159.6\ g\ Fe_2O_3}{1\ mol\ Fe_2O_3}\right) \quad \text{6-5}$$

$$\dot{m}_{Fe2O3} = 0.012 \frac{g}{min} = 0.7 \frac{g}{h}$$

Considering the area of the membrane, the hematite production rate is:

$$\frac{\dot{m}_{Fe2O3}}{A_{mem}} = \frac{0.7 \frac{g}{h}}{503x10^6\ m^2} = 1.4 \frac{kg}{h\ \ m^2} \quad \text{6-6}$$

The former calculations result in the production of 1.4 kg NPs per hour per square metre of membrane. The former estimation assumes no losses, fouling or agglomeration. However, assuming there will be losses associated to fouling or agglomeration and is not possible to achieve a 100 % conversion, a more conservative production rate of 1 kg of nanoparticles per hour per square metre of membrane is assume here. Nonetheless, such a value for the production rate of nanoparticle with the narrow size distribution shown would open the way to the large-scale manufacturing of nanoparticles with fine control over their properties.

Chapter 7: Synthesis of titanium dioxide using a continuous ME setup

The chapter evaluate the production of titanium dioxide nanoparticles using a ME setup fitted with a tubular aluminium oxide membrane operating in a crossflow configuration (Figure 3.2). To do so, the first objective is to assess the quality of NEs in terms of droplet size and size distribution.

Ten sections comprise the present chapter; Section 7.1 evaluate the effect of the interfacial tension force by the addition of surfactant in the continuous and the dispersed phase. Section 7.2 discusses the relation between droplet diameter and several process parameters (transmembrane pressure and crossflow velocity). The following one, Section 7.3 compares the experimental droplet size to several droplet size prediction models from the literature and evaluate the magnitude of the forces acting over a single droplet before its detachment from the membrane surface. The performance of the membrane emulsification rig is assessed using dimensionless numbers in Section 7.4 Section 7.5 estimates the fraction of active pores and droplet formation time under certain process conditions. Section 7.6 details the synthesis and crystal phase characterization of the titanium dioxide nanoparticles by TEM, Raman and XRD. Section 7.7 evaluates the incorporation of non-metal doping agents into the TiO_2 NP by FT-IR and XPS. The physicochemical sorption properties and pore parameters of the synthetized TiO_2 NP are presented in Section 7.8 , while Section 7.9 compares the material in terms of doping degree, crystal phase and band gap shift to different non-metal doped TiO_2 NP reported in the literature. Finally, 7.10 discusses the mass production rate for anatase nanoparticles using the crossflow ME setup. The content of the present chapter comprises a publication that is currently in preparation.

7.1 Interfacial tension measurements

Interfacial tension force measurements of the dispersed/continuous phase were carried out by the pendant drop method using a goniometer, as described in Section

3.3.6. Two types of surfactants were evaluated (Tween 20 and SDS) with different surfactant concentrations in the continuous phase (DI water). SFO was not used as dispersed phase in the tubular ME rig, as the former reacts with the organometallic compound, titanium (IV) 2-ethylhexanoate, needed to produce titanium oxide nanoparticles. Therefore, decane and hexane were selected as potential dispersed phases.

The IFT results in Figure 7.1 demonstrates that roughly at 1 % wt. Tween 20 in DW, the minimum IFT force has been reached, with equilibrium values close to 7.2 and 7.7 mN m^{-1} for hexane and decane, respectively. Nevertheless, for SDS a more pronounced decrease of the IFT force is observed, reaching the minimum IFT force at 0.5 % wt. SDS in DI water, with values of 3.4 and 7.7 mN m^{-1} for hexane and decane, respectively. The different behaviour of the IFT force using SDS compared to Tween 20 is due to a combined effect: the first one is that SDS molecules have higher adsorption kinetics compared to Tween 20, due to the smaller molecular weight, SDS (650 g mol^{-1}) and Tween 20 (1228 g mol^{-1}) as discussed in Section 5.3 . The second one is the existence of an electrostatic repulsion between the negative charged membrane surface (aluminium oxide) and the anionic SDS surfactant, that as soon as the surfactant molecules adsorb into the *oil/water* interface, the droplets become negatively charged and will detach from the membrane surface as soon as they are formed (Kukizaki, 2009). The results from Figure 7.1 shows the lowest IFT can be achieved with SDS as surfactant in the continuous phase and hexane was selected as dispersed phase.

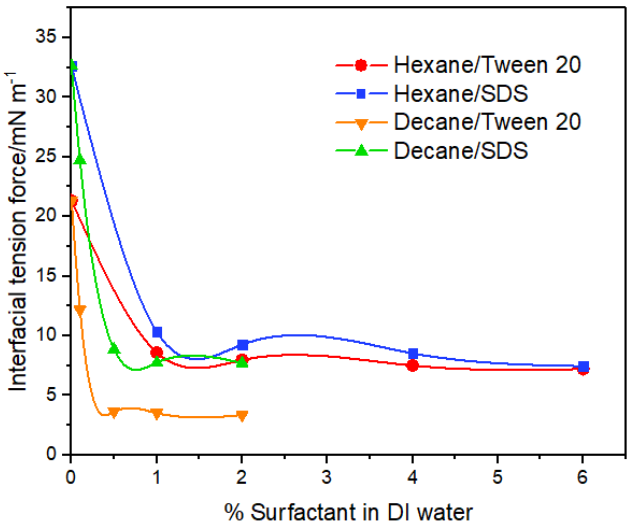

Figure 7.1 Interfacial tension measurements between the dispersed phase, either hexane or decane, and DI water (continuous phase) provided with either Tween 20 or SDS as surfactant.

Our experimental results are in good agreement with the experimental work reported by Hancocks et al. (2013) who evaluated the emulsion droplet size for different surfactant concentrations using a 1 µm SPG membrane and SDS as the surfactant. Their results indicate that the minimum droplet size was achieved for concentrations above 0.2 % wt. SDS and that above this concentration value, the droplet size is only affected by the hydrodynamic conditions of the ME rig. Nevertheless, our further experiments will be carried out using 2 % wt. SDS as optimal concentration in the continuous phase as a smaller pore size is used. In addition, when a microporous α-Al_2O_3 membrane is used, the dispersed phase droplets are generated by voids between small alumina particles (i.e. pores) in the membrane active layer. Figure 7.2a shows the full cross section of the tubular aluminium oxide membrane, while Figure 7.2b shows a closeup of the membrane active layer (δ_{active} = 65 µm). As the droplets are generated by voids, an essential requirement when using this type of membranes is to achieve a fast reduction of the IFT to avoid droplet coalescence and dispersed phase wetting over the membrane surface when adjacent droplets are growing (Wagdare et al., 2010a). To address the former problem, the incorporation of an additional surfactant in the dispersed phase, dioctyl sulfosuccinate or docusate, a compound commonly used as for chemical enhanced oil recovery (Negin et al., 2017), was evaluated to induce a faster reduction of the IFT. Docusate was evaluated as surfactant instead of Span 80, as the latter reacts with the titanium oxide precursor. The IFT results show that when 1 % wt. was added to the dispersed phase a further reduction up to 0.70 ± 0.1 mN m^{-1} was achieved.

Table 7.1 Interfacial tension force values of the system 1 % docusate in hexane/1 % SDS in DI water.

	Interfacial tension force/mN m^{-1}			
Reading number	1	2	3	Average
	0.62	0.77	0.60	0.7

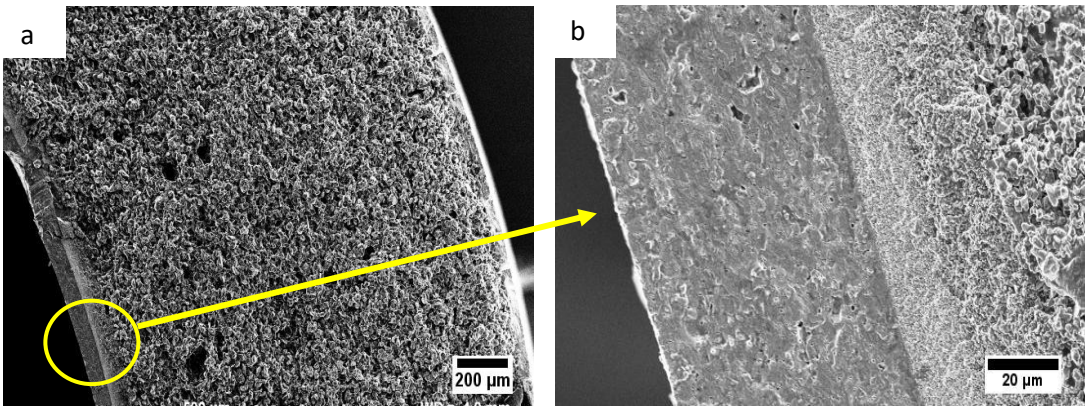

Figure 7.2 Cross section of the tubular aluminium oxide membrane b) close-up of the membrane active layer (δ_{active} = 65 µm).

7.2 Effect of transmembrane pressure

Under the former surfactant conditions (1 % docusate in hexane/1 % SDS in DI water), the calculated critical pressure is 28 kPa. Membrane emulsification experiments were carried out at two different transmembrane pressure values, which correspond to 2 and 3 times the critical pressure, respectively, for different crossflow velocities. Figure 7.3a and Figure 7.3b compares the DLS intensity curves of NEs obtained at different crossflow velocities using 56kPa and 84 kPa of transmembrane pressure, respectively. The results show a reduction in the droplet size and size distribution as the crossflow velocity is increased, due to an increase in shear stress that induces an earlier droplet detachment, as previously discussed in Section 5.3.

The average droplet size and size distribution of the former plots is in Figure 7.4a. The results show a decrease in the droplet size and size distribution as the crossflow velocity increases for both transmembrane pressures, with the sharpest decrease at the lowest shear stress, where a 52 % droplet size reduction is observed when the crossflow velocity is increased from 0.2 to 0.3 m s^{-1}. The last behaviour is a consequence of the higher shear stress produced until the droplet size becomes independent of the shear stress, a trend previously reported for a ME setup in a crossflow configuration (Katoh et al., 1996, Joscelyne and Trägårdh, 1999). In addition, a positive relation is observed between droplet size and transmembrane pressure, that results in the formation of larger droplets (Pathak, 2011). In addition, Figure 7.4b shows the ratio of the droplet size to pore size which is a common

parameter to evaluate the performance of a ME setup under specific conditions. Our results are ranging from 2.3 to 5.8, corresponding to the highest and lowest crossflow velocity, respectively. Although, reported values of the optimum ratio transmembrane pressure to capillary pressure are between 2.6 to 3.5 (Vladisavljević and Schubert, 2003), our experimental proportionality values are smaller compared to reported *c* values ranging between 4.6 to 9 for ceramic of membranes (Hancocks et al., 2013) and 2 to 10 for Shirasu porous glass (SPG) membranes (Charcosset, 2012a). A possible explanation is the additional incorporation of a surfactant in the dispersed phase that results in an earlier droplet detachment as described Section 5.2.

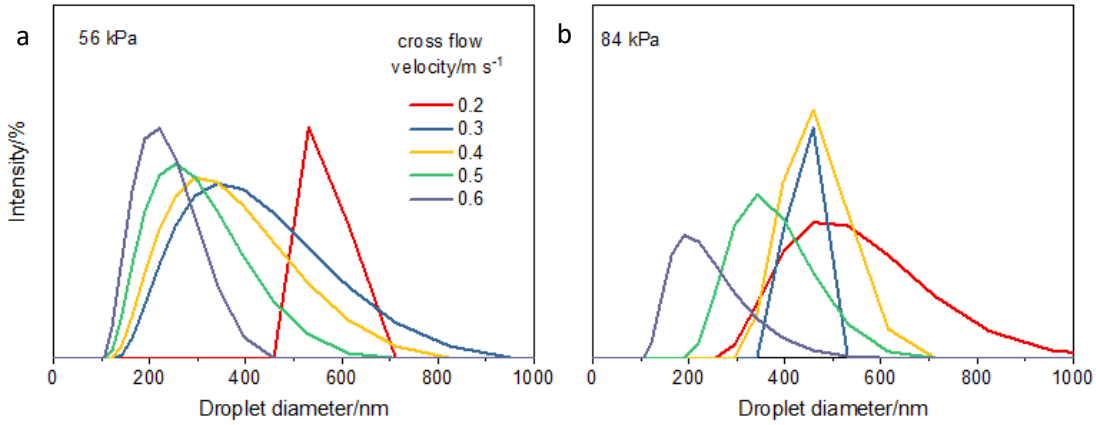

Figure 7.3 Dynamic light scattering analysis for NEs produced at a) 56 kPa and b) 84 kPa of transmembrane pressure at different crossflow velocities.

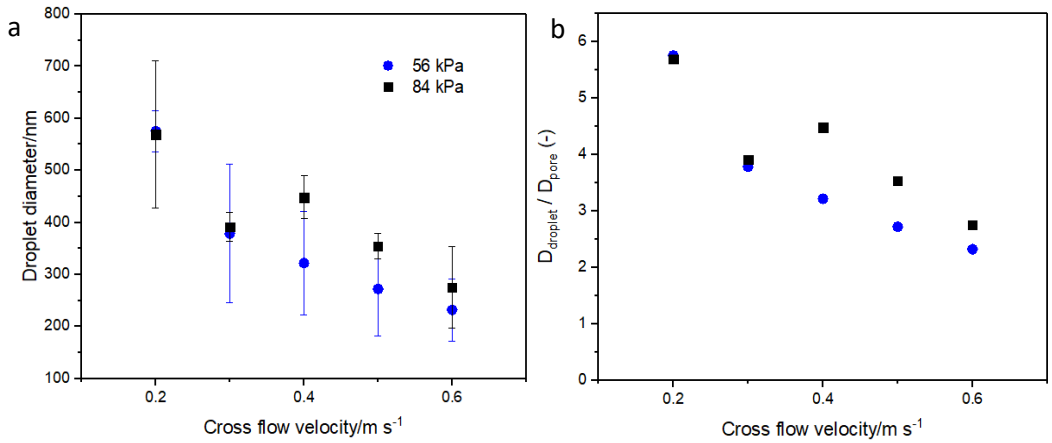

Figure 7.4 Droplet diameter against crossflow velocity and b) ratio droplet diameter to pore diameter against crossflow velocity.

7.3 Droplet formation mechanism

As discussed in Section 2.3.3 , the relative magnitude of all the forces acting over a single droplet prior its detachment determines its final size and it's possible to estimate them by calculating the shear stress from the correlation friction factor (Eq 2-12). Figure 7.5a shows the estimated magnitude of each force for all the crossflow velocities at 56 kPa. The results show there are three main forces acting over a single droplet before its detachment: interfacial tension, static pressure and drag force, while the buoyancy, dynamic lift and inertial force are several orders of magnitude smaller than the main forces. These results are in good agreement with previous reports on micrometre-scale droplets (Peng and Williams, 1998b, Matos et al., 2013). The interfacial tension force is the retaining force during droplet formation, while the main detaching forces are drag and static pressure force. The first one pushes the droplet in a parallel direction to the membrane surface, whereas the second one pushes the droplet in a perpendicular direction. Figure 7.5b shows the ratio of interfacial tension to drag force versus crossflow velocity to estimate the relative magnitude of their effects during droplet formation. The resulting curve shows that at crossflow velocities between 0.2 and 0.3 m s^{-1} the interfacial tension is almost 200 times the drag force. However, as the crossflow velocity is increased, the drag force becomes significant and a sudden decrease in their relative magnitude of both forces is observed. In addition, the positive relationship between crossflow velocity and static pressure force leads to an interplay that induces a quick droplet detachment.

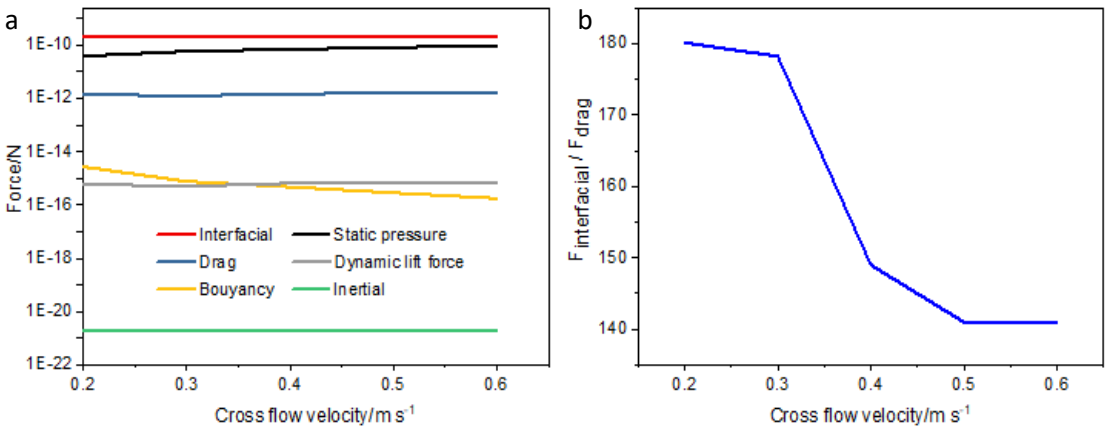

Figure 7.5 a) Estimation of the magnitude of the forces acting over a single droplet before its detachment, using the experimental droplet diameters from Figure 7.4, D_p = 100 nm, 56 kPa b) ratio of interfacial tension force to drag force at different crossflow velocities.

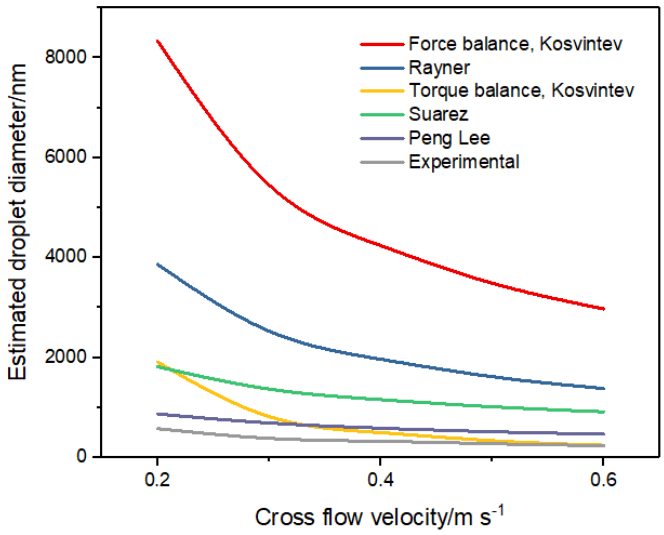

Figure 7.6 Comparison between droplet size estimations obtained from the five different models and the experimental data for a NEs prepared using a tubular ceramic membrane, D_p = 100 nm, 56 kPa.

The estimation of the magnitude of each force enabled the use of five different droplet size estimation models from the literature (Table 2.5) to estimate the droplet size and compared to experimental values for NEs obtained using a 100 nm aluminium oxide tubular membrane. Figure 7.6 compares the experimental and the estimated droplet diameters for the five models, the numerical data is reported in Table 7.2. As discussed in Section 5.7 , the force and the torque model developed by Kosvintsev et al. (2005) takes into account the interfacial tension force and the drag force, while the buoyancy and the inertial forces have been neglected. A decrease in the droplet diameter is observed as the shear stress increases, as in the experiments, but a comparison between the experimental values and the theoretical values from both models at the crossflow velocity, produces an overestimation of 1 181 % and 5 % of the droplet diameter for the force and torque balance, respectively. The model developed by Rayner and Trägårdh (2002), Table 2.5, as a force balance between the interfacial tension and the drag force also leads to an overestimation of the experimental data of 493 % for the highest shear stress. The results for the droplet size estimation model follow the trend shown in Figure 7.5b, as the model is a balance between the interfacial and drag force. Suárez et al. (2013) proposed a force balance between the static pressure force and drag force. An overestimation of 293 % for the highest crossflow velocity is obtained. The final model was developed by Lee and Mattia (2013) for crossflow ME with membrane with pores in the nanometre range. The model resulted in a 99 % overestimation of the droplet diameter at 0.6 m s^{-1}. From the five different droplet size estimation models, the torque balance from Kosvintsev

et al. (2005) resulted in almost an ideal fitting for crossflow velocities higher than 0.4 m s^{-1}. The model was developed by the assumption that the action of the shear stress produces a weekly deformed droplet and it is assumed that remains spherical. However, the small percentages of overestimation obtained is because at high shear values and the model asymptotically approaches to $D_d = 2r_p$ (Kosvintsev et al., 2005).

Table 7.2 Comparison of the experimental NEs obtained with an aluminium oxide tubular ceramic membrane (D_p = 100 nm) to current droplet size estimation models.

Crossflow velocity /m s^{-1}	Droplet diameter (nm)					
	Experimental values	Lee and Mattia (2013)	Rayner and Trägårdh (2002)	Torque balance	Force balance	Suarez et al. (2013)
				Kosvintsev et al. (2005)		
0.2	576	869	3 862	1 908	8 334	1 814
0.3	378	687	2 525	816	5 450	1 366
0.4	322	583	1 963	493	4 237	1 155
0.5	272	513	1 615	334	3 486	1 014
0.6	232	462	1 377	243	2 972	912

7.4 Bespoke NEs using dimensionless numbers

As discussed in Section 5.6 the Euler number is powerful tool to correlate the output of a ME rig, in terms of droplet size, under certain process and membrane parameters. Figure 7.7 relates the proportionality constant value to the Euler number for the tubular ceramic membranes at two different transmembrane pressures, showing a positive correlation between the Euler number and the proportionality constant. A power regression was used to fit the data for each transmembrane pressure and the equation that describes the data for each condition with their respective R^2 values can be found in Table 7.3. The correlation coefficient values are 0.99 and 0.87 for transmembrane pressures of 56 and 84 kPa, respectively. The obtained correlation coefficients for a tubular ceramic membrane (D_p = 100 nm) in a crossflow configuration are close to the obtained values for a stirred cell configuration with similar pore diameter range (Table 5.2).

Table 7.3 Euler number and correlation of the proportionality constant value for NEs produced using tubular aluminium oxide membranes at different transmembrane pressures

	56 kPa	84 kPa
$\frac{D_d}{D_p}$ =	$0.052Eu_{trans}^{0.83}$	$0.21Eu_{trans}^{0.54}$
R^2	0.98	0.76

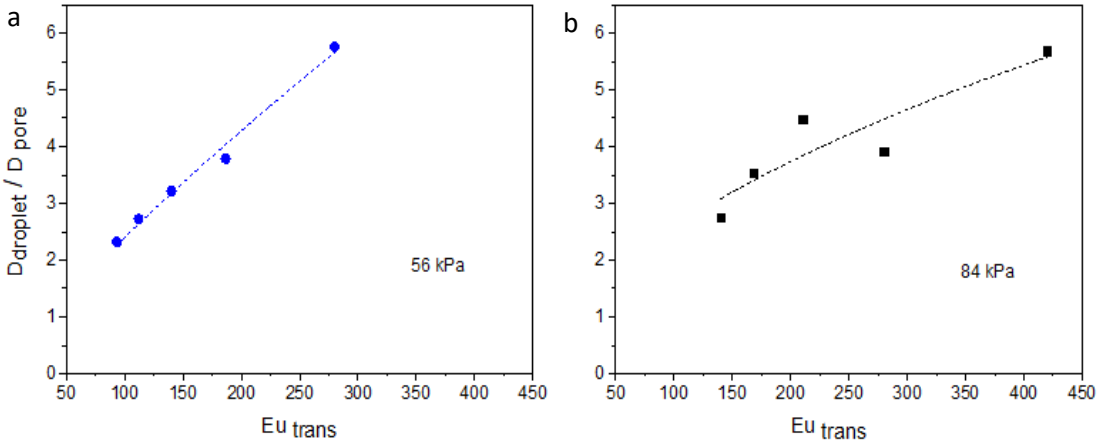

Figure 7.7 Droplet diameter to pore diameter against Euler number for NEs produced using tubular aluminium oxide membranes at a)56 kPa and b) 84 kPa.

7.5 Fraction of active pores

At industrial scale, an ideal ME rig should operate within a short production time, without compromising the quality of the emulsion. To achieve the former goal, the transmembrane pressure should be increased. However, the positive relation between the transmembrane pressure and the dispersed phase flux, results in a faster flow of dispersed phase through each pore and an increment on the fraction of active pores within the membrane. When the number of active pores increases, so does the probability of coalescence between droplets growing in adjacent pores. Therefore, several models have been developed to estimate the fraction of active pores, under certain process conditions and thus, estimate the risk of coalescence. For instance, Lepercq-Bost et al. (2010) developed a model were the fraction of active pores can be estimated by multiplying the total number of pores by the probability of

one of those pores being active, when the pores are distributed evenly in a square array. While Vladisavljevic and Schubert (2002) proposed an equation to estimate the maximum fraction of active pores in a square array, without producing droplet coalescence; both equations can be found in Table 7.4.

Table 7.4 Equations to estimate the fraction of active pores and maximum fraction of active pores

Fraction of active pores (Lepercq-Bost et al., 2008)	Maximum fraction of active pores (Vladisavljevic and Schubert, 2002)
$k_{act} = \frac{16 h_k \delta_{act} \mu_d J_d}{D_p^2 \varepsilon \Delta P}$	$k_{max} = \frac{1 \pi D_p^2}{4 \varepsilon D_d^2}$

where h_k is a constant, 4.5; δ_{act} is the membrane active layer thickness, 65 µm; 1.55 (Lepercq-Bost et al., 2008); ε is porosity, with values ranging from 0.45 to 0.55, according to the manufacturer (for the calculations, the selected value was 0.5). Table 7.5 shows the estimated values of the fraction of active pores and maximum fraction of active pores. For both transmembrane pressure along the different crossflow velocities the fraction of actives pores is below the threshold value of k_{max}. The former results demonstrate our working pressures are below the maximum working transmembrane pressure. Although, the model developed by Lepercq-Bost et al. (2010) is entirely based in a square pore arrangement, while our membranes consist of small aluminium oxide particles where the droplets are generated by the space between particles. The authors validated their data using an aluminium oxide membrane and SDS as surfactant, as they assume the fast diffusion coefficient of SDS will restrict droplet coalescence and the droplet is assumed to behave as a rigid sphere.

Schröder et al. (1998) proposed an equation to estimate the droplet formation time (t_f) from experimental data:

$$t_f = \frac{2 \varepsilon k_{act} D_d^3}{3 D_p^2 J_d} \qquad 7\text{-}1$$

In the former equation, the droplet formation time have a direct correlation with the porosity of the membrane, nevertheless this parameter is corrected with the term, fraction of active pores, as several reports demonstrate that in a ME process only a small fraction of the pores are active (Geerken et al., 2007). For instance,

Vladisavljevic and Schubert (2002) calculated that for SPG membranes, with pore diameters ranging from 0.4 to 6.6 µm, only 2 % of the pores were active when an *oil-in-water* emulsion was produced. Figure 7.8 shows the droplet formation time for 56 and 84 kPa. The values can be found in Table 7.5.

Table 7.5 Values of the estimated fraction of active pores (k_{act}), maximum fraction of active pores (k_{max}) and droplet formation time (t_f)

V_c/m s^{-1}	J_d*10^{-6}/m s^{-1}	Lepercq-Bost et al. (2008)	Vladisavljevic and Schubert (2002)	Schröder et al. (1998)
		k_{active}/-	k_{max}/-	$t_{formation}$*10^{-3}/s
0.20	8.93 (56 kPa)	0.045	0.05	29
0.30			0.12	8.2
0.40			0.17	5.0
0.50			0.24	3.0
0.60			0.32	1.9
0.20	13.4 (84 kPa)	0.045	0.05	19
0.30			0.11	6.0
0.40			0.09	9.0
0.50			0.14	4.5
0.60			0.23	2.1

Figure 7.8a and Figure 7.8b shows a decrease in the droplet formation time as the crossflow velocity increases, for the same transmembrane pressure, until reaches a plateau zone at the highest crossflow velocity. The former behaviour is due to an increment of the drag force, that induce a quicker detachment. In addition, the results show that increasing the transmembrane pressure decreases the droplet formation time, a trend in good agreement with previous reports (Abrahamse et al., 2002). The results were fitted using a power regression, the equation that describes the data can de found in Table 7.6

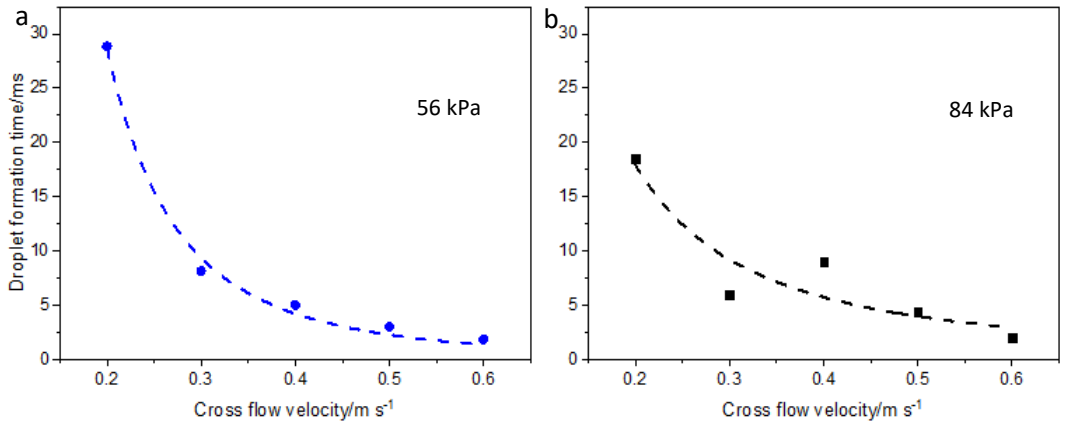

Figure 7.8 Droplet formation time against crossflow velocity for a) 56 kPa and b) 84 kPa using a tubular aluminium oxide membrane (D_p = 100 nm)

Table 7.6 Correlation of the droplet formation time and the crossflow velocity using tubular aluminium oxide membranes at different transmembrane pressures

	56 kPa	84 kPa
$t_{formation}$ =	$0.34v_c^{-2.75}$	$1.3v_c^{-1.6}$
R^2	0.98	0.67

7.6 Synthesis and characterization of titanium dioxide nanoparticles

To produce titanium dioxide nanoparticles, NEs were first produced using a tubular aluminium oxide ME setup operating in crossflow configuration. As discussed in Section 7.1 and Section 7.2 the best results were achieved using 1 % docusate in hexane/1 % SDS in DI water and crossflow velocities ranging from 0.4 to 0.6 m/s at 56 kPa of transmembrane pressure. Under the former ME conditions, titanium dioxide nanoparticles were produced using a liquid-liquid approach by dissolving in the dispersed phase an organometallic precursor, titanium (IV) 2-ethylhexanoate, $Ti(EH)_4$, prior its emulsification. The resultant NEs was collected and NH_4OH was added drop wise, with a 10 % molar excess of NH_4OH based on the stoichiometric amount of $Ti(EH)_4$ added, as described in Section 3.2.3. The reaction between $Ti(EH)_4$ and NH_4OH can be expressed as:

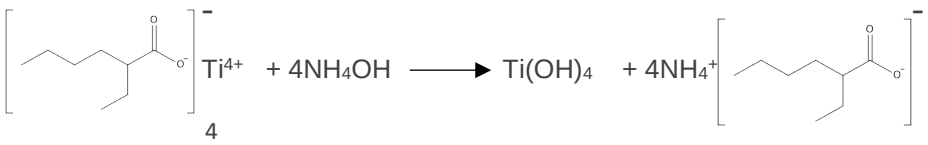

7-2

Equation 7-2 states the formation of titanium hydroxide, but its subsequent calcination produces titanium oxide by a dehydration mechanism, which is a characteristic pathway for the precipitation of titanium (Carp et al., 2004). Under this approach, TiO_2 nanoparticles were produced at three different crossflow velocities, 0.4, 0.5 and 0.6 m s^{-1} using a transmembrane pressure differential of 56 kPa and then calcined at 400 °C.

To obtain information about their size and crystal phase the calcined nanoparticles were characterized by XRD and TEM. Figure 7.9 shows the diffraction pattern for the obtained nanoparticles after calcination, which confirmed the presence of anatase as crystal phase, which is in good agreement with reported pressure-temperature phase diagrams for TiO_2, where anatase is the most stable phase up to temperatures below 600 °C at 1 atm (Dachille et al., 1968). The crystal size (D_{XRD}) of the resulting nanoparticles was calculated using the Scherrer equation:

$$D_{XRD} = \frac{K\lambda}{\beta cos\theta} \qquad 7\text{-}3$$

where K is a dimensionless factor with a value of 0.9, λ is the X-ray wavelength, 1.54×10^{-10} m, and β and θ are the line broadening at the half maximum intensity (FWHM) and Bragg angle for the most intense peak, respectively.

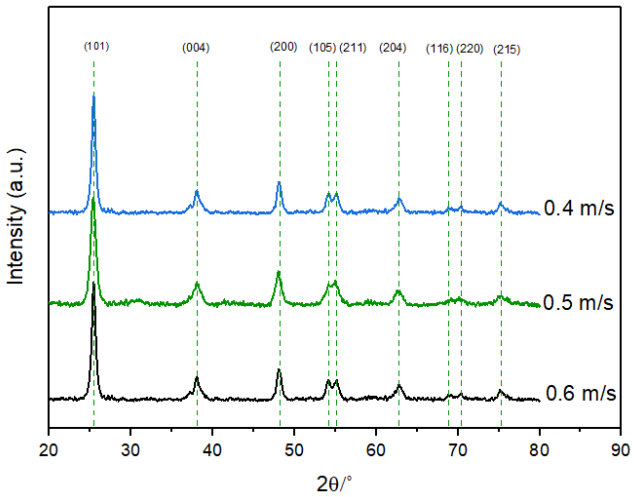

Figure 7.9 X–ray diffraction patterns of TiO_2 NPs synthetized by ME using different crossflow velocities.

The crystal size for each crossflow velocity can be found in Table 7.7. The results show a slightly decrease in crystal size as crossflow velocity increases. The last is due to a reduction of droplet size and thus the amount of reactant inside each droplet. However, only a small reduction in the particle size was achieved by varying crossflow velocity. Figure 7.10 shows several TEM micrographs for TiO_2 nanoparticles synthetized at 0.5 m s^{-1}, giving an average priamry particle size of 7.1 ± 2 nm, this sample is labelled as TiO_2 (400 °C). Nevertheless, drying and calcination of the NPs for their characterization leads to their agglomeration into clusters, with dimensions in the micrometre scale as observed in Figure 7.10a and Figure 7.11.

Table 7.7 Crystal size for TiO_2 nanoparticles estimated by Scherrer equation using the highest intensity peak from the XRD analysis, the facet (101).

Crossflow velocity/m s^{-1}	Crystal size/nm (XRD)
TiO_2 (400 °C)	
0.4	13.4
0.5	10.6
0.6	9.7
N/C-TiO_2	
0.5	11.4

In addition, non-metal doping was investigated using 0.5 m s^{-1} as crossflow velocity. The non-metal doping procedure was carried out by the addition of 8.0 g NH_4NO_3 after the emulsion formation, but prior the addition of NH_4OH as described in Section 3.2.3. The average primary crystal size using Scherrer equation for the non-metal doped nanoparticles is 11.4 nm (Table 7.7), labelled as N/C-TiO_2. Figure 7.11 shows the TEM micrographs for the N/C-TiO_2 nanoparticles with an average particle size of 12 ± 1 nm, which is in good agreement with the experimental data from XRD. An FFT analysis of the micrographs indicates the d-spacing is 0.35 nm which corresponds to the most intense peak of anatase (101) from XRD (Figure 7.9). For all the samples, TiO_2 (400 °C) and N/C-TiO_2 nanoparticles, the facet (101) is the most intense, which is the most commonly reported for nanoparticles (Shklover et al., 1997) due to its low surface energy (Lazzeri et al., 2001).

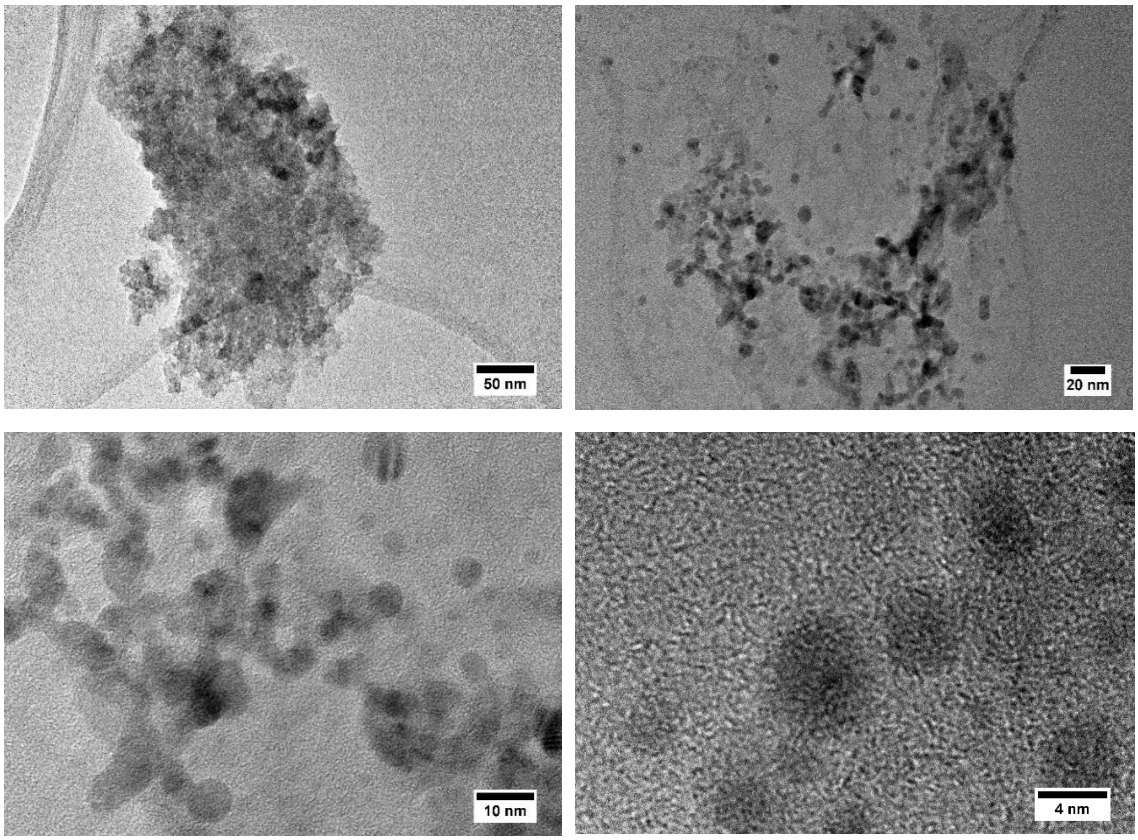

Figure 7.10 TEM micrographs for TiO_2 (400 °C) NP synthetized at 0.5 m/s as crossflow velocity.

Figure 7.12 shows the Raman spectrum of the as-synthetized TiO_2 nanoparticles and the TiO_2 NP with non-metal doping. In addition, N/C-TiO_2 NP were calcined at different temperatures to evaluate phase transition as a function of temperature. For anatase the reported Raman frequencies are 144, 197, 399, 513, 519 and 638 cm^{-1}, where the three bands at 144, 197 and 638 cm^{-1} are assigned to E_g modes (Lottici et al., 1993). The bands at 513 and 519 cm^{-1} are a doublet of the A_{g1} and B_{1g} modes. Then a weak band ~ 800 cm^{-1} is a doublet of the overtone located at 399 cm^{-1} (Balachandran and Eror, 1982). The reported Raman frequencies for rutile are 143 (B_{1g}), 447 (E_g), 612 cm^{-1} (A_{1g}), a broad band at 826 cm^{-1} (B_{2g}) and an additional band around 235 cm^{-1} which is a secondary scattering feature (Lottici et al., 1993). Titania particles were considered amorphous below 400 ˚C due to the lack of a well evolved XRD pattern, even though they provided an anatase or rutile patterns in their Raman spectra for all the calcination temperatures. For instance, in Figure 7.12 a noisy spectrum is observed for the as-synthetized TiO_2 NP and the ones calcined at 200 and 300 ˚C with distinctive Raman frequencies for both anatase and rutile. This

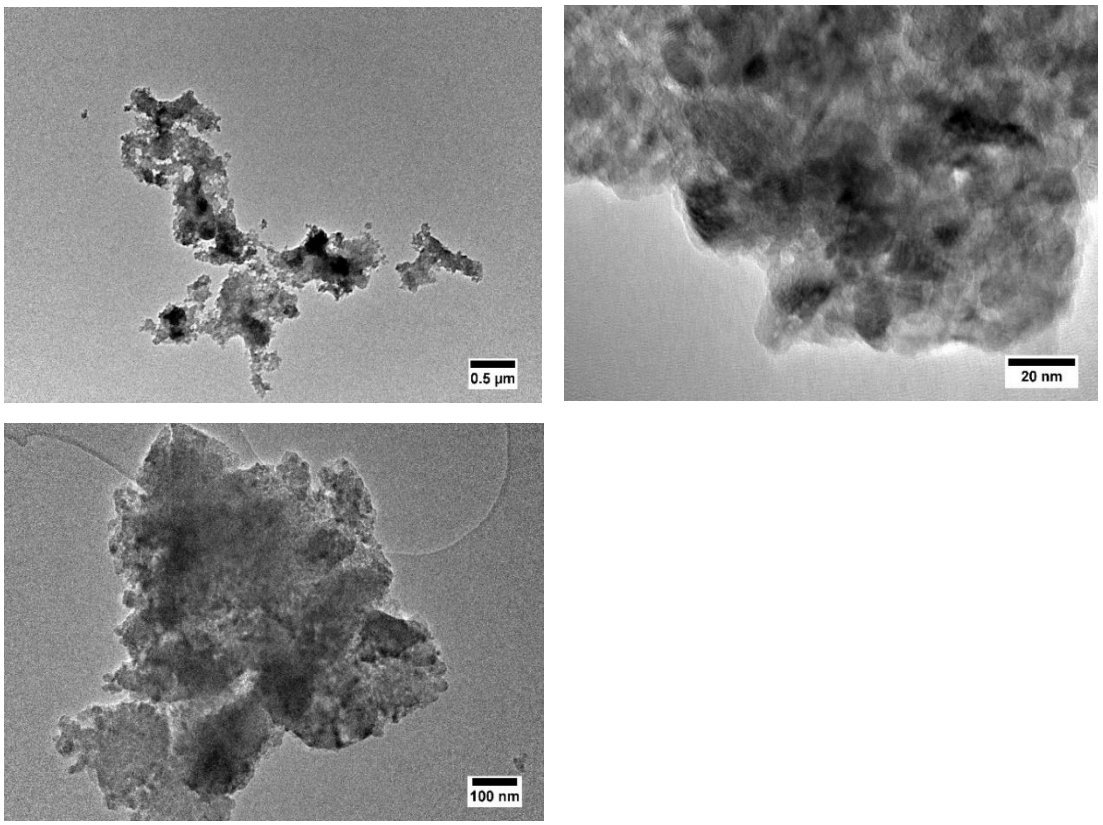

Figure 7.11 TEM micrographs for N/C-TiO_2 NPs synthetized at 0.5 m s^{-1} as crossflow velocity.

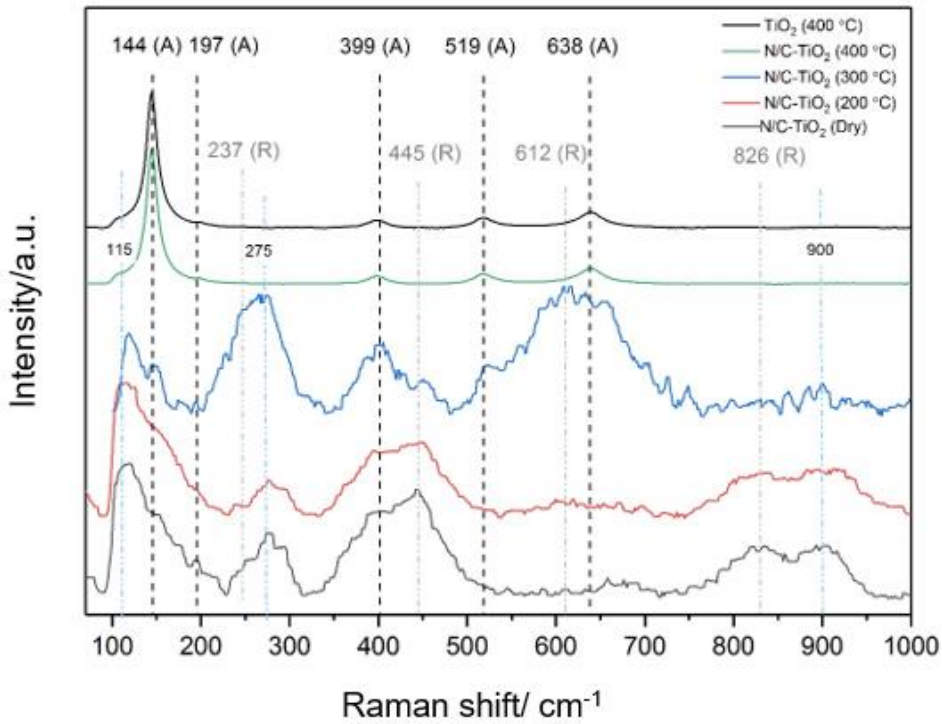

Figure 7.12 Raman spectra of TiO_2 (400 °C) and N/C-TiO_2 NPs calcined at different temperatures.

behaviour has been previously attributed to the presence of anatase- and rutile-like local structures that are interconnected with each other in the framework (Yoshitake and Abe, 2009). However, when the sample is calcined at 400 ºC with or without non-metal doping denote a well-defined spectrum with Raman frequencies corresponding to anatase.

7.7 Non-metal doping for TiO_2 nanoparticles

A FT-IR analysis was conducted to assess the incorporation of nitrogen in the TiO_2 matrix by the addition of NH_4NO_3. The nitrogen and carbon content of the TiO_2 NP was evaluated by calcining the samples at different temperatures (200, 300 and 400 °C) using a ramp of 5 °C min^{-1}. Figure 7.13 compares the FT-IR spectra of the TiO_2 and the non-metal doped TiO_2 NP calcined at different temperatures. The results for the non-metal doped TiO_2 nanoparticles (labelled as N/C-TiO_2) show a strong peak at 1383 cm^{-1} which has been attributed to the presence of nitrate groups (Wang et al., 2007). A decrease in the intensity of the former peak is observed as the calcination temperatures increases; being the calcined sample at 200 ˚C, the one with the highest nitrogen content, while only a small peak is observed for the N/C-TiO_2 calcined at 400 ˚C. The peak around 540 cm^{-1} is assigned to the stretching vibration of the Ti-O bond from the [TiO_6] octahedron (Yang and Zhou, 2007), while the distinctive peak at 1644

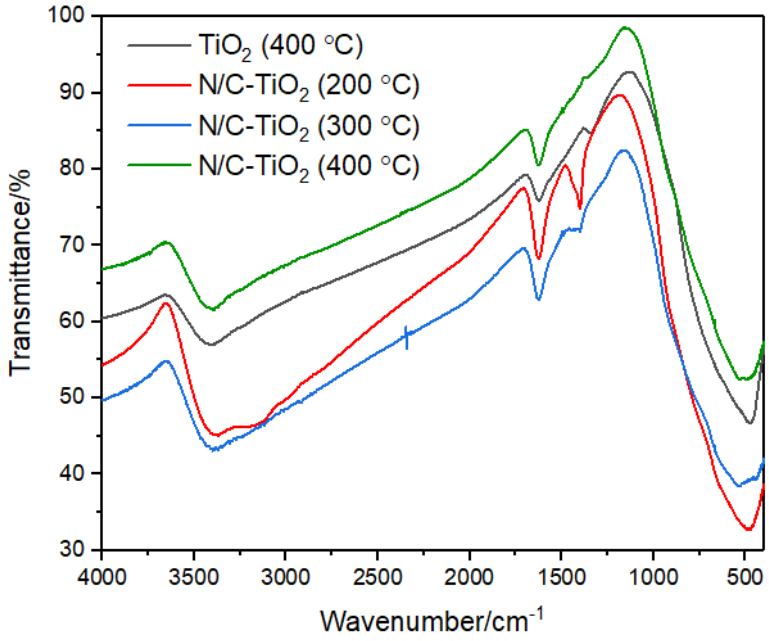

Figure 7.13 FT-IR spectra of the TiO_2 and non-metal doped TiO_2 nanoparticles calcined at different temperatures

cm^{-1}, correspond to the -OH bending vibration of absorbed water molecules.

An XPS analysis was conducted to further investigate the doping and composition of the TiO_2 (400 °C) and the N/C-TiO_2 NP. The global XPS profile for all the samples is shown in Figure 7.14a. The results show the incorporation of nitrogen and carbon within the TiO_2 matrix. Both of them, are well known non-metal doping agents (Fujishima et al., 2008). Therefore, the chemical structure of the TiO_2 samples is examined in four areas of the XPS spectrum. The first region from 280 to 292 eV corresponds to the C 1*s* core level (Figure 7.14b), a similar profile observed for the four samples with three distinctive peaks: the first one at 284 eV is associated with residual precursor on the surface of the titanium oxide (Yang et al., 2006); then a shoulder at 286 eV and a wide peak at 289 eV are due to oxidized carbon species C – O and COOH, respectively. Being the first peak associated with carbon residues on the surface of the TiO_2 from the SDS, while the second peak is due to carboxylic groups from the organometallic precursor (Park et al., 2009). However, the absence of the peak at 281.9 eV ascribed to C *1s* core level from Ti – C, which results from the substitution of O by C in the TiO_2 lattice is not observed in our experiments (Yang et al., 2008, Gu et al., 2008).

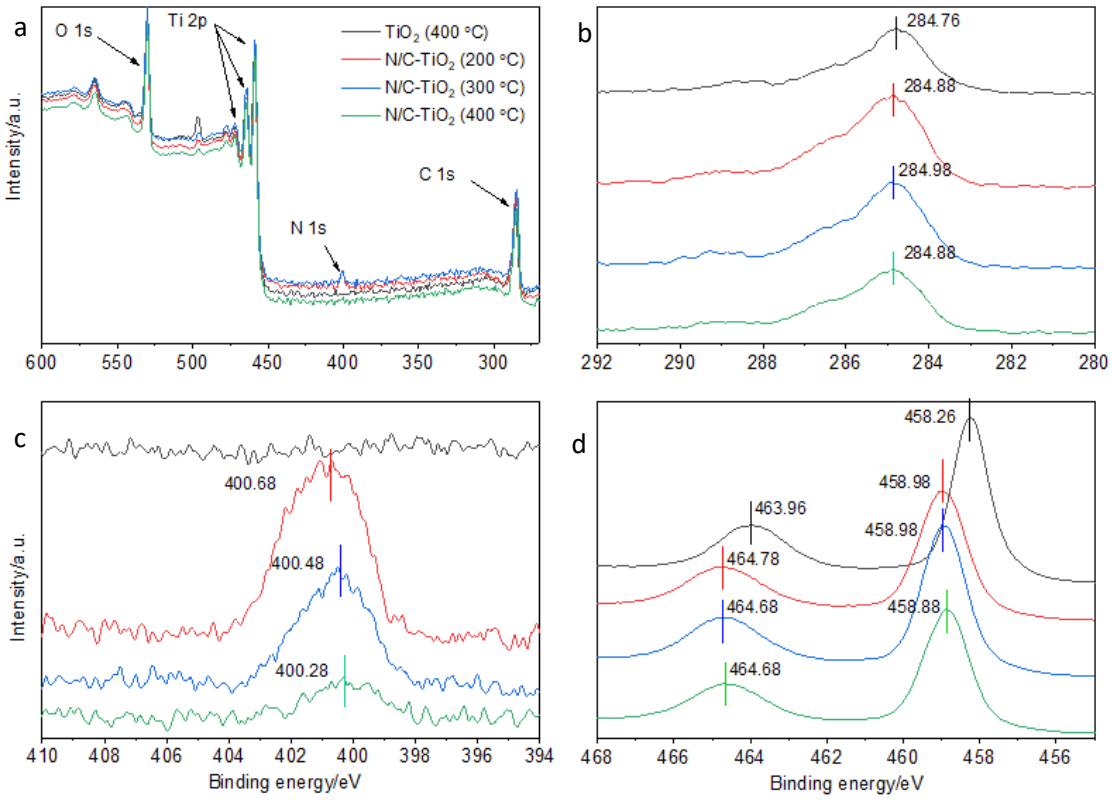

Figure 7.14 a) Global XPS analysis and core level peak of b) C *1s* c) N *1s* d) Ti *2p* of the doped and non-doped TiO_2 nanoparticles.

Figure 7.14c shows the region corresponding to the N *1s* core level for all the samples, which has a distinctive peak close to 400 eV. Reports in the literature, assign the former peak to interstitial nitrogen compounds in the form of N_xO_y (Reyes-Garcia et al., 2007), NH_x (Diwald et al., 2004) or chemisorbed N_2 (Saha and Tompkins, 1992), while a peak appearing between 396 to 397.5 is usually assigned to nitrogen substituting oxygen in the TiO_2 lattice (O-Ti-N) and the peak at 397.5 eV is ascribed to the N *1s* peak for Ti-N (Sakthivel et al., 2004). However, our experimental data in Figure 7.14c denote the presence only of interstitial nitrogen, due to the addition of NH_4NO_3 and NH_4OH during the synthesis. Figure 7.14d shows the characteristic core level peaks for Ti $2p_{3/2}$ and Ti $2p_{1/2}$ located at 464 and 458 eV, respectively. The peak separation for all the samples is 5.7 eV, which indicates titanium atoms have +4 as oxidation state (Wang et al., 2016) and confirms that nitrogen incorporation into the TiO_2 lattice is interstitial, as it didn't cause the reduction of the oxidation state of titanium to Ti^{+3} (when N substitutes a O in the TiO_2 lattice, O-Ti-N). For interstitial nitrogen it has been suggested the existence of Ti-O-N linkages, in which nitrogen species are directly bonded to an atom of oxygen in the TiO_2 lattice (Chen and Burda, 2004). From our experiments such nitrogen species can be either in the form of NO_3^- or NH_4^+, giving the distinctive peak around 400.4 eV for N *1s*. In addition, the increase of the BE for the N *1s* core level (Figure 7.14c) might be a consequence of the linkage between the N with an oxygen atom from the TiO_2 lattice. As O has a higher electronegativity cause a reduction of the electron density in the valence shell of N and leads to an increase in the BE of the electrons in the N *1s* core orbital (Lee et al., 2010). Furthermore, the results in Figure 7.14d shows a higher BE for the Ti *2p* core level is obtained for all the N/C-TiO_2 NP compared to the BE of the TiO_2 (400 °C) NP. These results suggest that the incorporation nitrogen and carbon, elements with higher electronegativity values, cause the reduction of the electron density of adjacent Ti atoms in the lattice (Lee et al., 2010)

Table 7.8 shows the concentration of nitrogen and carbon in the TiO_2 matrix, the results show an inverse correlation between calcination temperature and nitrogen content, a trend in good agreement with the results from FT-IR (Figure 7.13). The same trend is observed for carbon, which is in good agreement with previous publications (Park et al., 2009).

Table 7.8 XPS quantification of the nitrogen and carbon in the N/C-doped TiO_2 at different calcination temperatures.

Sample	Nitrogen/at. %	Carbon/at. %
TiO_2 (400 °C)	No detected	18.2
N/C-TiO_2 (200 °C)	1.29	21.8
N/C-TiO_2 (300 °C)	0.87	20.0
N/C-TiO_2 (400 °C)	0.40	18.9

Figure 7.15 shows the deconvoluted O *1s* peaks for the TiO_2 (400 °C) and the N/C-TiO_2 NP. The main peak observed around 530 eV is assigned to the regular lattice oxygen (Park et al., 2009), whereas the broad peak around 531.5 eV is assigned to absorbed water (Zhang et al., 2010). However, our experiments demonstrate a positive correlation between the magnitude of the former peak and the concentration of nitrogen in the sample, which might indicate its presence can be attributed to oxidized nitrogen species as other reports have previously suggested (Saha and

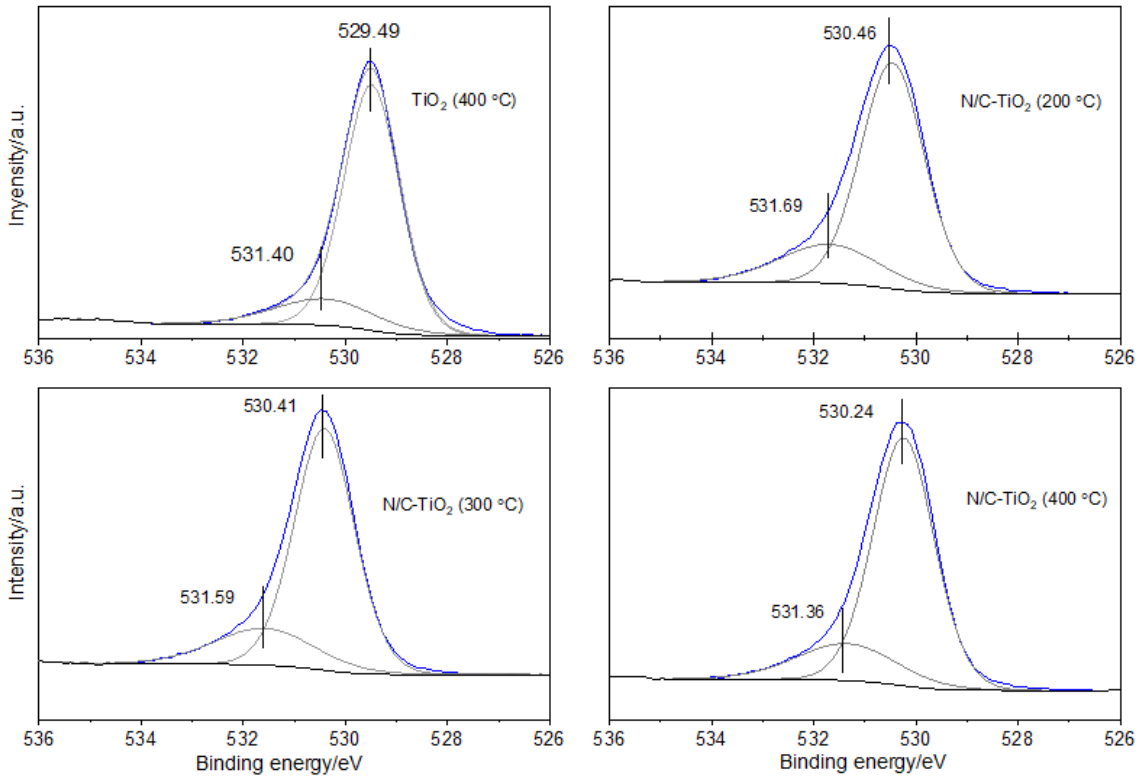

Figure 7.15 Deconvoluted O *1s* peaks for the non-doped and the N/C-doped TiO_2 nanoparticles under different calcination temperatures.

Tompkins, 1992, Chen and Burda, 2004, György et al., 2003). For the N/C-TiO_2 NP a decrease in the BE of the O 1*s* core level peak (530 eV) is observed as calcination temperature increases, which it has been attributed to the creation of oxygen vacancies due to carbon doping (Park et al., 2009). This trend is consistent with the reduction of carbon content in the sample as calcination temperature increases.

To further investigate the effect of the two non-metal doping agents, nitrogen and carbon; the optical properties of the TiO_2 NP were evaluated by diffuse reflectance UV-Vis spectroscopy and then compared to the spectrum of a commercial anatase, obtained under the same conditions (equipment, background line and day of analysis). Figure 7.16a show the UV-Vis diffuse reflectance spectra for all the samples. For the commercial sample, anatase, a sharp decrease in the absorption threshold is observed for wavelengths values above 400 nm, which indicates the lack of photocatalytic response of the commercial anatase in the visible spectrum. On the other hand, an absorption tail is observed over the region from 400 to 600 nm for the TiO_2 (400 °C) and the N/C-TiO_2 NP, which correspond to the visible light spectrum, indicating that carbon and nitrogen doping induce photocatalytic activity of TiO_2 NP in the visible spectrum. The band gap for each sample was derived from the extrapolation of the linear section in Figure 7.16a of the modified Kulbelka-Munk function against energy (Figure 7.16b). The band gap value for each sample can be found in Table 7.9. For the commercial sample the value is 3.03, which is close to the widely reported value for anatase, 3.1 eV (Carp et al., 2004).

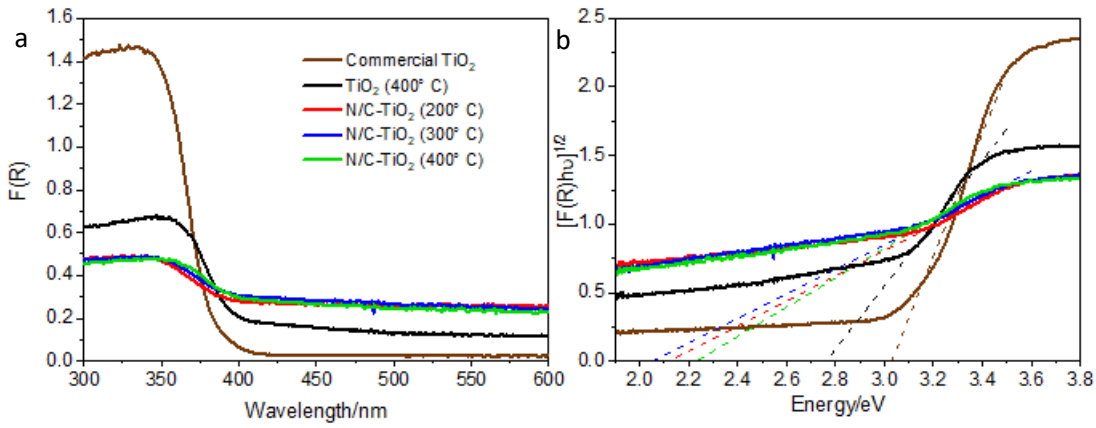

Figure 7.16 Diffuse reflectance spectra of the TiO_2 (400 °C) and N/C-TiO_2 NPs.

Table 7.9 Band gap value for a commercial anatase and for TiO_2 NP calcined at different temperatures.

Sample	Band gap/eV	Optical absorption threshold/nm
Commercial TiO_2	3.03	409
TiO_2 (400 °C)	2.76	449
N/C- TiO_2 (200 °C)	2.12	584
N/C- TiO_2 (300 °C)	2.05	604
N/C- TiO_2 (400 °C)	2.23	555

For the sample labelled as TiO_2 (400 °C) the obtained value is 2.76 eV, while the band gap for the non-metal doped samples (N/C- TiO_2) was ranging from 2.05 to 2.23 eV. The former results show a remarkably reduction in the band gap when nitrogen was added (N/C-TiO_2 NP) compared to a sample when only carbon was added, TiO_2 (400 °C), although higher concentrations of carbon are present in all the doped samples (

Table 7.8). Di Valentin et al. (2005a) carried out theoretical calculations using density functional theory (DFT) and their results show when anatase is synthesized under oxygen rich conditions a combination of interstitial and substitutional carbon (carbon that substitutes titanium in the matrix) are favoured, being the two species responsible for the band gap shift. However, their results indicate when carbon replaces titanium, no electronic states are found in the band gap and, only a small shrinking in the band gap is observed. These theoretical calculations are in good agreement with previous experimental reports (Sakthivel and Kisch, 2003), and our experimental results (Table 7.9). On the other hand, DFT calculations for nitrogen show that under oxygen rich conditions interstitial nitrogen is favoured. For this type of non-metal incorporation, nitrogen induce localized electronic states in the gap at 0.73 eV above the valence band compared to 0.14 eV for substitutional nitrogen (Di Valentin et al., 2005b). These results demonstrate that the addition of carbon and nitrogen during the synthesis improves the performance of NP under the action of visible light.

7.8 Comparison synthesis methods and band gap narrowing of TiO_2 nanoparticles.

As discussed before, non-metal doping is a commonly used strategy to improve the performance of TiO_2 NPs under the action of visible light. The first work was reported by Sato (1986), where a yellowish sample was obtained by the calcination of a

commercial titanium hydroxide sample that contained NH_4Cl impurities. The material showed a higher photocatalytic activity for the oxidation of carbon monoxide and ethane in the visible region; and since the former publication, intense efforts have been made to improve the photocatalytic performance of materials by the addition of non-metal doping agents. For instance, a common strategy is to incorporate nitrogen into the TiO_2 lattice is by the calcination of TiO_2 under a N_2 (Robben et al., 2012) or NH_3 (Irie et al., 2003b) atmosphere. For instance, Asahi et al. (2001) prepared a visible active photocatalyst by annealing a commercial TiO_2 powder at 550 ˚C in N_2 atmosphere for 4 h, their results show a higher photocatalytic activity for the degradation of methylene blue under the visible wavelength. However, the concentration of nitrogen in the TiO_2 lattice was 0.25 %. Irie et al. (2003a) reported nitrogen content can be tuned depending on the calcination temperature and achieving N incorporation up to 0.02 % when TiO_2 was calcined under a NH_3 atmosphere at 600 ˚C for 3 h. A similar approach is the oxidation of titanium nitride under an oxygen gas flow achieving nitrogen concentration up to 0.1 % (Morikawa et al., 2001).

Other non-metal elements have been studied to tune the band gap such as C, S, P, B, and F and even a combination of two non-metal elements have been explored. For instance, S-doped TiO_2 was synthetized by the oxidation of titanium disulphide (TiS_2) powder in air for the degradation under visible light of methylene blue (Umebayashi et al., 2003). Han et al. (2011) reported the fabrication of sulphur-doped TiO_2 films by a sol-gel route using sulphuric acid as a sulphur source and catalyst for the hydrolysis step for the degradation of a cyanotoxin, hepatotoxin microcystin-LR. Wu et al. (2007) synthetized carbon-doped TiO_2 microspheres by chemical vapour deposition using Titanium butoxide, $Ti(OC_4H_9)_4$, as a carbon and oxygen source. Their results show the formation of spheres varying their size from 100 nm to several micrometres depending on the gas carrier flow rate and achieving carbon concentrations up to 3 % and leading to an estimated band gap of 2.78 eV.

Although, it is difficult to compare among the different doping strategies, as each one has different synthesis conditions. It's possible to compare them from the band gap value that is achieved. Consequently, Table 7.10 gather different synthesis methods and doping metals for non-metal doping of TiO_2 NPs.

Table 7.10 Synthesis methods reported in the literature for non-metal doped TiO_2 NPs.

Synthesis method	Description	Band gap	References
	Nitrogen		
Sol-gel	3.0 g titanium isopropoxide were added dropwise to 15 ml H_2O under stirring. Addition of 4 ml HNO_3 while stirring for 1.5 h. Addition of NH_4OH until pH=9. Subsequent calcination from 250 – 650 °C for 2 h.	1.55 - 2.95	(Wang et al., 2007)
Plasma	Titanium sheets were polished then nitrogen was incorporated using a plasma nitriding furnace at 540 °C for 10 h.	2.6	(Jiang et al., 2011)
Calcination	Calcination of TiO_2 NPs at 400 °C in the presence of urea.	2.90 - 3.07	(Mitoraj and Kisch, 2010)
Calcination	Titanium NPs were produced and mixed in a tube furnace using an ammonia/argon atmosphere at temperatures ranging from 400 to 1100 °C.	2.36 - 2.97	(Zhang et al., 2009)
Microemulsion/ hydrothermal	The oil phase consisted of tetrabutyl titanate, Triton X-100 and hexanol, which are the precursor, surfactant and cosurfactant, respectively. The continuous phase was water. Triethylamine, urea and hydrazine were added as nitrogen sources when the emulsion was formed while the system was under agitation for 6 h. Then, the microemulsion was transferred into an autoclave and heated up to 120 °C for 13 h.	2.72 - 3.04	(Cong et al., 2007)

Carbon			
TiC oxidation	Annealing of TiC powder in air at 800 °C for 2 h.	2.95	(Choi et al., 2004)
Hydrothermal	Then tetra *n*-butyl ammonium hydroxide was added as a carbon source. The NP were dried and calcined at 600 °C for 3 h.	2.85	(Reddy et al., 2005)
Nitrogen/Sulphur			
Sol-gel	Titanium isopropoxide was mixed with NH_4SO_4 and slowly added to DI water and stirred. Dried at 100 °C for 24 h. Further calcination between 700 to 900 °C.	3.09 - 3.15	(Periyat et al., 2009)
Nitrogen/Carbon			
Sol-gel	0.02 mol titanium tetra *n*-butyl oxide were added dropwise to an aqueous solution of urea and tetrabutylammonium hydroxide. The solution was stirred for 24 h and then dried for 8 h at 100 °C. Finally calcined between 400 – 500 °C for 1 h.	2.95 - 3.17	(Chen et al., 2007)

7.9 Physicochemical sorption properties the titanium oxide nanoparticles

The physicochemical sorption properties and pore parameters of the TiO_2 NP were evaluated. Figure 7.17 shows the nitrogen adsorption-desorption isotherms of the TiO_2 NPs. For all the samples a Type IV isotherms are obtained according to the IUPAC classification (Sing, 1985). The sharp decline in the desorption curve in Figure 7.17a is an indicative of mesoporosity. The hysteresis formed is a H2 type, which is an indicative there is a diffusion bottle neck, due to the non-uniform pore size distribution (Venkatachalam et al., 2006).

The pore size distribution for all the samples is between 2 to 10 nm with an average pore diameter, indicating the existence of mesoporous (Figure 7.17b and Figure 7.17d). The former value was calculated from the adsorption branch of the nitrogen isotherm by the BJH method. The average pore size for each calcination temperature can be found in Table 7.11. The positive correlation between pore size and calcination temperature is consistent with reported trend in the literature (Han et al., 2011) as the data presented by BET as pore size is an accumulation of pore voids between particles (Venkatachalam et al., 2006, Gu et al., 2008). In addition, Table 7.11 compares the surface area of the TiO_2 NPs synthetized under our experimental conditions to the value of a commercially available anatase NPs. For the latter sample, the surface area is 15.8 $m^2 g^{-1}$, which is relatively low compared to the surface area of the synthetized TiO_2 NPs under our experimental conditions which values are ranging from 89.0 to 468 $m^2 g^{-1}$.

As expected, a negative correlation between the surface area and the calcination temperature is observed, due to the collapse of the pores as calcination temperature (Kim and Kwak, 2007). In addition, the results in Table 7.11 shows the surface area after calcination at 400 ˚C is 2.3 larger for the N/C-TiO_2 NP compared to the sample TiO_2 (400 °C). A possible explanation of the former behaviour is that the interstitial nitrogen helped to reduce the collapse of the porous structures due to the formation of linkages between the nitrogen and the oxygen atoms in the TiO_2 lattice, as discussed in Section 7.7 , XPS analysis. A similar trend was observed by Periyat et al. (2009) when nitrogen and sulphur were used as doping agents during the synthesis of TiO_2 NPs.

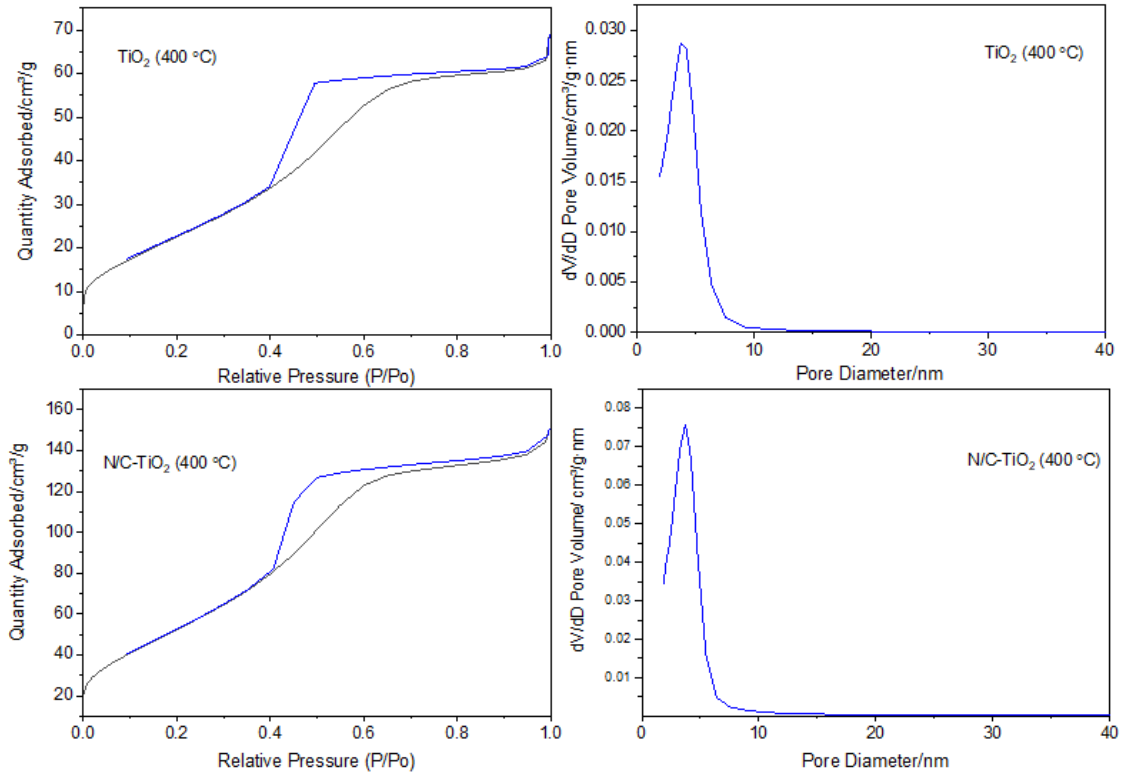

Figure 7.17 Nitrogen adsorption (—) and desorption (—) isotherms with its corresponding pore size distribution curve calculated from the adsorption branch of the nitrogen isotherm by the BJH method, for the non-doped, TIO_2 (400 °C) and the N/C-TiO_2 NPs.

Table 7.11 Psychochemical sorption properties of the non-doped and N/C-TiO_2 NP calcined at different temperatures.

Sample	Surface area/m^2 g^{-1}	Pore volume/cm^3 g^{-1}	Average pore size/nm
TiO_2 (Dry)	428.60	0.140	2.77
TiO_2 (400 ˚C)	89.11	0.102	3.40
N/C-TiO_2 (Dry)	468.25	0.168	2.91
N/C-TiO_2 (200 °C)	437.86	0.295	2.78
N/C-TiO_2 (300 °C)	351.42	0.157	3.02
N/C-TiO_2 (400 °C)	208.18	0.238	3.44
Commercial anatase	15.83	0.042	9.05

7.10 Productivity and manufacturing considerations for anatase nanoparticles produced by ME

The nanoparticle productivity was calculated starting from the flow rate of the dispersed phase, the average droplet size and the area of the membrane, which values are indicated in Table 7.12:

Table 7.12 Raw data to calculate the nanoparticle productivity for the semi-continuous ME setup.

A_{mem}/m^2	5.5x10^{-3}	Mw_{TiO2} / g mol^{-1}	79.9
$\rho_{Ti(EH)4}$ /g cm^{-3}	0.934	Q_{disp}/ml min^{-1}	6.55
$Mw_{Ti(EH)4}$ / g mol^{-1}	623.8		105 ml of a 33 % v/v $Ti(EH)_4$ in hexane
$Mw_{Ti(OH)4}$ / g mol^{-1}	115.9	V_{disp}/ml	

For the calculations the following assumptions are made:

3) That each droplet will convert into one hematite nanoparticle.
4) There is 100 % conversion of titanium precursor to titanium dioxide, as the following set of reactions indicates:

$$Ti(EH)_4 + 4NH_4OH \rightarrow Ti(OH)_4 + 4NH_4EH \quad \text{7-4}$$

$$Ti(OH)_4 \rightarrow TiO_2 + 2H_2O \quad \text{7-5}$$

The mass flow rate of the dispersed phase is given by the equation:

$$\dot{m}_{Ti(EH)4} = 0.33 \cdot Q_{disp} \cdot \rho_{Fe(EH)3} = 2.02 \frac{g}{min} \quad \text{7-6}$$

Assuming there is a 100 % conversion of the titanium precursor to TiO_2 and considering the stochiometric coefficients of the first reaction (Eq 7-4):

$$\dot{m}_{Ti(OH)4} = 2.02\ g\ Ti(EH)_4 \left(\frac{1\ mol\ Ti(EH)_4}{623.8\ g\ \ Ti(EH)_4}\right)\left(\frac{1\ mol\ Ti(OH)_4}{1\ mol\ Ti(EH)_4}\right)\left(\frac{115.9\ g\ Ti(OH)_4}{1\ mol\ Ti(OH)_4}\right) \quad \text{7-7}$$

$$\dot{m}_{Ti(OH)4} = 0.37\ \frac{g}{min}$$

The transformation of titanium hydroxide to titanium dioxide take place during the calcination (Eq 7-5) and the amount of obtained TiO_2 can be calculated by:

$$\dot{m}_{TiO2} = 0.37\ g\ Ti(OH)_4 \left(\frac{1\ mol\ Ti(OH)_4}{115.9\ g\ \ Ti(OH)_4}\right)\left(\frac{1\ mol\ TiO_2}{1\ mol\ Ti(OH)_4}\right)\left(\frac{79.9\ g\ TiO_2}{1\ mol\ TiO_2}\right) \quad 7\text{-}8$$

$$\dot{m}_{TiO2} = 0.26\ \frac{g}{min}$$

$$\frac{\dot{m}_{TiO2}}{A_{mem}} = \frac{15.5\ \frac{g}{h}}{5.5x10^{-3}\ m^2} = 2.8\ \frac{kg}{h\ \ m^2} \quad 7\text{-}9$$

The former calculations result in the production of 2.8 kg NPs per hour per square metre of membrane. However, a more conservative production rate of 2 kg of NPs can be considered based in the losses associate to fouling, agglomeration or the improbable 100 % conversion. Nonetheless, the former value indicates the potential use of a crossflow membrane emulsification setup for the large-scale production of NPs with a high control over their properties.

Conclusions

In the present PhD thesis there are several concluding remarks to highlight. It was possible to optimise the synthetises conditions to produce flat AAMs with a narrow pore size distribution. These were used to produce *oil-in-water* NEs in a dead-end stirred cell ME setup for the first time. In addition, ring-shaped AAMs were synthetized for the first time to produce *oil-in-water* NEs using a commercial stirred ME setup operating in a dead-end configuration; a systematic investigation of different process parameters showed that narrow NEs were produced. Finally, it is reported the production of hematite and titanium oxide NPs using a scalable *oil-in-water* ME setup for the first time.

The following sections summarize the key findings in each result chapter.

Synthesis of anodic alumina membranes, Chapter 4

Flat AAMs were fabricated with a narrow pore size distribution by a two-step anodization process, as this resulted in a higher pore size regularity compared to single anodization. AAMs were synthetized with anodizations potentials ranging from 20 to 80 V, with the results showing a positive correlation between pore diameter and anodization potential with a proportionality constant of 1.34 nm V^{-1}. The best synthesis conditions were achieved at 20 V using 0.50 M H_2SO_4 and 40 V using $C_2H_2O_4$ achieving pore diameters of 23 ± 2 and 58 ± 6 nm, respectively. However, anodization potentials higher than 70 V lead to the formation of pores with lower circularity and thus higher pore size distributions. Average pore growth rate and consequently membrane thickness was a function of the type of electrolyte and the anodization voltage. The data showed a positive correlation between the anodization voltage and the average pore growth. For instance, the average por growth rate for a 40 V and an 80 V AAMs were 5.7 and 13.4 µm h^{-1}, respectively.

Ring-shaped AAMs were successfully fabricated for the first time with the intention to produce NEs with a smaller coefficient of variation compared to a fully-porous membrane with the same average pore size. The membranes were synthetized using a 60 V anodization potential, which resulted in the formation of membranes with a pore diameter of 77 ± 9 nm. SEM micrographs of the transition zone between the aluminium support and the aluminium oxide porous section showed the formation of surface irregularities with an average extension of 14 ± 3 µm, compared to a membrane diameter of 41 mm. While small, the presence of this region could

nonetheless induce the formation of larger droplets or provide a contact surface for multiple droplets to coalesce.

Production of nanoemulsions using a flat AAM, Chapter 5

The flat AAMs were tested to produce *oil-in-water* NEs using a bespoke 3D printed dead-end stirred-cell ME setup. Different membrane, process and phase parameters were investigated. In ME, a critical aspect is a fast provision of surfactant during the droplet growth step, and this was achieved by the incorporation of surfactant in the dispersed phase, due to a small diffusion distance from the bulk of the dispersed phase to the *oil/water* interphase. The droplet size exhibited a negative correlation with the shear stress and droplet size distribution. The results demonstrated that the smaller the pore size, the lower the shear stress needed to achieve droplet detachment. As expected, the droplet size was proportional to the pore size (D_d/D_p) with values ranging from 1.8 to 3.5. These low proportionality values are due to the narrow pore size distribution that characterize AAMs, compared to other membranes. Five droplet size estimation models for ME were compared to experimental data. The five models led to an overestimation of the droplet size, especially at low rotational speeds. The model proposed by Lee and Mattia (2013), which, unlike the others, considers the effects of buoyancy and inertia, produced a better estimation across the entire range of rotational speeds, showing that these forces cannot be ignored at the nanoscale. Finally, it was observed that at values slightly below the threshold value of the critical capillary number, the droplet size became independent of the rotational speed.

Synthesis of hematite nanoparticles using a micropore setup, Chapter 6

It is reported for the first time the production of *oil-in-water* NEs using a commercial dead-end ME setup fitted with a ring-shaped AAM (D_p = 77 ± 9 nm). NEs were produced using 4 % Span 80 in SFO/1 % Tween 20 in DI water and under the former conditions, it was possible to achieve the formation of NEs droplets with proportionality constant values, D_d/D_p, as small as 2.8. Three droplet size estimation models were compared to experimental data, with the model developed by Lee and Mattia (2013) being the one with the smallest overestimation of the droplet size, equal to 22 %. The Euler number was used to gain an insight on the performance of the ME setup, as it relates the dispersed phase injection rate, calculated from the transmembrane pressure, to the rotational speed of the continuous phase. The results showed a highly positive linear correlation between the Euler number and the proportionality constant value (D_d/D_p).

Then, hematite NPs were synthetized using the semi-continuous ME process. The dispersed phase consisted of iron(III) 2-ethylhexanoate in 1 % docusate in hexane, while the continuous phase consisted of 1 % Tween 20 in DI water. The effect of the rotational speed over the droplet size and size distribution was evaluated. The results showed the formation of emulsions droplets as small as 206 ± 21 nm at 1000 rpm, while values of the ratio D_d/D_p were ranging from 2.8 to 6.2. The as-produced and calcined iron oxide nanoparticles were characterized by TEM, XRD, Raman and XPS. The results revealed the formation of hematite with particle size of ~4 nm for the as-synthetized sample and ~18 nm for the calcined samples. This is the first report on the production of metal oxide nanoparticles using a scalable, *oil-in-water* ME process. Based on the calculation of the nanoparticle production rate, this manufacturing method can produce up to 1.4 kg of nanoparticles per hour per metre square of membrane with a fine control of the particle size.

Synthesis of titanium oxide nanoparticles using a continuous ME setup, Chapter 7

First, *oil-in-water* NEs were produced using a 100 nm por size tubular aluminium oxide membrane operating in a crossflow ME rig. Experiments were conducted using 1 % SDS in water as continuous phase and 1 % docusate in hexane as dispersed phase. Under the former surfactant conditions, ME experiments were carried out at transmembrane pressure values of 56 kPa and 84 kPa, which corresponds to 2 and 3 times the critical pressure, respectively. The results showed a decrease in droplet size and size distribution as crossflow velocity increased for both transmembrane pressures, with the sharpest decrease at the lowest shear stress, where a 52 % droplet size reduction was observed when the crossflow velocity is increased from 0.2 to 0.3 m s^{-1}. In addition, a positive correlation was observed between droplet size and transmembrane pressure, resulting in the formation of larger droplets. Values of the ratio D_d/D_p were ranging from 2.3 to 5.8, corresponding to the highest and lowest crossflow velocity, respectively. Estimated values of the fraction of actives pores were below the threshold value of the maximum fraction of active pores, indicating that under our experimental conditions no coalescence was produced due to steric effects of droplets growing in adjacent pores. In addition, a decrease in the droplet formation time was observed as the crossflow velocity increased, for a constant transmembrane pressure. Five droplet size estimation models were compared to experimental data. The results showed the model developed by Kosvintsev et al. (2005) resulted in almost an ideal fitting for crossflow velocities higher than 0.4 m s^{-1}, with an

overestimation close to 5 %, the latter attributed to the fact that at high shear stress values the model asymptotically approaches $D_d = 2r_p$.

It is reported for the first time, the synthesis of titanium oxide NPs by producing *oil-in-water* NEs by the continuous ME setup. The dispersed phase consisted of titanium (IV) 2-ethylhexanoate and 1 % wt. dioctyl sulfosuccinate in hexane, while the continuous phase was 2 % wt. SDS in DI Water. Different crossflow velocities and transmembrane pressures were evaluated, the results showed a positive correlation between the droplet size and the pore size with proportionality constant values ranging from 2.3 to 5.8. In addition, a positive correlation was observed between dispersed phase droplet size and TiO_2 particle size, with values ranging from 9.7 to 13.4 nm. XRD, Raman and TEM experiments denote the production of anatase after calcination at 400 ºC. In addition, non-metal doping was investigated by the addition of NH_4NO_3 during the synthesis. FT-IR and XPS results demonstrated the successful incorporation of interstitial nitrogen and carbon in the TiO_2 lattice. UV-Vis experiments demonstrate that N/C-TiO_2 NP have a reduction of 1.05 eV in the band gap, which resulted in the formation of anatase nanoparticles with photocatalytic response in the visible light spectrum. BET experiments showed the surface area of the N/C-TiO_2 NP was 2.3 larger than the non-doped NP calcined at the same temperature. It was concluded that the former behaviour is due to the presence of doping agents which helped reduce the collapse of the porous structures due to the formation of linkages in the TiO_2 lattice during calcination. Based on the calculation of the NP production rate, this manufacturing method can produce up to 2.8 kg of NPs per hour per metre square of membrane.

Future work

This section will discuss several ideas to extend the present research.

Manufacturing of anodic alumina membranes by a hard anodization and production of NEs

The membranes synthetized in this PhD project were carried out by a process known as mild anodization. However, the main drawback of the former process is the extended anodization times, up to 12 h for a 40 V AAM, leading to aluminium oxide growth rates ranging from 2 to 6 μm h^{-1}. However, it is possible to overcome the former limitation by the production of AAMs by hard anodization; which is a process carried out at higher current densities and lower temperatures and achieving higher aluminium oxide growth rates, 50 - 100 μm h^{-1} (Lee et al., 2006). Although, hard anodization is not a process widely applied for the manufacturing of AAMs, as it's difficult to control structural parameters such as pore size and interpore distance (Li et al., 2008); however, there are several reports where a self-ordering porous structure by hard anodization has been achieved (Lee et al., 2006, Schwirn et al., 2008). Therefore, it is possible to assess the production of NEs; as to date there have not been experimental work on the production of NEs by AAMs synthetized by hard anodization. In addition, it is possible to assess the quality of the NEs produced by ME using AAMs synthetized by hard anodization. This would be a possible area to investigate as it is widely reported that the manufacturing of AAMs by hard anodization leads to the formation of AAMs with wider pore size distribution compared to AAMs synthetized by mild anodization. However, it might be possible to overcome the wider droplet size distribution by the addition of a second surfactant in the dispersed phase and produce NEs with a narrow droplet size distribution, similar as the results in Chapter 5.

Comparison of the droplet size distribution of NEs produced by ME using a fully porous and a ring-shaped AAMs

It would be interesting to synthesize a fully porous anodic alumina membrane to fit the commercial dead-end ME setup (Micropore LDC-1 dispersion cell) to produce NEs and compare quality of the emulsion, in terms of droplet size distribution, with

our results when the NEs were produced using a ring-shaped AAM. In addition, using the same ME setup will enable to keep constant the hydrodynamic and surfactant parameters for both experiments. This proposed future work it will be an attempt to compare the reported results by Stillwell et al. (2007) but using membranes with pores in the nanometre scale.

Development of a droplet size estimation model for NEs by ME

As discussed in Section 5.7 between the droplet size estimation models for membrane emulsification and the experimental data suggest the possible existance of an additional force that has an impact on the formation and detachment of droplets at the nanometre scale. The origin of this force might be attributed to electrostatic repulsions between the negatively charged groups on the surface of the aluminium oxide and the partially charged groups present in the surfactant structure. Although, the magnitude of electrostatic force should be negligible during the production of emulsions in the micrometre scale. This force might have a contribution when droplets in the nanometre scale are being produced. Therefore, it is possible to carry out experimental and theoretical work to investigate if electrostatic interactions between the membrane surface and the charge of the surfactants have a net contribution in droplet detachment at nanoscale, and thus develop a droplet size estimation model for NEs.

Degradation of endocrine disrupting compounds by TiO_2 and doped TiO_2 NPs

We are currently working on a research collaboration with Dr. Jannis Wenk to evaluate the photocatalytic degradation of phenol in water in a slurry reactor using the produced TiO_2 NP with and without doping agents. In addition, we will compare the photocatalytic performance of the TiO_2 NPs when the system is under the action of UV and visible light. Further lines or research might involve evaluating the incorporation of different non-metal doping agents in the TiO_2 lattice such as sulphur or evaluate the incorporation of nitrogen and sulphur by the addition of inorganic salts such as $(NH_4)_2SO_4$ to achieve a higher band gap reduction.

Removal of heavy metals using hematite and titanium oxide NPs

Adsorption is widely employed method used for the removal of heavy metals from water because is an inexpensive technology, flexible in design and operation in which is possible to achieve high-quality effluents. Recent reports suggest the utilization of nanosized materials for the removal of heavy metals due to their high surface area combined with their high adsorption capacities and selectivity (Hua et al., 2012). Among the reported nanosized adsorbents, ferric oxides, titanium oxides and cerium oxide are classified as promising materials for the removal of heavy metals from aqueous systems (Mishra et al., 1996, Van Benschoten et al., 1994, Engates and Shipley, 2011). Although, due to their small size, NPs are usually impregnated into porous supports to obtain composite materials, being polymeric beads or activated carbon widely used as supports (Pan et al., 2009). Under this approach, it is common to find reports where polymeric beads are treated to impregnate them with nanoparticles (Omi, 2001, Supsakulchai et al., 2002). However, the former synthesis methods are characterized for being time consuming methods, as it is first required the synthesis of the NPs and the polymeric beads, followed by the NP impregnation of the polymeric beads; for instance, the polymerization of the styrene is a process that take up to 12 h. However, a simpler approach was reported by Wang et al. (2012), in which they carried out the simultaneous photoinduced polymerization of styrene and reduction of a silver salt using X-rays to produce polystyrene beads doped with silver (Wang et al., 2012). In their results, they were able to produce PS particles with different sizes ranging from 125 nm to 150 nm by varying the ratio of styrene and polyvinyl pyrrolidone and the irradiation time from 30 to 300 s. Therefore, using a similar approach as the one described by Wang et al. (2012), it is possible to investigate the production of composite beads using a ME setup. The short synthesis times achieved by the authors combined with the tuneable emulsion production rate that characterize ME make them a suitable method to produce a wide variety of composite materials.

.

References

ABRAHAMSE, A., VAN LIEROP, R., VAN DER SMAN, R., VAN DER PADT, A. & BOOM, R. 2002. Analysis of droplet formation and interactions during cross-flow membrane emulsification. *Journal of membrane science,* 204**,** 125-137.

AITKEN, R. J., CHAUDHRY, M., BOXALL, A. & HULL, M. 2006. Manufacture and use of nanomaterials: current status in the UK and global trends. *Occupational medicine,* 56**,** 300-306.

ALKIRE, R. C., GOGOTSI, Y., SIMON, P. & EFTEKHARI, A. 2008. *Nanostructured materials in electrochemistry*, John Wiley & Sons.

ANTON, N., BENOIT, J.-P. & SAULNIER, P. 2008. Design and production of nanoparticles formulated from nano-emulsion templates—a review. *Journal of Controlled Release,* 128**,** 185-199.

ARONNIEMI, M., LAHTINEN, J. & HAUTOJÄRVI, P. 2004. Characterization of iron oxide thin films. *Surface and interface analysis,* 36**,** 1004-1006.

ASAHI, R. & MORIKAWA, T. 2007. Nitrogen complex species and its chemical nature in TiO 2 for visible-light sensitized photocatalysis. *Chemical Physics,* 339**,** 57-63.

ASAHI, R., MORIKAWA, T., IRIE, H. & OHWAKI, T. 2014. Nitrogen-doped titanium dioxide as visible-light-sensitive photocatalyst: designs, developments, and prospects. *Chemical reviews,* 114**,** 9824-9852.

ASAHI, R., MORIKAWA, T., OHWAKI, T., AOKI, K. & TAGA, Y. 2001. Visible-light photocatalysis in nitrogen-doped titanium oxides. *science,* 293**,** 269-271.

ASAMI, K., HASHIMOTO, K. & SHIMODAIRA, S. 1976. X-ray photoelectron spectrum of Fe2+ state in iron oxides. *Corrosion Science,* 16**,** 35-45.

BA, L. & LI, W. S. 2000. Influence of anodizing conditions on the ordered pore formation in anodic alumina. *Journal of Physics D: Applied Physics,* 33**,** 2527.

BALACHANDRAN, U. & EROR, N. 1982. Raman spectra of titanium dioxide. *Journal of Solid State Chemistry,* 42**,** 276-282.

BAUR, W. H. & KHAN, A. A. 1971. Rutile-type compounds. IV. SiO2, GeO2 and a comparison with other rutile-type structures. *Acta Crystallographica Section B: Structural Crystallography and Crystal Chemistry,* 27**,** 2133-2139.

BEROT, S., GIRAUDET, S., RIAUBLANC, A., ANTON, M. & POPINEAU, Y. 2003. Key Factors in Membrane Emulsification. *Chemical Engineering Research and Design,* 81**,** 1077-1082.

BIESINGER, M. C., PAYNE, B. P., GROSVENOR, A. P., LAU, L. W., GERSON, A. R. & SMART, R. S. C. 2011. Resolving surface chemical states in XPS analysis of first row transition metals, oxides and hydroxides: Cr, Mn, Fe, Co and Ni. *Applied Surface Science,* 257**,** 2717-2730.

BUMBRAH, G. S. & SHARMA, R. M. 2016. Raman spectroscopy – Basic principle, instrumentation and selected applications for the characterization of drugs of abuse. *Egyptian Journal of Forensic Sciences,* 6**,** 209-215.

CAI, J., MIAO, Y. Q., YU, B. Z., MA, P., LI, L. & FAN, H. M. 2017. Large-Scale, Facile Transfer of Oleic Acid-Stabilized Iron Oxide Nanoparticles to the Aqueous Phase for Biological Applications. *Langmuir,* 33**,** 1662-1669.

CAO, H., WANG, G., ZHANG, L., LIANG, Y., ZHANG, S. & ZHANG, X. 2006. Shape and Magnetic Properties of Single-Crystalline Hematite (α-Fe2O3) Nanocrystals. *ChemPhysChem,* 7**,** 1897-1901.

CARP, O., HUISMAN, C. L. & RELLER, A. 2004. Photoinduced reactivity of titanium dioxide. *Progress in solid state chemistry,* 32**,** 33-177.

CONG, Y., ZHANG, J., CHEN, F. & ANPO, M. 2007. Synthesis and characterization of nitrogen-doped TiO2 nanophotocatalyst with high visible light activity. *The Journal of Physical Chemistry C,* 111**,** 6976-6982.

CORNELL, R. M. & SCHWERTMANN, U. 2003. *The iron oxides: structure, properties, reactions, occurrences and uses*, John Wiley & Sons.

CHARCOSSET, C. 2009. Preparation of emulsions and particles by membrane emulsification for the food processing industry. *Journal of food engineering,* 92**,** 241-249.

CHARCOSSET, C. 2012a. 6 - Membranes for the preparation of emulsions and particles. *In:* CHARCOSSET, C. (ed.) *Membrane Processes in Biotechnologies and Pharmaceutics.* Amsterdam: Elsevier.

CHARCOSSET, C. 2012b. *Membrane Processes in Biotechnology and Pharmaceutics*, Elsevier.

CHARCOSSET, C., LIMAYEM, I. & FESSI, H. 2004. The membrane emulsification process—a review. *Journal of Chemical Technology & Biotechnology,* 79**,** 209-218.

CHATTERJEE, J., HAIK, Y. & CHEN, C.-J. 2003. Size dependent magnetic properties of iron oxide nanoparticles. *Journal of Magnetism and Magnetic Materials,* 257**,** 113-118.

CHEN, D., JIANG, Z., GENG, J., WANG, Q. & YANG, D. 2007. Carbon and nitrogen co-doped TiO2 with enhanced visible-light photocatalytic activity. *Industrial & Engineering Chemistry Research,* 46**,** 2741-2746.

CHEN, X. & BURDA, C. 2004. Photoelectron spectroscopic investigation of nitrogen-doped titania nanoparticles. *The Journal of Physical Chemistry B,* 108**,** 15446-15449.

CHERNYSHOVA, I., HOCHELLA JR, M. & MADDEN, A. 2007. Size-dependent structural transformations of hematite nanoparticles. 1. Phase transition. *Physical Chemistry Chemical Physics,* 9**,** 1736-1750.

CHOI, J., SAUER, G., NIELSCH, K., WEHRSPOHN, R. B. & GÖSELE, U. 2003. Hexagonally arranged monodisperse silver nanowires with adjustable diameter and high aspect ratio. *Chemistry of materials,* 15**,** 776-779.

CHOI, Y., UMEBAYASHI, T. & YOSHIKAWA, M. 2004. Fabrication and characterization of C-doped anatase TiO2 photocatalysts. *Journal of Materials Science,* 39**,** 1837-1839.

CHRISTOV, N., GANCHEV, D., VASSILEVA, N., DENKOV, N., DANOV, K. & KRALCHEVSKY, P. 2002. Capillary mechanisms in membrane emulsification: oil-in-water emulsions stabilized by Tween 20 and milk proteins. *Colloids and Surfaces A: Physicochemical and Engineering Aspects,* 209**,** 83-104.

DACHILLE, F., SIMONS, P. & ROY, R. 1968. Pressure-temperature studies of anatase, brookite, rutile and TiO2-II. *Am Mineral,* 53**,** 1929-1939.

DAMBOURNET, D., BELHAROUAK, I. & AMINE, K. 2009. Tailored preparation methods of TiO2 anatase, rutile, brookite: mechanism of formation and electrochemical properties. *Chemistry of materials,* 22**,** 1173-1179.

DAVIS, H. 1994. Factors determining emulsion type: Hydrophile—lipophile balance and beyond. *Colloids and Surfaces A: Physicochemical and Engineering Aspects,* 91**,** 9-24.

DE FARIA, D. & LOPES, F. 2007. Heated goethite and natural hematite: can Raman spectroscopy be used to differentiate them? *Vibrational Spectroscopy,* 45**,** 117-121.

DESAI, J., PATHAN, H., MIN, S.-K., JUNG, K.-D. & JOO, O. S. 2005. FT-IR, XPS and PEC characterization of spray deposited hematite thin films. *Applied Surface Science,* 252**,** 1870-1875.

DESCOSTES, M., MERCIER, F., THROMAT, N., BEAUCAIRE, C. & GAUTIER-SOYER, M. 2000. Use of XPS in the determination of chemical environment and oxidation state of iron and sulfur samples: constitution of a data basis in binding energies for Fe and S reference compounds and applications to the evidence of surface species of an oxidized pyrite in a carbonate medium. *Applied Surface Science,* 165**,** 288-302.

DI VALENTIN, C., PACCHIONI, G. & SELLONI, A. 2005a. Theory of carbon doping of titanium dioxide. *Chemistry of Materials,* 17**,** 6656-6665.

DI VALENTIN, C., PACCHIONI, G., SELLONI, A., LIVRAGHI, S. & GIAMELLO, E. 2005b. Characterization of paramagnetic species in N-doped TiO2 powders by EPR spectroscopy and DFT calculations. *The Journal of Physical Chemistry B,* 109**,** 11414-11419.

DIAMANDESCU, L., MIHAILA-TARABASANU, D., POPESCU-POGRION, N., TOTOVINA, A. & BIBICU, I. 1999. Hydrothermal synthesis and characterization of some polycrystalline α-iron oxides. *Ceramics International,* 25**,** 689-692.

DIEBOLD, U. 2003. The surface science of titanium dioxide. *Surface Science Reports,* 48**,** 53-229.

DIGGLE, J. W., DOWNIE, T. C. & GOULDING, C. 1969a. Anodic oxide films on aluminum. *Chemical Reviews,* 69**,** 365-405.

DIGGLE, J. W., DOWNIE, T. C. & GOULDING, C. W. 1969b. Anodic oxide films on aluminum. *Chemical Reviews,* 69**,** 365-405.

DIWALD, O., THOMPSON, T. L., ZUBKOV, T., GORALSKI, E. G., WALCK, S. D. & YATES, J. T. 2004. Photochemical activity of nitrogen-doped rutile TiO2 (110) in visible light. *The journal of physical chemistry B,* 108**,** 6004-6008.

DOWLING, A., CLIFT, R., GROBERT, N., HUTTON, D., OLIVER, R., O'NEILL, O., PETHICA, J., PIDGEON, N., PORRITT, J. & RYAN, J. 2004. Nanoscience and nanotechnologies: opportunities and uncertainties. Royal Society and Royal Academy of Engineering, London. UK.

DRELICH, J., FANG, C. & WHITE, C. 2002. Measurement of interfacial tension in fluid-fluid systems. *Encyclopedia of surface and colloid science,* 3**,** 3158-3163.

EBIHARA, K., TAKAHASHI, H. & NAGAYAMA, M. 1983. Structure and density of anodic oxide films formed on aluminium in oxalic acid solutions. *J. Met. Finish. Soc. Jpn,* 34**,** 548-553.

EGIDI, E., GASPARINI, G., HOLDICH, R. G., VLADISAVLJEVIĆ, G. T. & KOSVINTSEV, S. R. 2008. Membrane emulsification using membranes of regular pore spacing: Droplet size and uniformity in the presence of surface shear. *Journal of Membrane Science,* 323**,** 414-420.

ENGATES, K. E. & SHIPLEY, H. J. 2011. Adsorption of Pb, Cd, Cu, Zn, and Ni to titanium dioxide nanoparticles: effect of particle size, solid concentration, and exhaustion. *Environmental Science and Pollution Research,* 18**,** 386-395.

FIGUEROLA, A., DI CORATO, R., MANNA, L. & PELLEGRINO, T. 2010. From iron oxide nanoparticles towards advanced iron-based inorganic materials

designed for biomedical applications. *Pharmacological Research,* 62**,** 126-143.

FUJISHIMA, A. 1972. Electrochemical photolysis of water at a semiconductor electrode. *nature,* 238**,** 37-38.

FUJISHIMA, A., ZHANG, X. & TRYK, D. A. 2008. TiO 2 photocatalysis and related surface phenomena. *Surface Science Reports,* 63**,** 515-582.

FURNEAUX, R., RIGBY, W. & DAVIDSON, A. 1989. The formation of controlled-porosity membranes from anodically oxidized aluminium. *Nature,* 337**,** 147-149.

GARCIA-VERGARA, S. J., SKELDON, P., THOMPSON, G. E. & HABAZAKI, H. 2006. A flow model of porous anodic film growth on aluminium. *Electrochimica Acta,* 52**,** 681-687.

GEERKEN, M. J., LAMMERTINK, R. G. & WESSLING, M. 2007. Interfacial aspects of water drop formation at micro-engineered orifices. *Journal of colloid and interface science,* 312**,** 460-469.

GIORNO, L., LI, N. & DRIOLI, E. 2003. Preparation of oil-in-water emulsions using polyamide 10 kDa hollow fiber membrane. *Journal of membrane science,* 217**,** 173-180.

GODDEERIS, C., CUPPO, F., REYNAERS, H., BOUWMAN, W. & VAN DEN MOOTER, G. 2006. Light scattering measurements on microemulsions: estimation of droplet sizes. *International journal of pharmaceutics,* 312**,** 187-195.

GONG, J., BUTLER, W. H. & ZANGARI, G. 2010. Tailoring morphology in free-standing anodic aluminium oxide: Control of barrier layer opening down to the sub-10 nm diameter. *Nanoscale,* 2**,** 778-785.

GONG, X.-Q. & SELLONI, A. 2005. Reactivity of anatase TiO2 nanoparticles: the role of the minority (001) surface. *The Journal of Physical Chemistry B,* 109**,** 19560-19562.

GROSVENOR, A., KOBE, B., BIESINGER, M. & MCINTYRE, N. 2004a. Investigation of multiplet splitting of Fe 2p XPS spectra and bonding in iron compounds. *Surface and Interface Analysis,* 36**,** 1564-1574.

GROSVENOR, A., KOBE, B. & MCINTYRE, N. 2004b. Studies of the oxidation of iron by water vapour using X-ray photoelectron spectroscopy and QUASES™. *Surface Science,* 572**,** 217-227.

GU, D.-E., LU, Y. & YANG, B.-C. 2008. Facile preparation of micro–mesoporous carbon-doped TiO 2 photocatalysts with anatase crystalline walls under template-free condition. *Chemical Communications***,** 2453-2455.

GUO, H. & BARNARD, A. S. 2011. Thermodynamic modelling of nanomorphologies of hematite and goethite. *Journal of Materials Chemistry,* 21**,** 11566-11577.

GUPTA, S. M. & TRIPATHI, M. 2011. A review of TiO2 nanoparticles. *Chinese Science Bulletin,* 56**,** 1639.

GYÖRGY, E., DEL PINO, A. P., SERRA, P. & MORENZA, J. 2003. Depth profiling characterisation of the surface layer obtained by pulsed Nd: YAG laser irradiation of titanium in nitrogen. *Surface and Coatings Technology,* 173**,** 265-270.

HAN, C., PELAEZ, M., LIKODIMOS, V., KONTOS, A. G., FALARAS, P., O'SHEA, K. & DIONYSIOU, D. D. 2011. Innovative visible light-activated sulfur doped TiO2 films for water treatment. *Applied Catalysis B: Environmental,* 107**,** 77-87.

HANCOCKS, R., SPYROPOULOS, F. & NORTON, I. 2013. Comparisons between membranes for use in cross flow membrane emulsification. *Journal of Food Engineering,* 116**,** 382-389.

HENDREN, C. O., MESNARD, X., DRÖGE, J. & WIESNER, M. R. 2011. Estimating production data for five engineered nanomaterials as a basis for exposure assessment. ACS Publications.

HOAR, T. P. & MOTT, N. F. 1959. A mechanism for the formation of porous anodic oxide films on aluminium. *Journal of Physics and Chemistry of Solids,* 9**,** 97-99.

HUA, M., ZHANG, S., PAN, B., ZHANG, W., LV, L. & ZHANG, Q. 2012. Heavy metal removal from water/wastewater by nanosized metal oxides: a review. *Journal of hazardous materials,* 211**,** 317-331.

HYEON, T. 2003. Chemical synthesis of magnetic nanoparticles. *Chemical Communications***,** 927-934.

IRIE, H., WATANABE, Y. & HASHIMOTO, K. 2003a. Nitrogen-concentration dependence on photocatalytic activity of TiO2-x N x powders. *The Journal of Physical Chemistry B,* 107**,** 5483-5486.

IRIE, H., WATANABE, Y. & HASHIMOTO, K. 2003b. Nitrogen-Concentration Dependence on Photocatalytic Activity of TiO2-xNx Powders. *The Journal of Physical Chemistry B,* 107**,** 5483-5486.

JANSSENS, T. V., CLAUSEN, B. S., HVOLBÆK, B., FALSIG, H., CHRISTENSEN, C. H., BLIGAARD, T. & NØRSKOV, J. K. 2007. Insights into the reactivity of supported Au nanoparticles: combining theory and experiments. *Topics in Catalysis,* 44**,** 15-26.

JESSENSKY, O., MÜLLER, F. & GÖSELE, U. 1998. Self-organized formation of hexagonal pore arrays in anodic alumina. *Applied Physics Letters,* 72**,** 1173-1175.

JIANG, X., WANG, Y. & PAN, C. 2011. High Concentration Substitutional N-Doped TiO2 Film: Preparation, Characterization, and Photocatalytic Property. *Journal of the American Ceramic Society,* 94**,** 4078-4083.

JOSCELYNE, S. M. & TRÄGÅRDH, G. 1999. Food emulsions using membrane emulsification: conditions for producing small droplets. *Journal of Food Engineering,* 39**,** 59-64.

KALBACOVA, M., MACAK, J., SCHMIDT-STEIN, F., MIERKE, C. & SCHMUKI, P. 2008. TiO2 nanotubes: photocatalyst for cancer cell killing. *physica status solidi (RRL)–Rapid Research Letters,* 2**,** 194-196.

KATOH, R., ASANO, Y., FURUYA, A., SOTOYAMA, K. & TOMITA, M. 1996. Preparation of food emulsions using a membrane emulsification system. *Journal of Membrane Science,* 113**,** 131-135.

KAZUHITO, H., HIROSHI, I. & AKIRA, F. 2005. TiO 2 Photocatalysis: A Historical Overview and Future Prospects. *Japanese Journal of Applied Physics,* 44**,** 8269.

KEH, H. J. & CHEN, P. Y. 2001. Slow motion of a droplet between two parallel plane walls. *Chemical Engineering Science,* 56**,** 6863-6871.

KELLER, F., HUNTER, M. & ROBINSON, D. 1953. Structural features of oxide coatings on aluminum. *Journal of the Electrochemical Society,* 100**,** 411-419.

KIM, D., LEE, N., PARK, M., KIM, B. H., AN, K. & HYEON, T. 2009. Synthesis of Uniform Ferrimagnetic Magnetite Nanocubes. *Journal of the American Chemical Society,* 131**,** 454-455.

KIM, D. S. & KWAK, S.-Y. 2007. The hydrothermal synthesis of mesoporous TiO2 with high crystallinity, thermal stability, large surface area, and enhanced photocatalytic activity. *Applied Catalysis A: General,* 323**,** 110-118.

KOROLEVA, M. Y. & YURTOV, E. V. 2012. Nanoemulsions: the properties, methods of preparation and promising applications. *Russian Chemical Reviews,* 81**,** 21-43.

KOSVINTSEV, S. R., GASPARINI, G., HOLDICH, R. G., CUMMING, I. W. & STILLWELL, M. T. 2005. Liquid-liquid membrane dispersion in a stirred cell with and without controlled shear. *Industrial & engineering chemistry research,* 44**,** 9323-9330.

KUKIZAKI, M. 2009. Shirasu porous glass (SPG) membrane emulsification in the absence of shear flow at the membrane surface: Influence of surfactant type

and concentration, viscosities of dispersed and continuous phases, and transmembrane pressure. *Journal of Membrane Science,* 327**,** 234-243.

KWAN, W. P. & VOELKER, B. M. 2003. Rates of hydroxyl radical generation and organic compound oxidation in mineral-catalyzed Fenton-like systems. *Environmental science & technology,* 37**,** 1150-1158.

LAN, Y., LU, Y. & REN, Z. 2013. Mini review on photocatalysis of titanium dioxide nanoparticles and their solar applications. *Nano Energy,* 2**,** 1031-1045.

LAZZERI, M., VITTADINI, A. & SELLONI, A. 2001. Structure and energetics of stoichiometric TiO 2 anatase surfaces. *Physical Review B,* 63**,** 155409.

LEE, K. P., LEESE, H. & MATTIA, D. 2012. Water flow enhancement in hydrophilic nanochannels. *Nanoscale,* 4**,** 2621-2627.

LEE, K. P. & MATTIA, D. 2013. Manufacturing of Nanoemulsions Using Nanoporous Anodized Alumina Membranes: Experimental Investigation and Process Modeling. *Industrial & Engineering Chemistry Research,* 52**,** 14866-14874.

LEE, M. S., PARK, S. S., LEE, G.-D., JU, C.-S. & HONG, S.-S. 2005. Synthesis of TiO 2 particles by reverse microemulsion method using nonionic surfactants with different hydrophilic and hydrophobic group and their photocatalytic activity. *Catalysis Today,* 101**,** 283-290.

LEE, S., CHO, I.-S., LEE, D. K., KIM, D. W., NOH, T. H., KWAK, C. H., PARK, S., HONG, K. S., LEE, J.-K. & JUNG, H. S. 2010. Influence of nitrogen chemical states on photocatalytic activities of nitrogen-doped TiO 2 nanoparticles under visible light. *Journal of Photochemistry and Photobiology A: Chemistry,* 213**,** 129-135.

LEE, W., JI, R., GÖSELE, U. & NIELSCH, K. 2006. Fast fabrication of long-range ordered porous alumina membranes by hard anodization. *Nature materials,* 5**,** 741-747.

LEPERCQ-BOST, É., GIORGI, M.-L., ISAMBERT, A. & ARNAUD, C. 2008. Use of the capillary number for the prediction of droplet size in membrane emulsification. *Journal of membrane science,* 314**,** 76-89.

LEPERCQ-BOST, É., GIORGI, M.-L., ISAMBERT, A. & ARNAUD, C. 2010. Estimating the risk of coalescence in membrane emulsification. *Journal of Membrane Science,* 357**,** 36-46.

LI, A., MÜLLER, F., BIRNER, A., NIELSCH, K. & GÖSELE, U. 1998a. Hexagonal pore arrays with a 50–420 nm interpore distance formed by self-organization in anodic alumina. *Journal of Applied Physics,* 84**,** 6023-6026.

LI, F., ZHANG, L. & METZGER, R. M. 1998b. On the growth of highly ordered pores in anodized aluminum oxide. *Chemistry of materials,* 10**,** 2470-2480.

LI, Y., LING, Z., CHEN, S. & WANG, J. 2008. Fabrication of novel porous anodic alumina membranes by two-step hard anodization. *Nanotechnology,* 19**,** 225604.

LIAO, X., ZHU, J., ZHONG, W. & CHEN, H.-Y. 2001. Synthesis of amorphous Fe 2 O 3 nanoparticles by microwave irradiation. *Materials Letters,* 50**,** 341-346.

LILLO, M. & LOSIC, D. 2009. Pore opening detection for controlled dissolution of barrier oxide layer and fabrication of nanoporous alumina with through-hole morphology. *Journal of Membrane Science,* 327**,** 11-17.

LIN, H.-F., LIAO, S.-C. & HUNG, S.-W. 2005. The dc thermal plasma synthesis of ZnO nanoparticles for visible-light photocatalyst. *Journal of photochemistry and photobiology A: Chemistry,* 174**,** 82-87.

LINSEBIGLER, A. L., LU, G. & YATES JR, J. T. 1995. Photocatalysis on TiO2 surfaces: principles, mechanisms, and selected results. *Chemical reviews,* 95**,** 735-758.

LOHBAUER, U., WAGNER, A., BELLI, R., STOETZEL, C., HILPERT, A., KURLAND, H.-D., GRABOW, J. & MÜLLER, F. A. 2010. Zirconia nanoparticles prepared by laser vaporization as fillers for dental adhesives. *Acta Biomaterialia,* 6**,** 4539-4546.

LOTTICI, P., BERSANI, D., BRAGHINI, M. & MONTENERO, A. 1993. Raman scattering characterization of gel-derived titania glass. *Journal of materials science,* 28**,** 177-183.

MAJEWSKI, P. & THIERRY, B. 2007. Functionalized magnetite nanoparticles—synthesis, properties, and bio-applications. *Critical Reviews in Solid State and Materials Sciences,* 32**,** 203-215.

MASUDA, H. & FUKUDA, K. 1995. Ordered metal nanohole arrays made by a two-step replication of honeycomb structures of anodic alumina. *Science,* 268**,** 1466-1468.

MATOS, M., SUÁREZ, M., GUTIÉRREZ, G., COCA, J. & PAZOS, C. 2013. Emulsification with microfiltration ceramic membranes: A different approach to droplet formation mechanism. *Journal of Membrane Science,* 444**,** 345-358.

MCCLEMENTS, D. J. 2011. Edible nanoemulsions: fabrication, properties, and functional performance. *Soft Matter,* 7**,** 2297-2316.

MCCLEMENTS, D. J. 2012. Nanoemulsions versus microemulsions: terminology, differences, and similarities. *Soft Matter,* 8**,** 1719-1729.

MINE, Y., SHIMIZU, M. & NAKASHIMA, T. 1996. Preparation and stabilization of simple and multiple emulsions using a microporous glass membrane. *Colloids and Surfaces B: Biointerfaces,* 6**,** 261-268.

MISHRA, S. P., SINGH, V. K. & TIWARI, D. 1996. Radiotracer technique in adsorption study: Part XIV. Efficient removal of mercury from aqueous solutions by hydrous zirconium oxide. *Applied Radiation and Isotopes,* 47**,** 15-21.

MITORAJ, D. & KISCH, H. 2010. On the Mechanism of Urea-Induced Titania Modification. *Chemistry-A European Journal,* 16**,** 261-269.

MONTERO-MORENO, J. M., SARRET, M. & MÜLLER, C. 2007. Influence of the aluminum surface on the final results of a two-step anodizing. *Surface and Coatings Technology,* 201**,** 6352-6357.

MORIKAWA, T., ASAHI, R., OHWAKI, T., AOKI, K. & TAGA, Y. 2001. Band-gap narrowing of titanium dioxide by nitrogen doping. *Japanese Journal of Applied Physics,* 40**,** L561.

MOUSAVICHOUBEH, M., SHARIATY-NIASSAR, M. & GHADIRI, M. 2011. The effect of interfacial tension on secondary drop formation in electro-coalescence of water droplets in oil. *Chemical Engineering Science,* 66**,** 5330-5337.

MUNOZ, M., DE PEDRO, Z. M., CASAS, J. A. & RODRIGUEZ, J. J. 2015. Preparation of magnetite-based catalysts and their application in heterogeneous Fenton oxidation–a review. *Applied Catalysis B: Environmental,* 176**,** 249-265.

NAGATA, S. 1975. *Mixing: principles and applications*, Halsted Press.

NAKANO, Y., MORIKAWA, T., OHWAKI, T. & TAGA, Y. 2005. Deep-level optical spectroscopy investigation of N-doped TiO 2 films. *Applied Physics Letters,* 86**,** 132104.

NAKASHIMA, T., SHIMIZU, M. & KUKIZAKI, M. 1994. Monodisperse single and double emulsions and method of producing same. Google Patents.

NASIRPOURI, F., ABDOLLAHZADEH, M., ALMASI, M. & PARVINI-AHMADI, N. 2009. A comparison between self-ordering of nanopores in aluminium oxide films achieved by two-and three-step anodic oxidation. *Current Applied Physics,* 9**,** S91-S94.

NEGIN, C., ALI, S. & XIE, Q. 2017. Most common surfactants employed in chemical enhanced oil recovery. *Petroleum,* 3**,** 197-211.

NI, M., LEUNG, M. K., LEUNG, D. Y. & SUMATHY, K. 2007. A review and recent developments in photocatalytic water-splitting using TiO2 for hydrogen production. *Renewable and Sustainable Energy Reviews,* 11**,** 401-425.

NIELSCH, K., CHOI, J., SCHWIRN, K., WEHRSPOHN, R. B. & GÖSELE, U. 2002. Self-ordering regimes of porous alumina: the 10 porosity rule. *Nano letters,* 2**,** 677-680.

O'SULLIVAN, J. & WOOD, G. 1970. The morphology and mechanism of formation of porous anodic films on aluminium. *Proceedings of the Royal Society of London. A. Mathematical and Physical Sciences,* 317**,** 511-543.

OKOLI, C., SANCHEZ-DOMINGUEZ, M., BOUTONNET, M., JÄRÅS, S., CIVERA, C. N., SOLANS, C. & KUTTUVA, G. R. 2012. Comparison and functionalization study of microemulsion-prepared magnetic iron oxide nanoparticles. *Langmuir,* 28**,** 8479-8485.

OMI, A. K., Y. SHIMAMORI, A. SUPSAKULCHAI, M. NAGAI, G.-H. MA, S 2001. Magnetite (Fe 3 O 4) microcapsules prepared using a glass membrane and solvent removal. *Journal of microencapsulation,* 18**,** 749-765.

ONO, S., SAITO, M. & ASOH, H. 2004a. Self-ordering of anodic porous alumina induced by local current concentration: Burning. *Electrochemical and solid-state letters,* 7**,** B21-B24.

ONO, S., SAITO, M., ISHIGURO, M. & ASOH, H. 2004b. Controlling factor of self-ordering of anodic porous alumina. *Journal of The Electrochemical Society,* 151**,** B473-B478.

PALIBRODA, E. 1995. Aluminum porous oxide growth—II. On the rate determining step. *Electrochimica acta,* 40**,** 1051-1055.

PAN, B., PAN, B., ZHANG, W., LV, L., ZHANG, Q. & ZHENG, S. 2009. Development of polymeric and polymer-based hybrid adsorbents for pollutants removal from waters. *Chemical Engineering Journal,* 151**,** 19-29.

PARAMASIVAM, I., JHA, H., LIU, N. & SCHMUKI, P. 2012. A Review of Photocatalysis using Self-organized TiO2 Nanotubes and Other Ordered Oxide Nanostructures. *Small,* 8**,** 3073-3103.

PARK, Y., KIM, W., PARK, H., TACHIKAWA, T., MAJIMA, T. & CHOI, W. 2009. Carbon-doped TiO 2 photocatalyst synthesized without using an external carbon precursor and the visible light activity. *Applied Catalysis B: Environmental,* 91**,** 355-361.

PARKINSON, G. S. 2016. Iron oxide surfaces. *Surface Science Reports,* 71**,** 272-365.

PATERMARAKIS, G. 2009. The origin of nucleation and development of porous nanostructure of anodic alumina films. *Journal of Electroanalytical Chemistry,* 635**,** 39-50.

PATHAK, M. 2011. Numerical simulation of membrane emulsification: Effect of flow properties in the transition from dripping to jetting. *Journal of Membrane Science,* 382**,** 166-176.

PEMARTIN, K., SOLANS, C., VIDAL-LOPEZ, G. & SANCHEZ-DOMINGUEZ, M. 2012. Synthesis of ZnO and ZnO2 nanoparticles by the oil-in-water microemulsion reaction method. *Chemistry Letters,* 41**,** 1032-1034.

PENG, S. & WILLIAMS, R. A. 1998a. Controlled Production of Emulsions Using a Crossflow Membrane. *Particle & Particle Systems Characterization,* 15**,** 21-25.

PENG, S. J. & WILLIAMS, R. A. 1998b. Controlled Production of Emulsions Using a Crossflow Membrane: Part I: Droplet Formation from a Single Pore. *Chemical Engineering Research and Design,* 76**,** 894-901.

PERIYAT, P., MCCORMACK, D. E., HINDER, S. J. & PILLAI, S. C. 2009. One-pot synthesis of anionic (nitrogen) and cationic (sulfur) codoped high-temperature stable, visible light active, anatase photocatalysts. *The Journal of Physical Chemistry C,* 113**,** 3246-3253.

PIACENTINI, E., FIGOLI, A., GIORNO, L. & DRIOLI, E. 2010. 4.03 - Membrane Emulsification. *Comprehensive Membrane Science and Engineering.* Oxford: Elsevier.

PICCINNO, F., GOTTSCHALK, F., SEEGER, S. & NOWACK, B. 2012. Industrial production quantities and uses of ten engineered nanomaterials in Europe and the world. *Journal of Nanoparticle Research,* 14**,** 1109.

POINERN, G. E. J., ALI, N. & FAWCETT, D. 2011. Progress in nano-engineered anodic aluminum oxide membrane development. *Materials,* 4**,** 487-526.

RAMAMOORTHY, M., VANDERBILT, D. & KING-SMITH, R. 1994. First-principles calculations of the energetics of stoichiometric TiO 2 surfaces. *Physical Review B,* 49**,** 16721.

RAO, C. & KALYANIKUTTY, K. 2008. The liquid–liquid interface as a medium to generate nanocrystalline films of inorganic materials. *Accounts of chemical research,* 41**,** 489-499.

RAYNER, M. & TRÄGÅRDH, G. 2002. Membrane emulsification modelling: how can we get from characterisation to design? *Desalination,* 145**,** 165-172.

RAYNER, M., TRÄGÅRDH, G. & TRÄGÅRDH, C. 2005. The impact of mass transfer and interfacial expansion rate on droplet size in membrane emulsification processes. *Colloids and Surfaces A: Physicochemical and Engineering Aspects,* 266**,** 1-17.

REDDY, K. M., BARUWATI, B., JAYALAKSHMI, M., RAO, M. M. & MANORAMA, S. V. 2005. S-, N-and C-doped titanium dioxide nanoparticles: Synthesis, characterization and redox charge transfer study. *Journal of Solid State Chemistry,* 178**,** 3352-3358.

REYES-GARCIA, E. A., SUN, Y., REYES-GIL, K. & RAFTERY, D. 2007. 15N solid state NMR and EPR characterization of N-doped TiO2 photocatalysts. *The Journal of Physical Chemistry C,* 111**,** 2738-2748.

ROBBEN, L., ISMAIL, A. A., LOHMEIER, S. J., FELDHOFF, A., BAHNEMANN, D. W. & BUHL, J.-C. 2012. Facile Synthesis of Highly Ordered Mesoporous and Well Crystalline TiO2: Impact of Different Gas Atmosphere and Calcination Temperatures on Structural Properties. *Chemistry of Materials,* 24**,** 1268-1275.

SAHA, N. C. & TOMPKINS, H. G. 1992. Titanium nitride oxidation chemistry: An x-ray photoelectron spectroscopy study. *Journal of Applied Physics,* 72**,** 3072-3079.

SAKTHIVEL, S., JANCZAREK, M. & KISCH, H. 2004. Visible light activity and photoelectrochemical properties of nitrogen-doped TiO2. *The Journal of Physical Chemistry B,* 108**,** 19384-19387.

SAKTHIVEL, S. & KISCH, H. 2003. Daylight photocatalysis by carbon-modified titanium dioxide. *Angewandte Chemie International Edition,* 42**,** 4908-4911.

SANCHEZ-DOMINGUEZ, M., LIOTTA, L. F., DI CARLO, G., PANTALEO, G., VENEZIA, A. M., SOLANS, C. & BOUTONNET, M. 2010. Synthesis of CeO2, ZrO2, Ce0. 5Zr0. 5O2, and TiO2 nanoparticles by a novel oil-in-water microemulsion reaction method and their use as catalyst support for CO oxidation. *Catalysis today,* 158**,** 35-43.

SANTOS-CARBALLAL, D., ROLDAN, A., GRAU-CRESPO, R. & DE LEEUW, N. H. 2014. A DFT study of the structures, stabilities and redox behaviour of the major surfaces of magnetite Fe 3 O 4. *Physical Chemistry Chemical Physics,* 16**,** 21082-21097.

SARKAR, S., GUIBAL, E., QUIGNARD, F. & SENGUPTA, A. 2012. Polymer-supported metals and metal oxide nanoparticles: synthesis, characterization, and applications. *Journal of Nanoparticle Research,* 14**,** 715.

SATO, S. 1986. Photocatalytic activity of NOx-doped TiO2 in the visible light region. *Chemical physics letters,* 123**,** 126-128.

SCHMID, K. & RIEDIKER, M. 2008. Use of nanoparticles in Swiss industry: a targeted survey. ACS Publications.

SCHRÖDER, V., BEHREND, O. & SCHUBERT, H. 1998. Effect of dynamic interfacial tension on the emulsification process using microporous, ceramic membranes. *Journal of Colloid and Interface Science,* 202**,** 334-340.

SCHRÖDER, V. & SCHUBERT, H. 1999. Production of emulsions using microporous, ceramic membranes. *Colloids and Surfaces A: Physicochemical and Engineering Aspects,* 152**,** 103-109.

SCHUBERT, H. & ENGEL, R. 2004. Product and Formulation Engineering of Emulsions. *Chemical Engineering Research and Design,* 82**,** 1137-1143.

SCHWIRN, K., LEE, W., HILLEBRAND, R., STEINHART, M., NIELSCH, K. & GÖSELE, U. 2008. Self-ordered anodic aluminum oxide formed by H2SO4 hard anodization. *ACS nano,* 2**,** 302-310.

SELLONI, A. 2008. Crystal growth: anatase shows its reactive side. *Nature Materials,* 7**,** 613-615.

SHAIKHUTDINOV, S. K. & WEISS, W. 1999. Oxygen pressure dependence of the α-Fe 2 O 3 (0001) surface structure. *Surface Science,* 432**,** L627-L634.

SHI, J. & VERWEIJ, H. 2005. Synthesis and purification of oxide nanoparticle dispersions by modified emulsion precipitation. *Langmuir,* 21**,** 5570-5575.

SHKLOVER, V., NAZEERUDDIN, M.-K., ZAKEERUDDIN, S., BARBE, C., KAY, A., HAIBACH, T., STEURER, W., HERMANN, R., NISSEN, H.-U. & GRÄTZEL, M. 1997. Structure of nanocrystalline TiO2 powders and precursor to their highly efficient photosensitizer. *Chemistry of materials,* 9**,** 430-439.

SHUKLA, S., SEAL, S., VIJ, R. & BANDYOPADHYAY, S. 2003. Reduced activation energy for grain growth in nanocrystalline yttria-stabilized zirconia. *Nano letters,* 3**,** 397-401.

SILVA, P. S., MORELLI, S., DRAGOSAVAC, M. M., STAROV, V. M. & HOLDICH, R. G. 2017. Water in oil emulsions from hydrophobized metal membranes and characterization of dynamic interfacial tension in membrane emulsification. *Colloids and Surfaces A: Physicochemical and Engineering Aspects,* 532**,** 77-86.

SING, K. S. 1985. Reporting physisorption data for gas/solid systems with special reference to the determination of surface area and porosity (Recommendations 1984). *Pure and applied chemistry,* 57**,** 603-619.

SOLANS, C., IZQUIERDO, P., NOLLA, J., AZEMAR, N. & GARCIA-CELMA, M. J. 2005. Nano-emulsions. *Current Opinion in Colloid & Interface Science,* 10**,** 102-110.

SPYROPOULOS, F., LLOYD, D. M., HANCOCKS, R. D. & PAWLIK, A. K. 2014. Advances in membrane emulsification. Part B: recent developments in modelling and scale-up approaches. *Journal of the Science of Food and Agriculture,* 94**,** 628-638.

STILLWELL, M. T., HOLDICH, R. G., KOSVINTSEV, S. R., GASPARINI, G. & CUMMING, I. W. 2007. Stirred cell membrane emulsification and factors influencing dispersion drop size and uniformity. *Industrial & engineering chemistry research,* 46**,** 965-972.

SUÁREZ, M. A., GUTIÉRREZ, G., COCA, J. & PAZOS, C. 2013. Stirred tank membrane emulsification using flat metallic membranes: a dimensional analysis. *Chemical Engineering and Processing: Process Intensification,* 69**,** 31-43.

SUÁREZ, M. A., GUTIÉRREZ, G., MATOS, M., COCA, J. & PAZOS, C. 2014. Emulsification using tubular metallic membranes. *Chemical Engineering and Processing: Process Intensification,* 81**,** 24-34.

SULKA, G., STROOBANTS, S., MOSHCHALKOV, V., BORGHS, G. & CELIS, J.-P. 2002. Synthesis of well-ordered nanopores by anodizing aluminum foils in sulfuric acid. *Journal of the Electrochemical Society,* 149**,** D97-D103.

SULKA, G. D. & PARKOŁA, K. G. 2007. Temperature influence on well-ordered nanopore structures grown by anodization of aluminium in sulphuric acid. *Electrochimica Acta,* 52**,** 1880-1888.

SUPSAKULCHAI, A., MA, G., NAGAI, M. & OMI, S. 2002. Uniform titanium dioxide (TiO 2) microcapsules prepared by glass membrane emulsification with subsequent solvent evaporation. *Journal of microencapsulation,* 19**,** 425-449.

SUZUKI, K., FUJIKI, I. & HAGURA, Y. 1998. Preparation of corn oil/water and water/corn oil emulsions using PTFE membranes. *Food Science and Technology International, Tokyo,* 4**,** 164-167.

TEJA, A. S. & KOH, P.-Y. 2009. Synthesis, properties, and applications of magnetic iron oxide nanoparticles. *Progress in crystal growth and characterization of materials,* 55**,** 22-45.

THAMIDA, S. K. & CHANG, H.-C. 2002. Nanoscale pore formation dynamics during aluminum anodization. *Chaos: An Interdisciplinary Journal of Nonlinear Science,* 12**,** 240-251.

THANASUKARN, P., PONGSAWATMANIT, R. & MCCLEMENTS, D. J. 2004. Influence of emulsifier type on freeze-thaw stability of hydrogenated palm oil-in-water emulsions. *Food Hydrocolloids,* 18**,** 1033-1043.

THOMPSON, G. & WOOD, G. 1983. Anodic films on aluminum. *Treatise on Materials Science and Technology, Vol. 23. Corrosion: Aqueous Processed and Passive Films***,** 205-329.

TISEANU, C., COJOCARU, B., PARVULESCU, V. I., SANCHEZ-DOMINGUEZ, M., PRIMUS, P. A. & BOUTONNET, M. 2012. Order and disorder effects in nano-

ZrO 2 investigated by micro-Raman and spectrally and temporarily resolved photoluminescence. *Physical Chemistry Chemical Physics,* 14**,** 12970-12981.

TSUZUKI, T. 2009. Commercial scale production of inorganic nanoparticles. *International journal of nanotechnology,* 6**,** 567-578.

UMEBAYASHI, T., YAMAKI, T., TANAKA, S. & ASAI, K. 2003. Visible light-induced degradation of methylene blue on S-doped TiO2. *Chemistry Letters,* 32**,** 330-331.

VALENZUELA, R., FUENTES, M. C., PARRA, C., BAEZA, J., DURAN, N., SHARMA, S., KNOBEL, M. & FREER, J. 2009. Influence of stirring velocity on the synthesis of magnetite nanoparticles (Fe 3 O 4) by the co-precipitation method. *Journal of Alloys and Compounds,* 488**,** 227-231.

VAN BENSCHOTEN, J. E., REED, B. E., MATSUMOTO, M. R. & MCGARVEY, P. 1994. Metal removal by soil washing for an iron oxide coated sandy soil. *Water Environment Research,* 66**,** 168-174.

VENKATACHALAM, N., VINU, A., ANANDAN, S., ARABINDOO, B. & MURUGESAN, V. 2006. Visible light active photocatalytic degradation of bisphenol-A using nitrogen doped TiO2. *Journal of nanoscience and nanotechnology,* 6**,** 2499-2507.

VLADISAVLJEVIC, G. T. & SCHUBERT, H. 2002. Preparation and analysis of oil-in-water emulsions with a narrow droplet size distribution using Shirasu-porous-glass (SPG) membranes. *Desalination,* 144**,** 167-172.

VLADISAVLJEVIĆ, G. T. & SCHUBERT, H. 2003. Preparation of emulsions with a narrow particle size distribution using microporous α-alumina membranes. *Journal of dispersion science and technology,* 24**,** 811-819.

VLADISAVLJEVIĆ, G. T., TESCH, S. & SCHUBERT, H. 2002. Preparation of water-in-oil emulsions using microporous polypropylene hollow fibers: influence of some operating parameters on droplet size distribution. *Chemical Engineering and Processing: Process Intensification,* 41**,** 231-238.

VLADISAVLJEVIĆ, G. T. & WILLIAMS, R. A. 2005. Recent developments in manufacturing emulsions and particulate products using membranes. *Advances in colloid and interface science,* 113**,** 1-20.

VOHS, J. M. 1998. The surface science of metal oxides. By V. E. Henrich and P. A. Cox, Cambridge University Press, Cambridge, U.K., 1994, 464 pp. hardcover $99.95; paperback $39.95. *AIChE Journal,* 44**,** 502-503.

VRUBLEVSKY, I., PARKOUN, V., SOKOL, V., SCHRECKENBACH, J. & MARX, G. 2004. The study of the volume expansion of aluminum during porous oxide formation at galvanostatic regime. *Applied Surface Science,* 222**,** 215-225.

WAGDARE, N. A., MARCELIS, A. T. M., HO, O. B., BOOM, R. M. & VAN RIJN, C. J. M. 2010a. High throughput vegetable oil-in-water emulsification with a high porosity micro-engineered membrane. *Journal of Membrane Science,* 347**,** 1-7.

WAGDARE, N. A., MARCELIS, A. T. M., HO, O. B., BOOM, R. M. & VAN RIJN, C. J. M. 2010b. High throughput vegetable oil-in-water emulsification with a high porosity micro-engineered membrane. *Journal of Membrane Science,* 347**,** 1-7.

WANDELT, K. 1982. Photoemission studies of adsorbed oxygen and oxide layers. *Surface Science Reports,* 2**,** 1-121.

WANG, C.-W., TSENG, S.-J., PENG, S.-F., HWU, Y.-K. & LIN, C.-K. 2012. Functionalized polymer spheres via one-step photoinduced synthesis for antimicrobial activity and gene delivery. *Nanotechnology,* 23**,** 255103.

WANG, J., ZHU, W., ZHANG, Y. & LIU, S. 2007. An efficient two-step technique for nitrogen-doped titanium dioxide synthesizing: visible-light-induced photodecomposition of methylene blue. *The Journal of Physical Chemistry C,* 111**,** 1010-1014.

WANG, W., HOWE, J. Y. & GU, B. 2008. Structure and morphology evolution of hematite (α-Fe2O3) nanoparticles in forced hydrolysis of ferric chloride. *The Journal of Physical Chemistry C,* 112**,** 9203-9208.

WANG, Y., YANG, M., REN, L., ZHOU, W., YANG, K., YU, F., MENG, M., WU, S. & LI, S. 2016. Enhanced Raman Scattering in Copper-doped TiO 2 films. *Thin Solid Films,* 598**,** 311-314.

WEI, C., LIN, W. Y., ZAINAL, Z., WILLIAMS, N. E., ZHU, K., KRUZIC, A. P., SMITH, R. L. & RAJESHWAR, K. 1994. Bactericidal activity of TiO2 photocatalyst in aqueous media: toward a solar-assisted water disinfection system. *Environmental science & technology,* 28**,** 934-938.

WERNICK, S., PINNER, R. & SHEASBY, P. 1987. The surface treatments of aluminium and its alloys, ASM International and Finishing Publications Ltd. *Metals Park, Ohio***,** 773.

WHITE, W. B. 2005. Structure of Particles and the Structure of Crystals: Information from Vibrational Spectroscopy. *Journal of Ceramic Processing & Research,* 6**,** 1-9.

WILLEMS, V. D. W. 2005. Roadmap report on nanoparticles. *W&W Espana sl, Barcelona, Spain,* 157.

WILLIAMS, R., PENG, S., WHEELER, D., MORLEY, N., TAYLOR, D., WHALLEY, M. & HOULDSWORTH, D. 1998. Controlled Production of Emulsions Using a

Crossflow Membrane: Part II: Industrial Scale Manufacture. *Chemical Engineering Research and Design,* 76**,** 902-910.

WU, G., NISHIKAWA, T., OHTANI, B. & CHEN, A. 2007. Synthesis and Characterization of Carbon-Doped TiO2 Nanostructures with Enhanced Visible Light Response. *Chemistry of Materials,* 19**,** 4530-4537.

XIANG, B., ZHANG, Y., WANG, Z., LUO, X., ZHU, Y., ZHANG, H. & YU, D. 2005. Field-emission properties of TiO2 nanowire arrays. *Journal of Physics D: Applied Physics,* 38**,** 1152.

XU, J., LUO, G., CHEN, G. & WANG, J. 2005. Experimental and theoretical approaches on droplet formation from a micrometer screen hole. *Journal of Membrane Science,* 266**,** 121-131.

XU, T., ZANGARI, G. & METZGER, R. M. 2002. Periodic holes with 10 nm diameter produced by grazing Ar+ milling of the barrier layer in hexagonally ordered nanoporous alumina. *Nano Letters,* 2**,** 37-41.

XU, T. T., PINER, R. D. & RUOFF, R. S. 2003. An improved method to strip aluminum from porous anodic alumina films. *Langmuir,* 19**,** 1443-1445.

YAMASHITA, T. & HAYES, P. 2008. Analysis of XPS spectra of Fe2+ and Fe3+ ions in oxide materials. *Applied surface science,* 254**,** 2441-2449.

YANG, J., BAI, H., TAN, X. & LIAN, J. 2006. IR and XPS investigation of visible-light photocatalysis—Nitrogen–carbon-doped TiO 2 film. *Applied Surface Science,* 253**,** 1988-1994.

YANG, X., CAO, C., ERICKSON, L., HOHN, K., MAGHIRANG, R. & KLABUNDE, K. 2008. Synthesis of visible-light-active TiO 2-based photocatalysts by carbon and nitrogen doping. *Journal of Catalysis,* 260**,** 128-133.

YANG, Z. & ZHOU, A. 2007. Effects of nitrogen doping on microstructure and photocatalytic activity of nanocrystalline TiO 2 powders. *Journal of Wuhan University of Technology--Materials Science Edition,* 22**,** 457-461.

YAO, N. & WANG, Z. L. 2005. *Handbook of microscopy for nanotechnology*, Springer.

YOSHITAKE, H. & ABE, D. 2009. Raman spectroscopic study of the framework structure of amorphous mesoporous titania. *Microporous and Mesoporous Materials,* 119**,** 267-275.

YUAN, J., HE, F., SUN, D. & XIA, X. 2004. A simple method for preparation of through-hole porous anodic alumina membrane. *Chemistry of materials,* 16**,** 1841-1844.

ZALESKA, A. 2008. Doped-TiO2: a review. *Recent Patents on Engineering,* 2**,** 157-164.

ZARASKA, L., SULKA, G. D. & JASKUŁA, M. 2011. Anodic alumina membranes with defined pore diameters and thicknesses obtained by adjusting the anodizing duration and pore opening/widening time. *Journal of Solid State Electrochemistry,* 15**,** 2427-2436.

ZHANG, D., QI, L., MA, J. & CHENG, H. 2002. Formation of crystalline nanosized titania in reverse micelles at room temperature. *Journal of Materials Chemistry,* 12**,** 3677-3680.

ZHANG, H. & BANFIELD, J. F. 2005. Size dependence of the kinetic rate constant for phase transformation in TiO2 nanoparticles. *Chemistry of materials,* 17**,** 3421-3425.

ZHANG, L., CHENG, B., SHI, W. & SAMULSKI, E. T. 2005. In-situ electrochemical synthesis of 1-dimensional alumina nanostructures. *Journal of Materials Chemistry,* 15**,** 4889-4893.

ZHANG, L., HE, R. & GU, H.-C. 2006. Synthesis and kinetic shape and size evolution of magnetite nanoparticles. *Materials Research Bulletin,* 41**,** 260-267.

ZHANG, Z., GOODALL, J. B., MORGAN, D. J., BROWN, S., CLARK, R. J., KNOWLES, J. C., MORDAN, N. J., EVANS, J. R., CARLEY, A. F. & BOWKER, M. 2009. Photocatalytic activities of N-doped nano-titanias and titanium nitride. *Journal of the European Ceramic Society,* 29**,** 2343-2353.

ZHANG, Z., WANG, X., LONG, J., GU, Q., DING, Z. & FU, X. 2010. Nitrogen-doped titanium dioxide visible light photocatalyst: spectroscopic identification of photoactive centers. *Journal of Catalysis,* 276**,** 201-214.

ZHAO, L., ZHANG, H., XING, Y., SONG, S., YU, S., SHI, W., GUO, X., YANG, J., LEI, Y. & CAO, F. 2007. Morphology-controlled synthesis of magnetites with nanoporous structures and excellent magnetic properties. *Chemistry of Materials,* 20**,** 198-204.

ZHOU, W. & WANG, Z. L. 2007. *Scanning microscopy for nanotechnology: techniques and applications*, Springer science & business media.